

UNIVERSITY OF BIRMINGHAM

Adaptations to Skeletal Muscle Metabolism in Response to Altered NAD^+ Bioavailability

By

Lucy Oakey

A thesis submitted to the University of Birmingham

for the degree of

DOCTOR OF PHILOSOPHY

Institute of Metabolism and Systems Research
College of Medical and Dental Sciences
University of Birmingham
January 2020

UNIVERSITY OF
BIRMINGHAM

University of Birmingham Research Archive

e-theses repository

This unpublished thesis/dissertation is copyright of the author and/or third parties. The intellectual property rights of the author or third parties in respect of this work are as defined by The Copyright Designs and Patents Act 1988 or as modified by any successor legislation.

Any use made of information contained in this thesis/dissertation must be in accordance with that legislation and must be properly acknowledged. Further distribution or reproduction in any format is prohibited without the permission of the copyright holder.

Abstract

Skeletal muscle is central to energy homeostasis and metabolic health. Nicotinamide adenine dinucleotide (NAD^+) is a key modulator of energy metabolism and signalling. Reduced NAD^+ levels have been implicated in aging and in chronic disease states, such as diabetes. Therefore, approaches to augment NAD^+ have become popular.

This work aimed to use alternative models of differing NAD^+ bioavailability to investigate changes to molecular metabolism. Isotopic tracers were used and metabolic tracing was conducted to provide detailed analysis of central carbon metabolism. To achieve this combined 2D-^{1}H,^{13}C-heteronulcear single quantum coherence (HSQC) NMR spectroscopy and GCMS methods were employed. Further studies were conducted to explore the impact of altered NAD^+ metabolism *in vivo* using ^{13}C intravenous infusion and an exercise protocol.

Skeletal muscle showed efficient clearance of excess NAD^+ thought to maintain the tightly controlled NAD^+/NADH ratio. Metabolic tracing revealed elevated mitochondrial derived aspartate production in response to inhibition of nicotinamide phosphoribosyltransferase (NAMPT). An NAD^+ dependant block of glyceraldehyde phosphate dehydrogenase (GAPDH) was also evidenced through metabolite levels and label incorporation. This shows skeletal muscle retaining mitochondrial oxidative metabolism, suggesting differential effects of FK866 treatment on sub-cellular pyridine pools.

Overall the work highlighted how core carbon metabolic pathways are able to adapt to differing NAD^+ bioavailability in skeletal muscle.

For Tom, April and Archie

Acknowledgements

Firstly, I would like to say a huge thank you to my supervisor Prof. Gareth Lavery for all of his help and support throughout this project. He has been there to listen to my frustrations and excitement in equal measure and has been the best person to bounce ideas off to move this project forward. My second supervisor Dr. Craig Doig has also been instrumental in my journey. He is a wonderful teacher and his humour has kept me sane throughout.

I owe a huge thank you to Dr. Christian Ludwig. The metabolic tracing work within this thesis would not have been possible without Christian's continued support. I'd like to think that I provided some humour (not always intentional!) when teaching me these techniques and I'm so grateful for his patience.

Equally I would like to thank Dave, Yasir, Antje, Dean, Silke, Sam, Olivia and Ali who have all made my PhD experience great and have been brilliant colleagues. I must give a special thanks to Rachel. Thank you for such great memories, from being terrified to show you my work in lab meetings, to growing little humans together – I'm lucky to have had you around.

Mummy, not sure I can put into words! Thank you for everything – the unconditional love, endless belief and words of wisdom. You are my biggest cheerleader and to have you on the side lines is so special. Tim, Titch, Nana and Grandad - I hope you're proud (I'm finally getting a real job!).

Finally, I would like to thank my husband Tom. During my PhD we have had two beautiful children, April and Archie, and I am so blessed that we are on this journey

together. Tom is one of the hardest working men I know and despite him never getting passed the first line of this thesis he has given me the space and belief in myself to succeed.

Table of Contents

TABLE OF CONTENTS V

1. GENERAL INTRODUCTION 1

1.1. **Skeletal Muscle** 2
1.1.1. Structure and Function 2
1.1.2. Myogenesis 5
1.1.3. Fibre Type 7
1.1.4. Energy Metabolism in Skeletal Muscle 8
1.1.4.1. Phosphocreatine breakdown 10
1.1.4.2. Glycogen breakdown 10
1.1.4.3. Glucose metabolism 10
1.1.4.4. Fatty Acid β-Oxidation 12
1.1.4.5. Ketone Bodies 13
1.1.4.6. Amino Acid Oxidation 13
1.1.4.7. Oxidative Phosphorylation 13
1.1.5. Mitochondrial Metabolism 15

1.2. **NAD^+ History** 18
1.2.1. Sirtuins 21
1.2.2. ADP-ribose Transferases 23
1.2.3. cADP-ribose Synthases 25

1.3. **NAD^+ Biosynthesis** 26
1.3.1. *De Novo* Synthesis 27
1.3.2. Preiss-Handler Pathway 27
1.3.3. NAM Pathway 28
1.3.4. NR Pathway 32

1.4. **NAD^+ Compartmentalisation** 33

1.5. **NAD^+ in Skeletal Muscle** 35
1.5.1. Biosynthesis 35
1.5.2. Development and Regeneration 36
1.5.3. NAD^+ and Aging Muscle 37
1.5.4. NAD^+ and Metabolic Disease 39

1.6. **NAD^+ Augmentation** 40

1.7. **Thesis Rationale** 43

1.8. **Hypothesis** 44

1.9. **Aims** 44

2. GENERAL METHODS 46

2.1. **Tissue Culture 47**
2.1.1. C2C12 Cell Line 47
2.1.1.1. Proliferation 47
2.1.1.2. Differentiation 47
2.1.1.3. Freezing Down 48
2.1.1.4. Thawing Cells 48
2.1.2. Primary Muscle Cell Culture 48
2.1.2.1. Satellite Cell Isolation 49
2.1.2.2. Proliferation 50
2.1.2.3. Differentiation 50
2.1.3. Cell Treatments 51
2.1.3.1. Nicotinamide Riboside 51
2.1.3.2. Nicotinamide Mononucleotide 52
2.1.3.3. FK866 52

2.2. **Animal Sacrifice and Tissue Collection 52**

2.3. **Ribonucleic acid (RNA) Analysis 53**
2.3.1. RNA Extraction 53
2.3.2. RNA Quantification 54
2.3.3. Reverse Transcription of RNA 54
2.3.4. Real-time Polymerase Chain Reaction (qPCR) 55
2.3.4.1. TaqMan 55
2.3.4.2. SYBR Green 56
2.3.4.3. qPCR Analysis 58

2.4. **Protein Analysis 58**
2.4.1. Protein Extraction 58
2.4.2. Protein Quantification and Preparation 59
2.4.3. Immunoblotting 60

2.5. **High Resolution Respirometery 62**

2.6. **Nuclear Magnetic Resonance Spectroscopy 64**
2.6.1. Nuclear Spin 64
2.6.2. RF Pulse 67
2.6.3. Fourier Transformation 68
2.6.4. Chemical Shift 68
2.6.4.1. Splitting 71
2.6.5. 2D-NMR Spectroscopy 73
2.6.5.1. Carbon-Carbon Splitting 74
2.6.5.2. Stable Isotope Tracer Treatments 75
$^{13}C_2$-1,2-Glucose 75
$^{13}C_5$-Glutamine 75
$^{13}C_6$-Glucose 75
$^{13}C_{16}$-Sodium Palmitate 77
2.6.5.3. Limitations of NMR Spectroscopy 78
2.6.6. Experimental Methods 78
2.6.6.1. Extraction of Polar Metabolites 78

Extraction from Tissues 79
2.6.6.2. NMR Data Acquisition 79
2.6.6.3. NMR Data Analysis 80
1D-^{1}H-NMR spectra 80
2D-^{1}H,^{13}C-HSQC NMR spectra 81

2.7. **Gas Chromatography Mass Spectrometry 82**
2.7.1. Chemical Derivatisation 83
2.7.2. Gas Chromatography 84
2.7.3. Mass Spectrometry 85

2.8. **Liquid Chromatography Mass Spectrometry 86**
2.8.1. Extraction of Metabolites 86
2.8.2. LC-MS Data Acquisition and Analysis 87

2.9. **Fatty Acid Oxidation Measurement 88**

2.10. **NAD^+ Cycling Assay 89**

2.11. **Glycogen Assay 91**

2.12. ***In Vivo*** **Acute Exercise Study 92**
2.12.1. Acute Exercise Protocol 92
2.12.2. Indirect Calorimetry 94

2.13. ***In Vivo*** **Isotope Tracer Experiment 95**
2.13.1. $^{13}C_6$-Glucose Infusion 95

2.14. **Staining and Confocal Microscopy 96**

2.15. **Cell IQ 97**

2.16. **Statistical Analysis 97**

3. METABOLIC CONSEQUENCES OF NAD^+ EXCESS 99

3.1. **Introduction 100**

3.2. **Materials and Methods 102**
3.2.1. Cell Culture Treatments 102
3.2.1.1. Cell Culture Models 102
3.2.1.2. Cell Plating 102
3.2.1.3. $^{13}C_2$-1,2-Glucose Labelling 102
3.2.2. Extraction of Polar Metabolites for NMR Spectroscopy and GCMS Analysis 103
3.2.3. NMR and GCMS Data Acquisition 103
3.2.4. NAD^+ Cycling Assay 103
3.2.5. RNA Analysis 104
3.2.6. Acute Exercise Study 104
3.2.7. Data Analysis 104
3.2.7.1. GC-MS Analysis 104
3.2.7.2. 1D-^{1}H-NMR Analysis 105

3.2.7.3. 2D-^{1}H,^{13}C-NMR Analysis 105
3.2.7.4. Statistical Analysis 106

3.3. **Results 106**
3.3.1. NAD^+ Augmentation through NR Supplementation 106
3.3.2. NAD^+ Augmentation through NMN Supplementation 111
3.3.3. Comparison of NR and NMN as NAD^+ Precursors 112
3.3.4. NAD^+ Augmentation in Acute Exercise Study 115

3.4. **Discussion 119**
3.4.1. *In Vitro* augmentation of NAD^+ through NR and NMN Supplementation 119
3.4.2. Acute Exercise Study and the Metabolic Consequence of NR Supplementation 123

4. IMPACT OF NAD^+ DEPLETION ON CENTRAL CARBON METABOLISM 128

4.1. **Introduction 129**
4.1.1. Skeletal Muscle NAD^+ Biosynthesis 129
4.1.2. NAD^+ Decline 130

4.2. **Materials and Methods 131**
4.2.1. Cell Culture Treatments 131
4.2.1.1. Cell Culture Models 131
4.2.1.2. Cell Plating 131
4.2.1.3. $^{13}C_2$-1,2-Glucose Labelling 132
4.2.1.4. $^{13}C_5$-Glutamine Labelling 132
4.2.1.5. $^{13}C_{16}$-Palmitic Acid Labelling 132
4.2.1.6. $^{13}C_6$-Glucose Labelling 132
4.2.1.7. Malate-Aspartate Shuttle Inhibitor Treatment 133
4.2.2. Extraction of Polar Metabolites for NMR Spectroscopy and GC-MS Analysis 133
4.2.3. Extraction of Polar Metabolites for LCMS Analysis 133
4.2.4. High Resolution Respirometery 134
4.2.5. Fatty Acid Oxidation Assay 134
4.2.6. Glycogen Assay 135
4.2.7. Muscle Specific NAMPT KO Mouse Model 135
4.2.8. NMR and GCMS Data Acquisition 136
4.2.9. Data Analysis 136
4.2.9.1. GC-MS Analysis 136
4.2.9.2. 1D-^{1}H-NMR Analysis 136
4.2.9.3. 2D-^{1}H,^{13}C-NMR Analysis 136
4.2.9.4. Statistical Analysis 137

4.3. **Results 138**
4.3.1. Establishing Cell Models of NAD^+ Depletion and NR Rescue 138
4.3.2. Skeletal Muscle Bioenergetics Following NAD^+ Depletion 141
4.3.3. Effects of NAD^+ Depletion on Fatty Acid Oxidation 142
4.3.4. Effects of NAD^+ Depletion on Glycolytic and TCA Cycle Metabolites 144
4.3.5. NAD^+ Depletion Leads to Elevated Mitochondrial Derived Aspartate 150
4.3.5.1. Glutamine Use for Aspartate Production Following NAD^+ Depletion 153
4.3.5.2. Functional Use of Elevated Aspartate 154
4.3.5.3. Elevated Aspartate a Cellular Adaptation to NAD^+ Depletion 156

4.3.6. Primary Myotubes Express an Exaggerated Phenotype 158
4.3.7. Muscle Specific NAMPT KO Mouse Model 163

4.4. **Discussion 166**

5. CONSEQUENCE OF ELEVATED NRK PATHWAY ACTIVITY FOR PRIMARY MUSCLE CELL FUNCTION 176

5.1. **Introduction 177**

5.2. **Materials and Methods 179**
5.2.1. Cell Culture Treatments 179
5.2.1.1. Cell Culture Models 179
5.2.1.2. Cell Plating 179
5.2.2. RNA Analysis 179
5.2.3. NAD^+ Cycling Assay 180
5.2.4. Extraction of Polar Metabolites for GCMS Analysis 180
5.2.5. GCMS Data Acquisition 181
5.2.6. Protein Analysis 181
5.2.7. Staining and Confocal Microscopy 181
5.2.8. Cell IQ 182
5.2.9. Data Analysis 182
5.2.9.1. GC-MS Analysis 182
5.2.9.2. Statistical Analysis 183

5.3. **Results 183**
5.3.1. NAD^+ Biosynthesis Enzymes 183
5.3.2. NR Supplementation 185
5.3.3. Primary Model Imaging 187
5.3.4. Primary Development 188
5.3.5. Metabolomics 193

5.4. **Discussion 196**

6. FINAL DISCUSSION 201

7. APPENDIX A - ASSAY ON DEMAND TAQMAN PROBES 208

8. APPENDIX B – SYBR GREEN PRIMER SEQUENCE 209

9. APPENDIX C - ASSOCIATED MANUSCRIPT 210

10. REFERENCES 228

Table of Figures

Figure 1.1. Skeletal Muscle Structure. 3
Figure 1.2. Sliding Filament Theory 4
Figure 1.3. Embryonic Myogenesis. 6
Figure 1.4. Energy Metabolism 9
Figure 1.5. Glycolysis 11
Figure 1.6. Oxidative Phosphorylation 14
Figure 1.7. Mitochondrial Transcriptional and Post-Translational Adaptations to Endurance Exercise 17
Figure 1.8. Structure of NAD^+ 19
Figure 1.9. NAD^+ as a Redox Molecule 21
Figure 1.10. Cleavage of NAD^+ 21
Figure 1.11. NAD^+-consuming Enzymes 25
Figure 1.12. NAD^+ Synthesis and Consumption 26
Figure 1.13. De Novo NAD^+ Synthesis and the Preiss-Handler Pathway 28
Figure 1.14. NAMPT Salvage Pathway 28
Figure 1.15. NR as an NAD^+ Precursor 32
Figure 1.16. Subcellular Localisation of NAD^+ 35
Figure 1.17. NAD^+ in Aging and Metabolic Decline 39
Figure 1.18. NAD^+ Augmentation as a Therapeutic 41
Figure 2.1. Primary Skeletal Muscle Differentiation 50
Figure 2.2. Differentiated Primary Myotubes 51
Figure 2.3. SYBR Green Melt Curve 57
Figure 2.4. High Resolution Respirometery Graph 63
Figure 2.5. Carbon Isotope Examples 65
Figure 2.6. Spin States 66
Figure 2.7. Generation of a Signal 67
Figure 2.8. Unit Conversion 69
Figure 2.9. NAD^+ Quantification 70
Figure 2.10. Different Chemical Shifts 71
Figure 2.11. Splitting 72
Figure 2.12. Carbon-Carbon Splitting 74
Figure 2.13. $^{13}C_2$-1,2-Glucose Labelling Patterns 76
Figure 2.14. $^{13}C_5$-Glutamine Labelling Patterns 77
Figure 2.15. Multiplet Analysis of Carbon 2 of Glutamate 82
Figure 2.16. Gas Chromatography – Mass Spectrometry 83
Figure 2.17. Combined NMR and GCMS Analysis 86
Figure 2.18. Fatty Acid Oxidation Assay 89
Figure 2.19. NAD^+ Cycling Assay 90
Figure 2.20. Acclimatisation Protocol 93
Figure 2.21. Acute Exercise Protocol 94
Figure 2.22. Indirect Calorimetry 95
Figure 3.1. NAD^+ Augmentation in C2C12 Myotubes 108
Figure 3.2. Energetic Consequences of Excess NAD^+ 109
Figure 3.3. Percentage Change of NAD^+ and NADH 110
Figure 3.4. Gene Expression Analysis of NR treated C2C12s 111
Figure 3.5. NMN Supplementation of C2C12s 112
Figure 3.6. NAD^+ Augmentation in C2C12 and Primary Myotubes 114

Figure 3.7. Effect of Excess NAD^+ on Glycolysis and TCA Cycle Metabolism 115
Figure 3.8. Respiratory Exchange Ratio for Acute Exercise Mouse NAD^+ Augmentation Study 116
Figure 3.9. Energy Expenditure for Acute Exercise Mouse NAD^+ Augmentation Study 117
Figure 3.10. NAD^+ Quantification and Gene Expression Analysis for Acute Exercise Mouse NAD+ Augmentation Study 118
Figure 4.1. Inhibition of NAD^+ Biosynthesis in C2C12s 139
Figure 4.2. Chemical Inhibition of NAD^+ Biosynthesis in Primary Myotubes 140
Figure 4.3. Bioenergetics of C2C12s in Response to NAD^+ Depletion 142
Figure 4.4. Sodium Palmitate Labelling in C2C12s 143
Figure 4.5. Fatty Acid Oxidation following NAD^+ Depletion 144
Figure 4.6. Glycolytic Outputs, Lactate and Alanine, Unaffected by NAD^+ Depletion 145
Figure 4.7. Block in Glycolysis at GAPDH Following NAD^+ Depletion 147
Figure 4.8. Diagrammatic Representation of Block in Glycolysis 148
Figure 4.9. Fructose-6-phosphate Labelling Following NAD^+ Depletion 149
Figure 4.10. Glycolysis Pathway Analysis Following NAD^+ Depletion 150
Figure 4.11. Aspartate Multiplet Analysis 151
Figure 4.12. Aspartate Production Significantly Altered with NAD^+ Depletion 152
Figure 4.13. Pathway Utilisation for Aspartate Production Significantly Altered with NAD^+ Depletion 153
Figure 4.14. Glutamine Contribution to Aspartate Production 154
Figure 4.15. Aspartate Use for Nucleotide Synthesis 155
Figure 4.16. C2C12 Response to MAS Inhibitor Treatment 157
Figure 4.17. Aspartate Changes in Response to MAS Inhibitor Treatment 158
Figure 4.18. Primary Myotubes Show Elevated Label Incorporation into TCA Cycle Metabolites with NAD^+ Depletion 159
Figure 4.19. Primary Myotubes show Increased Glutamate Labelling 161
Figure 4.20. Primary Myotubes have an Exaggerated Phenotype 162
Figure 4.21. 1D-^{1}H-NMR Spectroscopy Analysis of Quadriceps Muscle from NAMPT KO Model 164
Figure 4.22. GCMS Ion Count Analysis of Quadriceps Muscle from NAMPT KO Model 165
Figure 5.1. NAD^+ Biosynthetic Enzymes 184
Figure 5.2. NR Supplementation 186
Figure 5.3. Primary Myotube Imaging 187
Figure 5.4. Gene Expression Analysis of NAD Biosynthetic Genes During Development 189
Figure 5.5. Gene Expression Analysis of Developmental Markers and Metabolic Genes 190
Figure 5.6. Live Cell Imaging Analysis 192
Figure 5.7. NAD+ Manipulation in NRK2 Tg Primary Model 194
Figure 5.8. NAD^+ Manipulation in NRK2 KO Primary Model 195
Figure 6.1. Adaptations to Skeletal Muscle Metabolism in Response to Altered NAD Bioavailability. 207

List of Tables

Table 1.1. - Fibre Types in Rodents and Humans [26]..... 8

Abbreviations

1D	1 Dimensional
1-MNA	Methylated nicotinamide
2D	2 Dimensional
5'-NTs	5'-nucleotidases
ADP	Adenosine diphosphate
ADPR	ADP-ribose
AMPK	AMP-activated protein kinase
ANCOVA	Analysis of covariance
ANOVA	Analysis of Variance
AO	L-aspartate oxidase
AOAA	Aminooxyacetic acid
APS	Ammonium persulfate
ART1	ADP-ribosyltransferase 1
ARTs	ADP-ribose transferases
ATF2	Activating transcription factor 2
ATP	Adenosine triphosphate
AU	Arbitrary units
B_0	External magnetic field strength
BSA	Bovine serum albumin
Ca^{2+}	Calcium
cADP	Cyclic-ADP
cDNA	Complementary DNA
CEE	Chicken embryo extract
Col1a1	Collagen Type I Alpha 1 Chain
Cox7a1	Cytochrome C Oxidase Subunit 7A1
Cr	Creatine
dCt	delta Ct
ddCt	delta dCt
DM	Differentiation medium
DMEM	Dulbecco's Modified Eagle's Medium
dNTPs	Deoxynucleotide triphosphates
DSS	4,4-dimethyl-4-silapentane-1-sulfonic acid
ECL	Electrochemiluminescence
ECM	Extracellular matrix
EDTA	Ethylenediaminetetraacetic acid
EI	Electron ionisation
ETC	Electron transport chain
FAD(H_2)	Flavin adenine dinucleotide
FBS	Foetal bovine serum

FCCP	Carbonylcyanide-*4*(trifluoromethoxy)phenylhydrazone
FGF	Fibroblast growth factor
FID	Free Induction Decay
FT	Fourier Transformation
G3P	Glyceraldehyde-3-phosphate
GADPH	Glyceraldehyde phosphate dehydrogenase
GCMS	Gas chromatography – Mass spectrometry
GM	Growth media
HCl	Hydrochloric acid
HDLs	High density lipoproteins
HFD	High fat diet
HS	Horse serum
HSQC	Heteronuclear Single Quantum Coherence
Hz	Hertz
I	Nuclear spin
IP	Intraperitoneal
ITGA7	Integrin alpha7
m/z	Mass-to-charge ratio
MAS	Malate-aspartate shuttle
MID	Mass isotopomer distribution
mM	Millimolar
MRFs	Myogenic regulatory transcription factors
MTBSTFA	N-tertbutyldimethylsilyl-N-methyltrifluoroacetamide
mtDNA	Mitochondrial DNA
MYF5	Myogenic factor 5 protein
MYF6	Myogenic factor 6 protein
MYOD	Myogenic differentiation protein 1
MYOG	Myogenin
NA	Nicotinic acid
NAADP	Nicotinic acid adenine dinucleotide phosphate
NaCl	Sodium chloride
NAD(H)	Nicotinamide adenine dinucleotide
NADK	Nicotinamide adenine dinucleotide kinase
NADP(H)	Nicotinamide adenine dinucleotide phosphate
NADS	Nicotinamide adenine dinucleotide synthase
NAM	Nicotinamide
NaMN	Nicotinic acid mononucleotide
NAMPT	Nicotinamide phosphoribosyltransferase
NaPRT	Nicotinic acid phosphoribosyltransferase
NaR	Nicotinic acid riboside
NFW	Nuclease free water

NMN	Nicotinamide mononucleotide
NMNAT	Nicotinamide mononucleotide adenylyltransferase
NMR	Nuclear magnetic resonance
Nmrk1	Nicotinamide riboside kinase 1 (gene)
Nmrk2	Nicotinamide riboside kinase 2 (gene)
NNMT	Nicotinamide n-methyltransferase
NOX	NADPH oxidases
NR	Nicotinamide riboside
NRF1-2	Nuclear respiratory factors 1 and 2
NRK1	Nicotinamide riboside kinase 1 (protein)
NRK2	Nicotinamide riboside kinase 2 (protein)
NRK2 KO	Nicotinamide riboside kinase 2 Knock Out
NRK2 Tg	Nicotinamide riboside kinase 2 Over Expresser
P/S	Penicillin/Streptomycin
P38 MAPK	p38 mitogen-activated protein kinase
PAR	Poly-ADP-ribose
PARPs	Poly-ADP-ribose polymerases
PBEF	Pre-B cell colony enhancing factor
PCr	Phosphocreatine
PGC1α	Peroxisome proliferator-activated receptor gamma, coactivator 1 alpha
Pi	Inorganic phosphate
Ppm	Parts per million
PPP	Pentose phosphate pathway
PRPP	Phosphoribosyl pyrophosphate
PTMs	Post-translational modifications
QA	Quinolinic acid
QAPRT	Quinolinic acid phosphoribosyltransferase
qPCR	Real-time Polymerase Chain Reaction
QS	Quinolinate synthase
RER	Respiratory exchange ratio
RF	Radiofrequency
RIPA	Radioimmunoprecipitation assay
RNA	Ribonucleic acid
ROS	Reactive oxygen species
Rpm	Revolutions per minute
SDS	Sodium dodecyl sulfate
SDS-PAGE	SDS – polyacrylamide gel electrophoresis
SIRT1	Sirtuin-1
TA	Tibialis anterior
TBDMSCl	Tertbutyldimethyl-chlorosilane
TBST	Tris-buffered saline with tween

TCA cycle	Tricarboxylic acid cycle
TEMED	Tetramethylethylenediamine
TFAM	Mitochondrial transcription factor A
TG	Triglycerides
tNAD	Total NAD; NAD^+ & NADH
tNADP	Total NADP; $NADP^+$ & NADPH
Trp	Tryptophan
UTP	Uridine triphosphate
v/v	Volume/volume
w/v	Weight/volume
Λ	Gyromagnetic ratio

1. General Introduction

This thesis will explore adaptations to skeletal muscle metabolism in response to altered nicotinamide adenine dinucleotide (NAD^+) levels. Skeletal muscle is a key organ involved in the maintenance of metabolic health through its' contribution to basal energy metabolism [1,2]. NAD^+ is a crucial cofactor for many metabolic reactions throughout the cell and a decline in the molecule has been associated with aging and metabolic disease [3–6]. Understanding the interplay between NAD^+ and carbon metabolism will help further our understanding of the metabolic consequence of NAD^+ decline.

1.1. Skeletal Muscle

Skeletal muscle is the largest organ in the human body, representing around 40 % of total body mass in a lean, healthy adult [7,8]. Skeletal muscle is under voluntary control of the somatic nervous system and is essential for locomotion and maintenance of body posture [9,10]. In addition to the generation of motile force, skeletal muscle has other significant functions including; contribution to basal energy metabolism, a nutrient store for carbohydrates and amino acids, and the generation of heat to maintain core body temperature [1,2].

1.1.1. Structure and Function

The architecture of skeletal muscle is well defined; each individual muscle is encased in the epimysium, a collagenous tissue layer - responsible for reducing friction against other muscles and bones [1,9,11,12]. Enclosed within the epimysium are bundles of muscle fibres referred to as fascicles, these are surrounded by a sheath of

collagen-containing connective tissue known as the perimysium. The final layer of connective tissue within muscles is the endomysium, which cover the individual muscle fibres [1], as shown in figure 1.1.

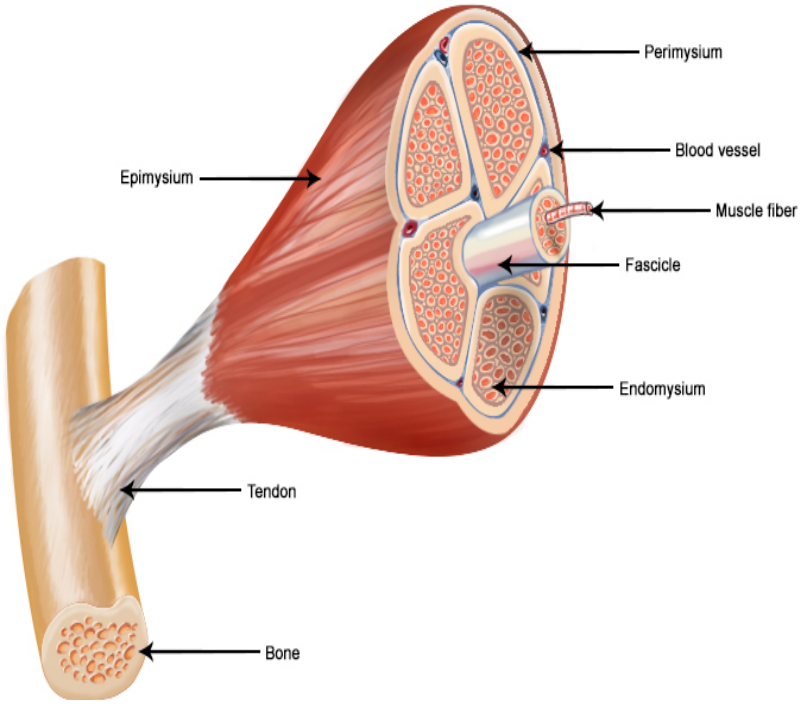


Figure 1.1. Skeletal Muscle Structure.
A layer of connective tissue called the epimysium surrounds each muscle in the body, the bundles of muscle fibres are enclosed in the perimysium and the individual fibres are sheathed in the endomysium. These collagenous connective tissues are continuous with the muscle tendon, which anchors the muscle to the bone [7].

Muscle fibres are multinucleated, elongated cells composed of aligned sarcomeres that create the striated appearance characteristic of skeletal muscle [13]. The sarcomere is the contractile unit of the muscle and combines both thin and thick filaments. The thin filaments form an actin, tropomyosin, troponin complex and the thick filaments are composed of myosin molecules [14,15]. As an action potential spreads across the sarcolemma, the cell membrane of the muscle, the t-tubules are depolarised causing a release of calcium (Ca^{2+}) from the sarcoplasmic reticulum [16]. The Ca^{2+} binds to troponin causing a conformational change in tropomyosin allowing

actin to interact with the myosin heads. Adenosine triphosphate (ATP) binds and breaks the actin-myosin cross bridge, the subsequent hydrolysis of ATP results in a change in angle of the myosin head and the formation of an actin-myosin bond. Release of adenosine diphosphate (ADP) and an inorganic phosphate (Pi) moves the myosin head relative to the actin filament, causing a shortening of the sarcomere, known as the power stroke. Providing there is enough ATP available, and the level of Ca^{2+} in the sarcoplasm remains high, another ATP is bound to the actin-myosin complex resulting in dissociation and the cycle is repeated, this is referred to as 'the sliding-filament theory', figure 1.2. [17,18].

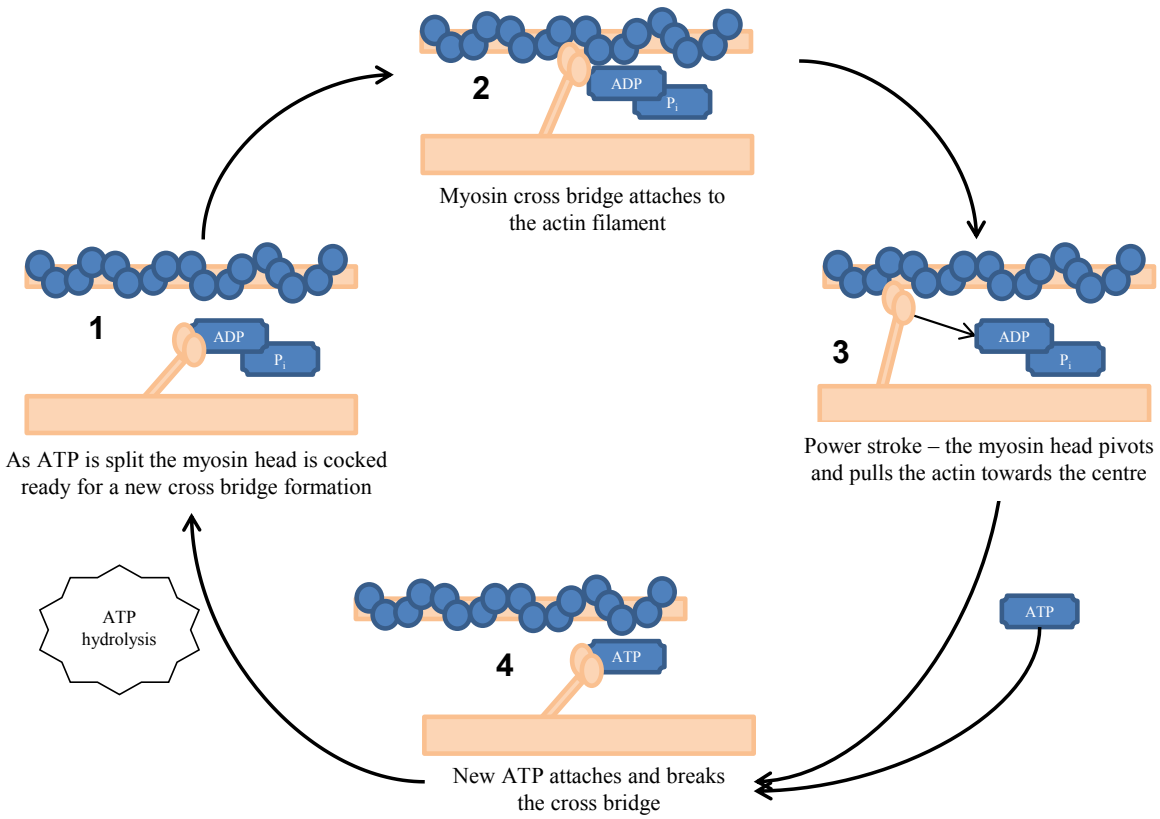


Figure 1.2. Sliding Filament Theory

Muscle contraction occurs through shortening of the sarcomeres. **1)** The hydrolysis of ATP to ADP and Pi resets the myosin head group ready to form **2)** a cross bridge between actin and myosin, release of the ADP and Pi causes the **3)** power stroke that moves the actin filament relative to myosin. **4)** Depending on the availability of ATP a new ATP molecule binds and causes the cross bridge to break and the cycle to start again.

1.1.2. Myogenesis

Mesoderm-derived embryonic progenitors are assigned to a myogenic lineage and proliferate to form mononucleate myoblasts, some of which will terminally differentiate and fuse together to create multinucleated myotubes; a simplified diagram can be seen in figure 1.3. [19]. Regeneration of muscle following injury, disease or after training depends on myogenic precursors called satellite cells, which are predominately quiescent and are located beneath the basal lamina [20]. Upon activation, satellite cells are able to proliferate and generate myoblasts which can fuse with each other or with existing myofibres to repair injured tissue [21]. Importantly, satellite cells are able to both regenerate muscle but are also responsible for maintaining their population through self-renewal [22]. This means that upon activation satellite cells will proliferate, undergoing asymmetric self-renewal [23]. Some cells become muscle progenitor cells which are committed to differentiation and some will maintain Pax7 expression and remain as satellite cells conserving their potential to regenerate muscle [24].

A number of myogenic regulatory transcription factors (MRFs) are involved in this process; myogenic factor 5 protein (MYF5), myogenic differentiation protein 1 (MYOD), myogenin (MYOG), and myogenic factor 6 protein (MYF6) are all expressed during skeletal muscle development. A number of studies have observed the redundancies of these proteins, with different knockout models displaying normal skeletal muscle phenotypes, highlighting the ability of alternative proteins to compensate for the loss of key MRFs [25].

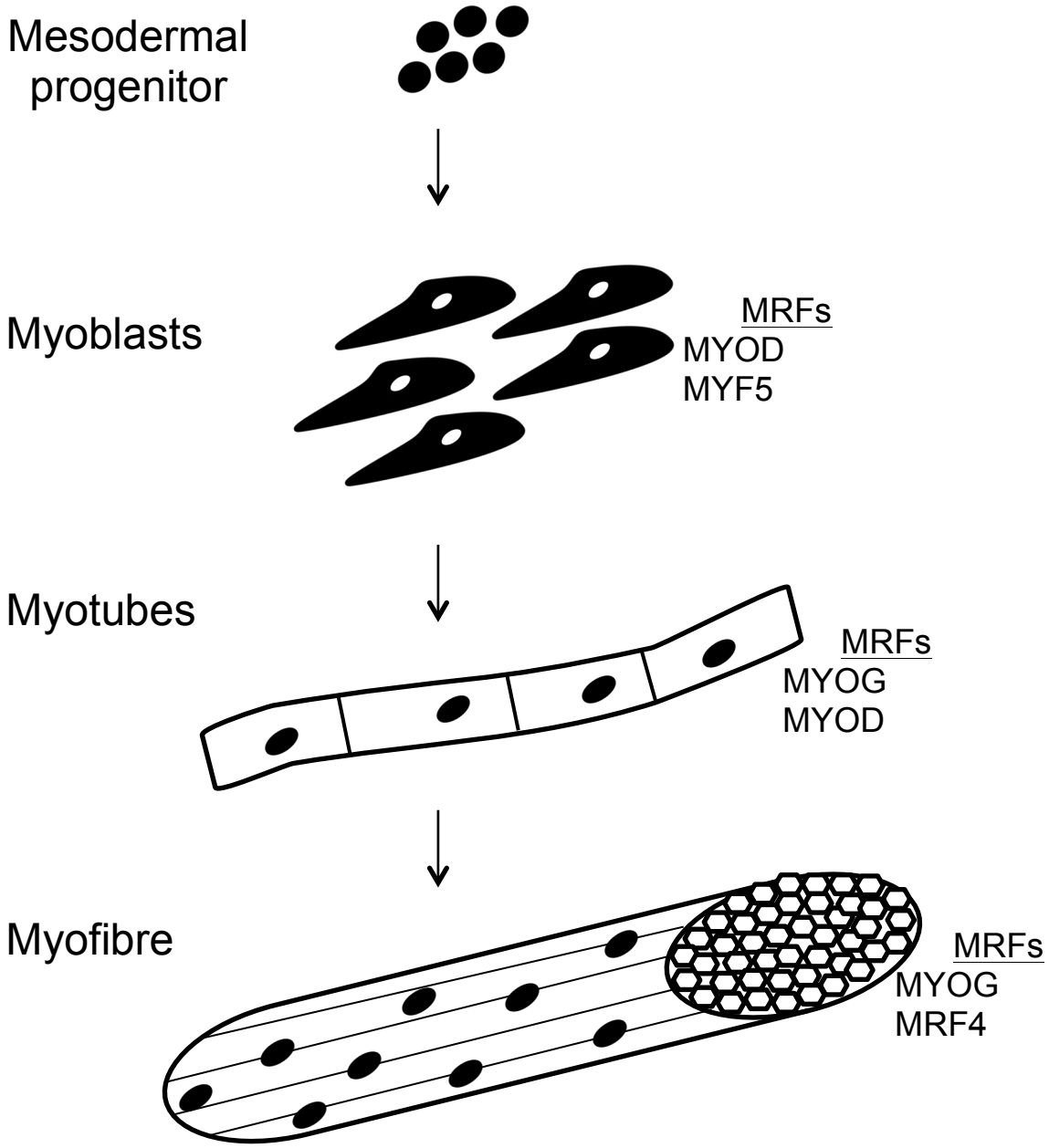


Figure 1.3. Embryonic Myogenesis.
The process of myogenesis begins with a mesodermal progenitor cell, which undergoes proliferation, expression of certain myogenic regulatory transcription factors (MRFs) commit the cell to terminal differentiation. The myoblasts fuse together to form myotubes before finally a myofibre and mature muscle is produced.

1.1.3. Fibre Type

Skeletal muscles are heterogeneous in cell type and fibre type and are composed of fibres with different structural and functional properties [26]. Fibre types are classified based on the isoform of myosin heavy chain present which influences the ATPase activity of the myosin and alters the speed of muscle contraction [27,28]. Type I, type IIa and IIx (IIb in rodents) fibres are found in muscle, with the main differences outlined in table 1.1.

Each muscle is comprised of a mixture of fibre types; the type with the highest percentage contribution defines the metabolic profile of that muscle. For example, postural muscles are composed of predominately type I fibres, whereas phasic muscles responsible for evoking movement have a high type II fibre contribution [29]. Type I fibres are slower in their kinetic response to force than type IIa/x fibres with a high myoglobin content and rich blood supply to support oxidative phosphorylation [30–32]. It has been reported that muscles are able to adapt their metabolic phenotype based on the contractile demand and therefore, alter their phenotypic profile, switching from one fibre type to another [31,33,34].

Table 1.1. - Fibre Types in Rodents and Humans [31]

	Fibre type			
Properties	Type I fibres	Type IIa fibres	Type IIx fibres	Type IIb fibres
Myosin heavy chain	MYH7	MYH2	MYH1	MYH4
Contraction time	Slow	Moderately fast	Fast	Very fast
Resistance to fatigue	High	Fairly high	Moderate	Low
Activity used for	Aerobic	Long-term anaerobic	Short-term anaerobic	Short-term anaerobic
Size of motor neuron	Small	Intermediate	Large	Very Large
Maximum duration of use	Hours	< 30 minutes	< 5 minutes	< 1 minute
Power produced	Low	Medium	High	Very high
Mitochondrial density	Very high	High	Medium	Low
Oxidative capacity	High	High	Intermediate	Low
Glycolytic capacity	Low	High	High	High
Major storage fuel	Triglycerides	Creatine phosphate, glycogen	ATP, creatine phosphate, glycogen (little)	ATP, creatine phosphate

1.1.4. Energy Metabolism in Skeletal Muscle

Skeletal muscle is unique in its ability to adapt its metabolism to suit the functional demand, possessing the ability to increase its metabolic rate dependant on the exercise intensity and duration [35]. Contraction of skeletal muscle requires ATP which is utilised by two main processes; the dissociation of the actin-myosin complex to trigger sarcomere shortening and for relaxation of the muscle through sarcoplasmic reticulum Ca^{2+} pumps [36,37]. Cells store around 8 mM of ATP but there is a high turnover therefore it is imperative that muscles are able to replenish the levels rapidly to allow for continued contraction during high energy demand [38].

Glucose, fatty acids and amino acids are the main substrates available to maintain energy homeostasis within an organism and can be used interchangeably depending on their availability or in response to given hormonal/neuronal cues, figure 1.4 [39,40]. Fatty acid oxidation is a main source of energy for skeletal muscle at rest and during mild-intensity exercise, with glucose oxidation surpassing fatty acid oxidation with increased exercise intensity [41].

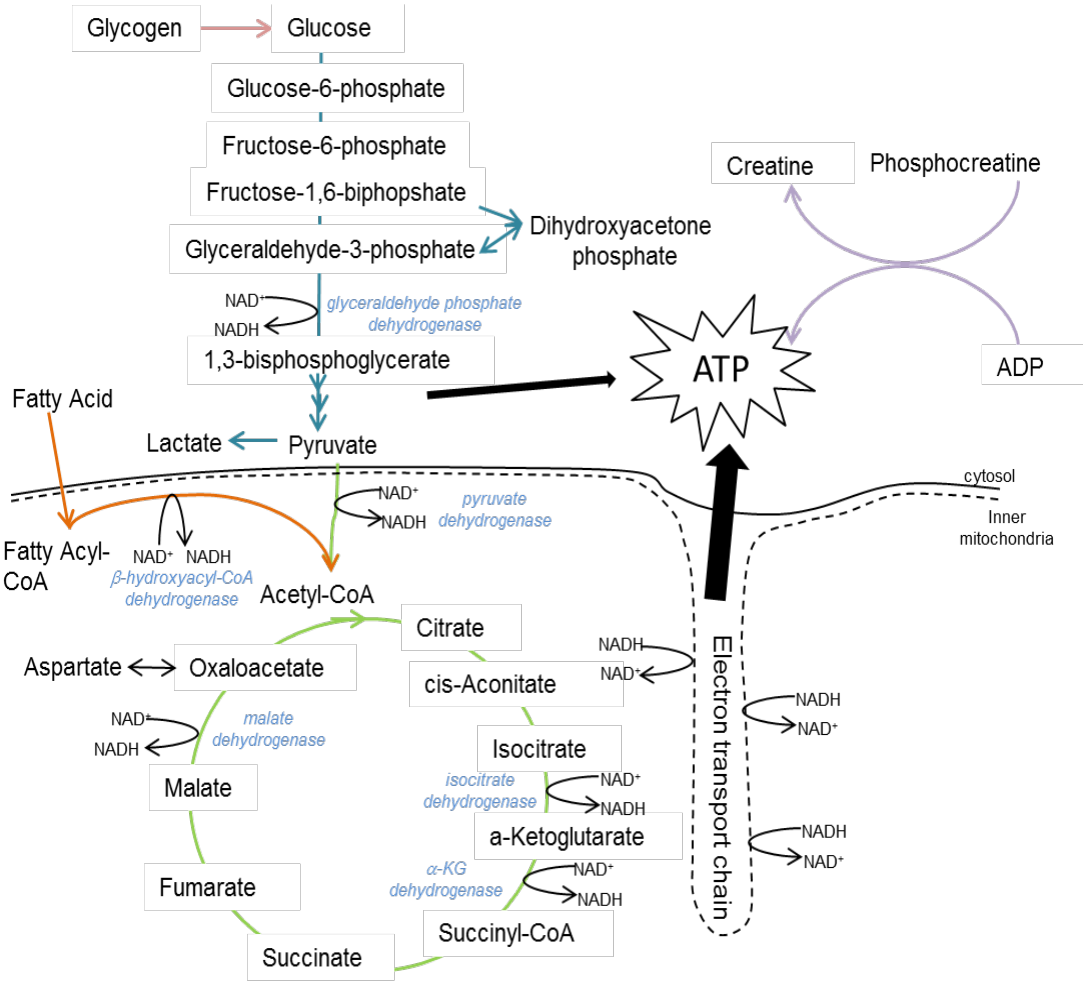


Figure 1.4. Energy Metabolism

The route to ATP production via phosphocreatine (purple arrows), glycogen (pink arrow), glucose (blue arrows) and fatty acids (orange arrows). During aerobic respiration, when there is oxygen present the pyruvate produced at the end of glycolysis passes through into the mitochondria and enters the TCA cycle (green). In cases of low oxygen, anaerobic respiration, the pyruvate is instead metabolised to lactate. This process is useful for maintaining NAD^+ levels for continual glycolysis but will result in a build-up of lactic acid within the muscle.

1.1.4.1. Phosphocreatine breakdown

Creatine kinase acts as a low-level ADP sensor and is consequently activated when ATP utilisation exceeds production, it catalyses the hydrolysis of phosphocreatine (PCr) resulting in the release of a phosphate group which is able to convert ADP to ATP [42–44]. The enzyme is localised at sites of high energy turnover within the cell, for example, it is intimately associated with the myosin ATPase allowing for regeneration of ATP directly at the source of depletion [45]. Upon initiation of exercise the levels of PCr are rapidly reduced, with myocytes utilising this as their primary energy source for 5-6 seconds before carbohydrate metabolism commences [46,47].

1.1.4.2. Glycogen breakdown

Glycogenolysis is the breakdown of glycogen stores consequently mobilising glucose-1-phosphate, which is subsequently converted to glucose-6-phosphate for use in glycolysis. As the duration of exercise prolongs the rate of glycogenolysis declines due to decreased glycogen levels, with alternative fuel sources used [48]. Glycogen phosphorylase, the catalyst involved, is activated through Ca^{2+} signalling in response to increased Pi, which is a marker of PCr breakdown and indicative of the onset of exercise, and adrenaline which is increased during the 'fight or flight' response [49–51].

1.1.4.3. Glucose metabolism

Glycolysis is the anaerobic breakdown of glucose into pyruvate within the cytosol, figure 1.5. This process is responsible for a net gain of two ATP molecules for every molecule of glucose and is the first step in cellular respiration. Glyceraldehyde phosphate dehydrogenase (GAPDH) is NAD^+ dependent, with NAD^+ reduced to NADH when converting glyceraldehyde-3-phosphate (G3P) to 1,3-bisphosphoglycerate [2].

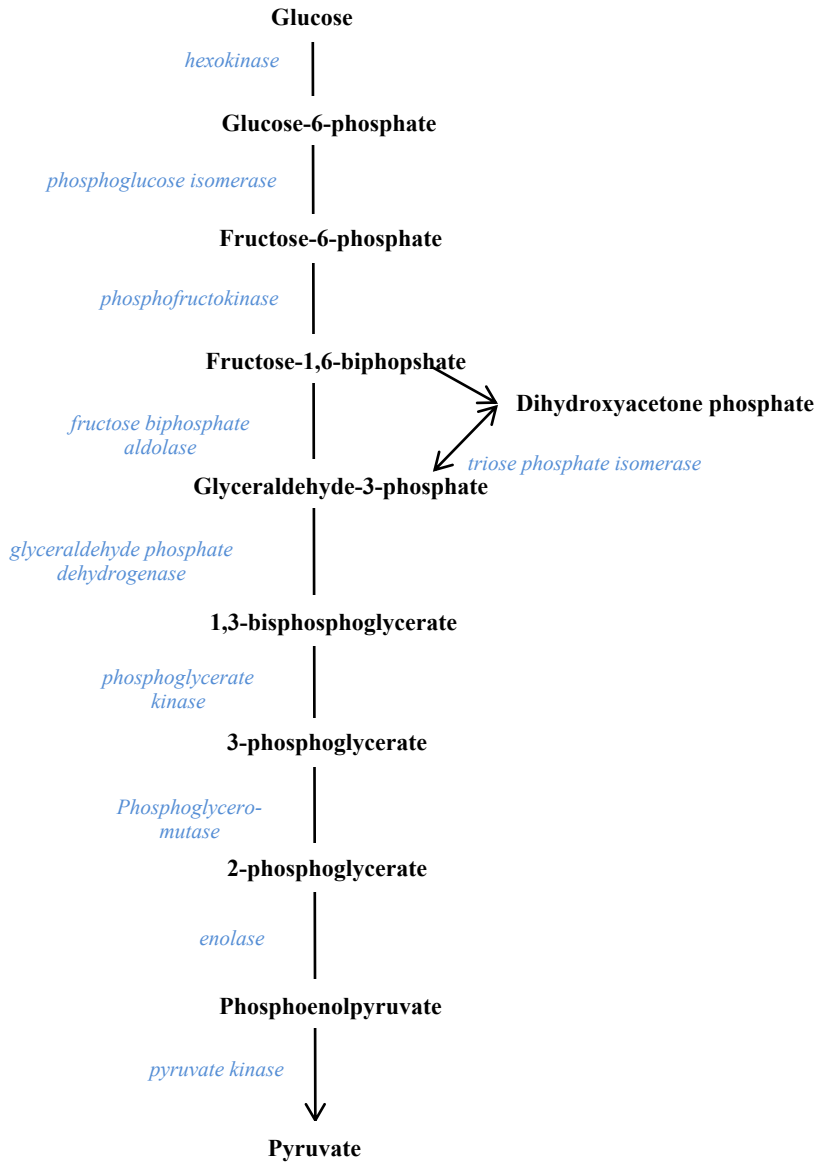


Figure 1.5. Glycolysis
Glucose is broken down by a sequence of enzymes to pyruvate. Fructose-1,6-biphosphate is cleaved from a 6 carbon molecule into two 3 carbon molecules, resulting in a doubling of the products downstream of it. Glyceraldehyde phosphate dehydrogenase is an NAD^+-dependant enzyme and therefore, 2 NAD^+ molecules are required to metabolise 1 molecule of glucose.

In anaerobic conditions pyruvate is converted into lactate within the cytosol, via lactate dehydrogenase, in order to generate NAD^+ to maintain glycolytic flux and ATP generation [52]. An alternative outcome for pyruvate is the addition of an amine group, catalysed by alanine transaminase, to produce alanine. Alanine is expelled from the

muscle cell and is transported, via the blood, to the liver where the reverse reaction occurs; the amine group enters the urea cycle and pyruvate is utilised for gluconeogenesis [53,54].

Pyruvate can also enter the mitochondria and either be converted to acetyl-CoA via pyruvate dehydrogenase or carboxylated to form oxaloacetate via pyruvate carboxylase in the presence of oxygen. Acetyl-CoA joins to oxaloacetate and initiates the tricarboxylic acid (TCA) cycle, which is a series of enzymatic reactions resulting in NADH and flavin adenine dinucleotide ($FADH_2$) production [55,56]. The current estimates suggest an ATP yield of 2 molecules from glycolysis, 2 from the TCA cycle and 34 from the electron transport chain, per molecule of glucose [57].

1.1.4.4. Fatty Acid β-Oxidation

Fatty acid oxidation is the catabolism of free fatty acids to produce acetyl-CoA within the mitochondria. This involves mobilisation of fatty acids from adipose tissue, these are then transported to skeletal muscle via the plasma where they enter the cell through fatty-acid binding proteins on the cell surface [58,59]. Once inside the cell an acyl-CoA group is added to the fatty acid, forming a long-chain acyl-CoA. The inner mitochondrial membrane is impermeable to these, therefore acyl-CoA molecules are first converted to acyl-carnitines prior to transport into the mitochondrial matrix [60,61].

β-oxidation then occurs which is the process of breaking down a long chain acyl-CoA molecule into 2-carbon acetyl-CoA molecules. During β-oxidation the reducing equivalents $FADH_2$ and NADH are produced from reduction of NAD^+ and FAD, which are used in the electron transport chain. The number of acetyl-CoA molecules produced at the end is dependent on the length of the fatty acid; these typically range

from 8 to 22 carbons [62]. The acetyl-CoA molecules produced are able to directly enter the TCA cycle for energy metabolism.

1.1.4.5. Ketone Bodies

During periods of starvation or prolonged exercise ketone bodies are produced [63]. In the liver oxaloacetate is directed to the gluconeogenic pathway meaning that it is unavailable for condensation with the acetyl-CoA molecules produced from fatty acid β-oxidation. This leads to acetyl-CoA molecules losing their coenzyme-A groups and forming acetoacetate, β-hydroxybutyrate or acetone [63]. These ketone bodies are released into the blood where they can be taken up by other tissues, converted back to acetyl-CoA and used in the TCA cycle for energy production.

1.1.4.6. Amino Acid Oxidation

Classically, amino acids are considered the building blocks for proteins but they can also be used for energy metabolism [64]. The amino group is removed and used to form ammonium which is excreted from the body via the urea cycle [65]. The rest of the molecule is then oxidised and enters the TCA cycle for ATP production.

Skeletal muscle is a reservoir of amino acids, stored as proteins, which can be broken down during periods of high-energy demand or when other carbon sources are low. It is important that protein synthesis during fed states balances protein degradation during fasted states, a disruption of this balance is often a characteristic of disease for example in cancer-cachexia or illness-related loss of appetite [66,67].

1.1.4.7. Oxidative Phosphorylation

The energy substrates mentioned above contribute to the generation of NADH which is ultimately used for ATP synthesis via the electron transport chain (ETC) in a process called oxidative phosphorylation [68]. A series of intermembrane protein

complexes are situated within the inner mitochondrial membrane and are responsible for transferring electrons from NADH and $FADH_2$ to oxygen, producing water. During this process hydrogen ions build up in the intermembrane space generating a proton-motive force. The flow back of the hydrogen ions into the matrix drives ATP synthase to produce ATP [57], figure 1.6.

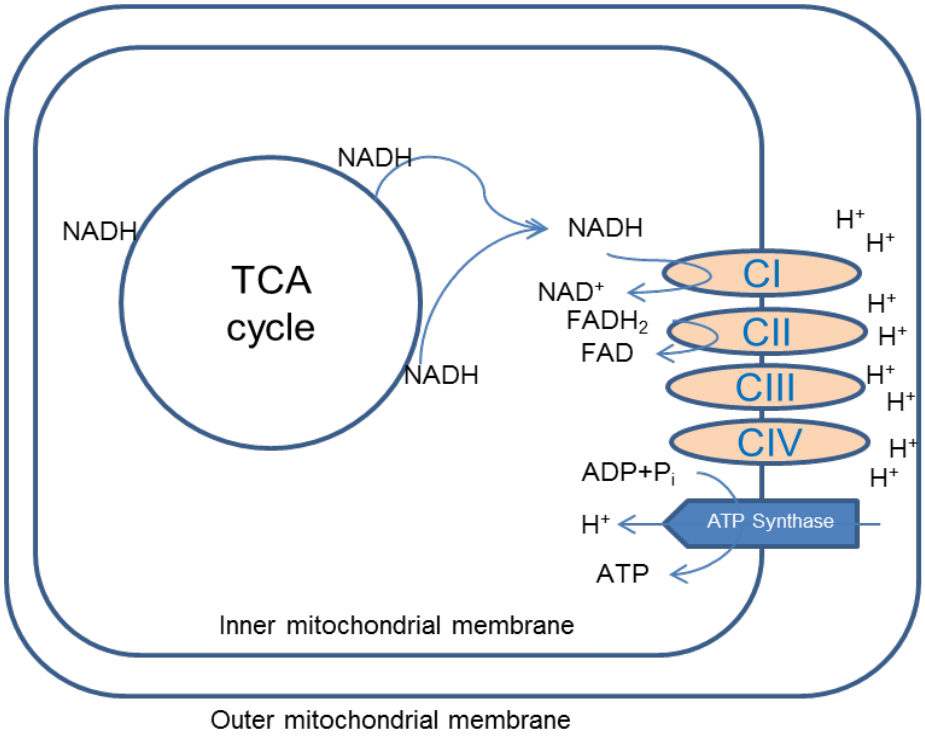


Figure 1.6. Oxidative Phosphorylation
Complex I (NADH dehydrogenase, ubiquinone), complex II (succinate dehydrogenase), complex III (ubiquinol-cytochrome c reductase), complex IV (cytochrome c oxidase) and complex V (ATP synthase). Electrons donated from NADH at CI and $FADH_2$ at CII pass through the electron transport chain and ultimately reduce O_2 to H_2O. This process also releases hydrogen ions, which are pumped through the inner mitochondrial membrane and generate an electrochemical proton gradient. This proton motive force drives ATP synthase to produce ATP.

It is important to note that whilst oxidative phosphorylation is very efficient a small number of electrons passing through the electron transport chain will form superoxide radicals [69]. In normal conditions these reactive oxygen species (ROS) are quickly

converted to H_2O_2 which in turn is reduced to H_2O [70]. ROS can be damaging for the cell in states of oxidative stress where the body is unable to neutralise it by the antioxidant defence system. High levels of ROS have been implicated in cancer, cardiovascular disease and in the aging process [71–73].

1.1.5. Mitochondrial Metabolism

Skeletal muscles ability to maintain metabolic homeostasis during periods of high energetic demand is a function of its high mitochondrial density. Mitochondria are double-membrane bound organelles believed to have once been prokaryotic organisms which, through a process called endosymbiosis, began to reside in the cytoplasm of eukaryotic cells [74,75]. Mitochondria possess their own DNA (mtDNA), which encodes for 37 genes and translates to 13 proteins that are vital to the function of the organelle [76,77]. mtDNA is susceptible to damage by high levels of ROS, due to its proximity to the formation of the superoxide radicals, and can result in mutated mtDNA that ultimately effects mitochondrial function [78,79].

The main role of the mitochondria is facilitating the generation of chemical energy, in the form of ATP. Calorie restriction and exercise training have shown to increase or maintain mitochondrial numbers within skeletal muscle of rats and humans [80–82].

Endurance exercise induces transcriptional and post-translational changes within skeletal muscle, with peroxisome proliferator-activated receptor gamma, coactivator 1 alpha (PGC1α) emerging as a ‘master regulator’ of mitochondrial biogenesis and function [83]. Transcriptional regulation can occur through p38 mitogen-activated protein kinase (p38 MAPK) and activating transcription factor 2 (ATF2) activation, to increase PGC1α expression in response to exercise [84]. In addition, energy stress

through exercise or calorie restriction can induce post-translational modifications of PGC1α through AMP-activated protein kinase (AMPK) mediated phosphorylation [85]. AMPK is activated in response to decreased energy within cells and triggers the translocation of PGC1α into nuclear and mitochondrial compartments where it promotes mitochondrial biogenesis [86]. Deacetylation of PGC1α can also occur by sirtuin-1 (SIRT1), in response to elevated NAD^+ levels, and can once again induce mitochondrial biogenesis through activation of the transcriptional regulators mitochondrial transcription factor A (TFAM) and nuclear respiratory factors 1 and 2 (NRF1-2) [87–90], figure 1.7.

Increasing functional mitochondria number is of interest as mitochondrial dysfunction is a large contributor to the molecular pathology of aging [91–93]. Impaired mitochondrial functioning is also a feature in cardiovascular diseases, diabetes, neurodegenerative diseases and autoimmune disease [94–96]. The dysfunction can be a result of reduced mitochondrial number, reduced substrate availability or a breakdown in the ATP-synthesis machinery [97]. A fall in mitochondrial oxidative capacity has been reported in aged liver of mice, rats and humans [98–100]. The beneficial effects of exercise are demonstrated by a 2-fold increase in mitochondrial capacity of gastrocnemius muscle reported in mice following a high intensity exercise study [101].

Metabolic health involves the ability to regulate blood sugar levels and cholesterol without the use of medication. This process relies heavily on correct metabolism. A key factor in ensuring effective mitochondrial metabolism is the availability of the essential cofactors FAD^+ and NAD^+ which are responsible for driving oxidoreductase reactions throughout the TCA cycle and the ETC [102,103].

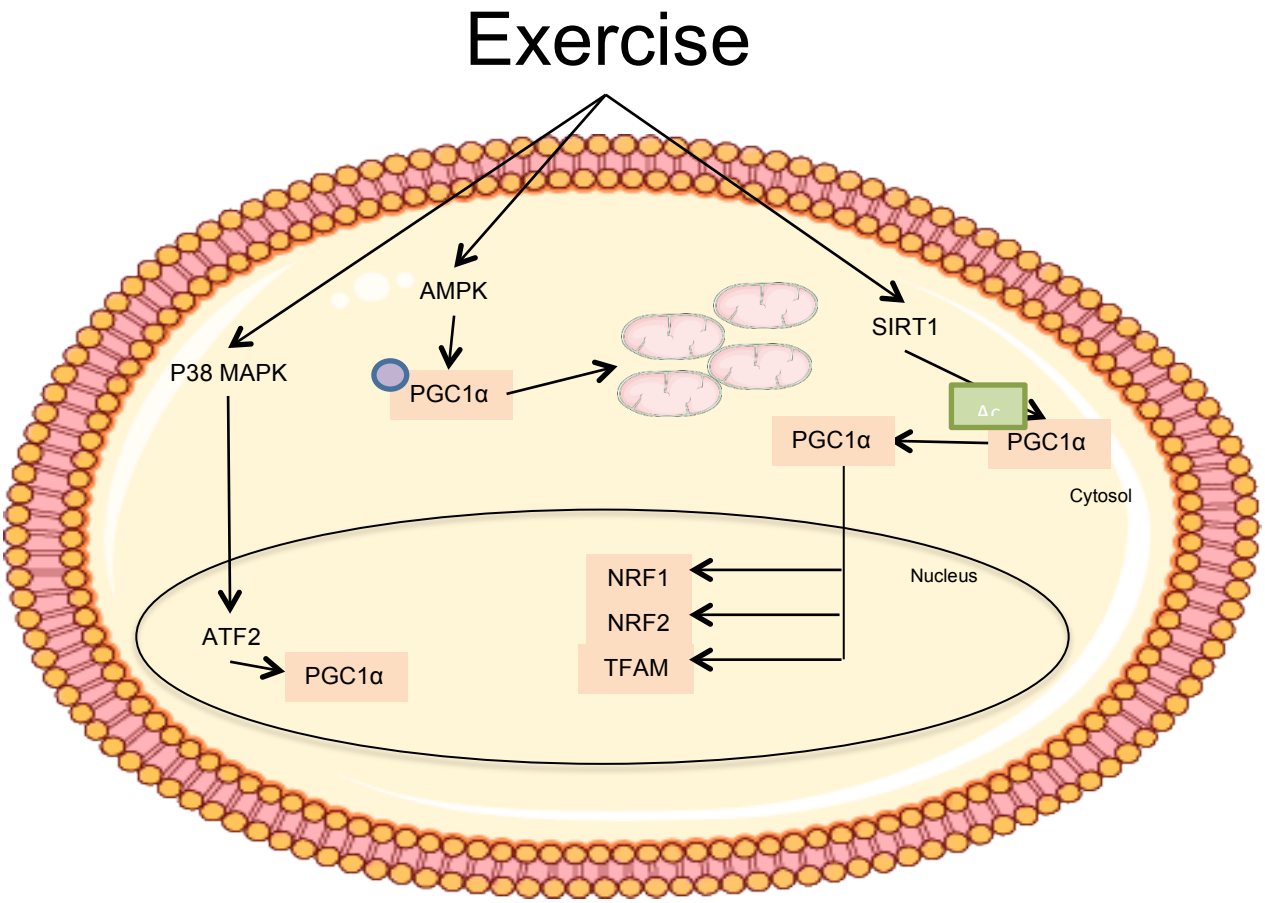


Figure 1.7. Mitochondrial Transcriptional and Post-Translational Adaptations to Endurance Exercise
Exercise leads to skeletal muscle adaptations within the cell. SIRT1 and AMPK act to post-translationally modify PGC1α, which in turn triggers mitochondrial biogenesis. SIRT1 deacetylates whilst AMPK phosphorylates. Another route to increased mitochondrial biogenesis is through the transcription of NRF1, NRF2 and TFAM. Transcriptional regulation also occurs through activation of p38 MAPK and ATF2, which work to increase expression of PGC1α. These adaptations in response to exercise ultimately increase the oxidative capacity of skeletal muscle.

1.2. NAD$^+$ History

The roles of NAD$^+$ discussed throughout the following sections highlight it as a key molecule, which is important for energy transfer and as a substrate for metabolic enzymes. NAD$^+$ is therefore central to metabolic function in skeletal muscle.

NAD$^+$ was discovered in 1904 by Sir Arthur Harden who identified a low molecular weight compound in yeast extracts that was essential for sugar fermentation, which he named cozymase [104]. In the late 1920s Hans von Euler-Chelpin became the first scientist to isolate cozymase and discover that it is composed of two nucleotides: nicotinamide mononucleotide (NMN) and AMP [105], figure 1.8. It was around this time that the disease pellagra was rapidly spreading across the USA, particularly in the southern states [106]. Pellagra was a disease characterised by the "four D's"; diarrhoea, dermatitis, dementia and death [107]. Joseph Goldberger identified that the cause of the disease was not an infection but in fact a dietary deficiency [108]. This research was continued by Conrad Elvehjem and colleagues who made the major discovery that the factor responsible for curing pellagra was nicotinic acid (NA), an NAD$^+$ precursor [109].

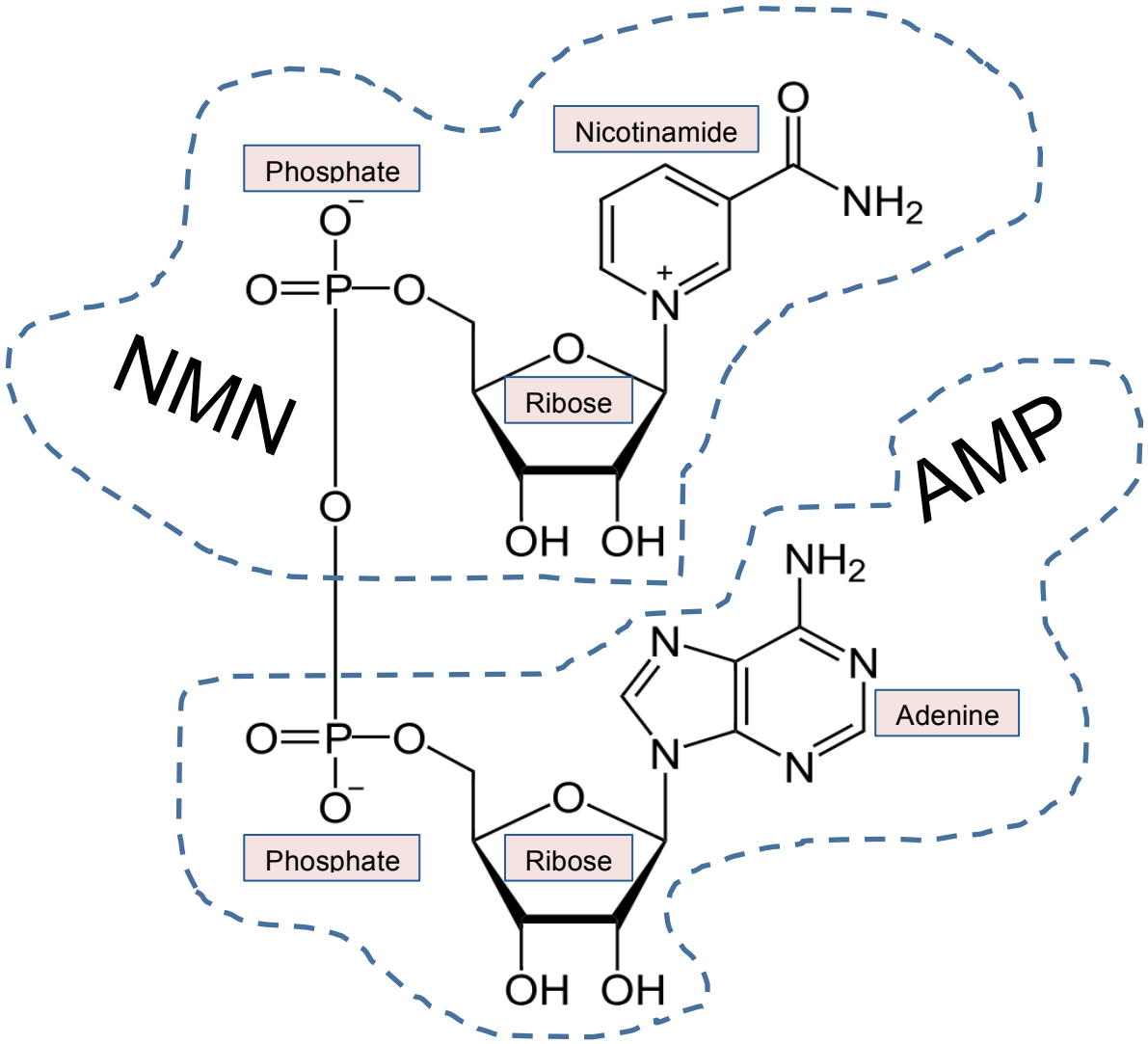


Figure 1.8. Structure of NAD^+
NAD^+ as a molecule is composed of two nucleosides. The first one has an adenine group attached to the ribose (AMP) and the second has a NAM attached (NMN) these are attached together through two phosphate groups.

The hydrogen transfer properties of NAD^+ were discovered by Otto Warburg in 1936 following his work in alcohol fermentation [105]. Oxidoreductase enzymes catalyse the

transfer of electrons from a molecule to oxidised NAD^+, thereby producing NADH and an oxidised molecule [110], figure 1.9. Dehydrogenase enzymes within glycolysis and the TCA cycle pass electrons to NAD^+ and produce NADH that is used in the ETC for ATP production, as discussed in *Section 1.1.4.7*.

NAD^+ is also phosphorylated by NAD kinases (NADKs) to generate nicotinamide adenine dinucleotide phosphate ($NADP^+$), which has electron-transfer properties of its own mostly involved in reductive biosynthesis [111,112]. NADPH is the reducing agent used by the cellular antioxidant defence system in its neutralisation of ROS [113]. However, it is also implicated in the generation of ROS through NADPH oxidases (NOX) located throughout the cell [114]. Maintenance of the NADPH pool is necessary to protect the cell from oxidative stress. The levels of $NADP^+$ are kept relatively low which is important for it to function as a signalling molecule [115–117].

Aside from the classical function of NAD^+ as a redox molecule it has more recently emerged as a key signalling molecule involved in modulating metabolism [118]. NAD^+ not only serves in transhydrogenase reactions but also acts as a substrate in certain reactions by donating ADP-ribose, being consumed in the process [119], figure 1.10. The main families of enzymes responsible for consuming NAD^+ within cells are sirtuins, ADP-ribose transferases and cyclic ADP (cADP)-ribose synthases [102,115,118].

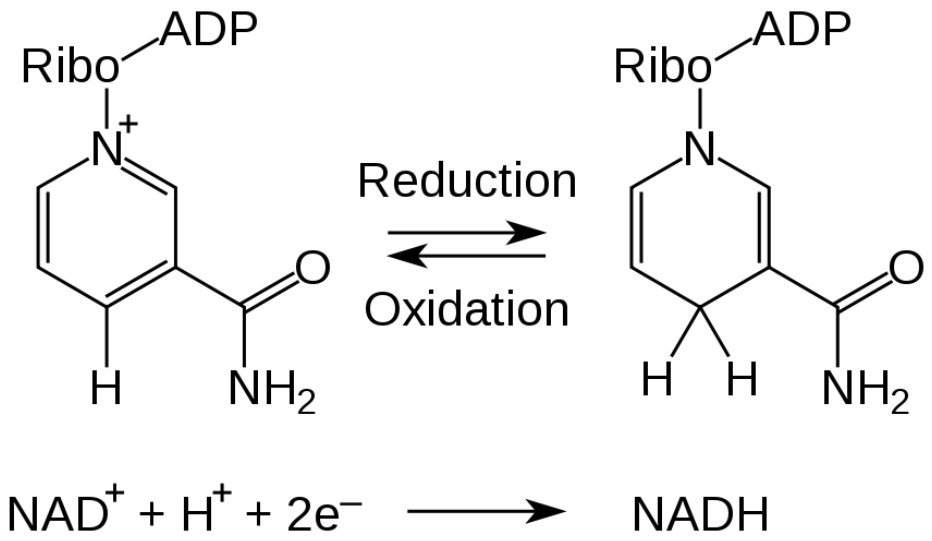


Figure 1.9. NAD^+ as a Redox Molecule
The classic function of NAD^+ is as a redox molecule. NAD^+ is an oxidising agent; it accepts a proton and two electrons and becomes reduced. Conversely, NADH is able to act as a reducing agent and donate those electrons. This pathway is crucial for the electron transport chain to generate the proton gradient across the mitochondrial membrane. The redox potential of NAD^+/NADH is also utilised by dehydrogenase enzymes throughout the cell, notably in glycolysis and the TCA cycle, implicating NAD^+/NADH as central to energy metabolism.

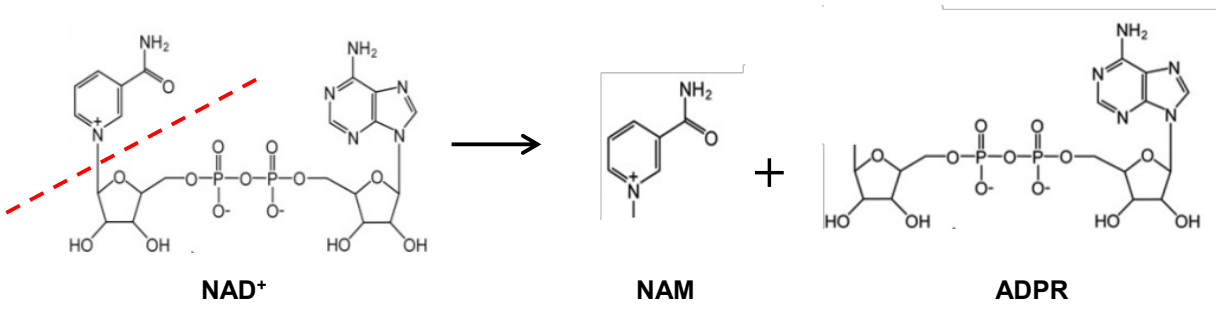


Figure 1.10. Cleavage of NAD^+
The degradation of NAD^+ occurs at the glycosidic bond (shown by red dashed line) leaving NAM and ADPR as by products.

1.2.1. Sirtuins

The sirtuin enzymes are predominately NAD^+-dependant protein deacetylases which alter the metabolic and transcriptomic profile of the cell [120,121]. Sirtuin activity consumes NAD^+ and releases nicotinamide (NAM), O-acetyl ADP ribose and a

deacetylated protein [102], figure 1.11A. There are seven sirtuin proteins; SIRT 1, 6 and 7 are predominantly nuclear proteins [122–124], SIRT 2 appears mostly in the cytosol [125] and SIRT 3, 4 and 5 are predominantly localised in mitochondria [124,126]. Sirtuins have a diverse range of roles within the cell and are crucial for maintaining cellular homeostasis [127].

Life span regulation was thought to be one of their more interesting roles. Work conducted in yeast suggested that increased expression of Sir2 could extend lifespan by up to 50 % following a stimulus such as calorie restriction [128–131]. This role of mediating cellular longevity has since been disputed following standardisation for the genetic background of the *Caenorhabditis elegans* and *Drosphila melanogaster* models, which resulted in no lifespan increase associated with elevated Sir2 levels [132].

SIRT1 is critical in linking cell metabolism to transcriptional regulation through its role in the deacetylation of histones to alter chromatin structure in response to external stimuli [133]. A new development has also linked SIRT1 to the circadian rhythm through deacetylation of histone targets such as H3K9 and H3K14 [133,134]. In order to maintain NAD^+ levels at the site of transcriptional regulation SIRT1 recruits nicotinamide mononucleotide adenyltransferase 1 (NMNAT1) and nicotinamide phosphoribosyltransferase (NAMPT), two NAD^+ biosynthesis genes to the site of action [135,136].

The sirtuin proteins are considered to act as metabolic sensors within the cell with the ability to react to metabolic cues, linking metabolic activity and genomic stability [120,137,138]. Nutrient deprivation requires a switch from the use of glucose as a fuel

source to fatty acid oxidation in skeletal muscle [139]. In the short term SIRT1 has been shown to both reduce and increase hepatic glucose production. Highlighting the differing effect this enzyme activity can have [140]. Further to this, SIRT1 also responds to the increase in NAD^+ that follows fasting by deacetylation of PGC1α, subsequently inducing an upregulation of genes linked to mitochondrial function and fatty acid utilisation [88]. As discussed in *Section 1.1.5.* SIRT1 is also able to respond to the increased NAD^+ levels that occur upon initiation of exercise through deacetylation of PGC1α and increased mitochondrial biogenesis [141].

The importance of SIRT1 in metabolic health is shown with mice fed a high fat diet (HFD) presenting with reduced insulin resistance in response to a SIRT1 agonist [142,143]. While overexpression of SIRT1 exhibits protective effects from HFD induced inflammation and also improved glucose tolerance [144]. Conversely, a decrease in the NAD^+-biosynthetic enzymes and SIRT expression has been shown in obesity [145]. Whilst it is unclear the cause of this reduced expression it is clear that maintaining cellular NAD^+ is essential for the correct functioning of the sirtuin enzymes.

It is widely accepted that activation of sirtuins is key to the maintenance of metabolic health [120,146–148]. Changes in metabolism, which have a concurrent change in NAD+ levels, can therefore regulate the activity of sirtuins and serve to modulate metabolism.

1.2.2. ADP-ribose Transferases

Another group of NAD^+-consuming enzymes are the ADP-ribose transferases (ARTs). A single ADP-ribose (ADPR) moiety released from NAD^+, figure 1.11B, covalently bonds to the side chain of a protein [149]. Poly-ADP-ribosyltransferases or

poly-ADP-ribose polymerases (PARPs) use NAD^+ as a substrate to repeatedly transfer ADPR to a target protein, creating long chains of poly-ADP-ribose (PAR), some of which have been shown to reach 200 ADPR units in length [150,151].

The role most associated with PARPs is their involvement in DNA repair [152]. PARPs are recruited to the sites of DNA damage as a result of genotoxic stress and are critical in repairing single-strand and double strand breaks [153]. The rapid generation of PAR aids recruitment of proteins to the site of DNA damage to aid in DNA repair [154]. PAR is subsequently catabolised by PAR glycohydrolase, which is an equally essential part of the process to maintain efficient and effective DNA repair machinery [155].

As PARPs are NAD^+ dependant enzymes they require a constant source of NAD^+ and therefore, similar to the sirtuin enzymes, they recruit NAD^+-biosynthetic enzymes to the source of the DNA damage [156]. PARP inhibitors have been identified as useful for metabolic dysfunction models based on limiting the NAD^+ depletion within the cell. Under cellular stress PARPs are considered the greatest NAD^+ consumers within the cell but it is important to appreciate that there is also considerable crosstalk between PARPs and other NAD^+ consuming enzyme. This crosstalk can impact on their activity through reduced NAD^+ availability but also through sirtuin activity leading to elevation of NAM which has shown to be an inhibitor of PARPs [157]. Further to this, it has been demonstrated that PARPs can be influenced by sirtuin activity through direct deacetylation of the protein, which ultimately reduces its catalytic activity [158]. There is also evidence of crosstalk between the two enzymes through regulation of transcription. A deletion of PARP2 resulted in increased sirtuin activity in cultured myotubes which was linked to elevated sirtuin expression, not just increased NAD^+

content [159]. This work highlights important crosstalk between these two key NAD^+ consuming enzymes [160,161].

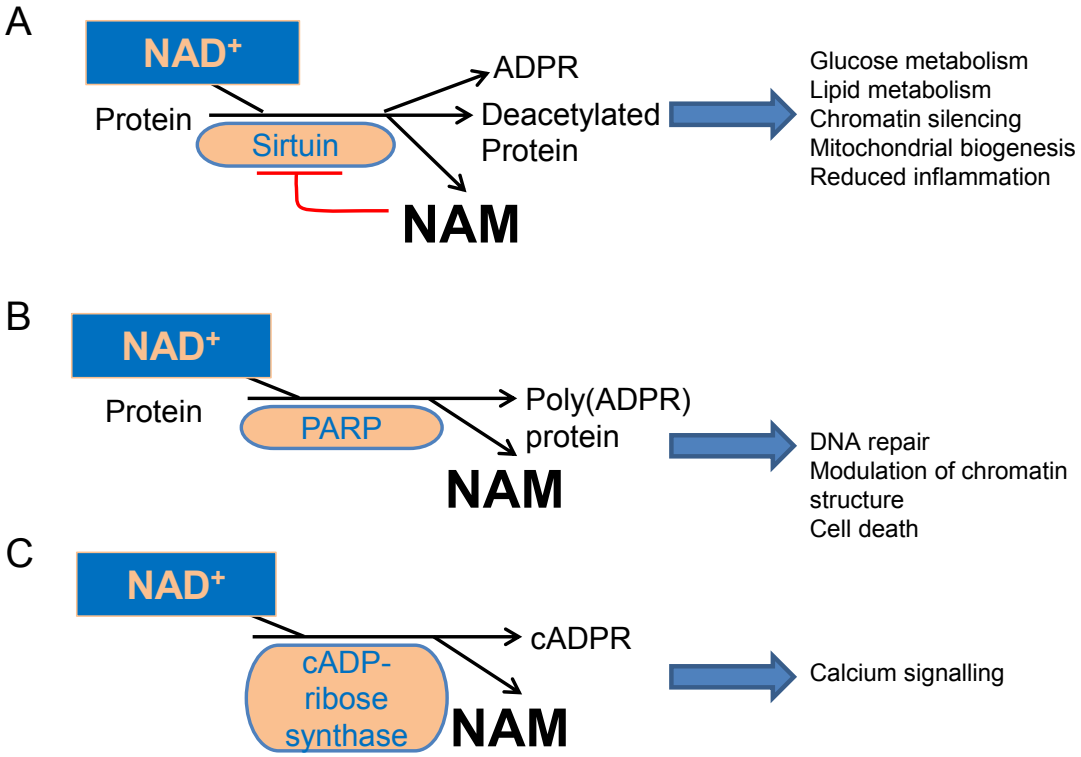


Figure 1.11. NAD^+-consuming Enzymes

(A) Sirtuin enzymes act to deacetylate a target protein, consuming NAD^+ in the process and releasing ADPR and NAM. NAM is an inhibitor of sirtuins which is one way the cell modulates the activity of the enzymes. Sirtuins have a role in metabolic health and have been implicated in a number of key processes within the cell. **(B)** PARPs utilise the ADPR released from NAD^+ and covalently bond it to the side chain of a target protein. Typically this is seen in cases of DNA damage, where the generation of PAR aids DNA repair. **(C)** cADP-ribose synthases generate cADPR, which is used in calcium signalling. It is involved in both calcium release from the sarcoplasmic reticulum as well as calcium influx through the membrane.

1.2.3. cADP-ribose Synthases

cADP-ribose synthases, CD38 and CD157, utilise NAD^+ to generate c-ADP ribose, they are also able to hydrolyse c-ADP ribose to ADPR, figure 1.11C, and can use $NADP^+$ as a substrate under acidic conditions to produce nicotinic acid adenine dinucleotide phosphate (NAADP) [162–164]. Each of these molecules are used as intracellular second messengers involved in calcium mobilisation and regulation of calcium fluxes [115–117].

These enzymes are major regulators of NAD^+ with CD38 knock out mice displaying a 20-fold increase in NAD^+ levels, leading to increased SIRT1 activity and enhanced energy expenditure [165,166]. Once again the relationship between the NAD^+ consuming enzymes is apparent, with NAD^+ availability being the major contributor to enzymatic activity [167].

1.3. NAD^+ Biosynthesis

NAD^+ synthesis is critical to cellular function as turnover of the molecule is high within cells. The main routes to NAD^+ production are through the essential amino acid tryptophan (Trp) or from vitamin B3 precursors nicotinic acid (NA), NAM and NR [119], figure 1.12.

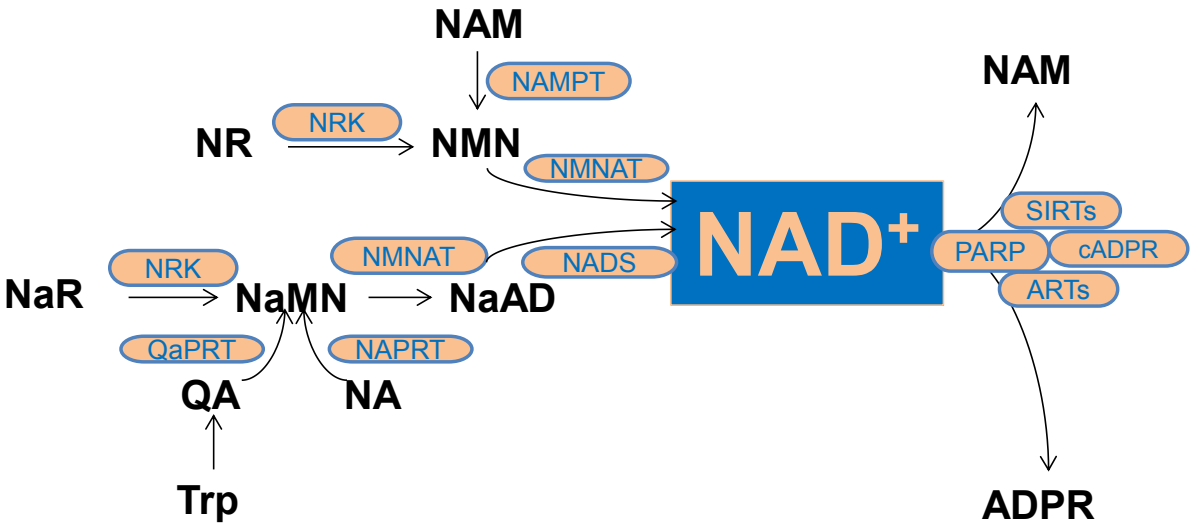


Figure 1.12. NAD^+ Synthesis and Consumption
An outline of the routes to NAD^+ via the 5 different entry points; Nam, NA, NR, NaR and Tryptophan (Trp) is shown with their corresponding enzymes. NAD^+ is broken down to NAM and ADPR upon consumption by the main consuming enzymes.

1.3.1. De Novo Synthesis

Trp is consumed in the diet through meat, eggs and dairy and is converted to quinolinic acid (QA) via the kynurenine pathway. The quinolinic acid phosphoribosyltransferase (QAPRT) enzyme exhibits dual decarboxylation and phosphoribosylation generating nicotinic acid mononucleotide (NaMN), using phosphoribosyl pyrophosphate (PRPP) as a cofactor. From here the mononucleotide is adenylated to its adenine dinucleotide, NaAD, which is finally amidated by nicotinamide adenine dinucleotide synthase (NADS) to form NAD^+, figure 1.13.

The kynurenine pathway predominately occurs in the liver, with the expression of QAPRT being particularly high in this tissue[168]. A study has shown that QAPRT knock out mice are still viable and show no developmental problems, indicating that this pathway is not the main source of NAD^+ synthesis *in vivo* [169]. In support of these findings it has been shown that tryptophan alone is not enough to support NAD^+ levels. Indicating that the *de novo* pathway only marginally supports the required cellular NAD^+ synthesis, with 60 mg of tryptophan required to provide the same levels of NAD^+ as 1 mg of niacin [170–172].

1.3.2. Preiss-Handler Pathway

Nicotinic acid phosphoribosyltransferase (NaPRT) is responsible for the phosphoribosylation of NA, again using PRPP as a cofactor. This enzyme is expressed in tissues that preferentially use NA as a substrate over NAM such as the heart, kidneys and red blood cells [171]. NaPRT converts NA to its corresponding mononucleotide, NaMN, which then follows the same path as *de novo* synthesis, utilising the NMNAT and NADS enzymes, figure 1.13.

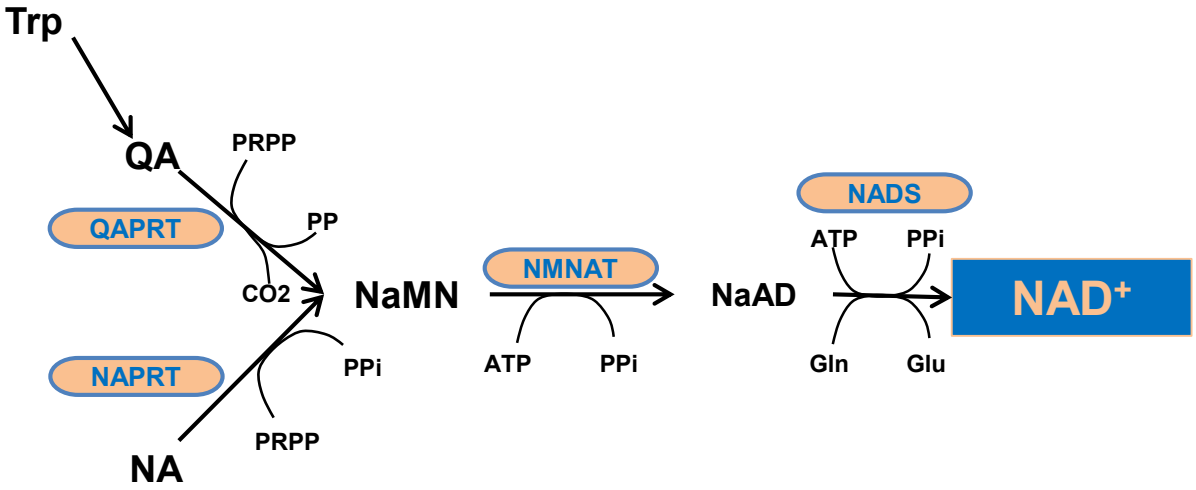


Figure 1.13. De Novo NAD^+ Synthesis and the Preiss-Handler Pathway
QA, derived from tryptophan, which is consumed in the diet, and NA share similar NAD^+ biosynthesis pathways with initial conversion to NaMN before NaAD and finally NAD^+. The cofactors required for each enzyme are outlined and show that 2 ATP molecules and glutamine are used for the conversion to NAD^+.

1.3.3. NAM Pathway

NAM can also be a precursor for NAD^+. Nicotinamide phosphoribosyltransferase (NAMPT) transfers a phosphoribosyl moiety from PRPP to NAM, producing NMN, which is ultimately adenylated to form NAD^+, figure 1.14.

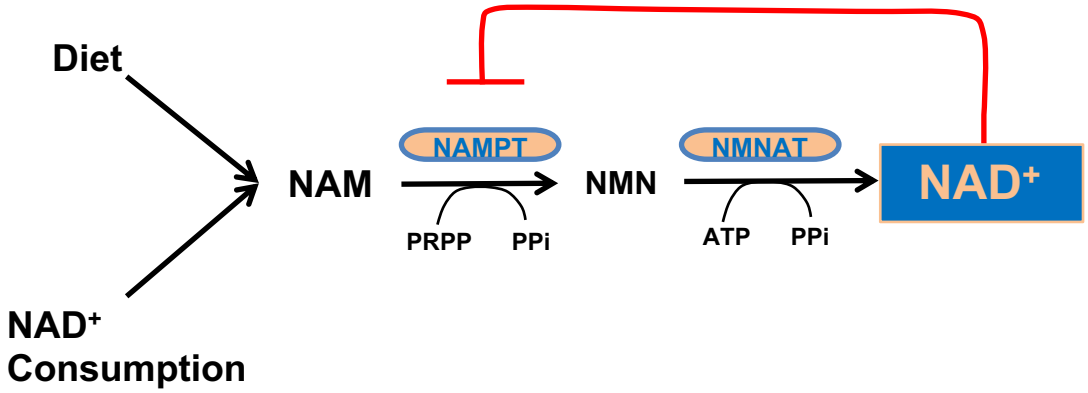


Figure 1.14. NAMPT Salvage Pathway
NAM can be consumed in the diet or generated as a by-product of NAD^+ consumption by enzymes. NAD^+ synthesis through NAMPT and NMNAT is a key salvage pathway and permits effective recycling of NAD^+ within the cell. At around 90 % of NAD's physiological concentration it has been shown to inhibit NAMPT, creating a feedback system to regulate NAD^+ levels.

NAM can be found in the body through dietary consumption of meat or eggs and is cleared from skeletal muscle cells as methylated NAM (MeNAM) [173]. NAM is also produced as a result of NAD^+ consumption by SIRTs, PARPs or cADP ribose synthases [102,119,149]. As this pathway is able to recycle NAD^+ following its consumption it is referred to as the NAMPT salvage pathway. NAMPT is ubiquitously expressed and is critical to development with complete NAMPT knock out being lethal in mice, highlighting the vital role of this pathway in mammalian cells [171,175].

NAMPT catalyses the rate limiting step in the pathway and can function with or without ATP. ATP causes a conformational change in the active site of the co-factor PRPP to increase its affinity for NAMPT, with K_M values in the nanomolar range [168]. Upon NAD^+ reaching 90 % of its physiological concentration there is an inhibition of NAMPT through a negative-feedback mechanism [176,177].

NAMPT expression is regulated through a circadian oscillatory pattern, which affects NAD^+ levels and activity of NAD^+-dependant enzymes throughout the day [178,179]. NAMPT was originally named ‘pre-B-cell colony enhancing factor’, before being identified and localised either inside or outside the cell, iNAMPT and eNAMPT respectively [171,180].

The functions of eNAMPT are controversial. It has been shown to be elevated in type 2 diabetes, thought to be the result of increased secretion from dysfunctional liver and white adipose tissue [181]. This was further supported by a study showing elevation of eNAMPT in HFD fed mice, with suggestions of pro-inflammatory actions [182,183]. The NAD^+-biosynthetic functions of eNAMPT are debated in the literature [164]. Evidence of increased NMN synthesis in response to elevated eNAMPT in brown

adipocytes supernatants suggests conservation of eNAMPT's NAD^+-biosynthetic potential [174]. This NMN production has been reported to be critical for correct islet cell functioning [184]. However, in direct contrast a study using blood plasma showed no formation of NMN or any degradation of ATP or PRPP, the products used [185]. Together this shows the controversial nature of eNAMPT's function [186].

iNAMPT has been shown to increase in skeletal muscle in response to exercise, as demonstrated by a significant increase in the level of NAMPT protein in a group of athletes compared to non-athletes [187]. It was postulated that increased NAMPT expression resulted in enhanced mitochondrial biogenesis within the skeletal muscle demonstrated by a significant increase in OXPHOS fluorescence, a quantification of mitochondrial volume, in the athletic group [187]. This was later supported by a study using an exercise simulation technique on a single muscle fibre. They reported that inhibition of NAMPT by FK866 reversed the increase in mitochondrial related mRNA expression seen with stimulation of the fibre [188]. A further human study took muscle biopsies before and after exercise and showed elevation of the NAMPT protein in response to aerobic and resistance training [189].

NAMPT expression has also shown to increase in response to glucose restriction with a corresponding increase in NAD^+ levels in C2C12 myotubes supplemented with 5mM vs. 25 mM glucose [141]. However, it does not appear that the beneficial effects reported are an isolated result of elevated NAMPT. Overexpression of the NAMPT protein was not sufficient to protect the muscle from HFD induced decline of oxidative function in young mice [6]. The study was successful in raising NAD^+ levels however reported a lack of change in the NAD^+/NADH ratio. This may explain the limited metabolic effect in the mice in response to HFD feeding. Further to this, the

compartment specific increase in NAD^+ may be a factor, with little effect on the mitochondrial pool shown in the study. In addition, there have been studies observing the effect of a HFD on NAMPT expression in different tissues. In liver and white adipose tissue a decrease in NAMPT expression was identified in response to a HFD; whereas in skeletal muscle there was no significant change to NAMPT expression [4].

In spite of an increase in NAMPT being associated with beneficial alterations to the cell, such as increased mitochondrial biogenesis, the protein has also shown to be overexpressed in oncogenesis. NAMPT and NAD are also up regulated in a range of immunological and inflammatory conditions such as psoriasis, irritable bowel disorder and Chron's. NAMPT inhibitors have proven beneficial in disease models of these and in type 1 diabetes [190,191]. A highly selective competitive inhibitor of NAMPT, FK866, has shown to cause a severe depletion of NAD^+ by binding to the NAM pocket of the enzyme and reducing the levels of NMN and therefore NAD^+ produced [180]. The reduction in NAMPT activity has shown to correlate with a loss of NAD^+ which is followed by a reduction in ATP, triggering apoptosis; this highlights NAMPT inhibition as a potential oncology treatment strategy [192–194].

The NAMPT protein is shown to be a key modulator of NAD^+ levels within the cell and thus regulates the activity of NAD^+-dependant enzymes. The tight regulation through metabolic cues implements this enzyme as central to the connection between NAD^+ availability and metabolic homeostasis [195].

1.3.4. NR Pathway

NR is a more recently discovered precursor of NAD^+ and has been detected in cow's milk, suggesting that it contributes to elevation of NAD^+ through the diet [196]. Nucleotides such as NAD^+, NMN and NaMN are unable to enter cells directly [170]. Instead they are degraded to their equivalent riboside, NR or NaR, via membrane bound ectoenzymes, 5'-nucleotidases (5'-NTs) such as CD73 [197–199], figure 1.15A. This reaction has been shown to occur intracellularly with the presence of 5'-NTs in the cytoplasm responsible for catalysing the dephosphorylation of the nucleotides. This results in NaR/NR, which are either re-phosphorylated or released through the membrane, meaning they are available for absorption by neighbouring cells [200].

Once absorbed the nucleotides are phosphorylated by nicotinamide riboside kinase 1 (NRK1), expressed ubiquitously, or nicotinamide riboside kinase 2 (NRK2), highly expressed in striated muscle, using ATP as a cofactor, releasing ADP in the process [201]. NR is converted to NMN and then to NAD^+ via the NMNAT enzymes, figure 1.15B [196].

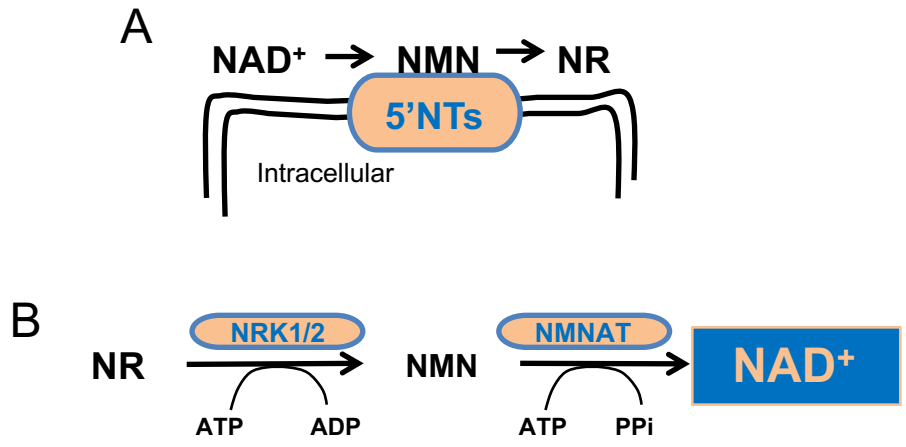


Figure 1.15. NR as an NAD^+ Precursor
(A) NAD^+ is unable to enter the cell directly; therefore it is first converted to NR using the 5'nucelotidases (5'NTs) such as CD73. **(B)** Once inside the cell NR is metabolised to NMN via the NRK enzymes before it is ultimately converted to NAD^+ via NMNAT.

NaR takes a longer route with its conversion to NaMN, then NaAD via NMNAT and finally to NAD^+ through NADS [202]. NRK1 and 2 are ~57 % similar to each other and are both related to uridine/cytidine kinase 2 found in humans [168,203]. These kinases are both able to phosphorylate cytidine however they favour NaR and NR as a substrate, based on their K_M values. NRK1 does not catalyse phosphorylation of uridine, unlike NRK2, although it does utilise GTP as a phosphodonor in NR reactions, whereas NRK2 is ATP specific [203]. Both NRK isoforms exhibit dual specificity for NaR and NR, although they have a higher affinity for the nicotinamide substrate over its corresponding nicotinic acid [168]. K_M values show that NRK2 has a lower affinity for ATP than NRK1, 250 uM vs. 4.8 uM, this would suggest that NRK2 was acting as an ATP sensor requiring a high ATP level before NAD^+ is synthesised. However, the resting muscle ATP concentration is between 5-8 mM, meaning there is sufficient ATP to activate NRK2 even at basal levels [38].

1.4. NAD^+ Compartmentalisation

Importantly, distribution of NAD^+ can affect the metabolic profile of the cell. NAD^+ is needed at the sites of NAD^+-mediated enzyme activity and therefore attempting to understand the subcellular localisation of NAD^+ is of interest [170,204].

Depending on cell type the mitochondria can contain around 70 % of the total cellular NAD^+ pool [205]. In order to achieve efficient glycolysis and oxidative phosphorylation, complex shuttle systems are employed such as the malate/aspartate and the glycerol-3-phosphate shuttles which facilitate the transport of reducing equivalents across the inner mitochondrial membrane [206,207]. NADH is unable to cross the inner

mitochondrial membrane and therefore it reduces a different molecule that can pass through, regenerating cytosolic NAD^+ as a result [207]. Once inside the mitochondria the reduced molecule is oxidised and the electrons contribute to the oxidative phosphorylation pathway [207].

The mitochondria express NAD^+ consuming enzymes and as evidenced through the requirement of the shuttle systems, NAD^+ is unable to directly enter the mitochondria. This suggests a mechanism for NAD^+ generation within the organelle itself. A mitoPARP construct was developed which enabled detection of NAD^+ in hepatocytes through PARPs enzymatic activity [170]. This was able to confirm NMN as the key mitochondrial precursor for NAD^+ generation in mammalian cells, with this study showing NMNAT3 as the only NAD^+ biosynthetic enzyme identified within the mitochondria [170]. However, one study showed NMNAT3 KO mice as having unchanged mitochondrial NAD^+ with another study showing that there was NAMPT expression in the mitochondria of liver cells, albeit much lower than cytosolic levels [208–210], figure 1. 16.

The mitochondria maintain a tight regulation of their NAD^+/NADH ratios which are estimated to be between 7 – 8 [211], with the cytoplasmic ratio ranging from 60 to 700 in a typical eukaryotic cell [212]. The recent development of a genetically encoded biosensor to measure NAD^+ has indicated that there are two distinct NAD^+ pools in kidney cells; mitochondrial and nucleocytoplasmic [213]. The separation between these two intracellular compartments appears vital for energy homeostasis. NAD^+ transporters found in yeast were expressed in the mitochondria of human cells resulting in increased mitochondrial NAD^+ but also negative effects on proliferation and a metabolic switch from oxidative phosphorylation to glycolysis [214].

This highlights that changes to NAD^+ levels within subcellular organelles can have a big impact on metabolism, through activity of NAD^+-dependant enzymes but also glycolysis and oxidative phosphorylation pathways.

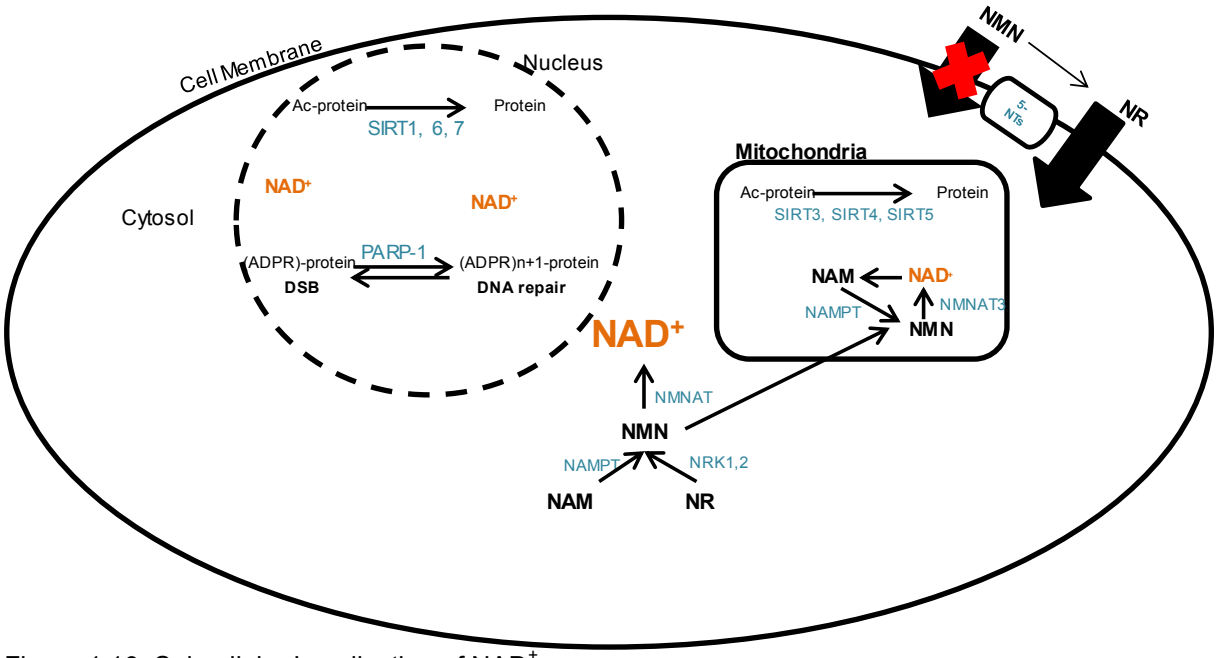


Figure 1.16. Subcellular Localisation of NAD^+

A representation of the subcellular compartmentalisation of NAD^+. There are two distinct pools of NAD^+; the nucleocytoplasmic where NAD^+ is able to pass through the nuclear membrane as required and the mitochondrial. The mitochondrial membrane is impermeable to NAD^+ and therefore its precursor, NMN, enters instead with NMNAT3 present within the mitochondria to generate NAD^+. There is also evidence of NAMPT expression to allow for NAM recycling. The expression of enzymes is related to the requirement; for example, PARPs are required for DNA repair and are therefore situated in the nucleus.

1.5. NAD^+ in Skeletal Muscle

1.5.1. Biosynthesis

The pathways responsible for skeletal muscle NAD^+ generation are the NAMPT and NRK salvage pathways. *De novo* synthesis and the Preiss-Handler pathways appear redundant in skeletal muscle due to undetectable NADS activity, a required enzyme for NAD^+ synthesis via these routes [202].

The muscle-specific expression of NRK2, an enzyme involved in the NRK salvage pathway, was thought to infer a key role of this enzyme in muscle NAD^+ biosynthesis

[199]. However, knock-out studies showed no obvious metabolic phenotype associated with this mouse model [199]. Double knock out models of NRK1 and 2 also show NAD^+ levels as comparable to wild-type mice, suggesting a redundancy of these enzymes for basal NAD^+ synthesis in skeletal muscle [199].

This indicates the NAMPT salvage pathway as the main route to NAD^+ synthesis in skeletal muscle evidenced by an 85 % reduction in muscle NAD^+ availability in response to depletion of NAMPT [215].

1.5.2. Development and Regeneration

NAD^+ biosynthesis has shown to have a role in organisation of the extracellular matrix (ECM) protein, laminin, during primary myotome development. ECM surrounds whole muscle, muscle fibre bundles and muscle fibres [216]. The adhesion of muscle cells to the ECM involves ADP-ribosylation of integrin alpha7 (ITGA7) by ADP-ribosyltransferase 1 (ART1) [217]. This is an NAD^+-dependent enzyme with the binding affinity of ITGA7 for laminin therefore affected by NAD^+ concentration [218]. Laminin is a major component of basement membranes with functional roles in skeletal muscle structure and signalling [219]. NRK2b is localised to myotendinous junctions of zebra fish where it phosphorylates NR to produce NMN, which is thought to be converted to NAD^+ by the highly conserved NMNAT [220]. NRK2b is responsible for providing NAD^+ to ART1, evidenced through NRK2b deficient zebra fish expressing disrupted laminin organisation, which was rescued through exogenous NAD^+ supplementation [220].

NAD^+ also appears crucial in regulating secondary muscle development with a decrease in NAD^+ levels observed as C2C12 myoblasts differentiate to myotubes [221].

Whilst the mechanism behind this change in NAD^+ is unclear it has been suggested to be a result of increased PARP1 activity in myoblasts [222]. As PARP1 is a major consumer of NAD^+ there is a reduced availability of NAD^+ leading to decreased SIRT1 activity permissive to muscle differentiation [161].

Muscle repair seems to also coincide with changing NAD^+ levels. SIRT1 has been shown to maintain satellite cell quiescence by repressing the transcription of myogenic genes [223]. Once activated, in response to muscle injury, the satellite cells undergo a metabolic switch from oxidative phosphorylation to glycolysis. As in development, this switch results in decreased NAD^+ levels ultimately resulting in decreased SIRT1 activity allowing for myogenic gene transcription [133].

1.5.3. **NAD^+ and Aging Muscle**

A loss of muscle mass and function during aging is referred to as sarcopenia [224]. A variety of factors are involved with the aging phenotype in relation to skeletal muscle, such as changes to the neuromuscular junction, loss of motor neurones and a decline in mitochondrial quality and activity [93,225,226].

The generation of ROS and its continuous damage of mtDNA can lead to impaired mitochondrial function with age, with defective ETC subunits and impaired oxidative capacity [227]. A skeletal muscle study identified ETC abnormalities increasing from 6 % at 49 years of age to 31 % at 92 years, with reports of age-related declines in mitochondrial mass, TCA cycle enzyme activity and ATP consumption [228–231]. Further work observed giant, dysfunctional mitochondria in aging muscles suggestive of impaired fusion/fission, resulting in a lower degradation of damaged mitochondria and lower oxidative capacity of the muscle [232].

As outlined in *Section 1.1.5.* mitochondria rely heavily on NAD^+ for energy metabolism and therefore a drop in NAD^+ could also contribute to reduced mitochondrial functionality. NAMPT protein expression has shown to be decreased in aged rat skeletal muscle [233]. This can help explain the decline in NAD^+ levels and oxidative capacity observed in various aging studies [3–5]. Overexpression of NAMPT has shown to cause higher baseline NAD^+ levels with a concurrent increase in the exercise capacity of aged mice [215].

The necessity of NAD^+ for SIRT1 activity is another factor that could lead to compromised muscle function during aging. The lower NAD^+ levels as a result of decreased NAMPT reduce SIRT1's effects on processes such as glucose metabolism and cell survival [129]. Activation of SIRT1 by a small molecule agonist, SRT1720, has shown to improve exercise endurance in aged mice and enhance overall muscle health span [234,235].

This highlights that whilst skeletal muscle aging is complex and a number of confounding factors are at play there is a central role for NAD^+ availability in maintaining skeletal muscle health, figure 1.17.

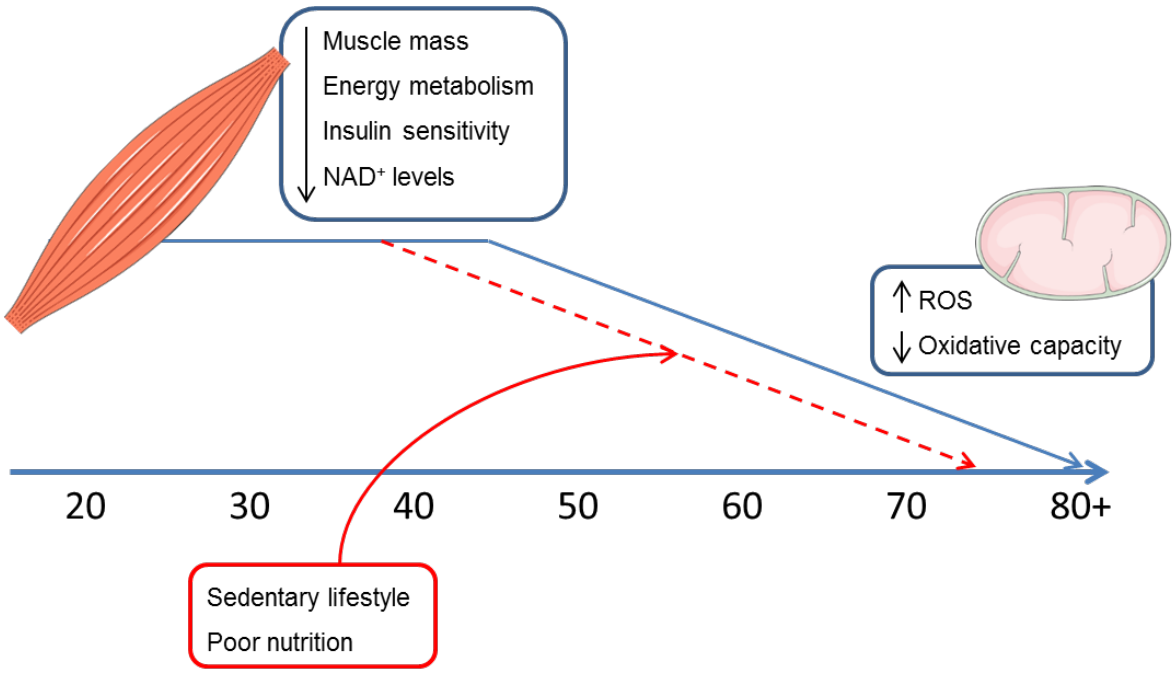


Figure 1.17. NAD^+ in Aging and Metabolic Decline
The result of age-related decline of skeletal muscle. A decline in muscle mass has been observed with age alongside reduced mitochondrial function. The mitochondria have elevated levels of ROS and a reduced oxidative capacity, which ultimately limits ATP synthesis and compromises skeletal muscle function. A decline in NAD^+ levels has been observed in aged muscle and this could be contributing to the impairment of oxidative phosphorylation. Metabolic disease can be a cause or consequence of muscle dysfunction. Certain factors can affect the health of skeletal muscle such as obesity and muscle disuse ultimately exaggerating the muscle decline seen with aging.

1.5.4. NAD^+ and Metabolic Disease

Skeletal muscle is major regulator of whole body metabolism and therefore muscle dysfunction can be both a cause and a consequence of metabolic disease [236], figure 1.17.

As the largest insulin sensitive tissue in the body the skeletal muscle plays a key role in transporting glucose into the cell in response to both insulin and exercise [2,237,238]. It has recently been suggested that insulin resistance in type 2 diabetes mellitus is likely a result of a deficiency in fatty acid oxidation due to impaired mitochondrial oxidative metabolism [239]. There has also shown to be a link between a sedentary lifestyle and changes to muscle metabolism, potentiating insulin resistance in skeletal muscle [240]. With a decline in NAD^+ reported in the skeletal muscle of HFD fed mice [6].

For optimal mitochondrial oxidative phosphorylation NAD^+ bioavailability is critical and perturbations to these levels could have detrimental effects on mitochondria and whole body metabolism. Together, these studies highlight how disruption to the normal physiology and NAD^+ levels within skeletal muscle can be a factor in the molecular pathology of diabetes and contribute to metabolic dysfunction.

1.6. NAD^+ Augmentation

In response to the finding that NAD^+ levels decline in mouse studies of aging and metabolic disease there has been a focus on NAD^+ augmentation as a therapeutic in these conditions, figure 1.18 [6,215].

NA supplementation has been shown to have beneficial effects in patients suffering from dyslipidaemia. It is able to reduce the levels of triglycerides (TG) through its inhibition of diacylglycerol acyltransferase 2 involved in TG synthesis and increase the number of high density lipoproteins (HDLs) in circulation [241,242]. This has also proven to be effective in type 2 diabetes mellitus patients to control lipid levels which prevents deposits that can lead to atherosclerosis [172]. The exact mechanism of action for the beneficial effects seen with NA supplementation remains unclear, however it has been hypothesised that it is the synthesis of NAD^+ and its downstream effects on sirtuins that result in the control of dyslipidaemia [243]. The main limitation to the use of NA in the clinic is the adverse effects. The supplement activates the GPR109A receptor on cells in the epidermal Langerhans which is responsible for a painful 'flushing' response, this results in reduced patient compliance and limits its pharmacological use [172,244].

NAM supplementation studies in mouse liver tissue showed an improvement in glucose homeostasis in mice on HFD, which resulted in lower levels of inflammation. However, the study did also show a marked reduction in NAMPT expression following administration of NAM, which ultimately limits its ability to generate NAD^+ [245]. This may be explained through NAM also being a potent non-competitive inhibitor of SIRT1, thereby limiting its NAD^+-boosting effects [157,158,].

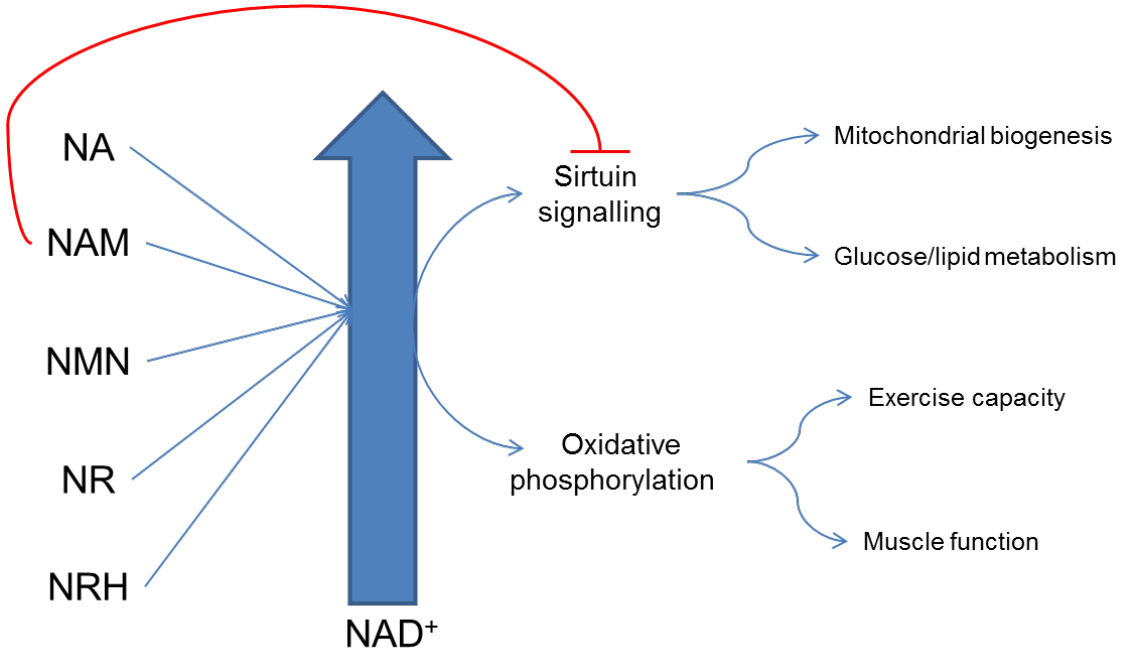


Figure 1.18. NAD^+ Augmentation as a Therapeutic
There are a number of routes to NAD^+ augmentation. NA is limited in its therapeutic use due to it causing a painful flushing response. NAM has shown to have an inhibitory effect on sirtuin signalling, thereby limiting its efficacy. NMN and NR are effective in animal models of obesity and diabetes. The response to increased NAD^+ levels is elevated sirtuin signalling, which ultimately aids in mitochondrial biogenesis and glucose metabolism. With high NAD^+ also having a direct effect on oxidative phosphorylation to help improve exercise oxidative capacity and therefore muscle function.

As NMN is downstream of the above precursors and is only one step away from NAD^+ generation it became a molecule of interest for NAD^+-boosting. A number of mouse models have been used for NMN supplementation studies. A single intraperitoneal (IP) injection of NMN was shown to improve glucose tolerance and

insulin secretion in a NAMPT deficient mouse model [174]. This beneficial effect of NMN has been reported in further studies of HFD mice, age-induced diabetic mice and in a chronic supplementation study in wild-type mice [4,247,248]. In addition to this, NMN has been reported to enhance skeletal muscle oxidative phosphorylation in aged mice, with additional improvements in learning and memory, cognitive and cardiac function shown [5,249–251]. There have been studies suggestive of an NMN transporter responsible for the uptake of NMN into cells [252]. However, further studies have established that in order for NMN to augment intracellular NAD^+ availability it must first be metabolised to NR outside the cell [199,253]. This is evidenced by the necessity of the NRK enzymes for the cell to utilise NMN for NAD^+ generation [199]. NMN is ultimately converted to NR and therefore exploring NR's therapeutic potential is of interest.

NR has been shown to be pharmacologically effective, with a recent study showing NR can safely elevate NAD metabolism in human blood [254]. Treatment with NR in a mouse model of Alzheimer's shows cognitive improvements with a marked increase in NAD^+ levels which promotes PGC-1α, resulting in increased β-secretase degradation [255]. Another study has also shown the beneficial effects of NR feeding with increased endurance performance in mice. Histological studies showed a higher level of succinate dehydrogenase staining in NR treated gastrocnemius muscle vs. non treated equivalents, suggesting a higher oxidative capacity as a result of supplementation [256]. In addition to this there was evidence of NR having a protective effect against HFD induced obesity and insulin resistance, as shown by a significant reduction in fat mass in response to NR as well as a significantly lowered blood insulin level [201]. NAD^+ repletion through NR supplementation shows great

improvements in muscle stem cell function, with NR preventing muscle stem cell senescence [257]. Whilst NR is evidently effective at exerting its therapeutic effects, oral administration is unable to deliver NR to the target tissues, instead it undergoes hepatic first pass metabolism and NAM is released into the blood [258]. Intravenous injection of NR also has its limitations as it has been shown to have a half-life of 3 minutes in whole blood, meaning that whilst NR can be detected in the blood following administration the main circulating product is NAM [258]. Although this clearly has beneficial effects, given the limitations of NAM as an NAD-booster it is of interest to try and deliver NR to target tissues intact [245].

A recent study has identified a novel compound, NRH, which is a reduced form of NR. Administration of the compound in various cell lines resulted in an increase in NAD^+ levels at least 2-fold above the same concentration of NR, which was replicated *in vivo* [259]. The compound has already shown to be effective at alleviating kidney disease and therefore could be a potential alternative to NR if further studies confirm its' therapeutic effects [260].

1.7. Thesis Rationale

NAD^+ is well established as a modulator of metabolic health, with key signalling roles in DNA repair, calcium signalling and energy metabolism. Changing NAD^+ levels have been implicated in a number of disease states, such as aging [261] and diabetes [236], and therefore therapies to increase NAD^+ have become popular.

Whilst the role of NAD^+ as a redox molecule in energy metabolism is known, understanding how skeletal muscle energy metabolism responds to altered NAD^+

states is not well defined. This work will generate a more detailed appreciation of how altering NAD^+ levels can affect central metabolic processes. Over supplementation studies will be used to assess adverse side effects in the context of skeletal muscle. With further work exploring the metabolic consequence of NAD^+ decline and how effective known NAD^+ precursors are as treatment strategies in these cases.

1.8. Hypothesis

I postulate that the metabolic route to energy production in skeletal muscle is impacted by altered NAD^+ bioavailability. Further to this, I hypothesise that enhanced NAD^+ biosynthesis may result in beneficial adaptations to metabolism and enhance exercise performance in mice.

1.9. Aims

The thesis questions to be addressed are outlined in the following five aims.

1. Establish the effects of excess NAD^+ on carbon metabolism *in vitro* in skeletal muscle cells and primary muscle cell models using 1D-^{1}H-NMR spectroscopy and combined 2D-^{1}H,^{13}C-NMR and GC-MS analysis (Chapter 3).

2. Define how administration of NR affects exercise performance in mice using indirect calorimetry (Chapter 3).

3. Develop C2C12 and primary muscle cell models of NAD^+ depletion to characterise changes in metabolite concentrations and understand how NAD^+ depletion affects central carbon metabolism (Chapter 4).

4. Investigate whether repletion of NAD^+ can help rescue the effects of NAD^+ depletion on central carbon metabolism in skeletal muscle cells (Chapter 4).

5. Develop a primary skeletal muscle cell culture model of an overexpressing NRK2 mouse to elucidate changes to energy metabolism and muscle cell development as a result of an altered NAD^+ biosynthetic pathway (Chapter 5).

2. General Methods

All products were ordered from Sigma-Aldrich, UK, unless otherwise stated.

2.1. Tissue Culture

2.1.1. C2C12 Cell Line

The C2C12 cell line is a well-established skeletal muscle cell model, C2C12 myoblasts were purchased from the European Collection of Cell Cultures (Salisbury, UK). The line was initially generated through serial passage of mouse myoblast cells derived from the thigh of C3H/HeJ mouse donors following crush injury [262]. The maximum passage number of the C2C12s was 18 to ensure consistency across different experiments.

2.1.1.1. Proliferation

The cells were grown in 75 cm^2 Greiner tissue culture flasks in growth medium (GM) consisting of Dulbecco's Modified Eagle's Medium (DMEM) supplemented with 10 % foetal bovine serum (FBS) and 1 % Penicillin/Streptomycin (P/S). The GM was replaced every 48 hours; once the myoblasts reached 70 % confluence they were split in to fresh flasks using Gibco TrypLE (ThermoFisher Scientific, UK) for maintenance or, if the cells were for an experiment, they were seeded into culture plates and fresh GM was added. Enough TrypLE was added to cover the bottom of the flask and they were left in the incubator for 5 minutes.

2.1.1.2. Differentiation

After the myoblasts were seeded into plates and were 70 % confluent, GM was replaced with differentiation medium (DM) consisting of DMEM with 5 % horse serum (HS) and 1 % P/S. The myoblasts were cultured in this media for 5 days prior to initiation of treatment, with the media replaced every 48 hours, which gave sufficient time for them to differentiate into multinucleated contractile myotubes.

2.1.1.3. Freezing Down

To ensure the stock of C2C12 myoblasts was maintained it was important to prepare the cells for long-term storage. The cells were cultured in 75 cm^2 flasks and trypsinised when 70 % confluent, they were washed in 10 ml of GM and centrifuged at 12,000 revolutions per minute (rpm) for 5 minutes at 20 ºC. The media was removed and the pellet was diluted in 5 ml of DMEM supplemented with 20 % FBS and 10 % DMSO. This solution was then divided between 5 cryovials, which were frozen slowly at -80 ºC at a rate of 1 ºC/min in a Freezing Container (Nalgene, Hereford, UK) using isopropanol. The cells were then transferred to liquid nitrogen.

2.1.1.4. Thawing Cells

To begin a fresh culture of C2C12s, the cryovials were removed from liquid nitrogen and quickly thawed by swirling in a water bath at 37 ºC. Once thawed the cells were transferred to a falcon tube with 10 ml GM added and spun down at 12,000 rpm for 5 minutes at 20 ºC. The supernatant was removed and the cell pellet was resuspended in GM pre-warmed to 37 ºC and transferred to a 25 cm^2 tissue culture flask. The cells were then grown following *section 2.1.1.1.*

2.1.2. **Primary Muscle Cell Culture**

Primary cell culture is a useful technique with cell characteristics found to be more reflective of those *in vivo*. Whilst the cells have a finite life span and they take more care to culture than C2C12s the data is important to confirm and support work conducted in immortalised cell lines.

Also of importance is the maintenance of *in vivo* genetic manipulations. Primary culture of mouse models with genetic variations will produce myotubes expressing

the same gene knock out or over expression as the parental tissue. This enables treatment of the cells in cell culture that may be complex or not possible *in vivo*.

2.1.2.1. Satellite Cell Isolation

Heterozygous breeding of the Nmrk2 knockout mouse line, C57BL/6NTac, (NRK2 KO) was conducted to provide litter matched WT and NRK2 KO mice for studies. The Nmrk2 over expresser line, C57BL/6NTac, was also utilised. Nmrk2 is the gene coding for the NRK2 protein.

Gastrocnemius muscle was collected from mice and placed in DMEM containing 0.2 % Collagenase from *Clostridium histolyticum*. This was left at 37 °C for 2 hours to allow for enzymatic digestion of the collagen that holds the muscle fibres together. The myofibres were washed in DMEM supplemented with 1 % P/S for an hour before being further mechanically digested using a pipette and left in the incubator for 2 hours.

All plates were coated with Matrigel (BD biosciences, US). This involved adding 2.5 % Matrigel (made up in DMEM +P/S) to the plates and leaving for 2 minutes before removing any excess, the plates were then placed in the incubator to allow the Matrigel to set.

DMEM containing 30 % FBS, 10 % HS, 1 % chick embryo extract (CEE) (Life Science Production, UK), 1 % P/S and 0.1 % fibroblast growth factor (FGF) (PeproTech, UK) was added to the Matrigel coated wells and using a Pasteur pipette the isolated myofibres were then transferred. The cells were then left for 72 hours to allow the satellite cells to migrate away from the myofibres.

2.1.2.2. Proliferation

Following satellite cell migration the media was replaced with proliferation media; DMEM supplemented with 10 % HS, 0.5 % CEE and 1 % P/S. This stage was to stimulate the satellite cells to proliferate. As outlined in *section 1.1.2* satellite cells undergo asymmetric division. This means that whilst most of the cells are committed to myoblast formation, some remain as satellite cells [23]. Typically the satellite cells were left to proliferate for 24 hours, figure 2.1.

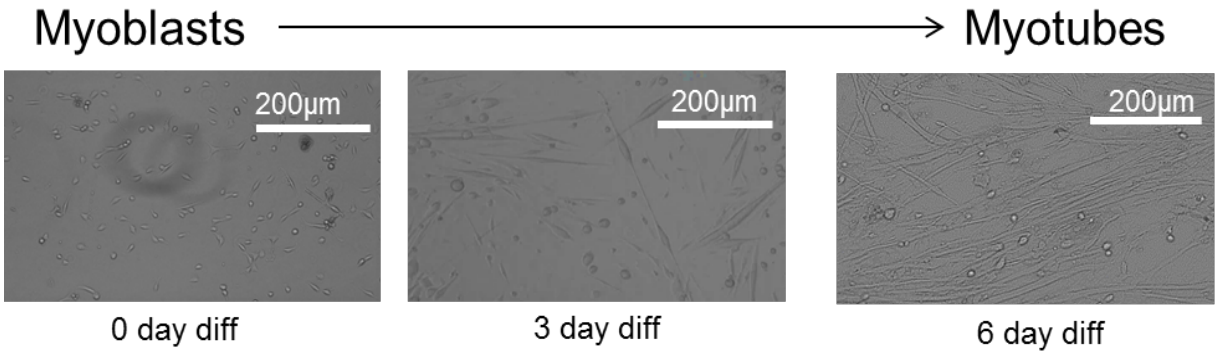


Figure 2.1. Primary Skeletal Muscle Differentiation
Primary myoblasts were seeded (left) and DM was added. The myoblasts begin to fuse together (centre) before becoming fully differentiated, multinucleated myotubes (right).

2.1.2.3. Differentiation

Differentiation media consisted of DMEM supplemented with 2 % HS, 0.5 % CEE and 1 % P/S. This stage was essential to allow the mononucleated myoblasts to fuse together to form multinucleated myotubes. The main differences between the media compositions are the reduction of the serum levels, which is permissive to differentiation. For the experiments within this thesis all primary cultures were left to differentiate for 6-8 days before any treatments were started, figure 2.2. Media was replaced every 48 hours.



Figure 2.2. Differentiated Primary Myotubes
Primary myotubes were cultured from gastrocnemius muscle and differentiated for 6-8 days to produce multinucleated myotubes.

2.1.3. Cell Treatments

Once all cells were differentiated into multinucleated myotubes cell treatments were initiated. For the final 24 hours of each experiment all media was replaced with serum-free media to minimise interaction of the serum with the treatments. It is important to note that the dosages used were selected as a tool to induce the NAD^+ concentration changes necessary.

2.1.3.1. Nicotinamide Riboside

NR (Chromadex, US) was dissolved in water to a concentration of 1 mM and was filter sterilised through a bacterial filter. The final concentration of NR added to the cells was 0.5 mM following a study showing this as the optimal concentration for elevated NAD^+ levels in C2C12s [201]. Sterile water was used as the vehicle control.

2.1.3.2. Nicotinamide Mononucleotide

NMN treatments were completed as a comparison to NR and therefore all concentrations were the same; 0.5 mM final concentration. Sterile water was used as the vehicle control.

2.1.3.3. FK866

FK866 was used to chemically inhibit NAMPT. It was dissolved in DMSO to a stock concentration of 11 mM and used at a final concentration of 50 nM. This concentration was selected as previous studies have shown these levels to be effective in cells according to a dose-response curve [263]. The cells were treated with FK866 for 24, 48 or 72 hours with treatments being re-added following media change. 0.001 % (v/v) DMSO was used as the vehicle control.

2.2. Animal Sacrifice and Tissue Collection

All experiments and procedures involving animals were approved by and performed under British Home Office Guidance (Animals Scientific Procedures) Act 1986.

Following *in vivo* experiments animals were sacrificed by cervical dislocation, cessation of circulation was confirmed prior to initiation of dissection. All tissues were snap-frozen in liquid nitrogen. The muscle tissues were taken with priority to minimise metabolite degradation and signalling changes. The soleus, tibialis anterior (TA), quadriceps, heart and liver were routinely collected following an experiment. The gastrocnemius muscle was used for primary cell culture.

The tissues were stored in -80 °C until required for analysis. Preparation of the tissue for analysis involved pulverisation of the tissue in liquid nitrogen using a Mortar &

Pestle (ThermoFisher Scientific, UK). The pulverised tissue was then weighed out. Typically 20 mg of tissue was required for RNA analysis, 30 mg for protein analysis, 10 mg for gas chromatography – mass spectrometry (GCMS) analysis and 10 mg for the NAD^+ Cycling Assay.

Once divided out for analysis the tissue was lysed in the appropriate buffer using a TissueLyser II (Quiagen, Germany) at 30 Hz for 3x 30 second intervals, or until completely lysed.

2.3. Ribonucleic acid (RNA) Analysis

RNA analysis was used to determine/quantify changes to the expression of particular genes in response to treatments.

2.3.1. RNA Extraction

TRIzol reagent (Invitrogen, UK) was used for RNA extraction, as it is effective at maintaining RNA integrity whilst dissolving biological material and denaturing proteins.

0.5 ml of TRIzol was added and cells were scraped and transferred to 2 ml safe-lock Eppendorf tubes (Eppendorf, UK), they were pipetted up and down to maximise lysis. For RNA extraction from tissue the steps outlined in *section 2.2.* were used, with 750 µl of TRIzol per sample.

To aid phase separation 200 µl of chloroform / ml of TRIzol reagent was added and the tube was vortexed for 5 seconds, this was left at room temperature for 5 minutes and then centrifuged at 4 °C at 12,000 rpm for 10 minutes. Three distinct phases

were formed at this stage. The upper aqueous phase contained the nucleic acids and was transferred to a new tube for precipitation, with care taken not to disturb the other phases to avoid contamination. 500 µl of isopropanol / ml of TRIzol reagent was added to the new tube and placed at -20 °C for 1-2 hours before being centrifuged again using the same settings.

After centrifugation an mRNA pellet had formed in the tube, the supernatant was removed with care taken not to disturb the pellet. The pellets were washed; 500 µl of 75 % ethanol per ml of TRIzol reagent was added and re-centrifuged using the above settings. Once again the supernatant was removed and discarded, the tubes were left open to allow the remaining ethanol to dry before the RNA pellet was re-suspended in 30 µl of nuclease free water (NFW).

2.3.2. RNA Quantification

The RNA concentration was measured using a NanoDrop (ThermoFisher Scientific, UK) to give the amount of ng/ml in each sample. 1 µl of NFW was added to the arm of the NanoDrop to make a blank measurement. Following this 1 µl of each sample was measured with the detection arm cleaned in between. A 260/280 nm ratio of between 1.8 and 2 was considered sufficient quality for use.

The volume of RNA needed to give 1 µg in 10 µl was diluted in NFW.

2.3.3. Reverse Transcription of RNA

The RNA now undergoes a process to produce a complementary strand of DNA (cDNA) using a High Capacity cDNA Reverse Transcription Kit (Applied Biosystems, USA) was utilised.

Per RNA sample 2 µl reverse transcription buffer, 0.8 µl deoxynucleotide triphosphates (dNTPs), 2 µl random primers, 1 µl reverse transcriptase and 4.2 µl NFW was added. These were added to a PCR machine and the following programme was run: 25 ºC for 10 mins, 37 ºC for 120 mins, 85 ºC for 5 mins and stored at 4 ºC until the end of the method.

The cDNA was diluted 1:3 in NFW to ensure plenty of sample for qPCR.

2.3.4. Real-time Polymerase Chain Reaction (qPCR)

Real-time PCR (qPCR) allows for the quantification of a specific gene within a sample. Through differing temperature cycles the gene product of interest is amplified and due to the presence of a fluorescent dye this is detected and reported.

A qPCR run results in three phases. The exponential phase where there is doubling of the product with every cycle, the linear phase where the reaction is slowing due to reagents running out and the plateau phase where the reaction stops.

For analysis of qPCR the phase of interest was the exponential phase as it provided the most accurate data. A threshold was set where the fluorescent intensity was above the background. The PCR cycle where the sample reached the threshold was reported as the Ct value and used for relative quantification.

2.3.4.1. TaqMan

TaqMan probes are sequence specific probes, which are added to the cDNA along with a master mix containing unlabelled primers. The PCR machine heats up leading to the denaturing of the cDNA strands. Upon cooling the sequence specific probe binds to the gene of interest. The probe has a reporter and a quencher attached to either end. Taq DNA polymerase binds to the primers and begins transcription to

produce new cDNA. If the gene of interest is present, and the probe has attached, the Taq polymerase will release the probe. This results in the reporter and the quencher no longer being in proximity, allowing the reporter to fluoresce. The real time increase can be monitored and used to create an amplification plot.

MicroAmp Optical 384-well Reaction Plates (ThermoFisher Scientific, UK) and Semi-Skirted 96-well PCR Plates (Star Lab, UK) were used for qPCR analysis. Preparation of qPCR plates with TaqMan probes involved 1 µl of cDNA added to the well along with 5 µl of SensiFAST Probe Hi-ROX Kit for 384-well plates and SensiFAST Probe Lo-ROX Kit for 96-well plates (Bioline, UK). 3.75 µl of NFW and 0.25 µl of the gene probe of interest were also added, a list of those used can be found in Appendix A. 18s was used as the housekeeper gene throughout. All samples were run in duplicate or triplicate. Plates were sealed with Axygen UltraClear Sealing Film (Corning, UK) and run on an ABI 7500 Real-time-PCR machine for 96-well plates and an ABI 7900HT Fast Real-Time PCR System for 384-well plates (ThermoFisher Scientific, UK) with a VIC reporter for the housekeeper and TAMRA for the other gene probes.

2.3.4.2. SYBR Green

SYBR green was used for detection of Nmrk2. The chemistry is different and requires the addition of a forward and reverse primer for the gene of interest. If the gene is present in the sample the primers will bind and the gene will be produced as a PCR product. The SYBR green dye fluoresces when bound to double-stranded DNA and therefore the signal will increase in real-time with the generation of product.

Specificity of the primers is assessed through melt curve analysis. Following the PCR run the thermocycler continues to detect levels of fluorescence whilst increasing its

temperature incrementally. The increasing temperature will denature the double-stranded PCR product. As SYBR green dye only fluoresces when bound to double-stranded DNA the dye will dissociate and the fluorescence intensity will decrease. The change in slope of the curve produced is plotted as a function of the temperature and this is referred to as the melt curve. As there should only be one PCR product produced during the qPCR run there should therefore only be one peak on the melt curve, figure 2.3. If multiple peaks appear this is suggestive of an inefficient reaction and would require further investigation.

Preparation of qPCR plates with SYBR green primers involved 1 µl of cDNA added to the well along with 5 µl of PowerUP SYBR Green master mix (ThermoFisher Scientific, UK), 3 µl of NFW, 0.5 µl of the forward primer and 0.5 µl of the reverse primer, details of which can be found in Appendix A. Plates were sealed and run on an ABI 7500 Real-time-PCR machine.

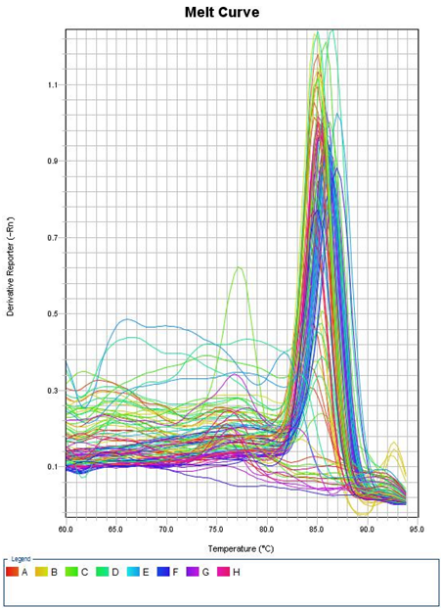


Figure 2.3. SYBR Green Melt Curve
Melt curves are used to assess specificity of the primers used. One peak should be shown on the graph, which shows one product was made during the qPCR run. Representative melt curve from Nmrk2 SYBR Green detection.

2.3.4.3. qPCR Analysis

The Ct values of the housekeeper gene, 18s, were subtracted from the Ct values of the genes of interest to give delta Ct (dCt). To express the data using arbitrary units (AU), dCt^(-2) is used, which makes larger numbers representative of higher expression and vice versa.

Sometimes this work involves comparison of different treatments or groups; therefore for each gene of interest the delta dCt (ddCt) is determined through subtraction of one dCt from the control group's dCt value. The ddCt is then used to calculate the fold change, the magnitude of the change, through the formula 2^{-ddCt}.

2.4. Protein Analysis

Methodology used to investigate changes in protein expression.

2.4.1. Protein Extraction

To extract protein from cells they were first washed with cold PBS. Then 500 μl radioimmunoprecipitation assay (RIPA) buffer (50 mM Tris-Cl (pH 8.0), 150 mM sodium chloride (NaCl), 1 % (w/v) Nonidet P-40, 0.5 % (w/v) sodium deoxycholate, 0.1 % (w/v) sodium dodecyl sulfate (SDS), 1 mM ethylenediaminetetraacetic acid (EDTA)) supplemented with a Pierce protease inhibitor tablet (per 10 ml RIPA) (Life Technologies, UK) was added. They were then scraped and transferred to a 2 ml safe-lock Eppendorf. For protein extraction from tissues the steps outlined in *section 2.2.* were used with 750 μl of RIPA solution. Samples were pelleted in a centrifuge at 12000 rpm for 10 minutes. The supernatant, containing the protein, was transferred to a new Eppendorf and used for analysis.

The detergents in the RIPA buffer are responsible for cell lysis with the protease inhibitor added to prevent proteolysis during extraction.

2.4.2. Protein Quantification and Preparation

Quantification of protein within the samples was calculated using the DC™ protein assay kit (BioRAD, UK). Bovine serum albumin (BSA) was used to prepare standards of between 0-10 mg protein in the buffer used for the protein extraction (in most cases RIPA buffer). 5 μl of the protein standards and the samples of unknown concentrations were added to a 96-well plate in duplicate. 200 μl of protein assay reagent B and 25 μl of a reagent A and S mixture was added to the samples, 20 μl of reagent S added per ml of reagent A.

Samples were incubated for 5 minutes at room temperature and then plates were read at 595 nm using a Victor3 1420 multilabel plate reader (PerkinElmer, USA). A standard curve was produced from the BSA standards. Using the equation of the line the sample concentrations could be extrapolated and used to calculate the necessary dilutions to produce samples with equal protein concentrations.

Typically 20 μg/μl of protein was prepared for one western blot gel. The samples were made up to 10 μl in distilled water and 2x Laemmli sample buffer was added (0.125 mM Tris-HCl pH 6.8, 4 % SDS, 0.004 % bromophenol blue, 10 % 2-mercaptoethanol, 20 % glycerol). Samples were then boiled for 3 minutes. The 2-mercaptoethanol reduces the disulphide bonds. The SDS detergent denatures the proteins and subunits and gives them an overall negative charge, allowing them to be separated based on their size. To aid protein loading into the gel the bromophenol blue acts as a dye with the glycerol increasing the density of the samples.

2.4.3. Immunoblotting

The samples were separated by weight using SDS – polyacrylamide gel electrophoresis (SDS-PAGE). SDS-PAGE apparatus (BioRAD, UK) was used and 10 % (v/v) acrylamide gels were made using ProtoGel reagents (National diagnostics, UK).

Resolving gels were first made (3.33 ml Acrylamide (30 %), 2.5 ml resolving buffer, 0.5 ml ammonium persulfate (APS) (1.5 % (w/v)), 3.67 ml distilled H_20 and 10 µl tetramethylethylenediamine (TEMED)). This was mixed and poured into a western blotting gate; ethanol was added on top to ensure the gel set in a straight line. Once set the ethanol was poured off and stacking gels were made (0.6 ml Acrylamide (30 %), 1.25 ml stacking buffer, 0.2 ml APS (1.5 % (w/v)), 2.6 ml distilled H_20 and 15 µl TEMED). This was loaded into the top of the gate and well combs added. This was also allowed to set before the gels were transferred to SDS-PAGE tanks (Bio-Rad, UK).

Migration buffer was added to aid separation; a 10X stock solution (0.25 M Tris, 1.92 M Glycine and 1 % SDS) was diluted to a working concentration and added to the tanks. The well combs were removed and 20 µl of the protein samples were loaded into the wells. A PAGE-Ruler Plus Prestained Protein Ladder (ThermoFisher Scientific, UK) was added with marked molecular weights to enable protein band molecular weights to be determined. Following sample loading the gels were run at 100 V using a power supply (BioRAD, UK) until the protein had migrated to the bottom of the gel.

The protein was then transferred to a nitrocellulose membrane using an iBlot according to the manufacturers protocol (ThermoFisher Scientific, UK). The membrane was subjected to a blocking agent, 5 % BSA in tris-buffered saline with Tween 20 (TBST) (10 mM tris, pH 8.0, 150 mM NaCl, 0.5 % Tween 20) for 1 hour rocking at room temperature, and then washed briefly with TBST. The membranes were incubated with NRK2 antibody (BioGenes, Germany) diluted in TBST (1:1000) and left rocking at 4 °C overnight. The membranes were washed the following morning with TBST 3x 15 minutes. Dako anti-rabbit horseradish peroxidase-conjugated secondary antibody (Agilent, US) was then added (1:10000) for 1 hour at room temperature and the wash step repeated. Loading control was assessed through α-tubulin (SC-5286) antibody (Santa Cruz Biotechnology, US) at (1:1000) with Dako anti-mouse horseradish peroxidase-conjugated secondary antibody (Agilent, US) added at (1:10000). Electrochemiluminescence (ECL) substrate (Bio-Rad, UK) was added to the membrane and left at room temperature for 5 minutes.

The excess ECL was blotted off the membranes and they were transferred to a developing cassette. In darkness blue-x-ray film (GE Healthcare Life Sciences, UK) was added to the cassette and the cassette was closed. Differing exposure times were used to get optimal results for the protein of interest. The films were developed in a Xograph compact X4 developer (Xograph healthcare, UK). All developed films were scanned into the computer.

2.5. High Resolution Respirometery

Mitochondrial function can be assessed through oxygen sensors and their ability to measure oxygen flux in cells and tissue. The oxidative capacity of the cell can be assessed through changes to oxygen levels in response to different substrates. Oroboros machines provide high-resolution respirometery.

The mitochondrial function of fully differentiated myotubes was assessed using a two-chamber Oxygraph (OROBOROS Instruments, Austria). Prior to loading into the chambers cells were removed from the plates by trypsin and spun down to form a pellet before being resuspended in 2 ml DMEM. Once within the chambers the cells were left to incubate for 10 minutes to measure their endogenous respiration.

Assessment of oxidation capacity was carried out by sequentially subjecting the cells to differing concentrations of inhibitors and uncouplers. Each was added once the oxygen flux had been stable for 5 minutes following the previous addition. Uncouplers and inhibitors (oligomycin, FCCP, rotenone and antimycin A) were diluted in absolute ethanol. Stocks were stored at -20 °C until required for use.

Prior to the experiment the stocks were thawed and checked for precipitation. A Hamilton syringe was then used to sequentially add the following:

- 1 µl of 5 mM oligomycin for a final concentration of 2.5 µM. This is an ATPase inhibitor and results in a disrupted mitochondrial proton gradient, which stops the electron transport chain. This stage is LEAK respiration as it accounts for the proton leak through the mitochondrial membrane during resting, non-phosphorylating electron transfer.

- Sequential 1 µl titrations of 0.5 mM carbonyl cyanide-*4*-(trifluoromethoxy)phenylhydrazone (FCCP). This is a protonophore and acts as an uncoupler by moving protons across the lipid bilayer. This is continued until maximal respiration is reached.
- 1 µl of 1 µM rotenone for a final concentration of 0.5 µM. This inhibits complex I and allows for assessment of complex II maximal respiratory capacity.
- Finally, 1 µl of 5 mM antimycin A for a final concentration of 2.5 µM. Complex III inhibition for determining the residual oxygen consumption.

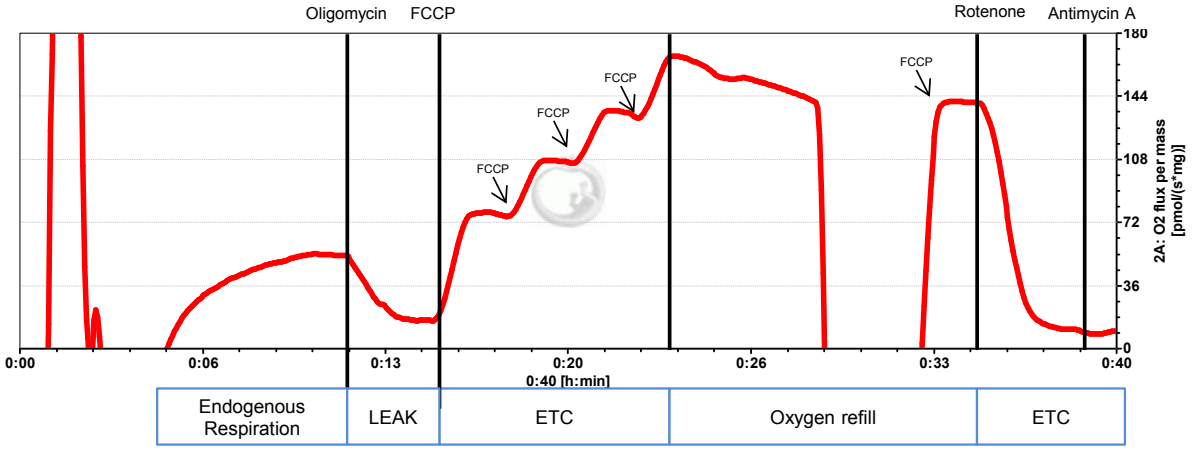


Figure 2.4. High Resolution Respirometery Graph
A two-chamber oxygraph was used to assess oxidation consumption in response to differing inhibitors and uncouplers. The graph above represents the time points each compound was added (black lines) with the red line representative of the oxygen flux within the chamber.

Throughout the experiment if the oxygen levels dropped too low the chamber could be opened and given time to refill with oxygen, all outlined in figure 2.4. Following the experiment the chamber contents were collected, pelleted and used in a Bio-Rad protein assay according to *section 2.4.1*. Together the data was used to determine the oxygen flux/mg of protein.

2.6. Nuclear Magnetic Resonance Spectroscopy

Nuclear magnetic resonance (NMR) spectroscopy is an analytical chemistry technique used to determine content and molecular structure of compounds. The theory behind NMR spectroscopy will be briefly discussed throughout the following section with detailed experimental procedures outlined in *Section 2.6.6.*

2.6.1. Nuclear Spin

NMR spectroscopy works on the principle of nuclear spin (*I*). An atom is comprised of protons and neutrons contained in the nucleus and electrons surrounding the nucleus in an electron cloud. When the number of protons and neutrons within an atomic nucleus are equal the spin of these particles is paired and therefore the nucleus has no overall spin, figure 2.5A. When a nucleus has an odd number of protons or neutrons as shown in figure 2.5B the spin of the nucleus is ½, these can be detected through NMR spectroscopy.

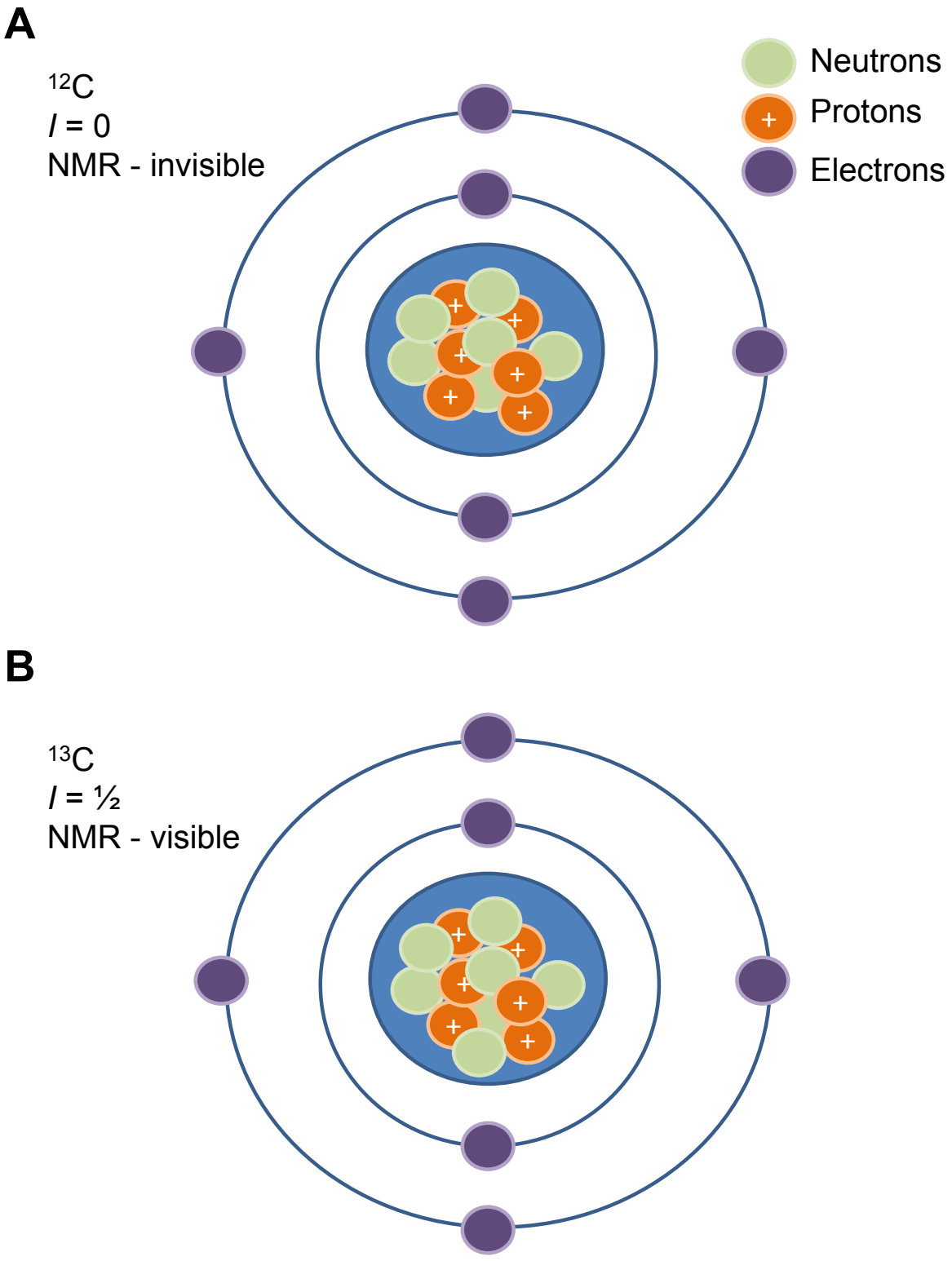


Figure 2.5. Carbon Isotope Examples
Carbon can exist with a different number of neutrons. (**A**) ^{12}C has an even number of protons and neutrons meaning it cannot be seen via NMR spectroscopy. (**B**) ^{13}C has an extra neutron, giving an odd number of neutrons and therefore generating a spin that can be viewed by NMR spectroscopy.

In the absence of an external magnetic field 'NMR-active' isotopes, nuclei that can be detected using NMR spectroscopy, are not aligned to any specific direction. The number of spin states possible for a given nucleus can be determined using the following equation: $2I+1$. For ^{1}H and ^{13}C atoms this means the nuclei can orientate in 2 spin states, α or β, upon application of an external magnetic field, figure 2.6A. Based on the principles of the Boltzmann distribution a higher proportion of nuclei will exist in the α spin-state as it has a lower energy level and is considered to be more stable than the β spin-state. The difference in energy between the two spin states is equal to the Larmor frequency, which is dictated by the nucleus specific gyromagnetic ratio (λ), and the external magnetic field strength (B_0), figure 2.6B.

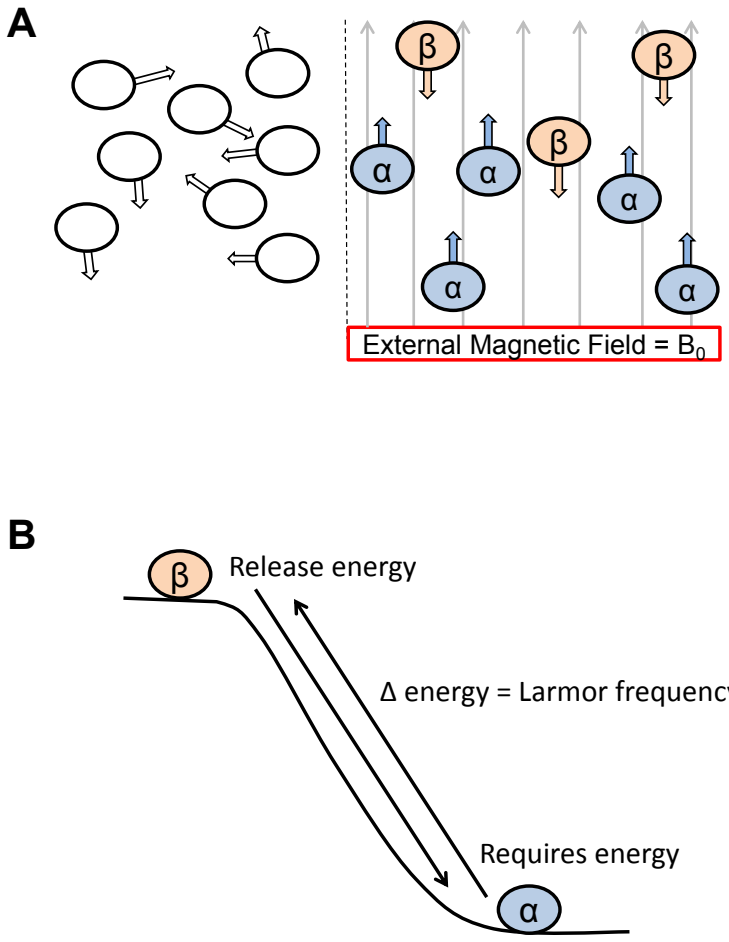


Figure 2.6. Spin States
(**A**) Nuclei moving into alignment, in either the α or β spin state, upon application of an external magnetic field. (**B**) The difference in energy between the two spin states is defined as the Larmor frequency.

2.6.2. RF Pulse

The summation of the individual magnetic fields of the nuclei is known as the net magnetisation and is often depicted as a single arrow to show the direction of the overall magnetisation of the molecule.

A radiofrequency (RF) pulse of electromagnetic radiation, matching the Larmor frequency, is applied perpendicular to the external magnetic field. As this matches the energy difference between the two spin states the nuclei absorb the energy and rotate in phase around the RF's axis in the xy plane, figure 2.7A. The Boltzmann distribution is disturbed, as the population of nuclei in the α and β states are now equal. The result is no net magnetisation along the Z-axis.

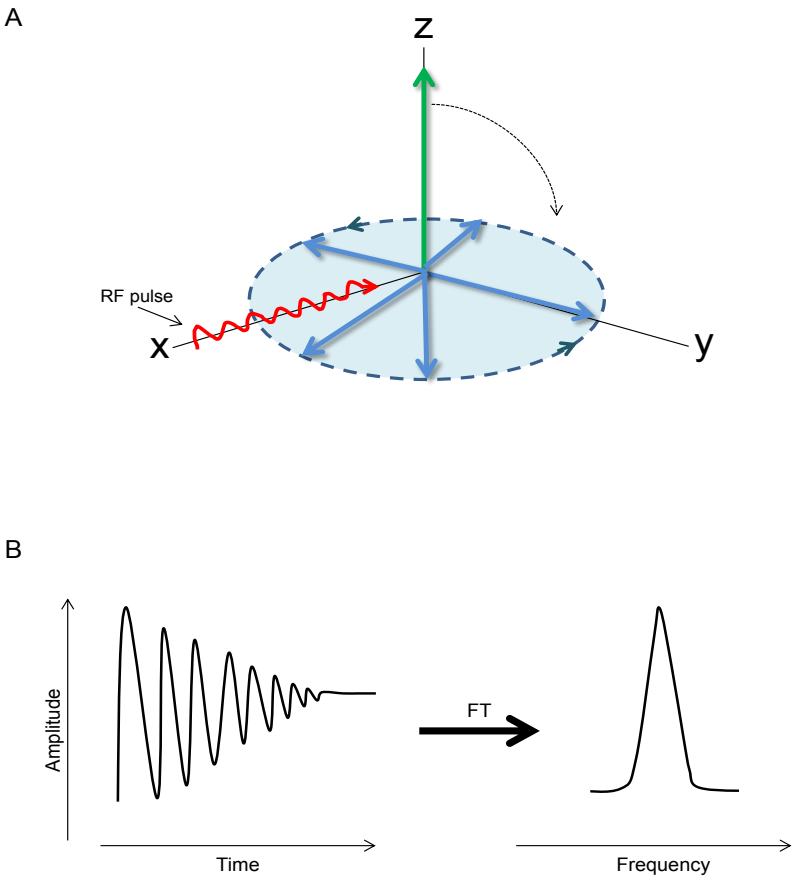


Figure 2.7. Generation of a Signal
(**A**) Application of an RF pulse causes the nuclei to rotate around xy plane. Cessation of the RF pulse causes relaxation of the nuclei, which allows for signal detection. This is called the Free Induction Decay (FID). (**B**) The signal generated is in the time domain and can be extremely complex, fourier transformation (FT) is conducted to convert the signal into the frequency domain.

At this stage the RF pulse is switched off to allow for relaxation. As the bulk magnetisation spirals around the Z-axis it creates oscillating magnetic moments in the Y-axis generating a signal, which induces a current in a receiver coil within the NMR spectrometer.

Individual nuclei precess at differing frequencies dependant on their chemical environment, meaning that the frequency of the current generated is slightly different. The signal produced is a summation of the individual signals from the different nuclei. The intensity of the signal detected gets smaller over time but the frequency remains constant; this is the Free Induction Decay (FID).

2.6.3. Fourier Transformation

The number of molecules within a sample can be calculated based on the concentration of ^{13}C-glucose used. The work in this thesis used 10 mM ^{13}C-glucose.

$$10^{-3}\ M \times 10^{-3}\ L = 10^{-6}\ moles$$

$$10^{-6} \times 6x10^{23} = 6x10^{17}\ atoms$$

Each atom contains a nucleus; the signal generated can be complex as a result of the combination of the different nuclei within the sample. In order to be able to interpret the data the signal needs to be converted from the time-domain to the frequency domain, a process known as Fourier Transformation (FT), figure 2.7B.

2.6.4. Chemical Shift

Absolute frequencies are measured in hertz (Hz). To simplify the reporting of the NMR signals, the frequencies are calculated with respect to a standard, for ^{1}H-NMR 4,4-dimethyl-4-silapentane-1-sulfonic acid (DSS) was used. The frequencies of the

signal expressed in Hz are directly proportional to the instrument's magnet strength. This allows for the conversion of the frequency in Hz into parts per million (ppm), figure 2.8. The frequency measurements are now independent of magnet strength and therefore comparison of spectra acquired on different spectrometers can be conducted.

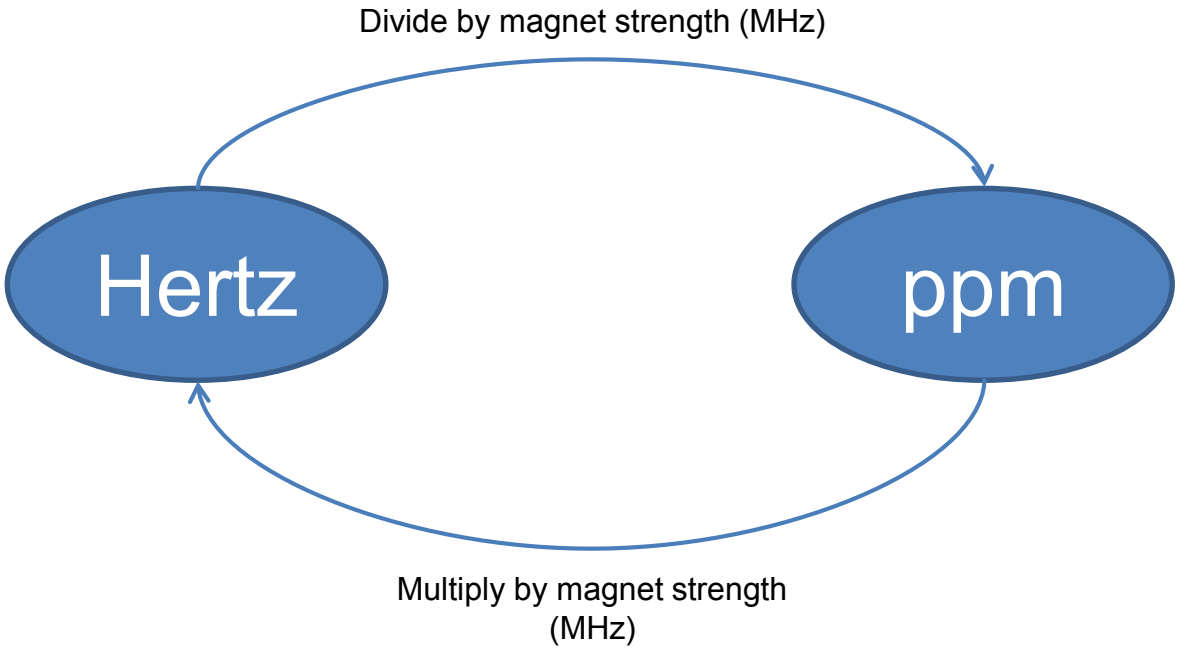


Figure 2.8. Unit Conversion
To enable comparison between spectrometers of different magnet strength, frequencies are converted from hertz (Hz) to parts per million (ppm).

Once this conversion has been processed the resonance frequency of the nuclei is referred to as its chemical shift. The reference compound is set to 0 ppm and each peak represents a different set of nuclei with a unique chemical environment. The area under each peak, the integral, is representative of the concentration of nuclei with the same resonance and it is this that allows accurate quantification of

metabolites. An example spectrum is shown in figure 2.9, showing the software fitting of the area under the curve of one of NAD^+'s peaks.

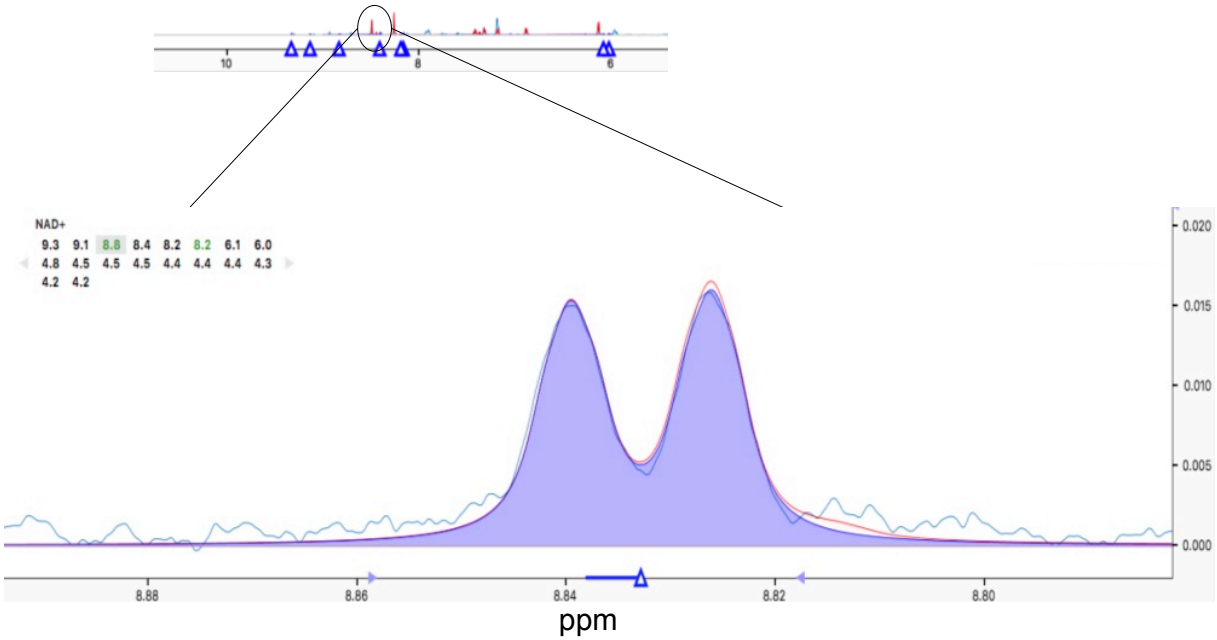


Figure 2.9. NAD^+ Quantification
An example spectrum from 1D-^{1}H-NMR spectroscopy showing fitting of the area under the curve for NAD^+. Each metabolite will have multiple peaks at different chemical shifts representing protons within different chemical environments. A peak was selected that was used to fit the metabolite. This was kept consistent across the different samples to enhance reliability.

A proton's location on a spectrum is determined by its chemical environment. Figure 2.10 shows two signals representing protons within two different chemical environments, exposed to different levels of shielding. A shielded nuclear environment is one in which the proton of interest has many electrons around it with opposing magnetic fields to B_0. This reduces the strength of the magnetic field 'felt' by the proton and therefore requires less energy to bring it into resonance. These protons appear upfield on the spectrum (lower ppm).

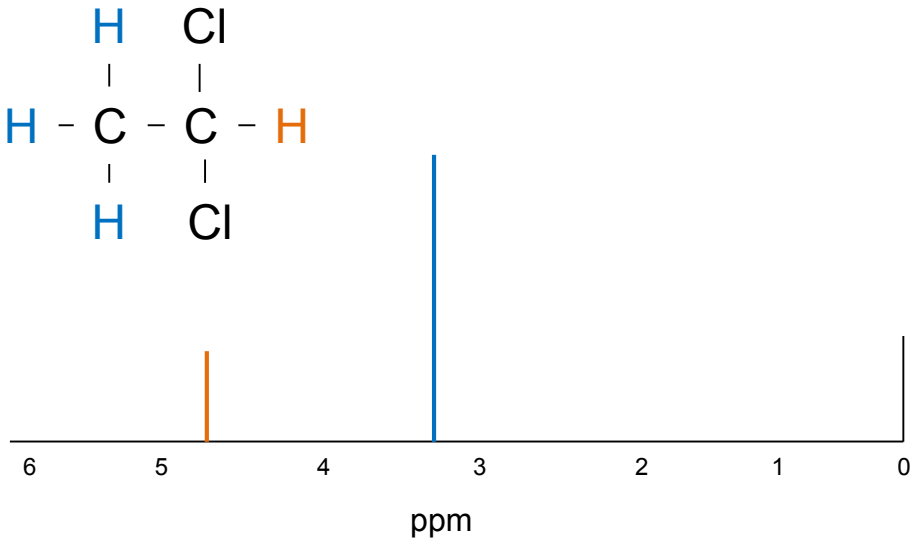


Figure 2.10. Different Chemical Shifts
Each peak on a spectrum is representative of a proton with a unique chemical environment. NMR spectra showing peaks representing the protons within 1-1-dichloroethane. The blue peak is from the protons within the methyl group; these are shielded and therefore appear upfield on the NMR spectra. The orange peak is from the proton attached to the neighbouring carbon; chlorine is electronegative and therefore pulls electrons away from the proton resulting in it appearing downfield on the spectra.

Conversely, a deshielded environment is one where the proton is close to an electronegative atom. This pulls the electrons away and exposes the proton, resulting in more energy needed to bring it into resonance. These appear downfield on the NMR spectra (higher ppm).

2.6.4.1. Splitting

A signal experiences splitting when an adjacent atom has another proton attached, as the two protons are close enough to exert a magnetic influence on each other. As shown in figure 2.11A the methyl group could have its three protons in different combinations of α or β. There are four possible situations, which results in the attached proton having its peak split into four. Figure 2.11B shows the possible spin states for the other proton, of which there are only two. This therefore splits the methyl group's peak into two, figure 2.11C.

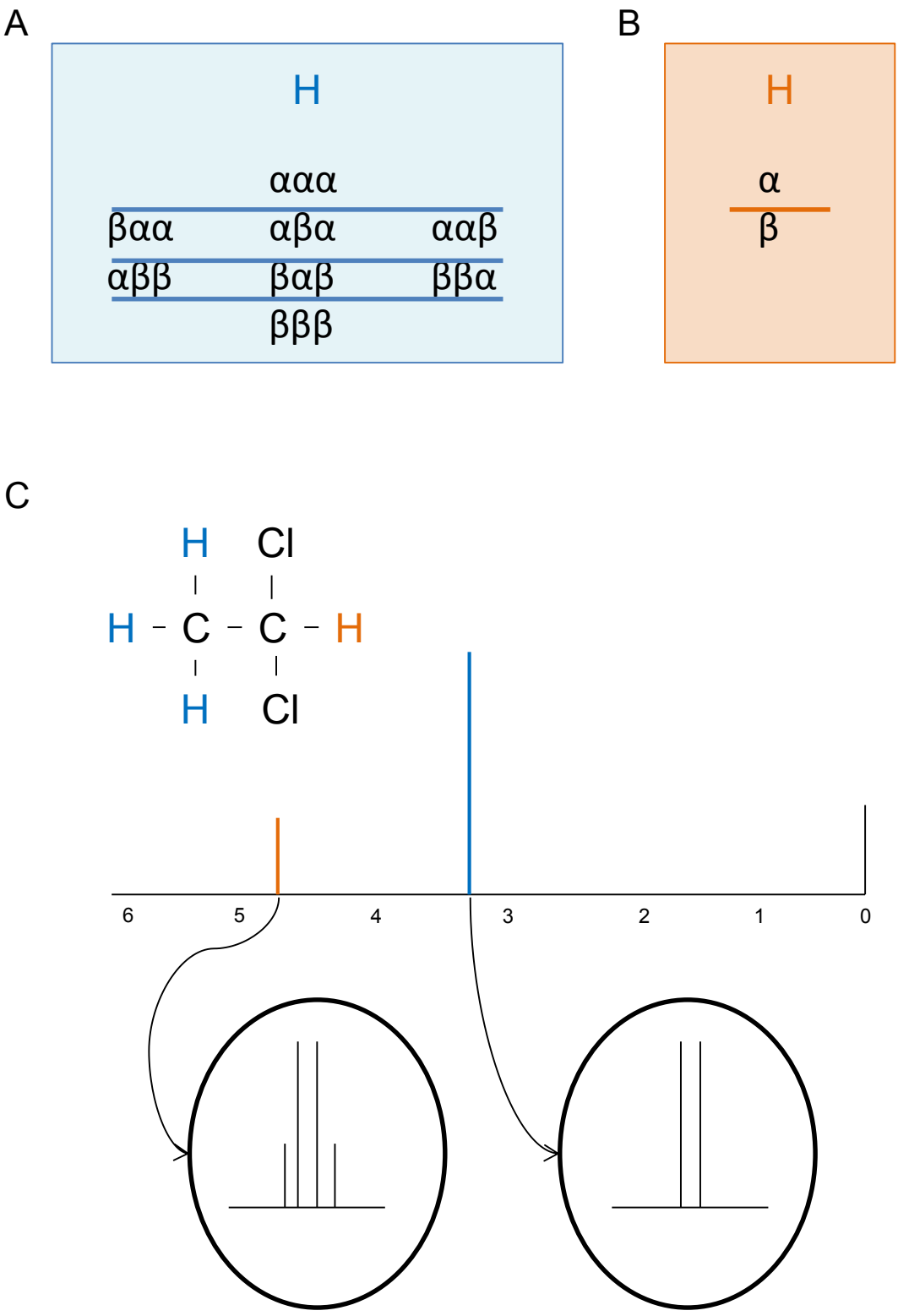


Figure 2.11. Splitting

A proton signal is split as a result of a neighboring proton's spin states. (**A**) shows the possible combination of spin states arising from the protons in the methyl group. (**B**) shows the spin states that the other proton could exist in. (**C**) shows the resultant splitting patterns.

The intensity of the peaks is dependent on the probability of that situation occurring. It is more likely that there will be two nuclei in the α or β state at any particular time which results in the peaks being split with a ratio of 1:3:3:1. With regard to the other proton, there is equal possibility of it existing as either α or β, meaning that the ratio is 1:1.

The distance between the split peaks is known as the J-coupling constant and is based on the chemical bond separating the protons. It is reported in Hz and is constant regardless of the strength of the spectrometer used.

2.6.5. 2D-NMR Spectroscopy

The work conducted within this project not only uses 1D-^{1}H-NMR spectroscopy to accurately quantify metabolites but also utilises 2D-^{1}H,^{13}C-NMR. Introducing a second dimension into the NMR spectra helps reduce spectral congestion and as a result improves resolution. Heteronuclear single quantum coherence (HSQC) spectroscopy involves ^{1}H nuclei and the nuclei of ^{13}C, the natural abundance of which is around 1.1%. The spectra generated have two frequency axes, one for each nucleus, ^{1}H on the x-axis and ^{13}C on the y-axis. A signal appears on the spectra whenever a proton is connected to a ^{13}C nucleus, with the coordinates of the point the chemical shift of the individual nuclei.

For the purpose of identifying metabolic information concerning the samples the cells are left to metabolise with ^{13}C. This increases the incorporation of ^{13}C into the metabolites and therefore increases the signal intensity for detection via HSQC-NMR.

2.6.5.1. Carbon-Carbon Splitting

In a similar way to the splitting observed with 1D-^{1}H-NMR, adjacent ^{13}C molecules result in splitting which can inform us on the labelling patterns within a particular metabolite. A diagrammatic representation of how a signal is split in response to different combinations of ^{13}C labelling is shown in figure 2.12. The percentage contribution of each labelling pattern or mass isotopomer distribution (MID) is calculated and this is used to determine pathway utilisation.

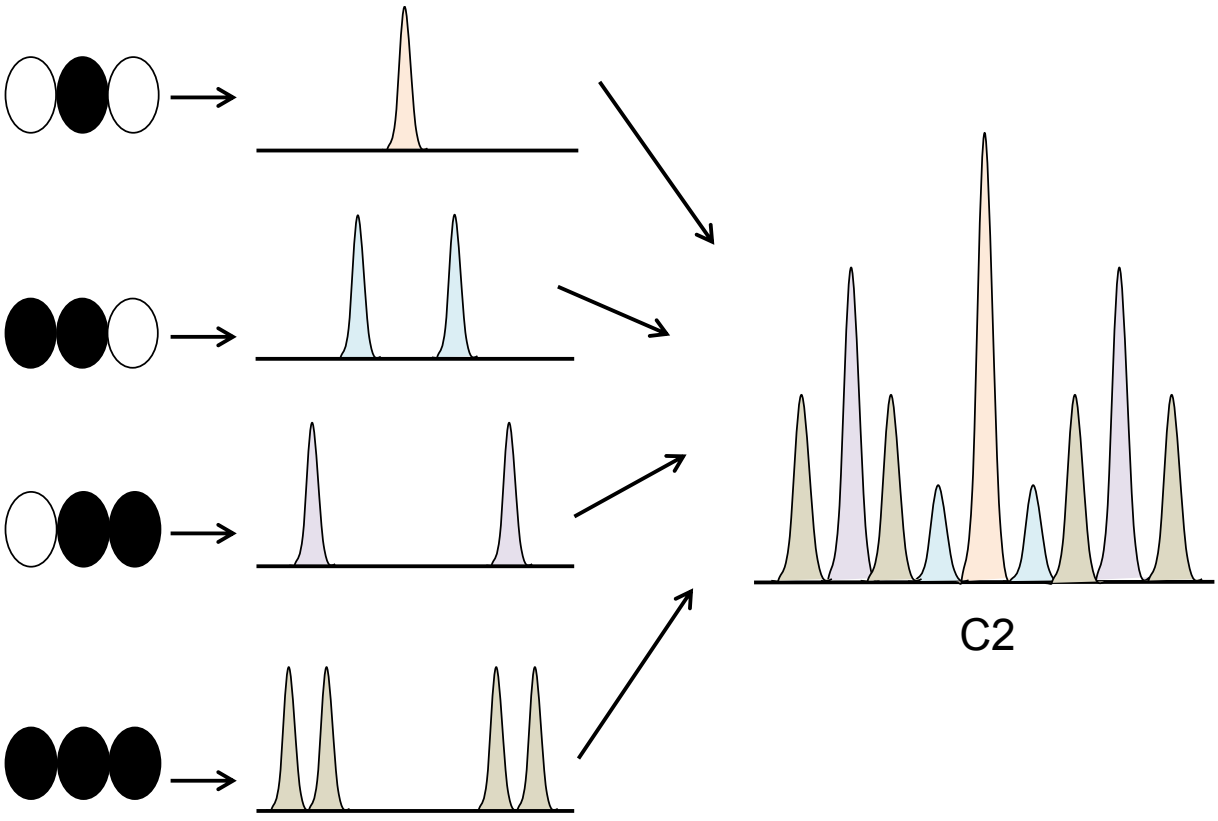


Figure 2.12. Carbon-Carbon Splitting
A carbon signal is split as a result of neighbouring ^{13}C molecules. The splitting of C2 is shown in response to different labelling patterns, with the overall spectrum a combination of the peaks.

2.6.5.2. Stable Isotope Tracer Treatments

^{13}C incorporation into a metabolite occurs when the isotopic tracer is metabolised by the cell and varies depending on the tracer used. This means that some tracers are more appropriate to investigate a hypothesis than others. The tracers used in this thesis are outlined below.

All tracers ordered from Sigma-Aldrich, UK.

$^{13}C_2$-1,2-Glucose

$^{13}C_2$-1,2-glucose is useful in determining whether metabolites have been produced via the pentose phosphate pathway (PPP) or straight through glycolysis, figure 2.13. Differential labelling patterns occur, which can be interpreted and used to infer changes to pathway use.

It is important to note during analysis that some molecules such as succinate and fumarate, are symmetrical meaning two different MIDs can occur via the same route.

$^{13}C_5$-Glutamine

For information regarding glutamate use within the TCA cycle it is helpful to use $^{13}C_5$-glutamine. This can inform on TCA cycle activity, as increased rounds will result in differential labelling of metabolites, figure 2.14.

$^{13}C_6$-Glucose

To increase the detectable signal in a sample it may be preferable to use $^{13}C_6$-glucose as opposed to $^{13}C_2$-1,2-glucose. This will result in higher levels of label incorporation into downstream metabolites, which is sometimes required for detection of metabolites with low abundance.

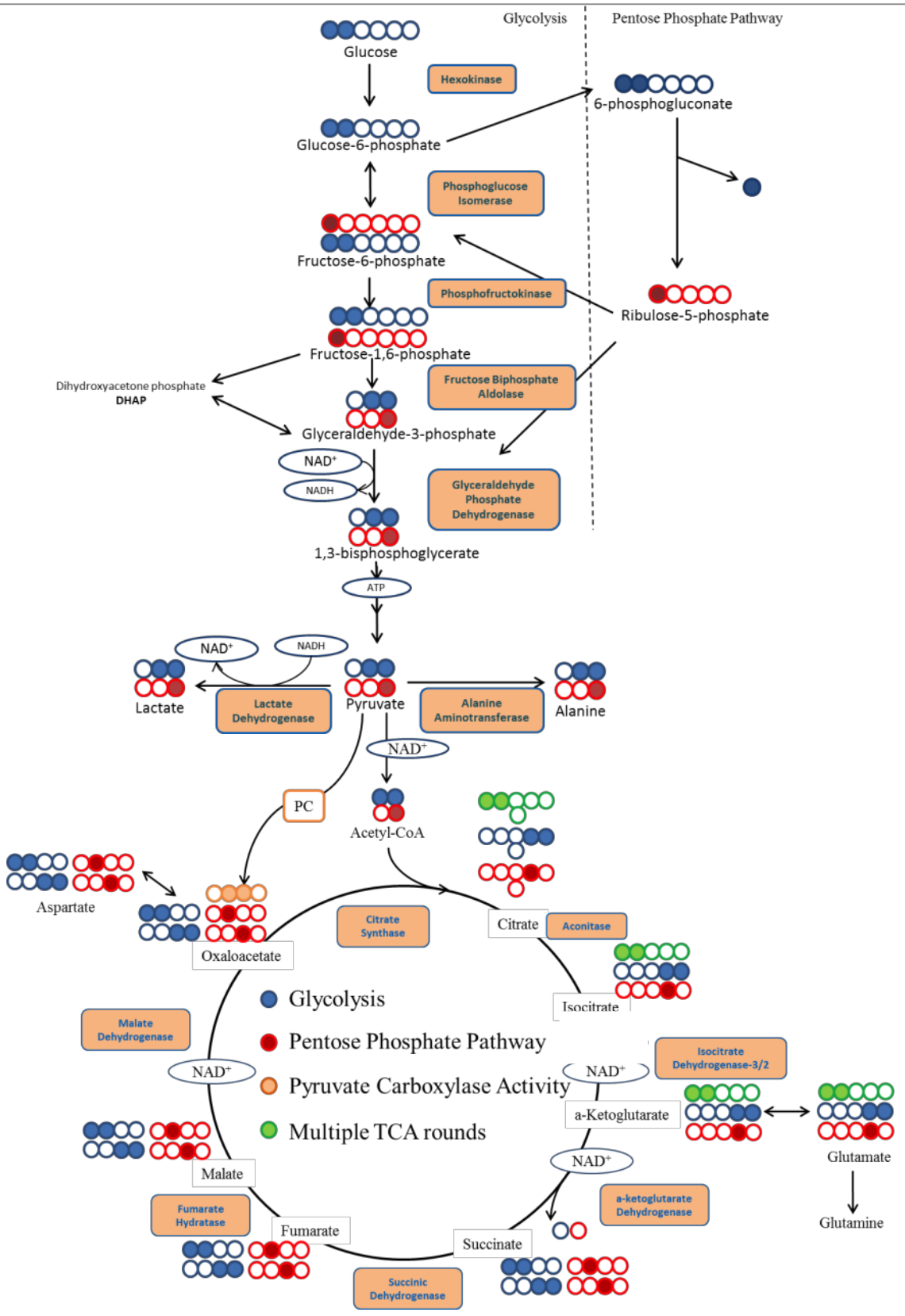


Figure 2.13. $^{13}C_2$-1,2-Glucose Labelling Patterns

$^{13}C_2$-1,2-Glucose can be used as a tracer to determine flux through glycolysis (blue), the pentose phosphate pathway (red), pyruvate carboxylase activity (orange) and the TCA cycle (green). The label incorporation into key metabolites can be measured by NMR spectroscopy and used to define the path of carbon, as shown above. This method can be used to identify routes of metabolism in response to treatments.

This isotope tracer is also less expensive and therefore unless there is a metabolic requirement for $^{13}C_2$-1,2-glucose, $^{13}C_6$-glucose is used.

$^{13}C_{16}$-Sodium Palmitate

This tracer is used to assess fatty acid oxidation. During fatty acid oxidation sodium palmitate is broken down, as discussed in *section 1.1.4.4.* and the ^{13}C is incorporated into the products.

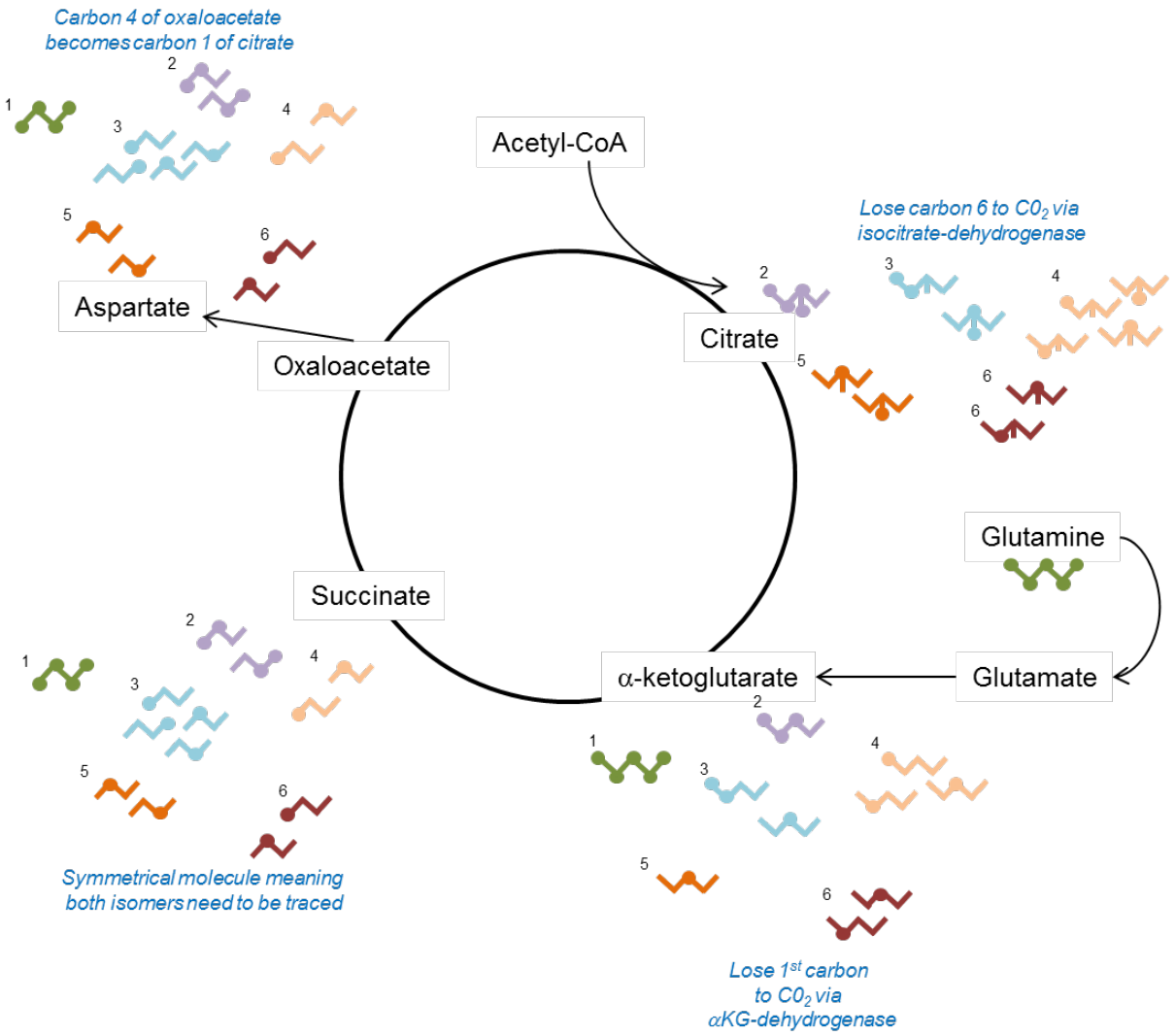


Figure 2.14. $^{13}C_5$-Glutamine Labelling Patterns
A diagrammatic representation of how metabolic tracing occurs using $^{13}C_5$-Glutamine. Allows differentiation of TCA cycle rounds using key TCA cycle metabolites.

2.6.5.3. Limitations of NMR Spectroscopy

This type of NMR spectroscopy can only detect proton-bearing carbon atoms, rendering some carbons invisible within the spectra. Further to this, a relatively high abundance of sample is required due to the low sensitivity of the technique. The analysis generates a ^{13}C labelling pattern, disregarding the ^{12}C contribution to the metabolite. This means that the labelling patterns provided are simply relative multiplet contributions with no reference to the unlabelled portion of the metabolite.

In order to address these limitations and generate a complete data set GCMS analysis is used, discussed further in *section 2.7*.

2.6.6. Experimental Methods

2.6.6.1. Extraction of Polar Metabolites

Typically cells for metabolomics were plated in 15 cm tissue culture dishes. To extract polar metabolites from cells media was discarded and the cells were washed three times with ice-cold 0.9 % saline solution, with care taken to ensure all saline was removed from the plate. Following the wash step the plates were placed on dry ice. 1.2 ml of methanol (-20 ºC) was added to cell plates to quench metabolism along with addition of 2.5 µg/ml of D6-glutaric acid as an internal standard. The cells were scraped and the contents transferred to a falcon tube where 1.2 ml of chloroform (-20 ºC) was added, which helps separate the non-polar metabolites. The tube was rocked at 4 ºC for 10 minutes, to help lyse the cells, before 1.2 ml pre-chilled HPLC-grade H_20 was added and left to rest on ice for 10 minutes.

Separation of the polar and non-polar fractions was achieved through centrifugation at 4 ºC on full speed for 15 minutes. The fractions were separated with the polar aqueous layer on the top and the non-polar on the bottom, these phases were

separated by a thin protein interface. 2 ml of the polar fraction was transferred to a new tube for NMR, with 200 µl of this removed for GC-MS. Both fractions were evaporated to dryness using a SpeedVac (ThermoFisher Scientific, UK) at 30 ºC for 4-5 hours and stored at -80 ºC until further analysis.

The non-polar fraction was removed and discarded leaving the protein interface intact in the falcon tube; these were left to dry overnight and then weighed. The protein weights were used for normalisation during analysis.

Extraction from Tissues

200 mg of tissue was pulverised using a steel Mortar & Pestle (ThermoFisher Scientific, UK) and the powdered sample was added to 1.5 ml of methanol. A probe sonicator was used 2x for 40 seconds to homogenise the tissue. Following this 1.5 ml of chloroform was added and the tubes were rocked at 4 ºC for 10 minutes. 1.3 ml pre-chilled HPLC-grade H_20 was added and left to rest on ice for 10 minutes. The slightly lower water volume was to account for water already within the tissue sample. The samples were then centrifuged and processed in the same way as cells.

2.6.6.2. NMR Data Acquisition

Once dry the NMR samples were reconstituted in 100 mM sodium phosphate buffer containing 500 µM DSS and 10 % D_2O, pH 7.0. To ensure complete lysis of the cells the samples were sonicated before being transferred to glass champagne vials. A Gilson liquid handling robotic system was used to move the samples into 1.7 mm NMR tubes (Cortecnet, USA), which could then be loaded into the NMR spectrometer.

A Bruker Avance III 600 MHz NMR spectrometer was used with a 1.7 mm z-PFG TCI Cryoprobe. The 2D-^{1}H,^{13}C-HSQC NMR spectra were acquired with echo/anti-echo

gradient coherence selection following pre-saturation which is necessary to suppress the water resonance. The spectral widths were set at 13.018 ppm and 160.0544 ppm in the direct and indirect dimension. The ^{1}H dimension involved acquisition of 512 complex data points and the ^{13}C indirect dimension used a non-uniform sampling scheme to acquire 29.9927% (2457) out of 8192 complex data points. The interscan relaxation delay was 1.5 s.

2D-^{1}H,^{13}C-HSQC spectra were reconstructed via the compressed sensing algorithm using the MDDNMR (version 2.5) and NMRPipe (version 9.2) software [264–266]. All spectra were processed without baseline correction as this can present challenges for the multiplet analysis procedure.

128 transients were acquired for each 1D-^{1}H-NMR spectrum with a relaxation delay of 4 s. Prior to the first acquisition the samples were automatically tuned and matched before they were shimmed to a DSS line width of <1 Hz. The 1D-^{1}H-NMR acquisition took ~15 minutes, with the 2D-^{1}H,^{13}C-HSQC NMR taking 4.5 hours, giving a total experiment time of 4 hours 45 minutes per sample.

2.6.6.3. NMR Data Analysis

1D-^{1}H-NMR spectra

MetaboLab software (version 1) was used to process the 1D-^{1}H-NMR spectra. The methyl group of lactate was used as a reference to calibrate the chemical shift prior to data analysis [267]. The spectra were zero-filled to 131,072 data points before FT was completed and the DSS signal was set to 0 ppm to calibrate the chemical shift. All spectra were manually phase corrected and baseline correction was conducted using a spline function. Quantification was completed using the Chenomx software

package (ChenomxINC, version 7.0), which required spectra to be saved in the Bruker format. All metabolite concentrations were normalised to pellet weight.

2D-^{1}H,^{13}C-HSQC NMR spectra

2D-^{1}H,^{13}C-HSQC NMR spectra analysis was also completed in MetaboLab. The spectra were referenced to lactate and manually phase corrected. For each metabolite the peaks were identified. Following this HSQC multiplet analysis was completed by fitting the simulated spectra to the experimental data. This allowed for the software to calculate the MID percentages, once labelling possibilities had been inputted.

An experimental example of the multiplet analysis conducted on carbon 2 of glutamate is shown in figure 2.15. The red line is the experimental data, which is fit to the simulated blue line. The signal is split as a result of adjacent ^{13}C labelled carbons, with the J-coupling constants shown for each.

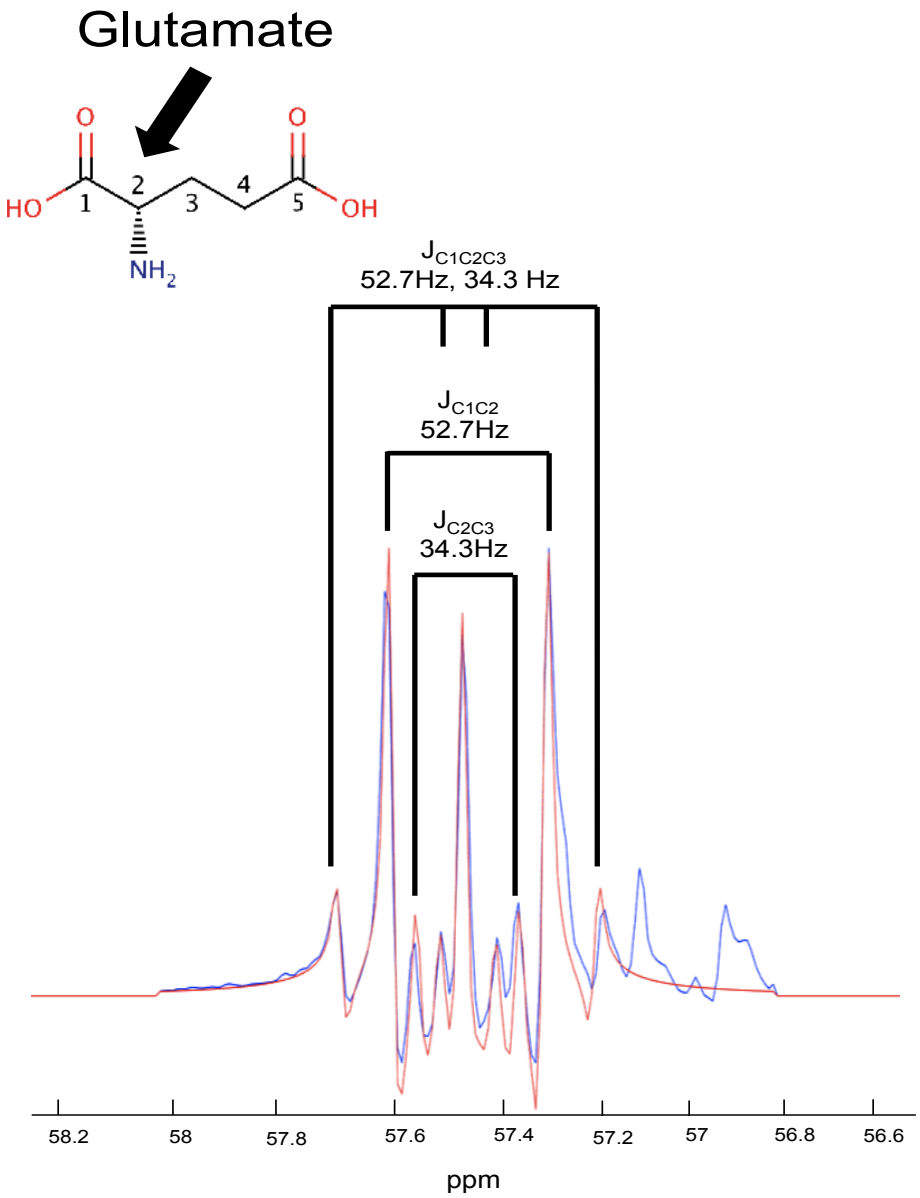


Figure 2.15. Multiplet Analysis of Carbon 2 of Glutamate
An example spectrum showing the peaks associated with carbon 2 of glutamate. The J-coupling constants are shown, which represent the width between the peaks relating to different labelling patterns.

2.7. Gas Chromatography Mass Spectrometry

GCMS is an alternative analytical technique that combines both gas chromatography and mass spectrometry. Polar, thermostable metabolites are separated and detected

allowing for relative quantification and information about individual components of a molecule, figure 2.16.

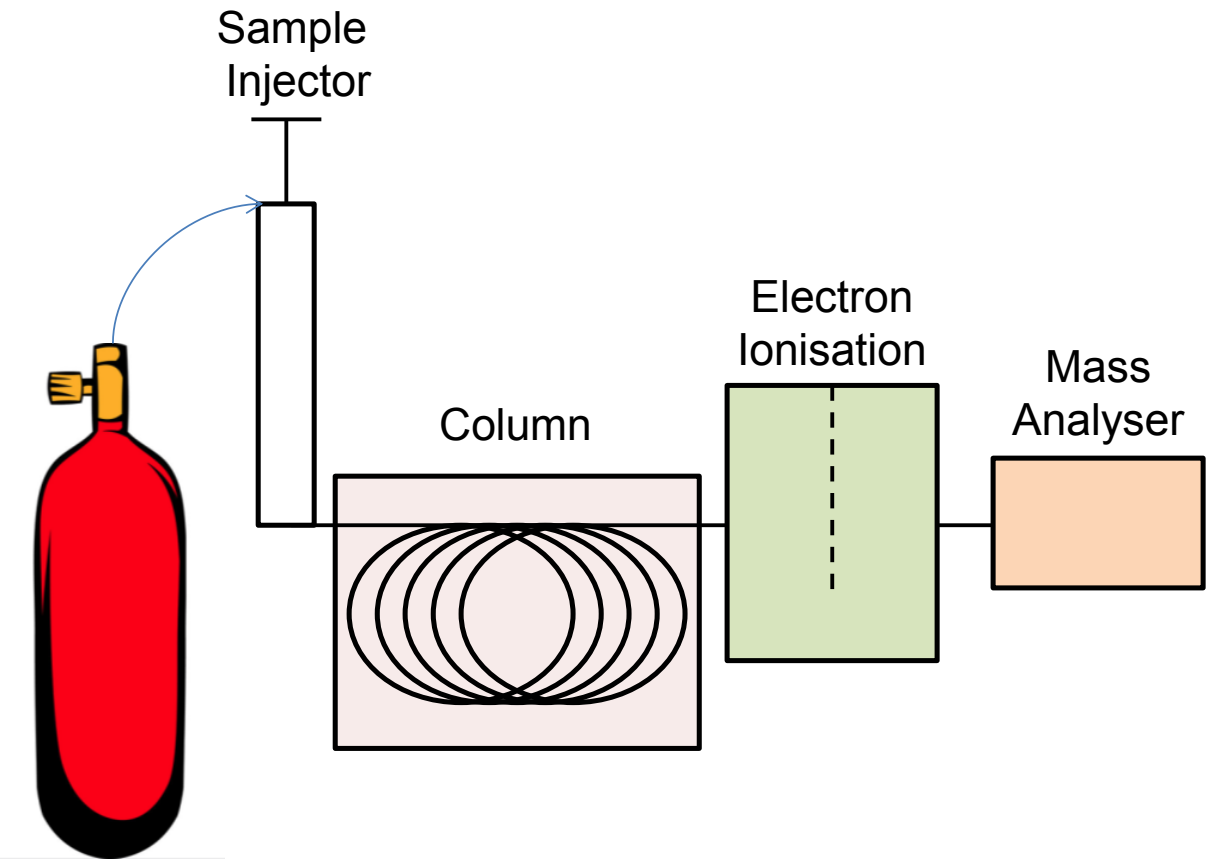


Figure 2.16. Gas Chromatography – Mass Spectrometry
The samples are injected into the machine and vaporised. A carrier gas, helium, is used to carry the sample along the column. Interactions of the molecules with the column separate out the different components of the sample. Once the molecule has reached the end of the column it undergoes electron ionisation where it forms ions and is fragmented. The fragments are detected by a mass analyser.

2.7.1. Chemical Derivatisation

The metabolites are extracted according to *Section 2.6.6.1.* Prior to the processing of the polar metabolite samples via GCMS they were first chemically derivatised. This step involved the introduction of a silyl group to the molecule in substitution for active hydrogen. Both the polarity of the molecule and the formation of hydrogen bonds are

reduced as a result. The silylated derivative has an increased volatility and is more thermostable to withstand the high temperatures without degradation.

The sample tubes were left open to ensure all moisture was removed before they were incubated at 95 °C. The extracts were solubilised in 40 µl of 2 % methoxyamine hydrochloric acid (HCl) in pyridine. The samples were vortexed for 1 minute before 5 minutes of high speed shaking; they were then incubated at 60 °C for 60 minutes. Following this incubation the samples were centrifuged at 13000 rpm 4 °C for 10 minutes before derivatisation reagent was added. This comprised of 60 µl N-tertbutyldimethylsilyl-N-methyltrifluoroacetamide (MTBSTFA) with 1% (w/v) tertbutyldimethyl-chlorosilane (TBDMSCI). The suspension was incubated for 1 hour at 60 °C in a closed tube to prevent evaporation. The samples were then centrifuged at 13000 rpm for 10 minutes at 4 °C and the clear supernatant was transferred to a chromatography vial with a glass insert (ThermoFisher Scientific, UK).

2.7.2. Gas Chromatography

The samples were injected and vaporised before being transferred to the chromatography column by the carrier gas. The interaction of the different molecules with the column separate out the components of the sample.

Derivatised samples were analysed using an Agilent 7890B Series GC/MSD gas chromatograph with a medium polar range polydimethylsiloxane GC column (DB35-MS), in association with a mass spectrometer (Agilent Technologies UK Limited, UK). The GC-MS was set up in splitless mode with the carrier gas, helium, set at a flow rate of 1 ml min^{-1} and the inlet liner temperature set to 270 °C. The oven temperature was set to 80 °C for 1 minute and then heated to 250 °C at a rate of 5 °C min^{-1}. This

temperature was ramped up further at 15 °C min^{-1} to 340 °C before being held for 6 minutes. Compound detection was conducted in full scan mode with 2-4 measurements taken per second in the mass range 50 to 650 m/z, the source temperature was 250 °C and the transfer line was 280 °C. A solvent delay time of 9 minutes was used to ensure the heating element did not switch on until the solvent had eluted from the column, thereby protecting the MS filament. In order to prevent contamination between samples the injector needle was cleaned three times prior to the each measurement with methanol and hexane.

2.7.3. Mass Spectrometry

The MS portion of the instrument measured the mass-to-charge ratio of ions. Once the column had separated the molecules within the sample they underwent electron ionisation (EI). Heated filaments emitted an electron current in a vacuum; the electrons collided with the gas phase molecules leaving the column to form ions. This form of ionisation is considered hard ionisation and results in high fragmentation of the molecule.

The mass analyser detected the mass-to-charge ratio (m/z) of the ions. Different metabolites fragment differently and each fragment has a different retention time. A qualifier ion is used to identify the metabolite and this enabled the software to quantify the abundance relative to other metabolites within the sample.

Isotopic labelling results in an increased mass with each addition of a ^{13}C, this can also be detected on the MS. Percentages are given for each isotopologue within a metabolite, informing on the unlabelled levels (M+0), presence of one ^{13}C (M+1), two ^{13}C (M+2), etc. The mass increments of a molecule detected through GCMS are

combined with the atom-specific information yielded from NMR spectroscopy [268]. Together the two techniques complement each other to provide a complete data set that can be reliably utilised for pathway analysis, figure 2.17.

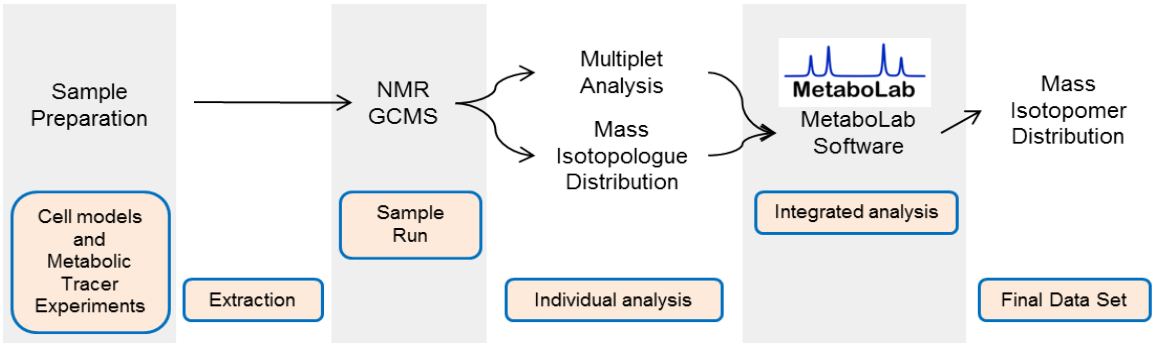


Figure 2.17. Combined NMR and GCMS Analysis
An outline of the workflow used for the metabolic tracer experiments. The integrated analysis using the MetaboLab software allows for a more confident readout of the mass isotopomer distribution for metabolites using both the percentage of mass isotopologues from the GCMS analysis alongside the multiplet analysis from the NMR data.

2.8. Liquid Chromatography Mass Spectrometry

LCMS is another analytical technique. This can often be used to identify different metabolites to GCMS, with a soft ionization process used.

2.8.1. Extraction of Metabolites

The cells were seeded into 6-well tissue culture plates for LCMS analysis. At the end of the protocol the cells were washed quickly with ice-cold PBS, with care taken to remove all PBS from the wells. Lysis buffer was prepared prior to initiation of the extraction protocol; 30 % acetonitrile, to lyse the cells, 20 % H_20 and 50 % methanol, to extract the polar metabolites. 500 µl of ice-cold lysis buffer was added to the wells and the cells were scrapped and transferred to a 2 ml safe-lock Eppendorf tube. The samples were vortexed for 45 seconds and then centrifuged at 13,000 rpm at 4 °C for

15 minutes. The supernatant, containing the polar metabolites, was transferred to a fresh Eppendorf tube. The protein pellets were dried out and weights used for normalisation.

2.8.2. LC-MS Data Acquisition and Analysis

Samples were sent to our collaborator, Oliver Maddocks, at the University of Glasgow. The prepared samples were analysed on an LC-MS platform consisting of an Accela 600 LC system and an Exactive mass spectrometer (ThermoScientific, UK). A Sequant ZIC-pHILIC column (4.6 mm x 150 mm, 5 µm) (Merck, USA) was used to separate the metabolites with the mobile phase mixed by A = 20 mM ammonium carbonate in water and B = acetonitrile. A gradient program starting at 20 % of A and linearly increasing to 80 % at 30 min was used followed by washing (92 % of A for 5 mins) and re-equilibration (20 % of A for 10 min) steps. The total run time of the method was 45 min. The LC stream was desolvated and ionised in the HESI probe. The Exactive mass spectrometer was operated in full scan mode over a mass range of 70–1,200 m/z at a resolution of 50,000 with polarity switching. The LCMS raw data was converted into mzML files by using ProteoWizard and imported to MZMine 2.10 for peak extraction and sample alignment. A house-made database including all possible ^{13}C isotopic m/z values of the relevant metabolites was used for the assignment of LCMS signals. Finally the peak areas were used for comparative quantification.

2.9. Fatty Acid Oxidation Measurement

Fatty acid oxidation is a key fuel source for skeletal muscle, therefore detecting changes in response to treatments was of importance. Cells were plated in 24-well Corning tissue culture plates and at the end of the protocol were washed twice with sterile PBS. DMEM was supplemented with 7 % BSA / 5 mM palmitate / 0.01 µCi / µL ^{14}C-palmitate (PerkinElmer, US) and 1 mM carnitine. If fatty acid oxidation occurred the ^{14}C-palmitate was broken down to produce $^{14}C0_2$ by the TCA cycle, figure 2.18. The fatty acid binds to the serum albumin, which enables uptake into the cytoplasm of the cell. Carnitine is responsible for the activation of the fatty acid and its transportation into the mitochondria, outlined in *Section 1.1.4.4*. Eppendorf tubes were used to create acidification vials with 200 µl of 1 M perchloric acid added to the tube. Filter paper was inserted into the cap of the Eppendorf tube with 1 M NaOH added to this.

500 µl of the supplemented DMEM was added to the cells. Plates were sealed using parafilm and left to incubate for 3 hours. Following the incubation, 400 µl of the media was transferred to the acidification vials, which were left for a further hour to allow for the absorption of radiolabelled CO_2 into the NaOH paper discs. The filter paper was then transferred to a scintillation vial containing 4 ml scintillation fluid. The radiolabel was measured over 3 minutes using a scintillation counter.

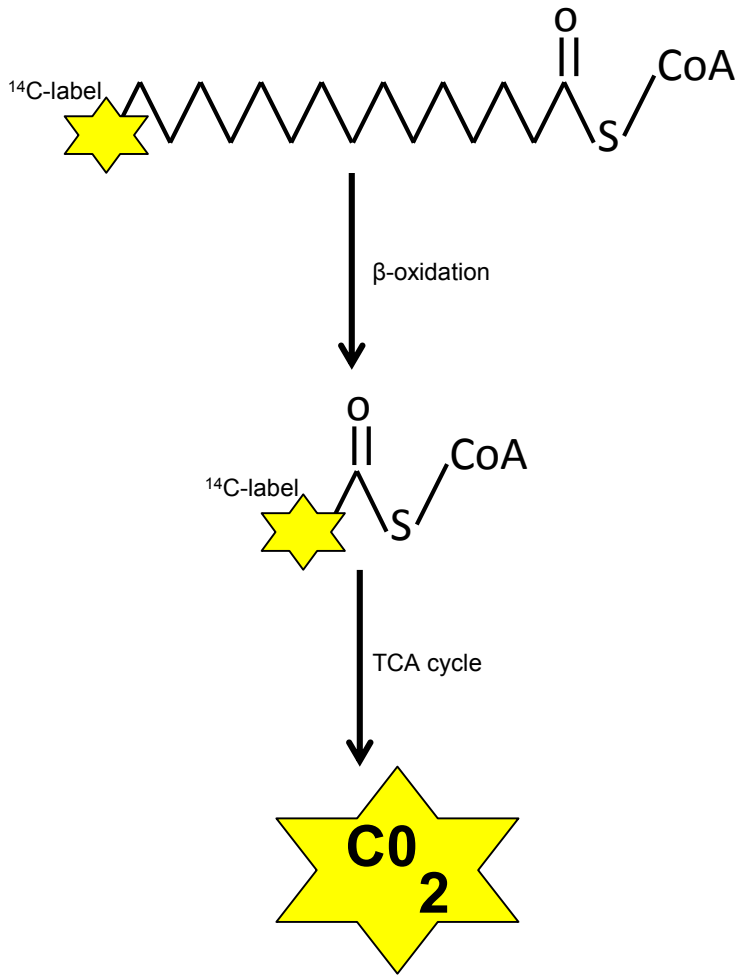


Figure 2.18. Fatty Acid Oxidation Assay
Radiolabelled sodium palmitate can undergo β-oxidation to produce radiolabelled acetyl CoA. This can be used in the TCA cycle and results in the release of radiolabelled CO_2. The levels of this can be detected using scintillation counting.

2.10. NAD$^+$ Cycling Assay

An NAD/NADH Assay Kit (Colorimetric) (Abcam, UK) was used for the detection of total NAD$^+$ and NADH within a sample. Ice-cold PBS was used to wash the cells with care taken to ensure all PBS was removed from the well. For 6-well tissue culture plates, 400 µl of ice-cold NAD extraction buffer was added and the cells were

scraped and transferred to Eppendorfs. The samples were freeze thawed twice, using dry ice, to lyse the cells. Following this, the cells were vortexed for 5 seconds before being centrifuged at 13000 rpm at 4°C for 5 minutes. The supernatant was transferred to a new tube and used for the total NAD measurement, of this 200 µl was taken for the NADH measurement. The NADH samples were heated for 30 minutes at 60 °C, to decompose the NAD within the sample.

The NADH standard was reconstituted in DMSO and sequentially added to a 96-well plate, from 0 to 180 pmol/well. The total NAD samples and NADH samples were added to the plate, diluted as necessary in NAD extraction buffer. The enzyme was added to cycling buffer and 100 µl was added to each well. The enzyme catalysed the reaction of the NAD cycling substrate in the buffer to an NAD cycling product, reducing NAD^+ in the process. The developer was reconstituted in H_2O and 10 µl was added to each well, the plates were left for 1-4 hours at room temperature. The NADH present in the wells reacted with the colorimetric probe in the developer to produce a coloured probe, figure 2.19. This was visualised using a plate reader at 450 nm at different time points within the 1-4 hours. The intensity of the colour correlated with the quantity of NADH present.

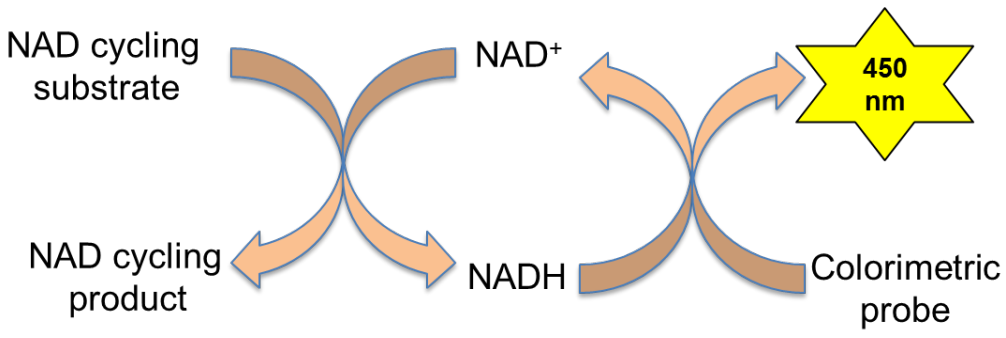


Figure 2.19. NAD^+ Cycling Assay
An assay kit was used for the measurement of NAD^+ and NADH in a sample. The NAD^+ is converted into NADH, which reacts with a colorimetric probe allowing for detection.

The analysis of the data involved plotting of an NADH standard curve from the standard samples. The concentrations of the unknown samples were extrapolated from the standard curve using their absorbance. The NADH measurement was subtracted from the total NAD(H) concentration to give a value for NAD^+. From here the NAD^+/NADH ratio could be calculated.

All data was normalised to the protein concentration, which was calculated using a Bio-Rad protein assay according to *Section 2.4.2.* BSA standards were made up in NAD extraction buffer to match the sample solutions.

2.11. Glycogen Assay

A glycogen assay kit (Abcam, UK) was used to quantify glycogen levels within the samples. The assay is colorimetric and involves the hydrolysis of glycogen to glucose by the glucoamylase enzyme. Glucose is further oxidised which produces a product that reacts with an OxiRed probe.

The cells were washed with ice-cold PBS and scraped in 200 µl of distilled water, pipetting up and down to increase homogenisation. The samples were boiled for 10 minutes to inactivate any enzymes before centrifugation at 4 °C at 13,000 rpm for 10 minutes. The supernatant was transferred to a new tube.

A 96-well plate was used with 50 µl of samples and standards added to the plate diluted in hydrolysis buffer as appropriate. 2 µl of hydrolysis enzyme mix was added to all reaction wells and left to incubate for 30 minutes. 50 µl of reaction mix was made consisting of 46 µl of development buffer, 2 µl of development enzyme and 2 µl

of OxiRed probe. This was added to all reaction wells and again left to incubate for 30 minutes, protected from light. The plates were read immediately following incubation using a Victor3 1420 multilabel plate reader at 570 nm.

The kit contained standards, which were used to create a standard curve. The concentration of glycogen within the samples could be extrapolated from the graph. All data was normalised to the protein concentration, which was calculated using a Bio-Rad protein assay according to *Section 2.4.2.* BSA standards were made up in distilled water to match the sample solutions.

2.12. In Vivo Acute Exercise Study

Wild-type C57BL/6 mice were used for metabolic phenotyping. A fully automated indirect gas calorimetry system was used in combination with the CaloTreadmill System (TSE, Germany). All components were controlled by the PhenoMaster software which also acquired data at one minute intervals.

2.12.1. Acute Exercise Protocol

An acclimatisation protocol comprising of a steady increase in treadmill speed over four days was used to train the mice before the acute exercise protocol was initiated, figure 2.20. The training treadmill allowed for the training of 6 mice at once, speeding up the acclimatisation process. This was optimised to allow the mice enough exposure to the treadmill to facilitate their run without training them. An area at the back of the treadmill was available to the mice as a refuge. An air puff system could be used three times to encourage the mice to resume exercise; if refuge continued to be sought the mouse was removed and placed back into their home cage.

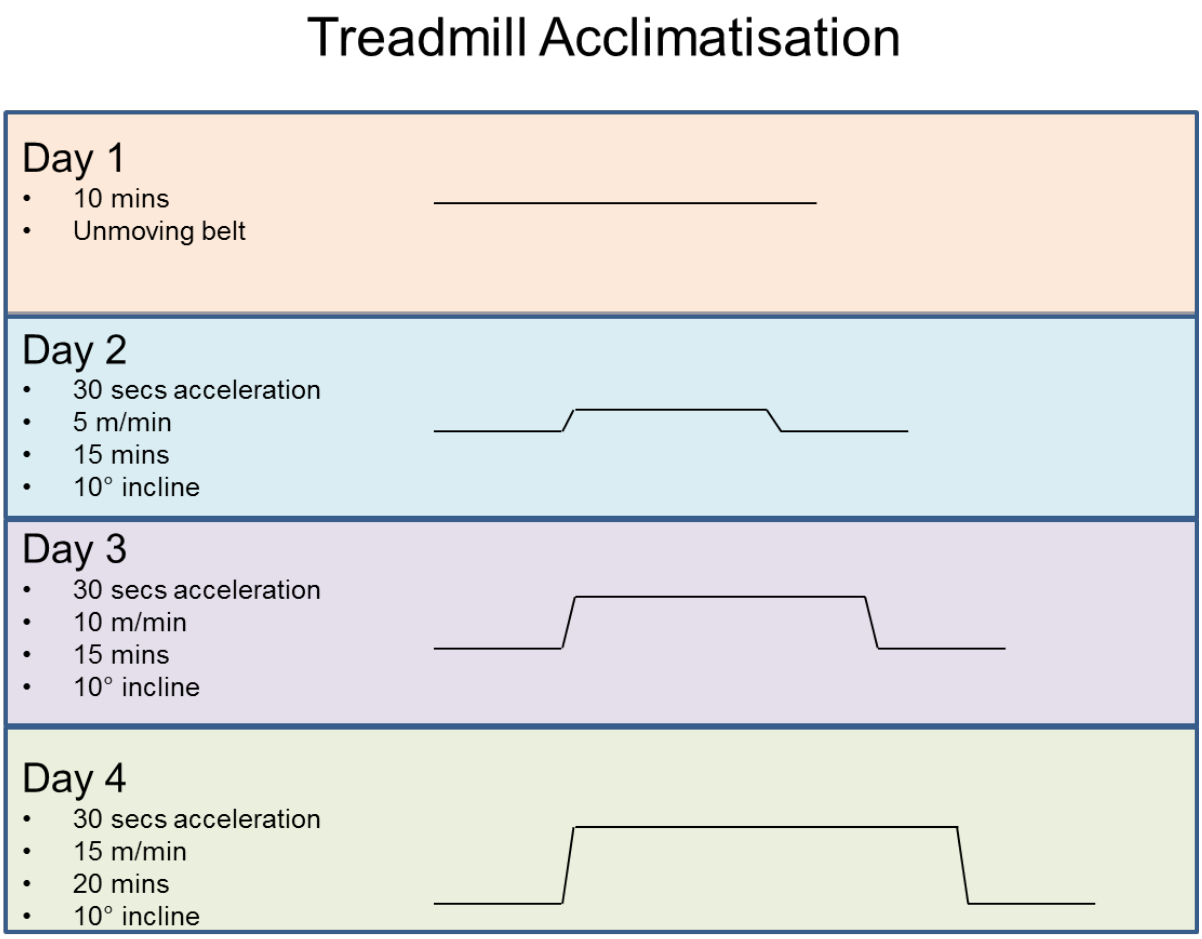


Figure 2.20. Acclimatisation Protocol
A training treadmill was used to allow acclimatisation of up to 6 mice at once. There was a steady increase in treadmill speed across 4 days prior to the acute exercise protocol.

Following acclimatisation the acute exercise protocol was carried out in the CaloTreadmill system, figure 2.21. Prior to the acute exercise session the mice were fasted for 3 hours to standardise food consumption across the group and minimise impact on indirect calorimetry. All mice were weighed prior to entering the CaloTreadmill with the bodyweight recorded in the software to enable accurate data analysis.

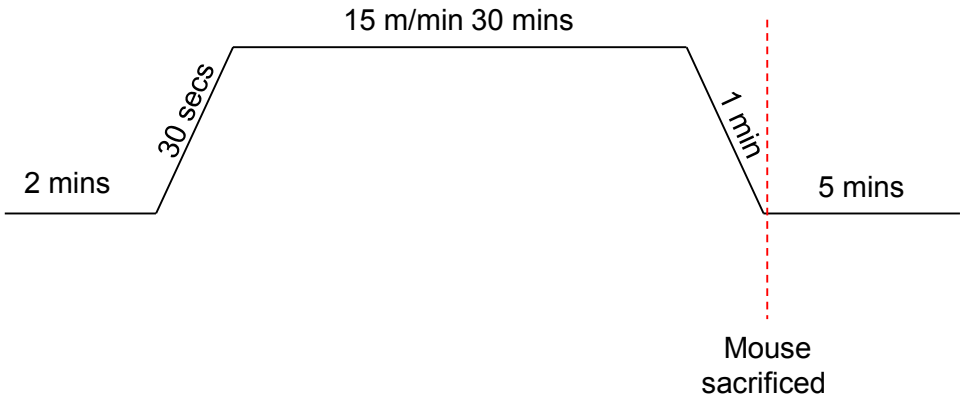


Figure 2.21. Acute Exercise Protocol
The mice had 2 minutes to acclimatise to the CaloTreadmill before the treadmill began running. The acceleration was over 30 sec to a final speed of 15 m/min for 30 min. The mice were sacrificed immediately following the end of the protocol, shown by red dashed line.

2.12.2. Indirect Calorimetry

Indirect calorimetry is a respiratory test that measures the levels of CO_2 and O_2 in expelled air, figure 2.22. It is used to inform on whole body energy metabolism and can define macronutrient substrate use through analysis of gas exchange.

The respiratory exchange ratio (RER) is the ratio of CO_2 produced by the body and O_2 consumed by the body. The energy production pathways for lipids, proteins and carbohydrates are different and therefore utilise and produce differing levels of O_2 and CO_2. If the body is solely metabolising lipids the RER is 0.7, for proteins it is 0.8 and 1.0 for carbohydrate. The PhenoMaster software also calculated the heat produced by the animal. This shows changes to energy expenditure as a result of the exercise protocol.

The mice were sacrificed immediately following deceleration to minimise metabolite degradation and acute signalling changes.

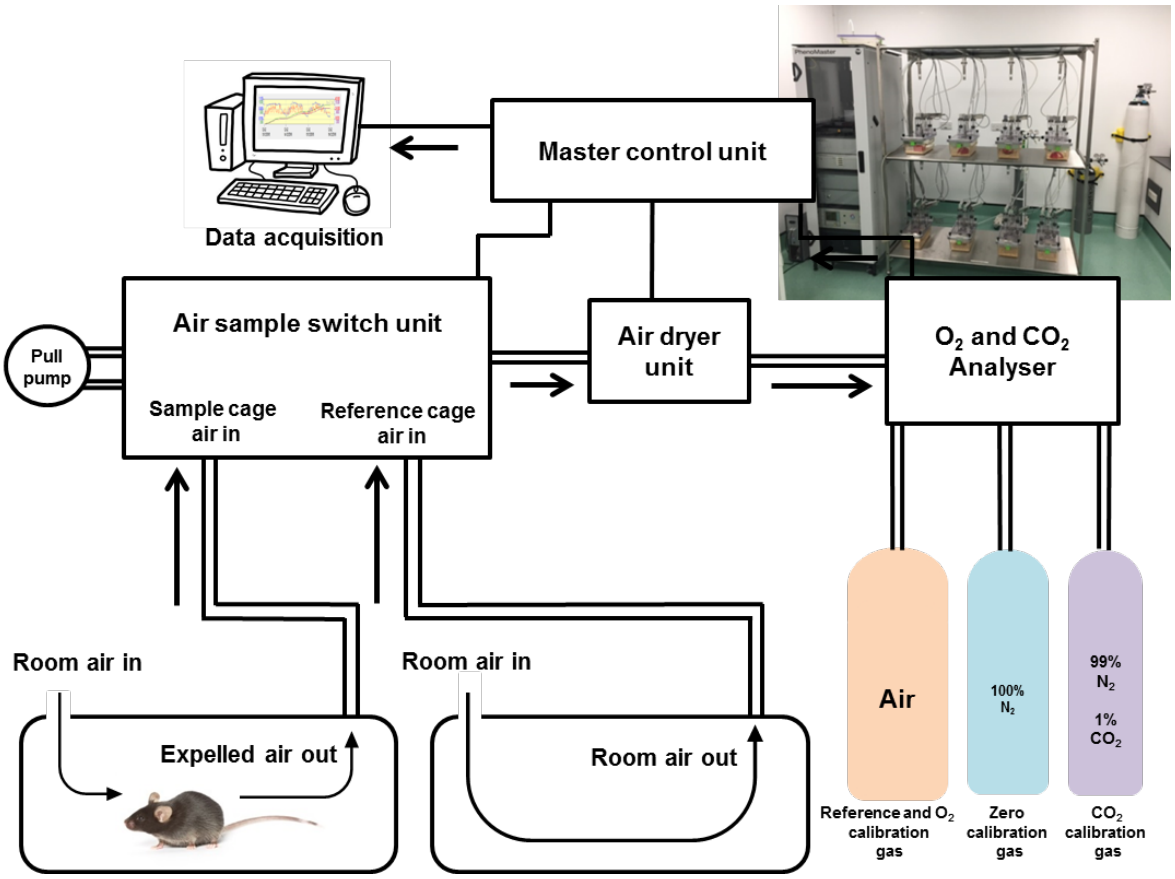


Figure 2.22. Indirect Calorimetry
A fully automated indirect gas calorimetry system was used in combination with the CaloTreadmill System. The levels of CO_2 and O_2 within expelled air is analysed to give estimated energy expenditure and the RER, which enables inference of macronutrient substrate utilisation. The PhenoMaster software processes all data acquisition and analysis.

2.13. In Vivo Isotope Tracer Experiment

Collaboration was established with Jonas Treebak, University of Copenhagen. A tamoxifen induced NAMPT knockdown mouse model was utilised for the work.

2.13.1. $^{13}C_6$-Glucose Infusion

The mice were surgically cannulised a week before the infusion was conducted to ensure time to heal. On the day of the infusion the mice were fasted for 2 hours, this was staggered to allow time for collection of the animals.

The mice were connected to a syringe pump and initially injected with a bolus of $^{13}C_6$-glucose at 6 mg/kg/min for 5 minutes. Following this there was a steady infusion at 2 mg/kg/min for 115 minutes. At the end of the protocol the mice were immediately sacrificed and tissues were dissected and snap-frozen.

2.14. Staining and Confocal Microscopy

Primary cells were seeded in 8-well slides (Ibidi, Germany) and differentiated according to *Section 5.2.1.2.* Each well was washed once with 250 µl PBS before 250 µl of wheat germ agglutinin solution (1:200) was added. Following a 10 minute incubation with the antibody in the dark the cells were washed with PBS three times.

The cells were then fixed using 250 µl of Fixation buffer (Invitrogen, UK) for 15 minutes. A perm-buffer solution was made (1:10 in water) using Intracellular Staining Perm Wash Buffer (Biolegend, USA). The cells were washed twice in the solution buffer being incubated in 250 µl for 10 minutes.

Actin was stained using ActinGreen 488 ReadyProbes (Invitrogen, UK). 2 drops of antibody per ml of Perm Buffer was made and cells were incubated for 30 minutes. The final stain is for the nuclei. DAPI is diluted 1:3000 in Perm Buffer before 250 µl is added to the slides and incubated for 1 minute.

The final step involves three washes in Perm Buffer followed by two PBS washes. 250 µl of PBS was left in each well before processing on the confocal microscope.

The imaging on the confocal microscope showed actin in green with blue nuclear staining. Allowing for detection of the myotubes in both the wild-type and transgenic models.

2.15. Cell IQ

Live cell imaging was conducted using a Cell-IQ (CM Technologies, Germany). Primary cells were seeded into a 6-well plate and a specialised plate lid was used with a gas inlet tube. This was connected in the machine and the door closed. The machine itself acts to incubate the cells during imaging.

Images were taken every 45 minutes of the cells during development. 3 areas of each well were selected for imaging and comparison between wild-type and transgenic models were made. The analysis was conducted based on detection of specific cell types. The software was 'taught' what each cell type looked like by creating a library of images for reference. Once this was completed the analysis was run on each image to give an area of the cell covered by the different cells.

2.16. Statistical Analysis

All statistics have been carried out using the GraphPad Prism 6 software. One-way ANOVA analysis has been conducted on the concentrations of metabolites. MIDs have been analysed within the individual pathways, with significance tested between the groups as opposed to between the pathways using one-way ANOVAs. Dunnett's multiple comparison tests were used as all comparisons were to a common control group. Statistical significance was shown by * $p<0.05$, ** $p<0.01$, *** $p<0.001$.

Analysis of covariance (ANCOVA) was used for statistical analysis of the indirect calorimetry measurements. Other methods involve the average measurements being compared to average body weight. ANCOVAs overcome this as they allow the comparison of two independent variables (measurement and body weight) and fit a line of best fit. Linear regression is then used to assess whether the groups are significantly different.

For graphs with two or more groups, for example, where both cell models are displayed on one graph, two-way ANOVAs were conducted. Sidak's multiple comparisons test was used for post hoc analysis when the significant changes between the genotypes at a specific point were of interest. When the significance within each group and between the groups was tested Tukey's multiple comparisons test was used following two-way ANOVA.

3. Metabolic Consequences of NAD^+ Excess

3.1. Introduction

Skeletal muscle has functions not limited to movement that are essential to healthy living such as posture, nutrient storage and maintenance of body temperature [1,2,9,10]. The role of NAD^+ within skeletal muscle has expanded over recent years with the discovery of NAD^+-consuming enzymes that are involved in various cellular functions from DNA repair to calcium signalling [94,144]. The classical role of NAD^+ is as a cofactor responsible for facilitating electron transfer for transhydrogenase enzymes. These oxidoreductase reactions occur throughout glycolysis and the TCA cycle rendering NAD^+ as an essential component for efficient oxidative phosphorylation.

There are various factors that can determine the metabolic health of skeletal muscle. Sarcopenia is characterised as a form of age-related muscle wasting with a progressive loss of mass and function [224]. Leading a sedentary lifestyle can also lead to atrophy, which can be characterised as increased protein degradation or decreased protein synthesis, or a combination of the two [269]. As NAD^+ has such a pivotal role in energy metabolism the decline of NAD^+ observed in aging is thought to impact skeletal muscle health and contribute to some chronic diseases and the aging phenotype [4,5,215]. NAD^+ reductions of between 20 and 50 % have been reported in muscle tissue of aged mice with a corresponding impairment in mitochondrial function [4,5,215]. Low NAD^+ can impact mitochondrial function, cellular senescence and can alter cellular communications all of which contribute to aging [5,256,261,270].

Therefore, strategies to increase NAD^+ levels have become prominent research areas. Augmentation of muscle NAD^+ levels through precursor supplementation (i.e. NR and NMN) may be a means to improve metabolic capacity and function in a range of age-related disease states [271]. NMN has shown to be effective at

ameliorating the decline in mitochondrial oxidative metabolism observed in aged mice, as well as improving glucose tolerance and insulin secretion in cases of diabetes and obesity [4,5]. Supplementation of NR protected against high-fat diet induced weight gain, improved glucose tolerance and improved lifespan by delaying senescence in stem cells [256,257,272]. In addition, NR was beneficial in restoring muscle mass and mitochondrial respiratory capacity in a muscle specific NAMPT KO mouse model, and has crucially been shown to safely elevate NAD^+ metabolism in humans [215,254]. However, chronically increasing NAD^+ beyond normal physiological levels could have a wider impact on metabolic homeostasis, which is yet to be fully understood. With the potential of over supplementation of the NAD metabolome having adverse effects not being fully appreciated on the field.

Understanding the role of NAD^+ in central carbon metabolism is important to realise the impact excess NAD^+ could have on metabolic health. As numerous metabolic pathways often result in the same metabolite pool it is difficult to ascertain the source and therefore the route to the end product.

In this chapter we aim to overcome this through use of a stable isotope tracer, $^{13}C_2$-[1,2]-D-Glucose, and combined 2D-^{1}H,^{13}C-NMR spectroscopy and GC-MS analysis to identify labelling patterns of metabolites and thereby elucidate pathway usage [268]. Identifying adaptations to pathway use in response to excess NAD^+ levels will provide an insight into the effects that NAD^+ augmentation strategies could have on skeletal muscle carbon metabolism.

3.2. Materials and Methods

All products ordered from Sigma-Aldrich, UK, unless otherwise stated.

3.2.1. Cell Culture Treatments

3.2.1.1. Cell Culture Models

All work was first carried out in a C2C12 cell culture model before results were confirmed in a primary myotube model using wild-type C57/black 6 mice. The primary cell culture protocol is described in detail in *Section 2.1.2.*

3.2.1.2. Cell Plating

C2C12s were seeded into 15 cm^2 dishes in GM at a seeding density of 2,000,000 cells/plate. The cells were cultured in DM for 5 days with the media changed every other day. Primary myoblasts were divided equally between cell culture plates and left in plating media for 72 hours, followed by primary proliferation media for 24 hours and finally primary differentiation media for 6 days, with media changes every other day.

Once differentiated into myotubes the cells were either left as control or treated with 0.5 mM NR (Chromadex) or NMN for 4 or 24 hours.

3.2.1.3. $^{13}C_2$-1,2-Glucose Labelling

Freshly made flux media was added to the myotubes 24 hours prior to extraction. This consisted of 8.3 g of DMEM powder (without glucose, L-glutamine, phenol red, sodium pyruvate or sodium bicarbonate), diluted in 1 litre of distilled water, supplemented with 2 mM glutamine and 45 mM sodium bicarbonate. 10 mM $^{13}C_2$-1,2-D-Glucose was then added and the cells were left to metabolise for 24 hours.

3.2.2. Extraction of Polar Metabolites for NMR Spectroscopy and GCMS Analysis

All extractions were carried out according to *Section 2.6.6.1.* Briefly, media was aspirated and cells were washed with ice-cold 0.9 % saline solution. Plates were placed on dry ice to quench metabolism and 1.2 ml pre-chilled HPLC-grade methanol with 2.5 µg/ml of D6-glutaric acid added as an internal standard. The cells were scraped and transferred to a falcon tube where 1.2 ml of pre-chilled HPLC-grade chloroform was added. The tube was rocked at 4 °C for 10 minutes before 1.2 ml of pre-chilled HPLC-grade H_2O was added and left to rest on ice for 10 minutes. Centrifugation of the samples at 4 °C, 14,200 rpm for 15 minutes allowed separation of the polar and non-polar fractions. 2 ml of the polar fraction was stored for NMR analysis, with 200 µl removed for GC-MS. Both fractions were evaporated to dryness using a SpeedVac at 30 °C for 4–5 hours and stored at -80 °C until further analysis. Protein pellet weights were used for normalisation during analysis.

3.2.3. NMR and GCMS Data Acquisition

Detailed explanations of both the NMR and GCMS data acquisition can be found in *Section 2.6.6.2.* and *Section 2.7.* respectively.

3.2.4. NAD^+ Cycling Assay

Once cells were fully differentiated they were treated with 0.5 mM NR for 4 or 24 hours. The NAD^+ cycling assay was then carried out according to the instructions, which are outlined in detail in *Section 2.10.* Briefly, the cells were washed with PBS and extraction buffer was added. Following two rounds of freeze-thawing the cells were centrifuged at 13000 rpm at 4 °C for 5 minutes and the supernatant collected for total NAD measurements. 200 µl of this was heated for NADH measurements. An

enzyme was added to a cycling buffer, which resulted in all NAD^+ within the samples being reduced to NADH. A colorimetric probe was used to visualise and quantify the NADH within the samples.

3.2.5. RNA Analysis

Gene expression data was analysed using rt-qPCR, a detailed outline can be found in *Section 2.3.4*. Briefly, 1 µl of cDNA from each sample was used with 5 µl of master mix, 3.75 µl of NFW and 0.25 µl of the gene probe of interest. Gene probes used were NRK1, NAMPT, PGC1α, SIRT1, Cox7a1 and Col1a1, details of which can be found in Appendix A. All genes were referenced to 18s as the housekeeping gene.

3.2.6. Acute Exercise Study

Wild-type C57BL/6 mice were used for the acute exercise study with details outlined in *Section 2.12.* The mice were run on a CaloTreadmill at the beginning of the protocol. They were then subjected to 3 days of IP injections of either 400 mg/kg NR or the same calculated volume of PBS. Following the injections the mice were run again on the CaloTreadmill and immediately sacrificed to prevent metabolite degradation and acute signalling changes.

3.2.7. Data Analysis

3.2.7.1. GC-MS Analysis

The GCMS analysis was made up of two parts; ion quantification and mass isotopomer distribution. The relative quantification of metabolites was achieved through ion quantification. For each metabolite the associated ions that occurred as a result of the GCMS run could be reconfigured and used to inform on the levels of the metabolite within the sample. Without a standard curve present this information could

not be absolutely quantified, but instead samples undergoing differing treatments within the same GCMS run were compared.

The mass isotopomer distribution was important for the understanding of the metabolic pathways used within the cell. GCMS analysis was able to report the mass of the metabolite +0, +1, +2, +3, etc. based on the number of ^{13}C atoms present. This data did not inform on the position of the labelled carbon but on the number contained within the metabolite.

3.2.7.2. 1D-^{1}H-NMR Analysis

All 1D-^{1}H-NMR analysis was completed using Chenomx 7.0 (ChenomxINC). Chenomx is a user-friendly package allowing for the identification of metabolite concentrations within an NMR sample. Detailed outline shown in *Section 2.6.6.3.*

3.2.7.3. 2D-^{1}H,^{13}C-NMR Analysis

All 2D-^{1}H,^{13}C-NMR analysis was completed using MetaboLab. The spectra were automatically phase corrected following a script with manual adjustment as necessary. All spectra were referenced to lactic acid within the reference library. Each metabolite was assigned manually, the peaks were identified for each metabolite and then multiplet analysis was carried out. An option to add GCMS data was a feature of the software, to strengthen the data and help to visualise any 'NMR-blind' carbons within the metabolite. The potential isotopomers were identified with a 0 used to represent a ^{12}C and a 1 representative of a ^{13}C; the programme fitted the data as closely as possible to the experimental results. The resultant data were MIDs for each metabolite within each sample, informing on the position of the labelled carbon(s) within the molecule. Detailed outline shown in *Section 2.6.6.3.*

3.2.7.4. Statistical Analysis

All statistics have been carried out using the GraphPad Prism 6 software. One-way ANOVA analysis has been conducted on the concentrations of metabolites. MIDs have been analysed within the individual pathways, with significance tested between the groups as opposed to between the pathways using one-way ANOVAs. Dunnett's multiple comparison tests were used as all comparisons were to a common control group. Statistical significance was shown by * $p<0.05$, ** $p<0.01$, *** $p<0.001$.

Analysis of covariance (ANCOVA) was used for statistical analysis of the indirect calorimetry measurements. Linear regression was used to assess whether the groups are significantly different.

For graphs with two or more groups, for example, where both cell models are displayed on one graph, two-way ANOVAs were conducted. Sidak's multiple comparisons test was used for post hoc analysis when the significant changes between the genotypes at a specific point were of interest. When the significance within each group and between the groups was tested Tukey's multiple comparisons test was used following two-way ANOVA.

3.3. Results

3.3.1. NAD^+ Augmentation through NR Supplementation

NAD^+ is a key regulator of metabolic health, with a decline observed in aging and in some disease conditions [4,5,215]. Strategies to augment NAD^+ have therefore become a prominent research area with NR recently shown to safely elevate NAD^+ metabolism in humans [254,273]. In order to decide the most appropriate NR treatment time C2C12s were supplemented with 0.5 mM NR for 4 and 24 hours. 1D-^{1}H-NMR

spectroscopy was employed to assess changes to metabolite levels in response to the different treatments. As NADH is unstable it is oxidised to NAD^+ during extraction, therefore any NAD^+ measurement from 1D-^{1}H-NMR spectroscopy is actually total NAD (tNAD). This also occurs with $NADP^+$ and therefore measurements are total NADP (tNADP). Whilst 4 and 24 hour NR treatment resulted in significantly elevated tNAD, the 4 hour treatment reached a greater significance above control, figure 3.1A. Although tNADP showed small increases in response to the NR treatments this was not significant, figure 3.1B.

NAM, which is both a breakdown product and precursor of NAD^+, was elevated 10-fold above control with both treatment times, figure 3.1C. To establish changes in NAM clearance, analysis of the downstream products of NAM was conducted. Nicotinamide N-oxide was not detected in any samples and MeNAM was once again significantly elevated in response to both treatments, figure 3.1D. Exposure of C2C12 myotubes to 24 hours of NR resulted in a greater increase in MeNAM, compared to the 4-hour treatment.

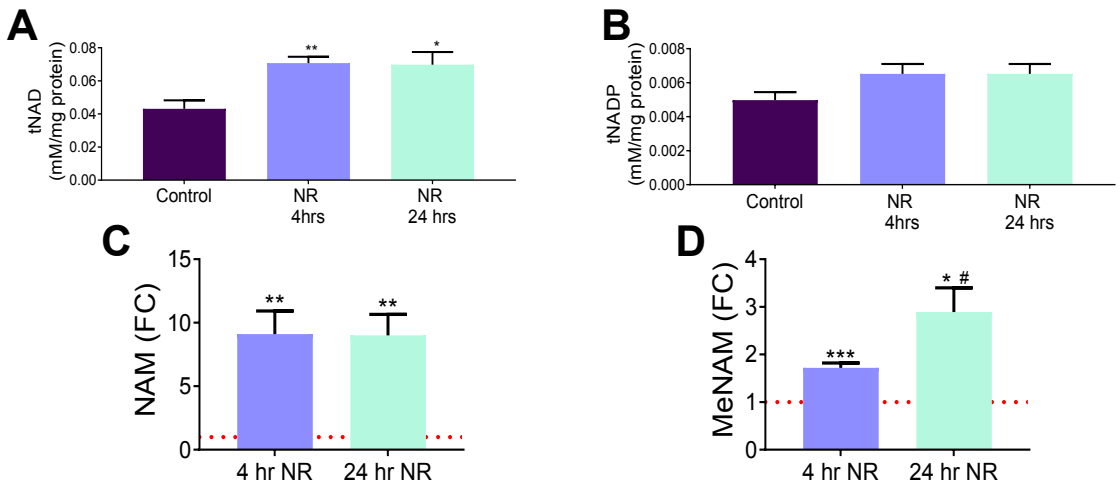


Figure 3.1. NAD+ Augmentation in C2C12 Myotubes

1D-^{1}H-NMR spectroscopy shows **(A)** tNAD and **(B)** tNADP concentrations in C2C12s in response to 4 and 24-hour NR supplementation. Fold-change compared to control shown for **(C)** NAM and **(D)** MeNAM.

p<0.05, ** p<0.01, ***p<0.005; One-way ANOVA performed on data; Dunnett's multiple comparison test, treatment compared to control.

Fold change statistics conducted on actual values, compared to control, shown by *. 4 hr NR compared to 24 hr NR shown by unpaired t-test # p<0.05.

All data are normalised to protein and are the mean ±SEM, C2C12s *n=4*. Red dotted line indicates control group set at 1.

Investigation of other key metabolites involved in energy production showed no change to overall ATP and ADP levels, figure 3.2A. To confirm whether the cells were maintaining their ATP levels through buffering the PCr/Cr ratio was calculated using 1D-^{1}H-NMR spectroscopy measurements, with no change seen, figure 3.2B. To further understand whether there was any impact of the excess tNAD on glycolysis (figure 3.2C) or TCA cycle metabolism (figure 3.2D) combined 2D-^{1}H,^{13}C-NMR spectroscopy and GCMS analysis was conducted. The pathway analysis showed no significant changes in any treatment group investigated.

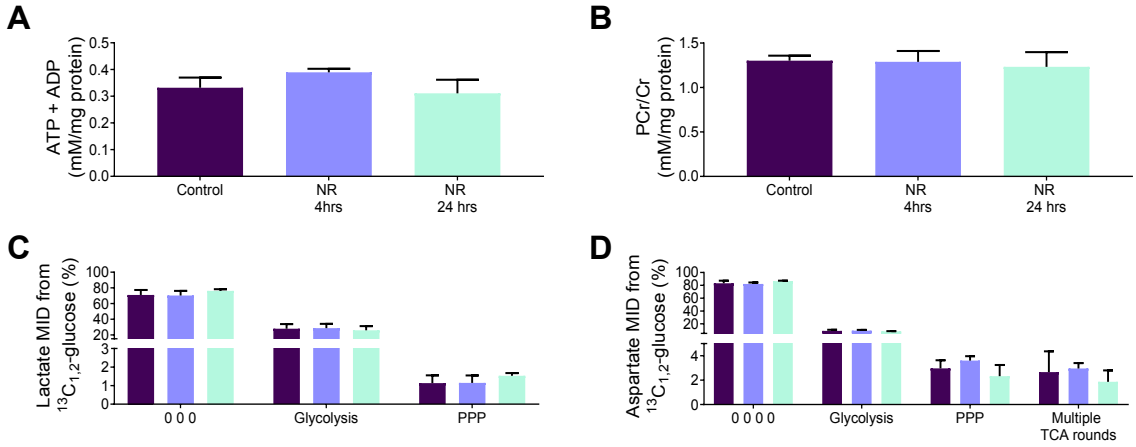


Figure 3.2. Energetic Consequences of Excess NAD^+

Energetic status of the cell was investigated using 1D-^{1}H-NMR spectroscopy **(A)** combined ATP and ADP and **(B)** the phosphocreatine (PCr)/ creatine (Cr) ratio. Combined analysis of 2D-^{1}H,^{13}C-NMR ($^{13}C_{1,2}$-glucose) and GC-MS data of **(C)** lactate and **(D)** aspartate.

One-way ANOVA performed on raw data; Dunnett's multiple comparison test, treatment compared to control. All data are normalised to protein and are the mean ±SEM, C2C12s *n=4*.

As energy metabolism relies heavily on NAD^+ and its ratio with NADH we expected a change to central carbon metabolism with NR treatment. We had shown the elevation of tNAD through NMR spectroscopy but wanted to investigate the ratio between NAD^+ and NADH. Due to the instability of NADH a specific assay was required to enable accurate quantification. The assay showed a significant increase in NAD^+ in both treatment groups, with 4 hour NR resulting in a 312 % increase and 24 hours resulting in a 243 % increase above control, figure 3.3A. A similar result was shown in the NADH data, figure 3.3B, which therefore resulted in no overall change in the NAD/NADH ratio between the groups, figure 3.3C.

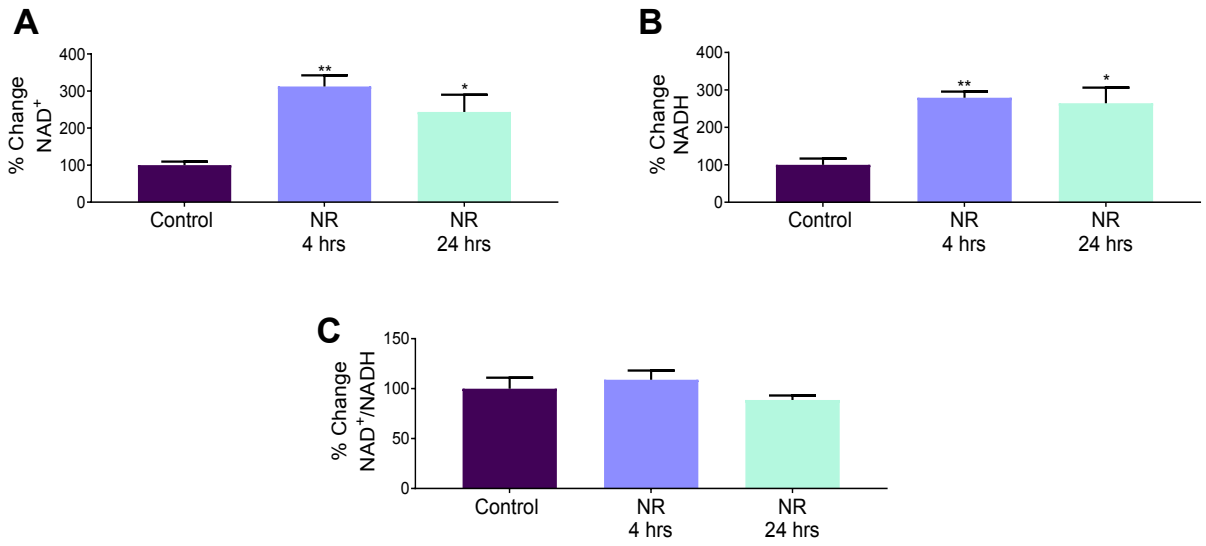


Figure 3.3. Percentage Change of NAD^+ and NADH

The percentage change of **(A)** NAD^+, **(B)** NADH and **(C)** NAD^+/NADH ratio compared to control. * p<0.05, ** p<0.01; One-way ANOVA performed on raw data; Dunnett's multiple comparison test, treatment compared to control. All data are the mean ±SEM, C2C12s n=3.

Altering NAD^+ levels within the cell may have a feedback mechanism to some NAD^+ biosynthetic genes. We therefore measured gene expression levels of Nmrk1, Nmrk2 and NAMPT with no change shown across the different treatment groups, figure 3.4A-C. The link between NAD^+ and SIRT1's deacetylation of histones highlights the impact NAD^+ can have on transcriptional regulation [133]. Gene expression of SIRT1 itself was investigated as well as PGC1α, which is known to be transcriptionally regulated by energy changes [84] - neither gene showed changes in any treatment group, figure 3.4D-E. To investigate mitochondrial effects and structural changes to the cell, Cytochrome C Oxidase Subunit 7A1 (Cox7a1) and Collagen Type I Alpha 1 Chain (Col1a1) were also examined but no changes were shown, figure 3.4F-G.

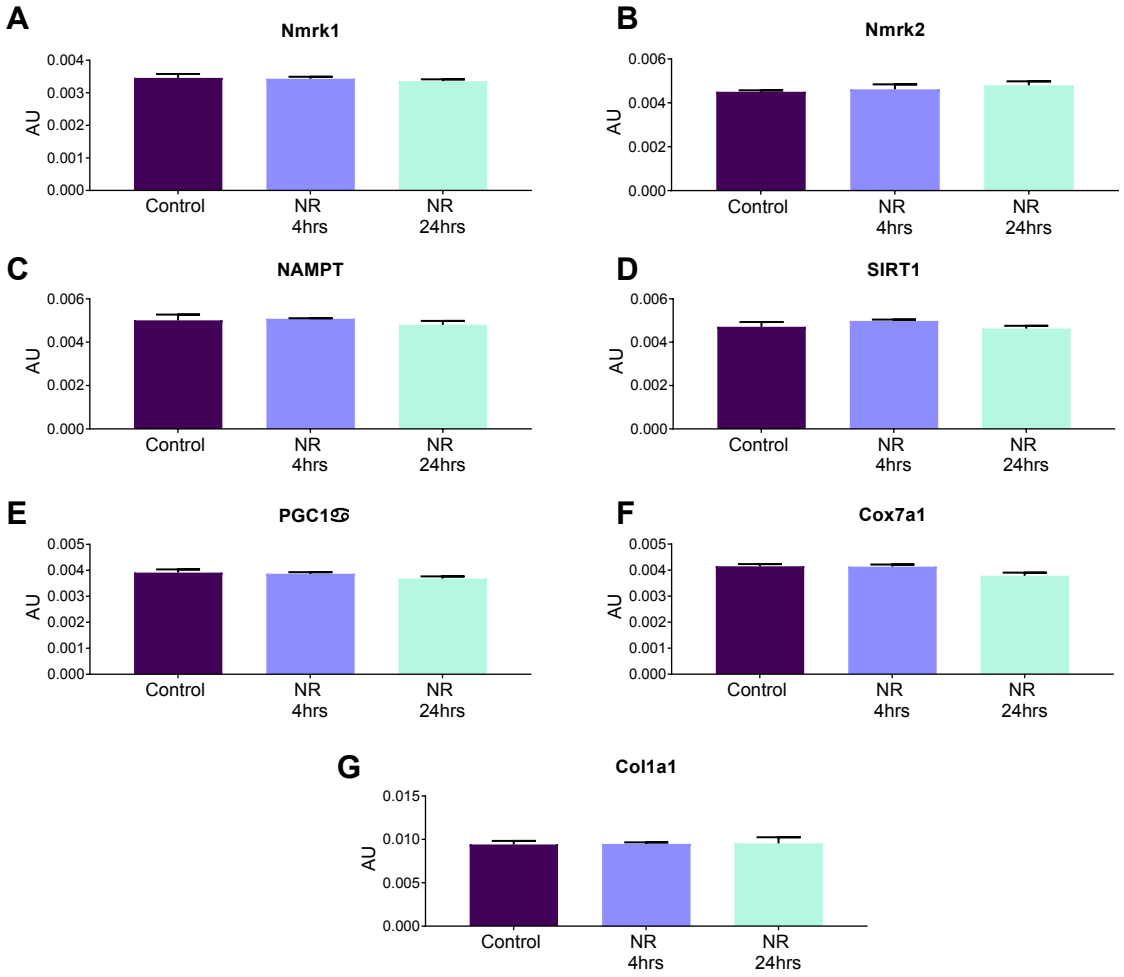


Figure 3.4. Gene Expression Analysis of NR treated C2C12s
Gene expression changes in response to 0.5 mM NR treatment for 4 or 24 hours. **(A)** Nmrk1, **(B)** Nmrk2, **(C)** Nampt, **(C)** Sirt1, **(D)** Pgc1α, **(E)** Cox7a1 and **(F)** Col1a1.
AU; arbitrary units
One-way ANOVA performed on raw data; Dunnett's multiple comparison test, treatment compared to control. All data are the mean ±SEM, C2C12s n=3.

3.3.2. NAD+ Augmentation through NMN Supplementation

A similar study was conducted using 0.5 mM NMN as an NAD^+ precursor for 4 and 24 hours. Both NMN treatments resulted in significantly elevated tNAD levels compared to control, as shown in the NR study. The 4 hour treatment resulted in a greater elevation of tNAD above control levels than 24 hour treatment, figure 3.5A. There were no changes to tNADP, figure 3.5B. Energy metabolism was seemingly

unaffected as evidenced by stable ATP+ADP measurements, PCr/Cr ratios, and alanine and aspartate levels, figure 3.5C-F.

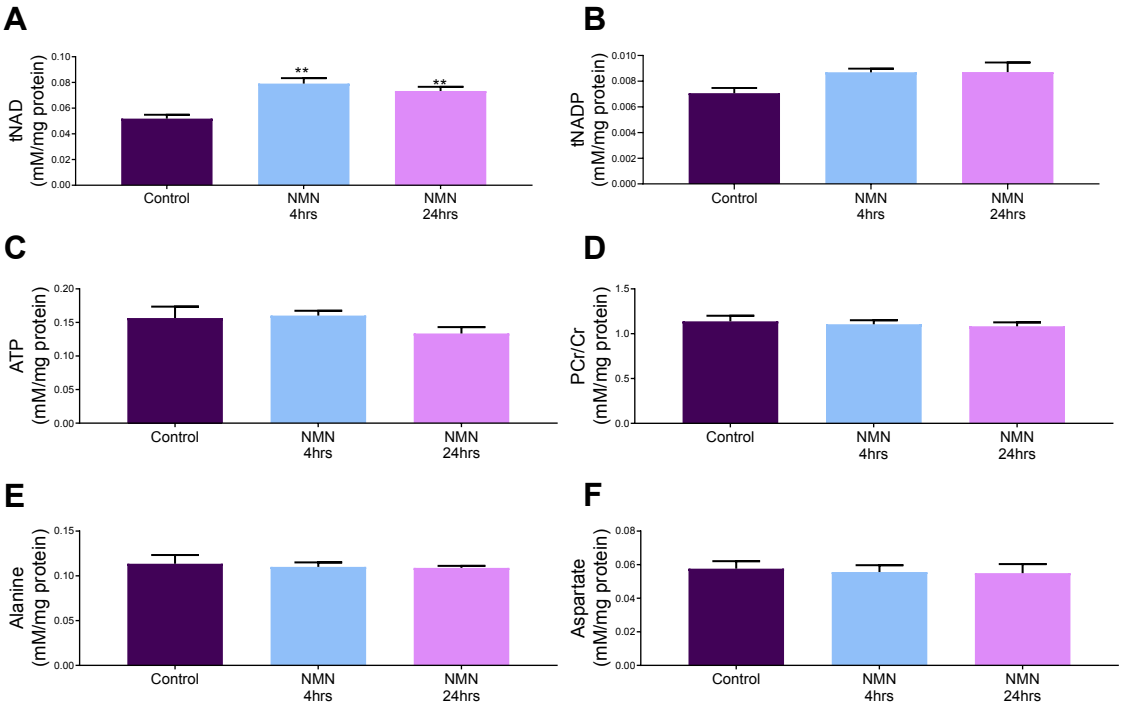


Figure 3.5. NMN Supplementation of C2C12s
Key metabolites identified through 1D-^{1}H-NMR spectroscopy **(A)** tNAD, **(B)** tNADP, **(C)** ATP, **(D)** PCr/Cr ratio, **(E)** Alanine and **(F)** Aspartate following supplementation of 0.5 mM NMN for 4 or 24 hours.
** $p<0.01$; One-way ANOVA performed on raw data; Dunnett's multiple comparisons test, treatment compared to control. All data are the mean ±SEM, C2C12s n=3.

3.3.3. Comparison of NR and NMN as NAD+ Precursors

The pathway to NAD+ biosynthesis taken by exogenous NMN and NR is shown in figure 3.6A. A comparison was conducted between 4 hour NR and NMN treatment alongside primary myotubes being treated with NR for 4 hours. Although tNAD was increased more significantly above control with NMN than NR there was no significant difference between the two precursors, figure 3.6B. The primary myotubes

reflect C2C12 in their response to 4 hour NR treatment, figure 3.6C. tNADP showed no significant change across any treatment in either cell model, figure 3.6D-E.

NAM measurements are shown as fold-changes compared to control, NR increased NAM 9-fold and NMN increased NAM 1.8-fold which were both significantly elevated over control levels, figure 3.6F. The responses between the two precursors are also significantly different. Primary myotubes expressed a 6.8-fold increase above control in response to 4 hour NR treatment, figure 3.6G. The clearance product of NAM metabolism is MeNAM; NR caused a significant increase in MeNAM compared to control. NMN did not have an effect on MeNAM and therefore its response was significantly different to that of NR, figure 3.6H. The primary myotubes showed no change in MeNAM levels when supplemented with 4 hours of NR, figure 3.6I.

Metabolic tracing revealed no change to lactate in regard to concentration or route to production in either C2C12s in response to NR or NMN or in primary myotubes supplemented with NR, figure 3.7A-C. As lactate was used as a readout of glycolysis, aspartate was used as a surrogate marker of TCA cycle metabolism. Once again, there were no changes across any treatment group in any cell model, figure 3.7D-F.

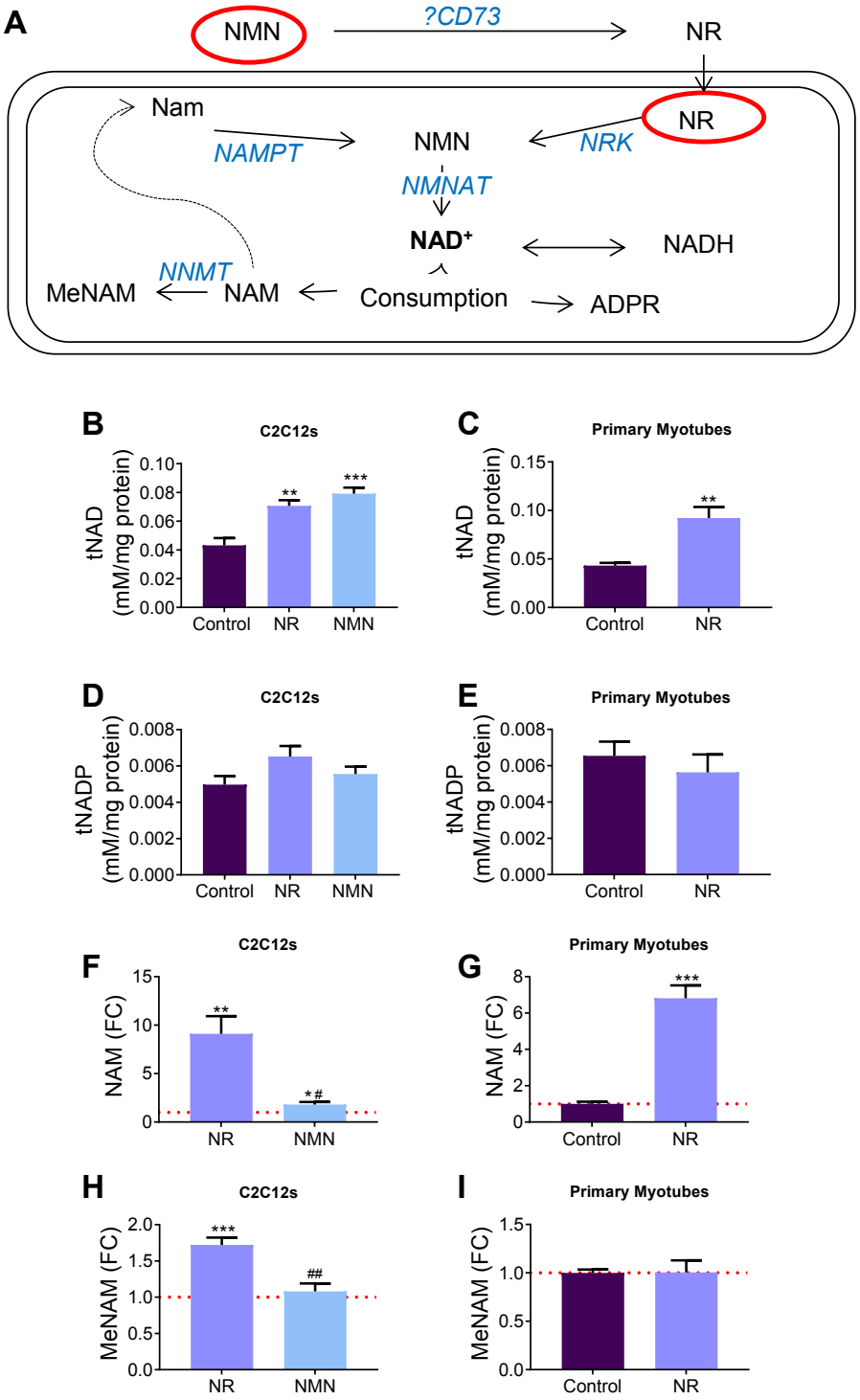


Figure 3.6. NAD+ Augmentation in C2C12 and Primary Myotubes

Differentiated C2C12 and primary myotubes were treated with NR or NMN (0.5 mM) for 4 hours, pathway shown in (**A**). Key metabolites were identified and quantified using 1D-^{1}H-NMR spectroscopy and used to inform on the energetic status of the cell; (**B**, **C**) tNAD, (**D**, **E**) tNADP. Fold-change compared to control was shown for (**F**, **G**) nicotinamide (NAM) and (**H**–**I**) methylated-nicotinamide (MeNAM); red line is representative of control levels.

* p<0.05, ** p<0.01, ***p<0.005; One-way ANOVA performed on raw data; Dunnett's multiple comparison test, treatment compared to control.

Fold change statistics conducted on actual values, compared to control, shown by *. NR compared to NMN shown by unpaired t-test # p<0.05, ## p<0.01.

All data are the mean ±SEM, C2C12s n=6. Primary myotubes n=4. FC, fold change compared to control.

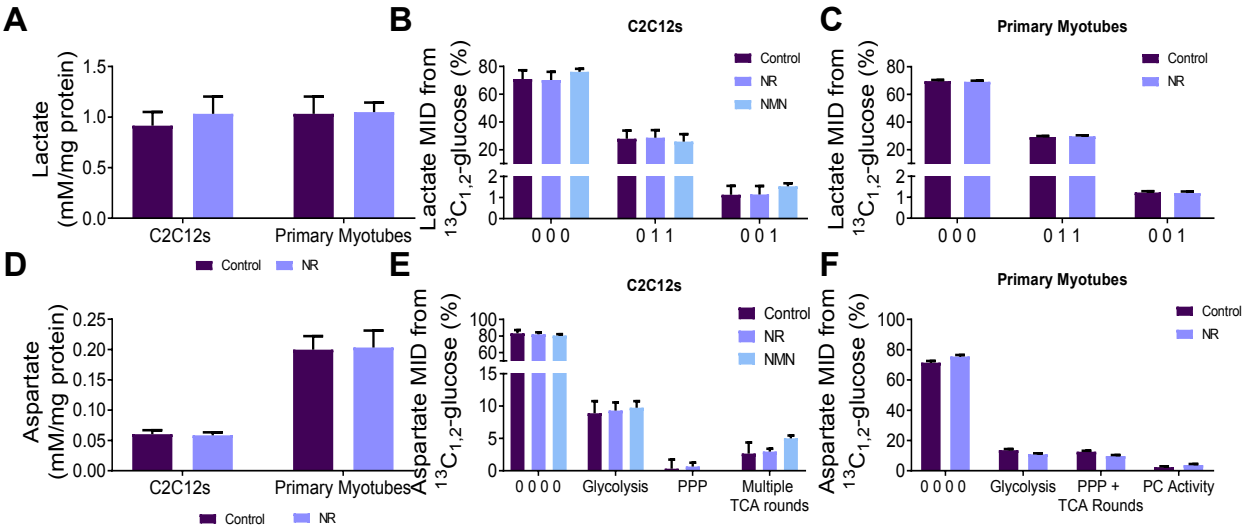


Figure 3.7. Effect of Excess NAD+ on Glycolysis and TCA Cycle Metabolism

Concentration and labelling patterns detected through 1D-^{1}H-NMR spectroscopy and combined analysis of 2D-^{1}H,^{13}C-NMR and GC-MS data. Analysis of lactate **(A)** concentration and MIDs from **(B)** C2C12s and **(C)** primary myotubes with supplementation of NR and/or NMN. Aspartate **(D)** concentration and MIDs from **(E)** C2C12s and **(F)** primary myotubes.

MIDs, Mass Isotopomer Distributions; ^{13}C represented by 1 with ^{12}C represented by 0; % MID of total metabolite.

Glycolysis 1100+0011; *TCA rounds + PPP* 0100+0010, 1111, 0111+1110, 1000+0001; *PC Activity* 0110

* p<0.05, ** p<0.01, ***p<0.005; One-way ANOVA performed on raw data; Dunnett's multiple comparison test, treatment compared to control. All data are the mean ±SEM, C2C12s n=6. Primary myotubes n=4.

3.3.4. NAD+ Augmentation in Acute Exercise Study

To investigate the impact of NAD+ augmentation on metabolism *in vivo* an acute exercise study was conducted before and after NR supplementation. The acute exercise study involved the mice running on a CaloTreadmill prior to treatment, followed by 3 days of 400 mg/kg NR or PBS *i.p.* injection and then another CaloTreadmill run. The RER for all four groups is shown in figure 3.8 with no real change shown between the traces. The difference in the initial RER before the run begins highlights the high variability between different mice.

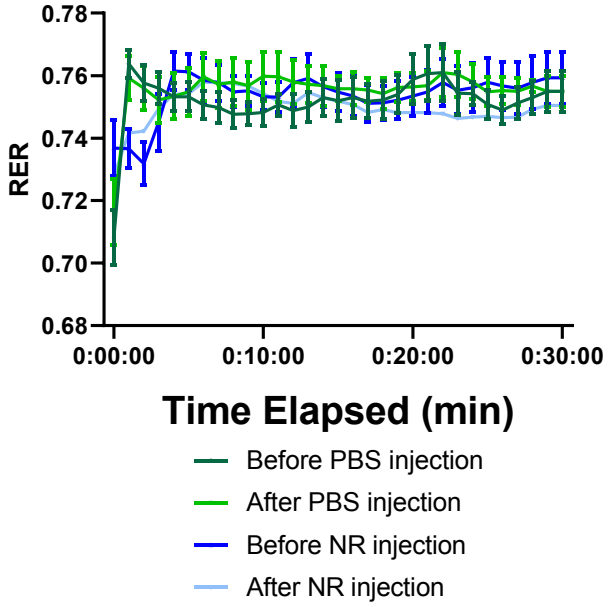


Figure 3.8. Respiratory Exchange Ratio for Acute Exercise Mouse NAD+ Augmentation Study
Trace of RER for a mouse acute exercise study completing 30 mins running on a CaloTreadmill, one run before and one after injection with either PBS or 400 mg/kg/day of NR for 3 days.
PBS n=5; NR n=12. All data points are the mean ±SEM.

To understand whether there were any significant changes before and after injection the average data for each measurement was plotted against the individual mouse's body weight. Whilst a small difference can be observed between the heat measurements lines of best fit in the PBS injected animals, this change is not significant, figure 3.9A. The NR treated animals heat measurement lines were identical before and after injection, despite the body weight altering, figure 3.9B. As the heat measurement is a function of the VO_2 and VCO_2 the graphs are identical albeit with different units, figure 3.9C-F.

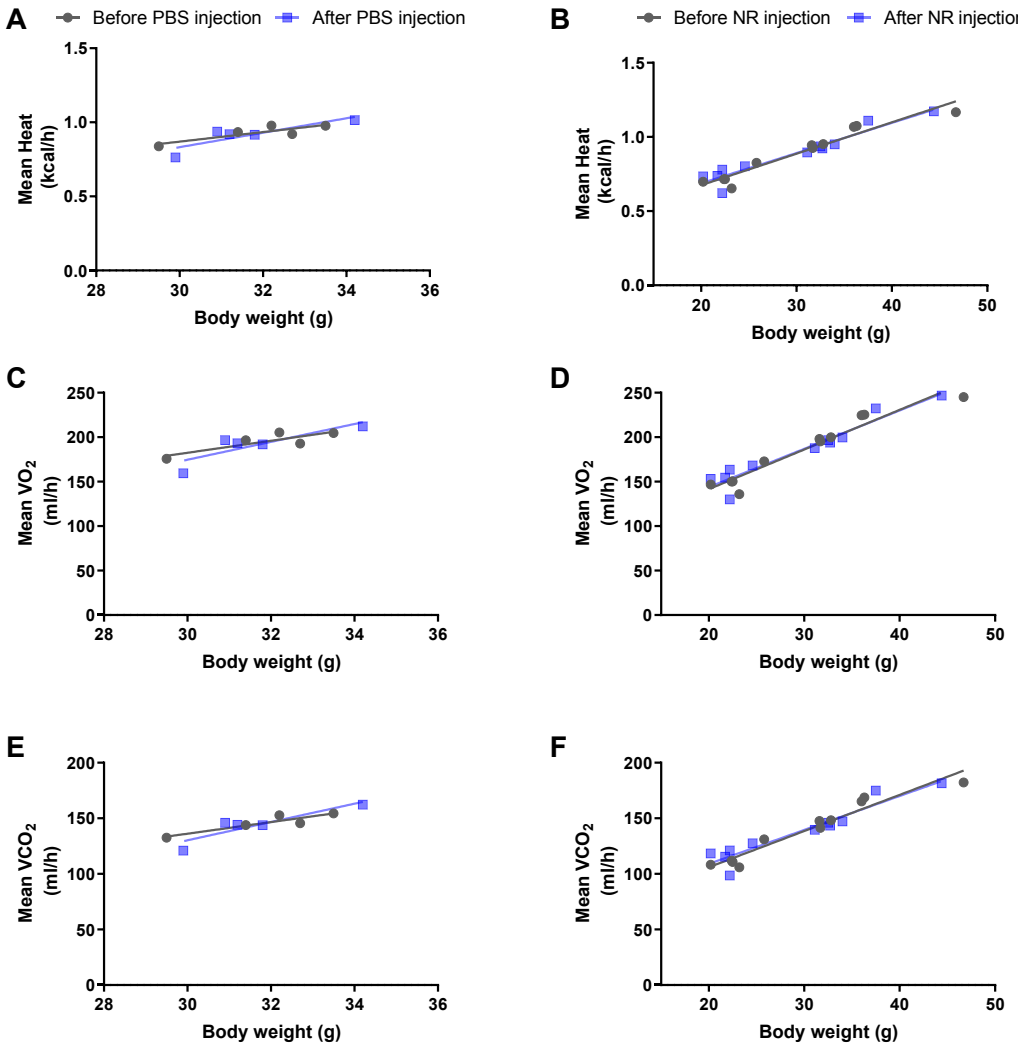


Figure 3.9. Energy Expenditure for Acute Exercise Mouse NAD+ Augmentation Study
Mouse acute exercise study completing 30 mins running on a CaloTreadmill, one run before and one after injection with either PBS or 400 mg/kg/day of NR for 3 days. The **(A-B)** heat, **(C-D)** VO_2 and **(E-F)** VCO_2 shown before and after injections.
All data is the value plotted against the individual mouse's weight. Linear regression used to identify significant changes between the groups.
PBS n=5; NR n=12.

An NAD^+/NADH cycling assay was used on quadriceps muscles of the animals from the acute exercise study. The results were unexpected, with a significant decrease in NAD^+ in response to NR supplementation following exercise, figure 3.10A. There was also a small, insignificant drop in NADH, which protected the NAD^+/NADH ratio from any significant change, figure 3.10B.

Gene expression changes in NR treated mice were shown compared to PBS control. There was no change across any of the genes investigated, figure 3.10C.

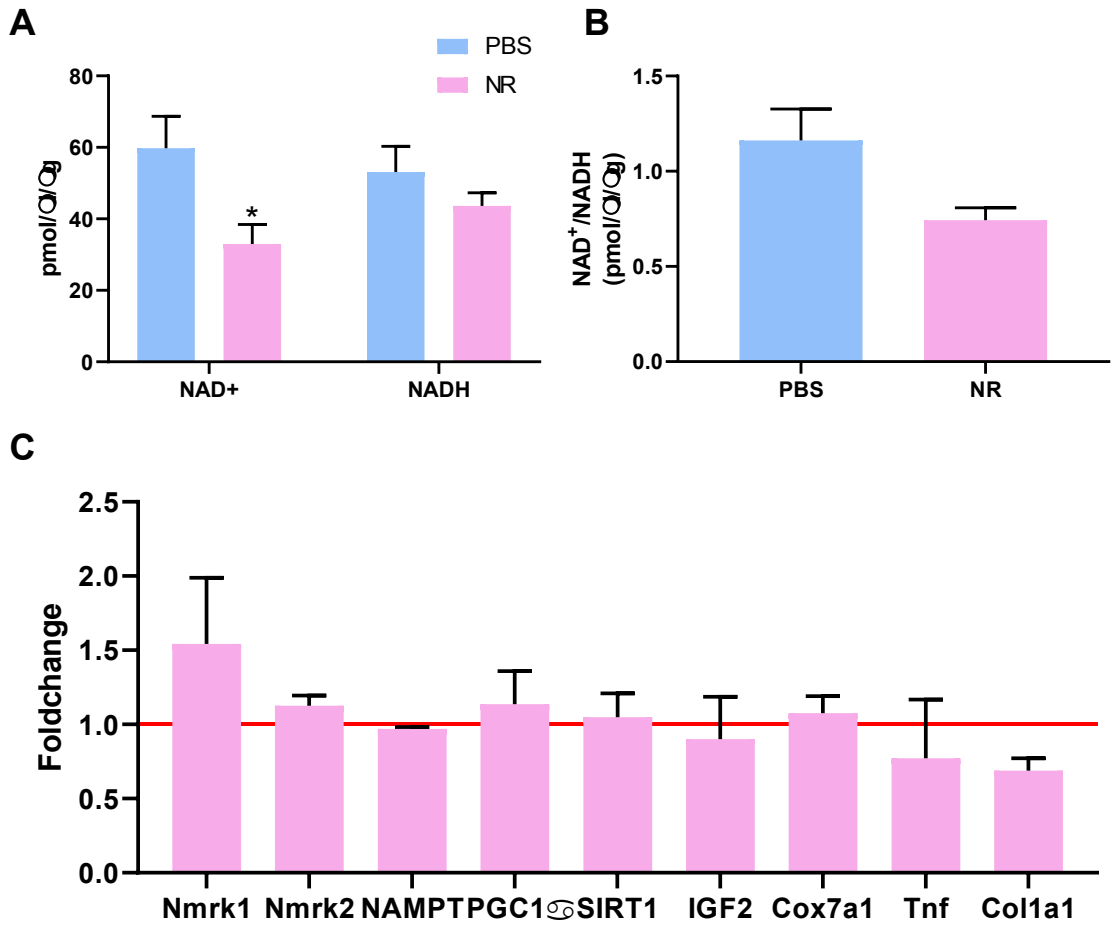


Figure 3.10. NAD+ Quantification and Gene Expression Analysis for Acute Exercise Mouse NAD+ Augmentation Study

NAD+ cycling assay used to take **(A)** NAD+ and NADH measurements from quadriceps muscle of mice on the acute exercise study. **(B)** NAD+/NADH ratio in quadriceps muscle. Blue bars represent mice injected with PBS with pink bars showing NR treated mice. **(C)** Gene expression data shown as fold change of NR treated mice compared to PBS controls.

PBS n=5; NR n=5. All data are the mean ±SEM. Two-way ANOVAs used to test significance of **(A)** and **(C)**, with Sidak's multiple comparisons test used to compare NR to PBS groups. Unpaired t-test conducted on **(B)**.

3.4. Discussion

3.4.1. In Vitro augmentation of NAD^+ through NR and NMN Supplementation

There is a current research focus on augmentation of NAD^+ levels for treatment of chronic diseases. This stems from observations of increased cellular NAD^+ content in response to exercise and calorie restriction, which are both considered key lifestyle changes that improve quality of life [187,274,275]. This is widely accepted in the field; however, little has been done to show the impact that excess NAD^+ could have on core cellular metabolism in skeletal muscle.

Supplementation with NR and NMN in both C2C12 and primary myotubes resulted in an increase of tNAD, which was shown to be both an increase in NAD^+ and NADH by the cycling assay. The cell rapidly adapted to this by increasing NAD^+ clearance through NAM and MeNAM. Treating myotubes with NR for 4 or 24 hours showed little difference in terms of NAD^+ augmentation induced effects on energy metabolism or gene expression. The key difference was in the clearance of NAD^+. NAM levels were comparable however there was a significant increase of MeNAM from 4 hour NR treatment to 24 hour. This is an expected result of the increased time of exposure to NAD^+ excess ultimately translating to elevated clearance.

Increased NAM and MeNAM clearance will lead to increased levels circulating in the blood and ultimately elevated excretion in the urine. An elevation of NAM in the blood will result in increased substrate availability for eNAMPT, extracellular NAMPT. eNAMPT was previously referred to as pre-B cell colony enhancing factor (PBEF) or Vistafin due to it initially being shown to augment pre-B cell colony formation [276]. A study has evidenced the prominent role of eNAMPT in diabetes pathophysiology [183]. Disruption to glycaemic control, insulin resistance and islet dysfunction were induced

through HFD feeding in mice, with a concurrent increase in eNAMPT secretion [183]. Addition of an anti-eNAMPT antibody, which blocked the enzyme, resulted in a reversal of the phenotype [183]. Further to this, elevated eNAMPT has been seen in cases of irritable bowel disease and rheumatoid arthritis [277,278]. As NAM is a NAMPT substrate this suggests that the increased clearance, through NR and NMN supplementation, could lead to altered pancreatic islet cell functioning and systemic inflammation. However, it is reported that it is the eNAMPT-monomer that is secreted in response to HFD feeding and that initiates these metabolic changes [183]. This suggests that in a healthy subject there may be limited secretion of the eNAMPT monomer. Further to this the monomer is also shown not to have any NAD^+-biosynthetic activity, through no change in serum NMN in response to increased eNAMPT-monomer levels [183]. Therefore, it is possible that despite increased circulating NAM it may not act as an eNAMPT substrate, through limited enzyme availability or through a lack of catalytic ability. Equally, the elevated NAM could be taken up directly into cells and utilised to produce NAD^+.

Further to this, these metabolites are reportedly able to cross the blood-brain barrier where there is strong evidence that they exhibit neuroprotection [279–281]. However, at high concentrations these molecules can have a toxic effect on neurons as shown in Parkinson's and Huntington's disease mouse models [282,283]. With a human study observing elevated expression of nicotinamide n-methyltransferase (NNMT), the enzyme responsible for the metabolism of NAM to MeNAM, thought to lead to neurodegeneration [284]. Similarly, NAM has been shown to be effective for management of hyperphosphatemia in patients with renal disease [285]. It is also suggested to be a uremic toxin contributing to thrombocytopenia in chronic renal

failure patients, highlighting different effects with different concentrations [286,287]. Whilst there have been studies showing NR safely elevates NAD^+ in humans it is important to appreciate that creating a state of NAD^+ excess could potentially have adverse effects in the context of the CNS, kidney function or systemic inflammation such as psoriasis, irritable bowel syndrome and Chron's disease [254,288,289].

The methods employed are able to detect changes to pathway use and therefore show alterations to energy metabolism. Neither precursor treatment resulted in any overall change to concentration or route to production of key glycolytic and TCA cycle metabolites. This therefore suggests that the increased clearance of NAM and MeNAM was an adaptation used to protect the careful redox balance and ensure central carbon metabolism was unaffected [290]. Another indicator of protected redox status is evidenced through the NAD^+/NADH cycling assay data, showing an increase in NAD^+ is matched with an equal increase in NADH. This ultimately results in stable NAD^+/NADH ratios, which ensures correct energy metabolism functioning.

Supplementation with NR and NMN have shown similar therapeutic effects in disease conditions in rodents, enhancing metabolic health and ameliorating age-related decline [271]. This work highlighted a key difference between the NAD^+ precursors with a greater elevation of the clearance products, NAM and MeNAM, in NR compared to NMN treated cells. Through inhibition of nucleoside transporters and nucleotide degradation it has been shown that NAD^+ is unable to enter the cell directly and must be first broken down into NR or NAM [170]. Recent studies have shown the requirement of the NRK enzymes for metabolism of exogenous NMN to NAD^+ [199,253]. As intracellularly NMN is downstream of NR in the NAD^+ biosynthetic pathway this suggests that NMN is not able to directly enter the cell. Based on

NMN's reliance for the NRK enzymes, observed in skeletal muscle myotubes and hepatocytes, it has been postulated that NMN is converted to NR outside the cell before entering [199,253]. This therefore introduces a delay between NMN supplementation and cellular uptake, which could account for the reduction in clearance compared to NR. A group have suggested that NMN uptake into cells takes minutes, which they say is evidence of an NMN transporter [252]. Another possible explanation for the elevated NAM detected with NR may be due to instability in culture medium, meaning it is possible that we are measuring NAM taken up by cells from the media due to NR degradation as opposed to intracellular NAD^+ consumption. However, in opposition to this theory, it has been shown through use of labelled NR that NR is taken up whole into hepatocytes over a 24 hour period [253].

With regard to clearance of NAD^+ there were differences between the two models used, C2C12s and primary myotubes. As previously discussed primary cells do not always act in concordance with their associated cell lines [291]. In this study there was less NAM elevation in primary myotubes compared to C2C12s in response to NR supplementation. This difference was further evident in relation to MeNAM, where there was no increase above control in primary myotubes. Possible reasons for this may be increased MeNAM secretion from primary myotubes. Alternatively, it may be suggestive of a lower affinity of NNMT for NAM [292]. Therefore the primary model may have required a higher NAM concentration to produce the equivalent MeNAM level compared to C2C12 myotubes. Ultimately there is a range of responses at play and different models will be suited to exploring different research questions.

A comparison of the absolute amount of NAD^+ in the C2C12 and primary myotube samples with previously reported levels showed some discrepancies. Mitochondrial

NAD^+ levels have been reported in two studies as around 4 nmol/mg of protein which were both measured using an NAD^+ cycling assay kit [215,293]. In muscle tissue the reported values were around 0.4 nM, 10-fold less, with human blood showing 0.03 nM of NAD^+ [215,254,294]. C2C12 NAD^+ data was reported in different ways in the literature. The key difference was the method of measurement and normalisation of the data with some groups reporting data per million of cells and others using protein weight. There was a lot of variability between units used, once converted into the same units comparisons could be made. My data shows tNAD concentrations of 40 µmol/mg, Canto *et al*. has shown concentrations of 500 µmol/mg [256] with Davila *et al*. reporting 5000 µmol/mg [293]. The Canto *et al*. work was analysed using an enzymatic kit, Davila *et al.* used LC-MS methods with my work analysed using NMR spectroscopy. These inconsistencies could occur as a result of difference in normalisation, the tNAD measurements in my samples before correction to protein weight were 400 µmol/mg, which is in line with Canto *et al.'s* findings. Trammel & Brenner show levels of NAD^+ as 260 µM in a glioma cell line with normalisation based on pre-seeding cell counts, showing differences again [295]. Also, the loss of NADH to NAD^+ during extraction is an issue and could potentially make the NAD^+ measurements appear significantly higher than they are. The lack of standardisation between groups causes discrepancies in the reporting of NAD^+ concentration and highlights the problem with accurate, reliable NAD^+ measurement.

3.4.2. Acute Exercise Study and the Metabolic Consequence of NR Supplementation

The acute exercise study aimed to measure the energy expenditure of mice before and after supplementation with NR or a placebo, PBS via *i.p.* injection. The result

was that there was no significant change in any group. The RER, CO_2 production/O_2 use, informs on the substrate usage, with 0.7 being lipid metabolism and 1 the sole use of carbohydrates. Living a sedentary lifestyle has been shown to increase the RER, thereby metabolising more carbohydrates than lipids, ultimately resulting in increased fat mass [296]. With the opposite also true, physically fit individuals show a lower RER and therefore have elevated fat oxidation [297]. The acute exercise protocol was intentionally designed to ensure the mice were 'untrained'. This could not be completely controlled for, as under the Home Office licence for this project the mice were required to have 3 days of acclimatisation prior to the measurements. Therefore, if a mouse was more active on the treadmill during these sessions compared to one who sought refuge regularly the levels of exercise exposure would be different. We attempted to control for this by removing any who did not participate well before the experiment began.

Upon initiation of exercise the RER increased from around 0.70 to 0.76 in all mice. The increase in RER with exercise was expected, a previous study showed a steady increase in RER with increased treadmill speed [298]. This suggests the subjects were beginning to use their muscle glycogen stores as exercise intensity increases. As our protocol was at a fixed speed the RER graph plateaued during the experiment. Importantly there was no change before or after NR supplementation.

The energy expenditure is estimated through the VO_2 and VCO_2. This informs on the amount of energy used by the mice at any point within the protocol. Once again, there was no change before or after NR supplementation. A recent paper expressed the need for data of this type to be analysed using ANCOVAs to allow for changes in bodyweight and not show false changes in the data [299].

The absence of change in any parameters within this work could be a result of the NR supplementation not augmenting skeletal muscle NAD^+, the augmentation occurring but not impacting energy expenditure or the exercise intensity not being high enough to induce a response.

Typically exercise studies aim to reach VO_2 max, meaning the maximal oxygen intake that can be consumed by an individual when exercising. In order to identify VO_2 max the animals are forced to partake in the exercise, this was beyond the scope of our animal license and therefore our protocol is submaximal. One paper reports the VO_2 max of adult C57BL/6J mice as 25 m/min [298], whereas our top treadmill speed was 15 m/min. Previous reports of NR supplementation in combination with exercise have forced animals to exercise to exhaustion. One study showed an adverse effect of NR with a reduction in energy expenditure as a result of the NAD^+ precursor supplementation [300]. However, previous studies have shown NR supplementation to be beneficial for muscle physiology and improve exhaustion times following just 1 week of treatment [215]. Neither of these papers analysed their data using ANCOVA, this therefore could mean that any differences are a function of altered body weights as opposed to true responses to NR. The disparity between these results and other published findings once again highlights how differences in protocol set up, treatment length and measurements can impact outputs.

The NAD^+/NADH cycling assay results initially caused speculation as to whether the experiment had worked. However, it is important to note the question, does NR supplementation affect energy expenditure, which we achieved through comparison between PBS and NR injected animals. The data could be interpreted as NAD^+ is reduced following exercise with NR supplementation, however this is hard to

determine given the lack of un-exercised controls. An increase in skeletal muscle NAD^+ has been reported using this NR supplementation method in non-exercise animals [301]. Therefore, despite not having pre and post NR supplementation data we expected an increase in this cohort following the *i.p.* injection.

The data may also be suggesting that NR supplemented mice showed a smaller increase in NAD^+ in response to exercise, compared to PBS controls. Previous exercise work has shown that there is a lower increase in the NAD^+/NADH ratio during the same level of exercise in trained versus untrained rats [302]. This could suggest that NR supplementation had a similar effect to exercise training in the mice, meaning that their NAD^+ levels did not rise as much in response to exercise. Comparisons with previously reported exercise data are difficult as often people show data in reference to VO_2 max [302–304].

Here we sought to understand if there were differential responses to NR or PBS treatment in skeletal muscle of exercised mice. Of the genes investigated there were no differences between the PBS and NR group.

Overall, although NR supplementation appeared to alter skeletal muscle NAD^+ metabolism through changes in NAD^+ levels following exercise, compared to PBS control. This did not impact energy expenditure, substrate utilisation or gene expression with the exercise protocol employed in this study.

In the context of this design the cells were able to adapt their metabolism to cope with increased NAD^+ turnover. The studies conducted are able to address acute NAD^+ excess, showing that skeletal muscle protects its carbon metabolism by elevating clearance. However, long term there may be a negative impact of over

supplementation of NAD^+ precursors. Adverse systemic effects to cleared methyl groups may become apparent over time. Further to this, a longer exposure may identify chronic effects to skeletal muscle structure, transcriptional regulation or interplay with NAD^+ dependant enzymes such as PARPs or sirtuins. This work has highlighted the efficient adaptations skeletal muscle has to cope with excess NAD^+ and leads to further questions as to whether this would be maintained with chronic over supplementation. P7C3 is a commercially available NAMPT activator, which has been utilised to elevate NAD^+ levels. Further to this a recently developed compound has also been identified and can be used to activate NAMPT showing the varied methods employed to boost NAD^+ levels [305].

4. Impact of NAD^+ Depletion on Central Carbon Metabolism

4.1. Introduction

NAD^+ is an essential cofactor responsible for facilitating oxidoreductase reactions throughout glycolysis, the TCA cycle, and the ETC [103,306]. Metabolically active tissues require efficient ATP production to meet functional demand. ATP is produced through the ETC and therefore heavily relies on NAD^+/NADH redox homeostasis [38].

Sirtuins, PARPs and CD38s have been shown to consume NAD^+ in order to exert their effect within the cell such as contributing to DNA repair, mitochondrial biogenesis and calcium signalling [102,115–117,152]. As a result of this consumption it is important that the NAD^+ levels are restored to enable NAD^+ to continue to act as an intracellular signalling molecule. The routes to NAD^+ production are through either biosynthetic or salvage pathways [161,307,308].

4.1.1. Skeletal Muscle NAD^+ Biosynthesis

Skeletal muscle is central to whole body energy metabolism. This is evidenced by pathological changes to skeletal muscle having a role in disease states such as obesity, diabetes and sarcopenia [67,309,310].

Maintenance of NAD^+ levels is important in maintaining muscle health. Two routes to NAD^+ production have been established in skeletal muscle. NAM conversion to NMN via the NAMPT enzyme involves both NAM consumed in the diet as well as NAM released from NAD^+ degradation by enzymes. The more recently discovered route is via the NRK enzymes which are able to utilise NR to generate NMN [196,202,203]. As NMN is the common product these two pathways converge and produce NAD^+ via the NMNAT enzymes [311].

4.1.2. NAD+ Decline

NAD+ decline has been well documented in ageing and chronic disease mouse models [312,313]. A reduction in levels of between 20 and 50 % have been reported in muscle tissue of aged mice with an associated impairment in mitochondrial function [4–6,215,270,308]. The cause of this reduction is unclear. It may be the result of reduced NAD+ biosynthesis, increased NAD+ breakdown or a combination of both.

The molecular mechanism involved in the aetiology of aging has been associated with a decline in NAD+ [231]. Further to this, reduced NAD+ availability has been shown to impose functional limitations on skeletal muscle [259]. With impaired NAD+ biosynthesis contributing to muscle dysfunction observed in common metabolic disease, such as type II diabetes [213].

The decline in NAD+ not only poses a problem for the NAD+ consuming enzymes but also energy metabolism as a whole. NAD+ plays a central role in accepting electrons from glycolytic and TCA cycle metabolites with NADH ultimately being the driving force behind ATP synthesis [68]. This highlights NAD+/NADH as vital to central carbon metabolism and shows how a decline in NAD+ could be fatal to the cell. Based on the low NAD+ levels reported in chronic disease we sought to investigate the impact this may have on carbon metabolism.

Previous work conducted in cancer cells and a muscle-specific NAMPT KO mouse model identified key changes to metabolite levels in response to low NAD+ [180,215,263]. Whilst inferences can be made about energy metabolism from metabolite levels understanding changes to pathway utilisation requires more detailed analysis.

This chapter aims to help us understand how skeletal muscle cells adapt their energy metabolism pathways in response to NAD^+ depletion, through NAMPT inhibition, as well as whether the addition of NR can ameliorate any changes observed. Metabolic tracers were added and samples were analysed using combined 2D-^{1}H,^{13}C-NMR spectroscopy and GCMS, allowing for pathway utilisation analysis.

4.2. Materials and Methods

All products ordered from Sigma-Aldrich, UK, unless otherwise stated.

4.2.1. Cell Culture Treatments

4.2.1.1. Cell Culture Models

All work was carried out in a C2C12 cell culture model before results were confirmed in a primary myotube model using wild-type C57BL/6N mice. The primary cell culture protocol is described in detail in *Section 2.1.2.*

4.2.1.2. Cell Plating

C2C12s were seeded into 15 cm dishes in GM at a seeding density of 2,000,000 cells/plate. The cells were cultured in DM for 5 days with the media changed every other day. Primary myoblasts were divided equally between cell culture plates and left in plating media for 72 hours, followed by primary proliferation media for 24 hours and finally primary differentiation media for 6 days, with media changes every other day.

Once differentiated into myotubes the cells were either left as control, treated with 50 nM FK866 for 24 or 48 hours to model NAD^+ depletion, or co-treated with FK866 and 0.5 mM NR (Chromadex) for 4 hours.

4.2.1.3. $^{13}C_2$-1,2-Glucose Labelling

Freshly made flux media was added to the cells 24 hours prior to extraction; this consisted of 8.3 g of DMEM powder (without glucose, L-glutamine, phenol red, sodium pyruvate or sodium bicarbonate), diluted in 1 litre of distilled water, supplemented with 2 mM glutamine and 45 mM sodium bicarbonate. 10 mM $^{13}C_2$-1,2-D-Glucose was then added and the cells were left to metabolise for 24 hours.

4.2.1.4. $^{13}C_5$-Glutamine Labelling

Flux media consists of 8.3 g of DMEM powder (without glucose, L-glutamine, phenol red, sodium pyruvate or sodium bicarbonate), diluted in 1 litre of distilled water, supplemented with 10 mM glucose and 45 mM sodium bicarbonate. 2 mM $^{13}C_5$-glutamine was then added and the cells were left to metabolise for 24 hours.

4.2.1.5. $^{13}C_{16}$-Palmitic Acid Labelling

Palmitic acid was dissolved in NaOH to a final concentration of 50 mM at 70 °C. 1 part of the solution was mixed with 4 parts 12.5 % free fatty acid free BSA to give a 10 mM solution.

Following differentiation the cells were supplemented with 50 µM of the BSA conjugated $^{13}C_{16}$-palmitic acid for 3 days. Serum-free media was added for the last 24 hours consisting of 8.3 g of DMEM powder (without glucose, L-glutamine, phenol red, sodium pyruvate or sodium bicarbonate), diluted in 1 litre of distilled water, supplemented with 2 mM glutamine, 10 mM glucose and 45 mM sodium bicarbonate.

4.2.1.6. $^{13}C_6$-Glucose Labelling

Freshly made flux media was added to the cells 24 hours prior to extraction; 8.3 g of DMEM powder (without glucose, L-glutamine, phenol red, sodium pyruvate or sodium bicarbonate), diluted in 1 litre of distilled water, supplemented with 2 mM glutamine

and 45 mM sodium bicarbonate. 10 mM $^{13}C_6$-D-Glucose was then added and the cells were left to metabolise for 24 hours.

4.2.1.7. Malate-Aspartate Shuttle Inhibitor Treatment

Differentiated C2C12s were treated with 0.5 mM aminooxyacetic acid (AOAA) for 24 hours with or without 0.5 mM NR for 4 hours.

4.2.2. Extraction of Polar Metabolites for NMR Spectroscopy and GC-MS Analysis

All extractions were carried out according to *Section 2.6.6.1.* Briefly, media was aspirated and cells were washed with ice-cold 0.9% saline solution. Plates were placed on dry ice to quench metabolism and 1.2 ml pre-chilled HPLC-grade methanol with 2.5 µg/ml of D6-glutaric acid added as an internal standard. The cells were scraped and transferred to a falcon tube where 1.2 ml of pre-chilled HPLC-grade chloroform was added. The tube was rocked at 4 °C for 10 minutes before 1.2 ml of pre-chilled HPLC-grade H_2O was added and left to rest on ice for 10 minutes. Centrifugation of the samples at 4 °C, 14,200 rpm for 15 minutes allowed separation of the polar and non-polar fractions. 2 ml of the polar fraction was stored for NMR analysis, with 200 µl removed for GC-MS. Both fractions were evaporated to dryness using a SpeedVac at 30 °C for 4–5 hours and stored at -80 °C until further analysis. Protein pellet weights were used for normalisation during analysis.

4.2.3. Extraction of Polar Metabolites for LCMS Analysis

Cells were cultured according to *Section 3.2.1.4.* with all extractions carried out according to *Section 2.8.1.* Briefly, cells were washed with PBS and then scraped into an Eppendorf containing a lysis buffer (30 % acetonitrile, 20 % H_20 and 50 % methanol). Samples were vortexed for 45 seconds and then centrifuged at 13,000

rpm at 4 °C for 15 minutes. The supernatant was used for analysis. The protein pellets were dried out and weights used for normalisation.

4.2.4. High Resolution Respirometery

Cells were cultured in 6-well plates and treated with 50 nM FK866 for 48 or 72 hours. Treatment was re-added with each media change. Cells were added to a two-chamber oxygraph and subjected to 2.5 mM oligomycin, sequential additions of 0.5 mM FCCP, 0.5 mM rotenone and 2.5 mM antimycin A.

Chamber contents were collected at the end of the protocol and used in a Bio-Rad protein assay for normalisation. The data used was following mitochondrial uncoupling to show maximal respiration of the cells with the given treatments.

4.2.5. Fatty Acid Oxidation Assay

Cells were plated in 24-well tissue culture plates and treated with 50 nM FK866 for 48 hours with and without 0.5 mM NR for 4 hours. The media was changed to low glucose DMEM for the final 24 hours of the protocol. $^{14}C_1$-palmitate and 1 mM carnitine was added to a DMEM and BSA solution. The positive control was 24 hour treatment with 50 μM trolox, an antioxidant which has shown to increase β-oxidation [314,315]. The negative control was a 4 hour treatment with 2 mM oxfenicine, a carnitine palmitoyltransferase inhibitor [316].

Acidification vials were made up. 200 μl of 1 M perchloric acid was added to an Eppendorf with filter paper inserted into the cap with 1 M NaOH added. 500 μl of the supplemented DMEM was added to the cells. Plates were sealed using parafilm and left to incubate for 3 hours. Following incubation, 400 μl of the media was transferred to the acidification vials, which were left for a further hour. The filter paper was

transferred to a scintillation vial containing 4 ml scintillation fluid. The radiolabel was measured over 3 minutes using a scintillation counter.

4.2.6. Glycogen Assay

The cells were seeded in 6-well plates and differentiated for 5 days. The cells were treated with FK866 for 48 hours, with and without NR for 4 hours. The positive and negative controls were; 24 hour treatment with insulin U-350 (350 units of insulin per ml) and 8 hour exposure to low glucose media with no glutamine, respectively.

The plates were extracted according to *Section 2.11.*

4.2.7. Muscle Specific NAMPT KO Mouse Model

7 wild-type and 7 muscle-specific NAMPT KO mice (C57Black) were connected to syringe pumps and injected with $^{13}C_6$-glucose at 6 mg/kg/min for 5 minutes. This model was developed and experiments executed in Copenhagen in Jonas Treebak's laboratory. Following this there was a steady infusion at 2 mg/kg/min for 115 minutes. At the end of the protocol the mice were immediately sacrificed and tissues were dissected and snap-frozen.

The processing and metabolite extraction from these tissues is detailed in *Section 2.6.6.1.* Briefly, quadriceps muscles were pulverised using a Mortar & Pestle before being added to 1.5 ml of methanol. A probe sonicator was used for 2x 40 seconds before 1.5 ml of chloroform was added. The tubes were rocked at 4 ºC for 10 minutes and 1.3 ml of H_2O was added. The samples were centrifuged at 4°C at 14,200 rpm for 15 minutes and the top aqueous layer collected for polar metabolite investigation by NMR spectroscopy and GC-MS.

4.2.8. NMR and GCMS Data Acquisition

Detailed explanations of both the NMR and GCMS data acquisition can be found in *Section 2.6.6.2.* and *Section 2.7.* respectively.

4.2.9. Data Analysis

4.2.9.1. GC-MS Analysis

The GCMS analysis was made up of two parts; ion quantification and mass isotopomer distribution. The relative quantification of metabolites was achieved through ion quantification. For each metabolite the associated ions that occurred as a result of the GC-MS run could be reconfigured and used to inform on the levels of the metabolite within the sample. Without a standard curve present this information could not be absolutely quantified, but instead samples undergoing differing treatments within the same GC-MS run were compared.

The mass isotopomer distribution was important for the understanding of the metabolic pathways used within the cell. GC-MS analysis was able to report the mass of the metabolite +0, +1, +2, and +3, based on the number of ^{13}C atoms present. This data did not inform on the position of the labelled carbon but on the number contained within the metabolite.

4.2.9.2. 1D-^{1}H-NMR Analysis

All 1D-^{1}H-NMR analysis was completed using Chenomx 7.0 (ChenomxINC). Chenomx is a user-friendly package allowing for the identification of metabolite concentrations within an NMR sample.

4.2.9.3. 2D-^{1}H,^{13}C-NMR Analysis

All 2D-^{1}H,^{13}C-NMR analysis was completed using MetaboLab. The spectra were automatically phase corrected following a script with manual adjustment as

necessary. All spectra were referenced to lactic acid within the reference library. Each metabolite was assigned manually, the peaks were identified for each metabolite and then multiplet analysis was carried out. An option to add GCMS data was a feature of the software, to strengthen the data and help to visualise any 'NMR-blind' carbons within the metabolite. The potential isotopomers were identified with a 0 used to represent a ^{12}C and a 1 representative of a ^{13}C; the programme fitted the data as closely as possible to the experimental results. The resultant data were MIDs for each metabolite within each sample, informing on the position of the labelled carbon(s) within the molecule.

4.2.9.4. Statistical Analysis

All statistics have been carried out using the GraphPad Prism 6 software. One-way ANOVA analysis has been conducted on the concentrations of metabolites. MIDs have been analysed within the individual pathways, with significance tested between the groups as opposed to between the pathways using one-way ANOVAs. Dunnett's multiple comparison tests were used as all comparisons were to a common control group. Statistical significance was shown by * $p<0.05$, ** $p<0.01$, *** $p<0.001$.

For graphs with two or more groups, for example, where all treatments in C2C12s and primary's are displayed on one graph, two-way ANOVAs were conducted. Sidak's multiple comparisons test was used for post hoc analysis when the significant changes between the treatments at a specific point were of interest. When the significance within each group and between the groups was tested Tukey's multiple comparisons test was used following two-way ANOVA.

4.3. Results

4.3.1. Establishing Cell Models of NAD^+ Depletion and NR Rescue

The decline in NAD^+ associated with ageing and metabolic diseases has prompted research into the impact this has on energy metabolism. In order to manipulate NAD^+ levels within a system and observe the changes to energy metabolism a model of NAD^+ depletion was generated by treating C2C12 myotubes with the NAMPT inhibitor, FK866. The cells were also treated with the NAD^+ precursor, NR, which bypasses NAMPT on route to NAD^+ biosynthesis and therefore should not be affected by FK866, figure 4.1A.

To confirm this model was effective, 1D-^{1}H-NMR spectroscopy was used to establish tNAD levels in response to the different treatments. As mentioned previously, the instability of NADH and NADPH results in their oxidation to NAD^+ and $NADP^+$ during extraction meaning 1D-^{1}H-NMR spectroscopy NAD measurements are total NAD(P) (tNAD(P)). The levels of tNAD were significantly reduced in a time-dependent manner with an 82 % reduction after 24-hours and a 95 % reduction following 48-hour FK866 treatment. These levels were rescued by a 4-hour treatment with NR figure 4.1B. The levels of tNADP were also significantly supressed by FK866 and restored with NR, figure 4.1C. The levels of NAM remained unchanged by FK866 treatment but were significantly elevated in response to NR, figure 4.1D. This increase in NAM did not impact NAM clearance through MeNAM as levels remained constant through the different treatment groups, figure 4.1E.

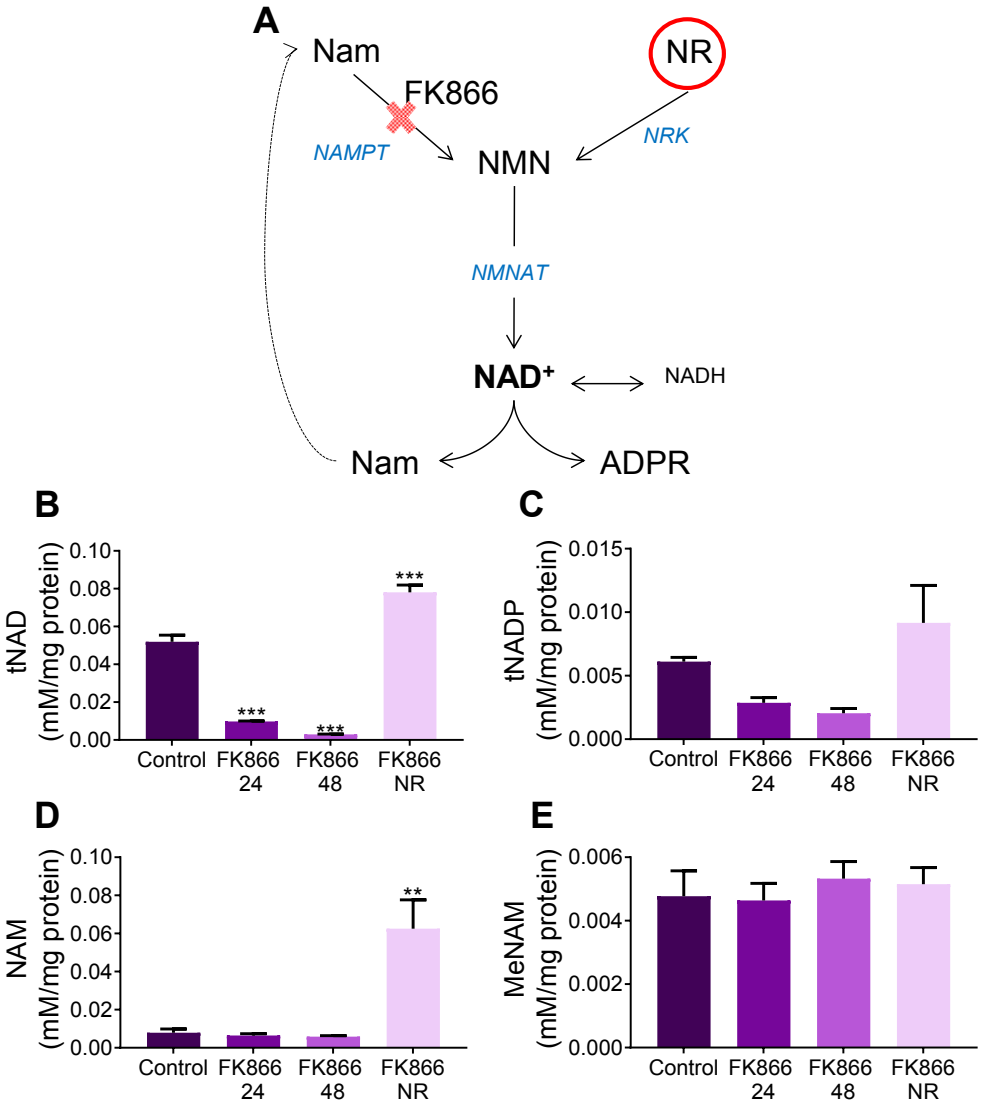


Figure 4.1. Inhibition of NAD+ Biosynthesis in C2C12s

Differentiated C2C12s were treated with FK866 (50 nM) for 24 or 48 hours. Cells treated with FK866 for 48 hours were supplemented with NR (0.5 mM) for 4 hours, pathway shown in **(A)**. Key metabolites were identified and quantified using 1D-^{1}H-NMR spectroscopy and used to establish whether the cell model had worked; **(B)** tNAD, **(C)** tNADP, **D)** NAM and **E)** MeNAM.

** p<0.01, ***p<0.005; One-way ANOVA performed on data; Dunnett's multiple comparison test, treatment compared to control. All data are normalised to protein and are the mean ±SEM, C2C12s *n=4*.

Once established in C2C12s, primary myotubes were cultured and the same treatments applied with a view to develop two separate culture systems to investigate changes to central carbon metabolism. As before, tNAD was significantly decreased with FK866 treatment and 'boosted' above control with NR, figure 4.2A. tNADP was also significantly affected with tNAD depletion and normalised with addition of NR, figure 4.2B. NAM was once again unchanged through tNAD depletion but saw an increase in response to NR treatment, figure 4.2C.

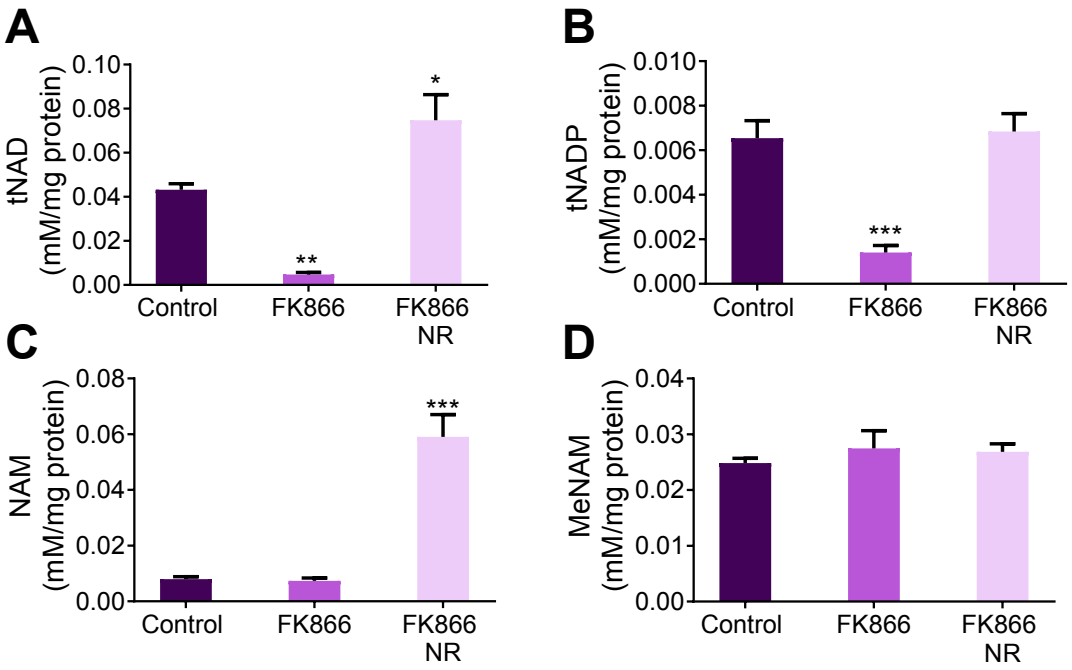


Figure 4.2. Chemical Inhibition of NAD+ Biosynthesis in Primary Myotubes

Primary myotubes were treated with FK866 (50 nM) for 48 hours. Cells treated with FK866 for 48 hours were supplemented with NR (0.5 mM) for 4 hours. Key metabolites were identified and quantified using 1D-^{1}H-NMR spectroscopy and used to establish whether the cell model had worked; **(A)** tNAD, **(B)** tNADP, **C)** NAM and **D)** MeNAM.

* p<0.05, ** p<0.01, ***p<0.005; One-way ANOVA performed on data; Dunnett's multiple comparison test, treatment compared to control. All data are normalised to protein and are the mean ±SEM, Primary myotubes *n=4*.

Together this data shows significant tNAD depletion following FK866 treatment, which is evidence of both NAD^+ and NADH reduction. This work shows two cell culture systems each showing the same response to differing NAD^+ bioavailability.

4.3.2. Skeletal Muscle Bioenergetics Following NAD^+ Depletion

NAD^+ is critical for energy redox pathways, thus its depletion would be expected to have an impact on the bioenergetics of the muscle cell. Investigation of ATP + ADP was shown to have no change across the treatment groups figure 4.3A. However, the PCr/Cr ratio, which is a key buffering system within cells, was significantly reduced following NAD^+ depletion in both C2C12s and primary myotubes. This was returned to control levels after a 4-hour NR supplementation figure 4.3B. The lactate/pyruvate ratio was calculated through the m+2 portion of the MID from the GCMS analysis. This showed a significant increase in FK866 treated C2C12s, which was normalised with NAD^+ repletion via NR, but no such changes were observed in the primary myotubes, figure 4.3C.

To further understand the bioenergetics of the cell in response to NAD^+ depletion, C2C12 myotubes were treated with FK866 for 48 and 72 hours and subjected to high resolution respirometery, figure 4.3D. There were no significant changes to the maximal respiration as shown through O_2 fluxes however, following 72 hours FK866 treatment there was a trend downwards from control levels.

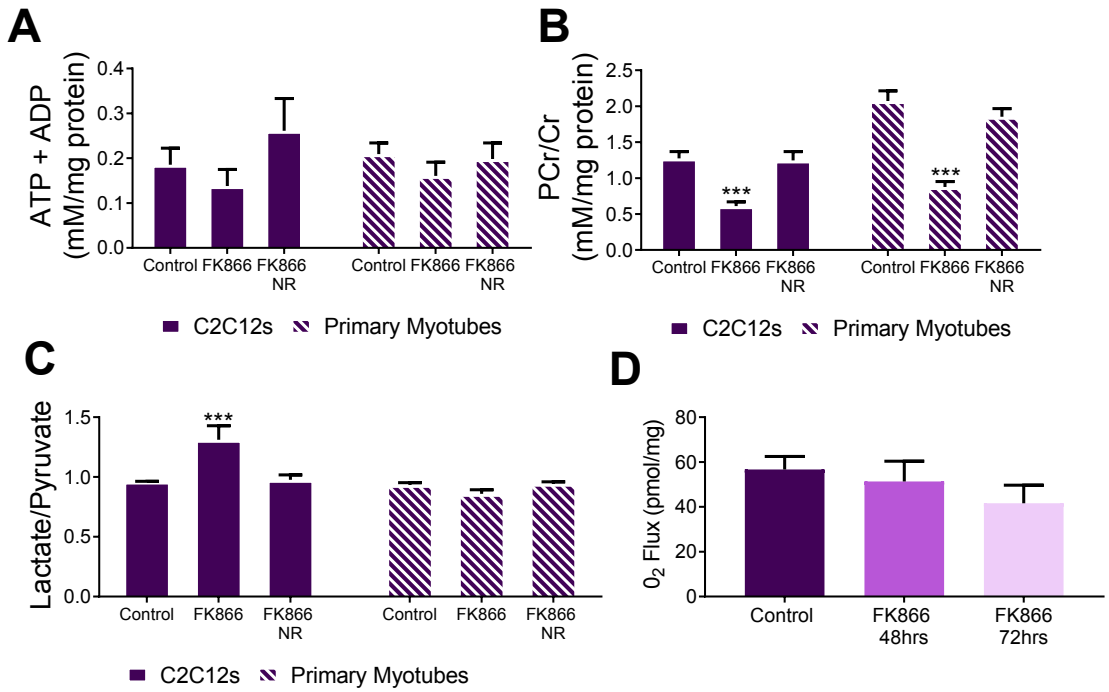


Figure 4.3. Bioenergetics of C2C12s in Response to NAD+ Depletion

Key metabolites were identified and quantified using 1D-^{1}H-NMR spectroscopy and used to inform on the energetic status of the cell; **(A)** combined ATP and ADP and **(B)** the phosphocreatine (PCr)/ creatine (Cr) ratio. **(C)** Lactate/Pyruvate ratio from GC-MS analysis using the m=2 portion of the MID. **D)** High resolution respirometery was carried out on differentiated C2C12s treated with 50 nM FK866 for 48 or 72 hours.

***p<0.005; Two-way ANOVA performed on raw data; Sidak's multiple comparisons test, significant changes between the treatments compared. All data are normalised to protein and are the mean ±SEM, C2C12s *n=6*. Primary myotubes *n=4*.

4.3.3. Effects of NAD+ Depletion on Fatty Acid Oxidation

The fatty acid oxidation pathway has a heavy reliance on NAD$^+$ as discussed in *section 1.1.4.4*. This therefore led us to hypothesise that the use of fatty acids for energy metabolism would be affected by FK866 treatment and the consequential severe NAD$^+$ depletion. To investigate this we attempted a sodium palmitate labelling experiment where $^{13}C_{16}$-palmitic acid was added to the cells and they were left to metabolise for 72 hours. Following GCMS analysis there was no evidence of ^{13}C incorporation into any of the metabolites, figure 4.4.

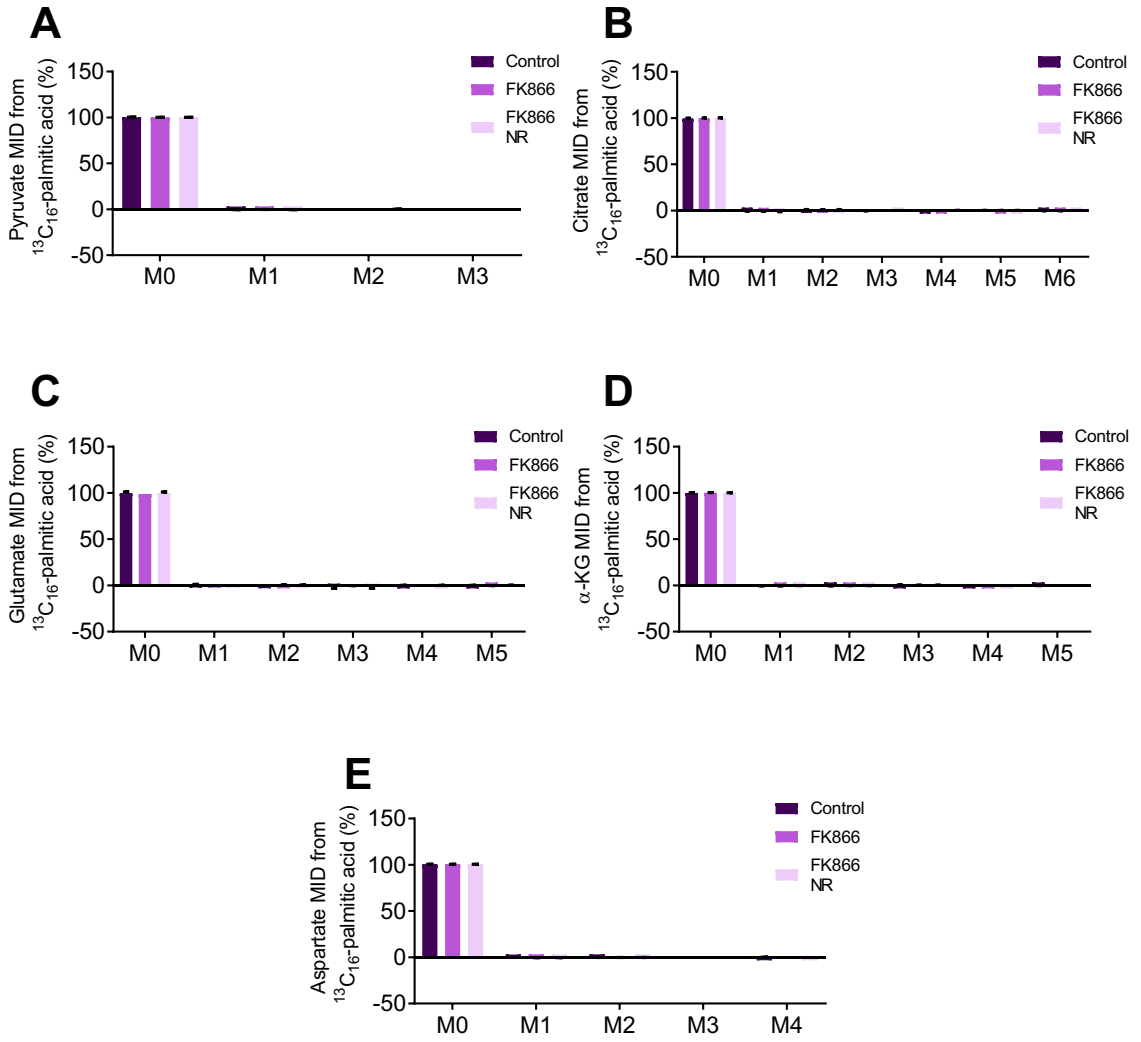


Figure 4.4. Sodium Palmitate Labelling in C2C12s
C2C12s were metabolised with $^{13}C_{16}$-sodium palmitate for 72 hours. They were treated with 50 nM FK866 for 48 hours with and without 0.5 mM for 4 hours and GCMS analysis was conducted to show label incorporation into **A)** pyruvate, **B)** citrate, **C)** glutamate, **D)** α-KG and **E)** aspartate.
All data are the mean ±SEM, C2C12s *n=3*.

An alternative method was employed to observe changes to fatty acid oxidation as a result of altered NAD^+ bioavailability. C2C12s were metabolised with BSA and ^{14}C-palmitate and the CO_2 released was captured and used for scintillation counting. Based on our hypothesis FK866 treatment was expected to reduce the levels of $^{14}CO_2$ detected and imply an inhibition of fatty acid oxidation through NAD^+ depletion. This was not observed, with the levels comparable to control and co-treatment with NR, figure 4.5. 24 hour treatment with 50 µM trolox.

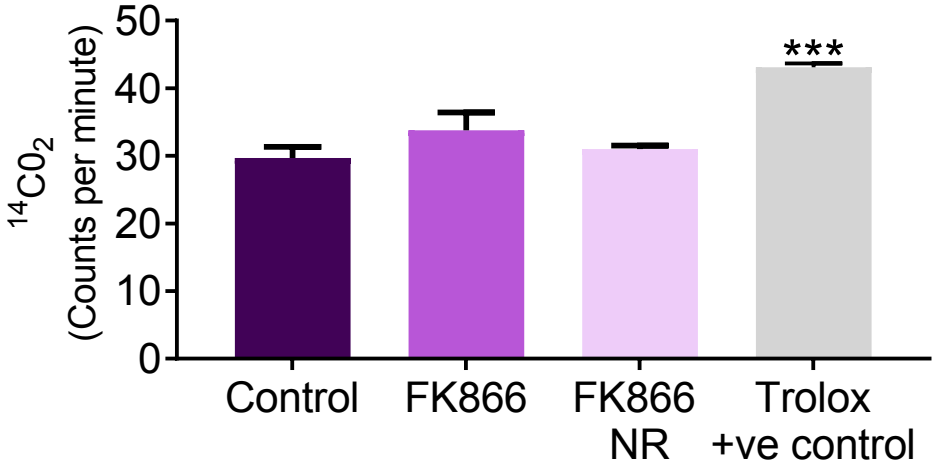


Figure 4.5. Fatty Acid Oxidation following NAD^+ Depletion
C2C12s were treated with FK866 (50 nM) for 48 hours and NR (0.5 mM) for 4 hours. 24 hour Trolox (50 µM) was used as a positive control. $^{14}C_1$-palmitic acid was added to the cells and the levels of ^{14}C incorporated in to CO_2 were detected through scintillation counting.
***p<0.005; One-way ANOVA performed on data; Dunnett's multiple comparisons test, treatment compared to control. All data are normalised to protein and are the mean ±SEM, C2C12s *n=3*.

4.3.4. Effects of NAD^+ Depletion on Glycolytic and TCA Cycle Metabolites

To observe any NAD^+-dependant changes to glycolysis, primary outputs were investigated. Concentrations of lactate remained constant throughout the different groups in both C2C12s and primary myotubes, figure 4.6A. Further to this, there was no significant change observed in the labelling patterns of lactate with FK866 or combined FK866 and NR treatment, figure 4.6B-C. Alanine levels were variable within the different groups in the C2C12 model, albeit no significant differences were observed, figure 4.6D. Once again the primary myotubes showed no significant differences in alanine concentration in any of the treatment groups, figure 4.6E. The labelling pattern analysis of alanine was conducted in the same way as for lactate. The flow of carbon through glycolysis and the pentose phosphate pathway PPP can be differentiated, with a slight increased proportion of carbon passing through

glycolysis as a result of FK866 treatment. This however was not significant in either cell model, C2C12 of primary myotubes, figure 4.6F-G.

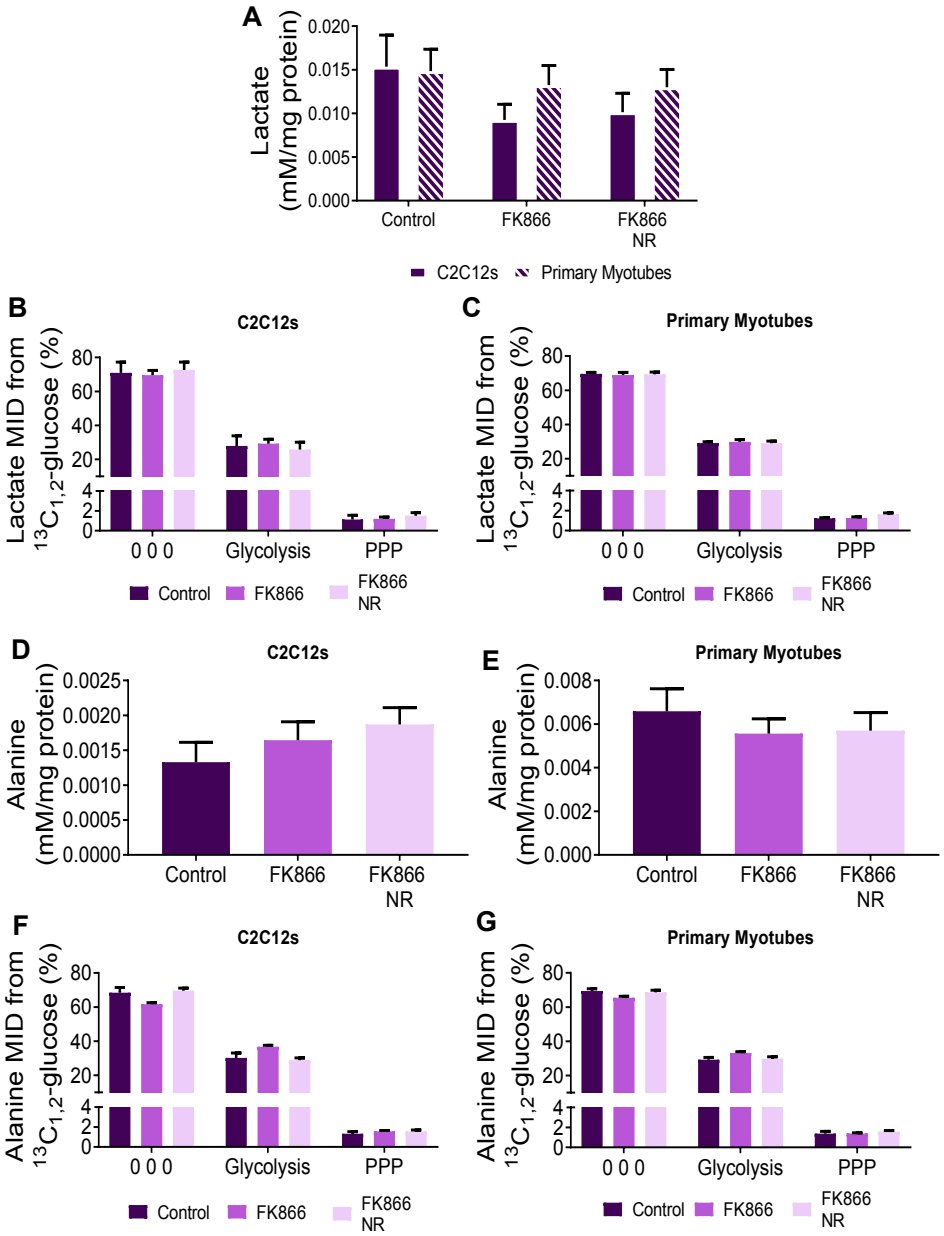


Figure 4.6. Glycolytic Outputs, Lactate and Alanine, Unaffected by NAD+ Depletion

Differentiated C2C12 and primary myotubes were treated with FK866 (50 nM) for 48 hours with and without NR (0.5 mM) for 4 hours. 1D-^{1}H-NMR spectroscopy shows **(A)** Lactate concentration in C2C12 and primary myotubes (mM/mg of protein). Combined 2D-^{1}H-^{13}C-NMR and GC-MS analysis shows pathway contribution to lactate in **(B)** C2C12 and **(C)** primary myotubes. Alanine concentration (mM/mg of protein) in **(D)** C2C12s and **(E)** primary myotubes with alanine pathway analysis in **(F)** C2C12 and **(G)** primary myotubes.

Two-way ANOVA performed on lactate concentrations; Tukey's multiple comparisons test compare between treatments and within groups. One-way ANOVA performed on the rest of the data, with individual pathways assessed independently; Dunnett's multiple comparisons test, treatment compared to control. All data are normalised to protein and are the mean ±SEM, *n=4*.

With no clear effects of FK866 on the outputs of glycolysis we sought to understand changes occurring within the pathway itself. The first NAD^+ dependent step of glycolysis is GAPDH, where the enzyme catalyses the oxidation and phosphorylation of glyceraldehyde-3-phosphate to 1,3-bisphosphoglycerate, reducing NAD^+ in the process. GCMS analysis of metabolites above GAPDH showed an elevation of GAP after 48-hours that was not present after 24-hour FK866 treatment in the C2C12s, figure 4.7A. GAP was not detected in the primary myotubes, possibly due to turnover of the metabolite. However, G3P was identified which is crucial for the functioning of the G3P shuttle, important for maintaining the redox potential across the inner mitochondrial membrane. This was elevated in the primary myotubes in response to 48-hour FK866 treatment, figure 4.7B. The 4-hour NR supplementation was sufficient to normalise the levels of GAP in the C2C12s, however the levels of G3P were still significantly elevated following treatment, figure 4.7A-B.

An elevation of the metabolite preceding the GAPDH enzyme was suggestive of a block of glycolysis at this point. To investigate this further relative quantification of downstream TCA metabolites was employed to ascertain whether the NAD^+ decline was halting glycolytic outputs into the mitochondria and thereby limiting metabolite levels. Once again there appeared to be a time-dependent decrease in citrate (figure 4.7C), α-KG (figure 4.7E) and malate (figure 4.7G) with FK866 treatment for 24 and 48-hour. Treatment with NR increased the levels of α-KG and malate back to control but was not sufficient to normalise citrate levels in C2C12 myotubes. Citrate levels were not affected by FK866 in the primary myotubes, figure 4.7D. However, 48-hour FK866 treatment significantly reduced the levels of α-KG (figure 4.7F) and malate (figure 4.7H), which were bought back to control levels through 4-hour NR treatment.

A diagrammatic representation of the data is shown in figure 4.8, where the effects of NAMPT inhibition by FK866 are shown to feed in to glycolysis and ultimately impact TCA metabolite levels.

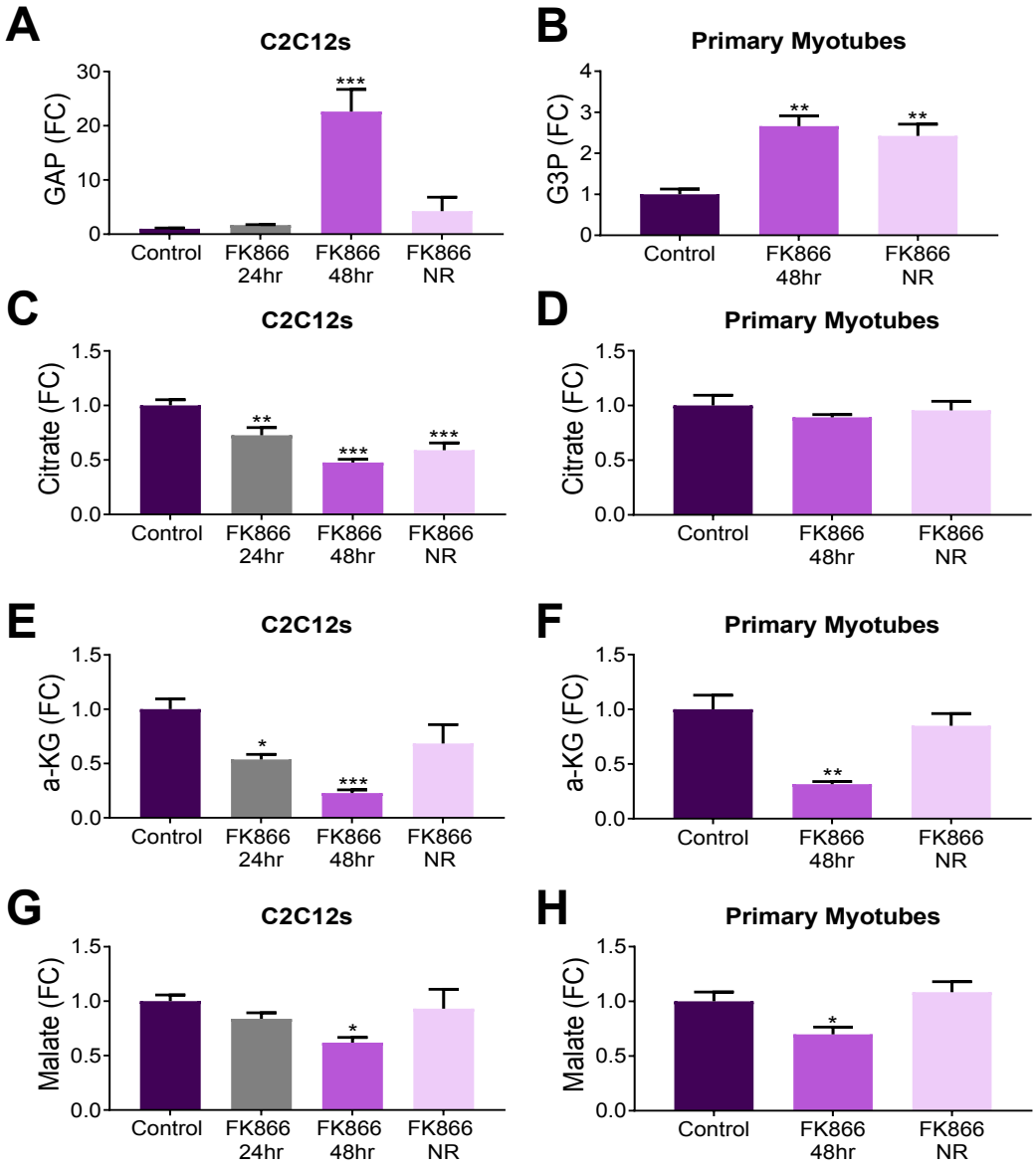


Figure 4.7. Block in Glycolysis at GAPDH Following NAD+ Depletion

Data shown are fold changes of ion counts from GCMS compared to control in both NAD+ deplete (FK866; 24 h and 48 h) and replete (FK866; 48 h + NR; 4 h) cells, showing (**A**) glyceraldehyde-3-phosphate (GAP), (**B**) glycerol-3-phosphate (G3P), (**C**, **D**) citrate, (**E**, **F**) a-ketoglutarate, (**G**, **H**) malate. * p<0.05, ** p<0.01, ***p<0.005; One-way ANOVA performed on raw data; Dunnett's multiple comparison test, treatment compared to control. All data are normalised to protein and are the mean fold-changes ±SEM, *n=4*.

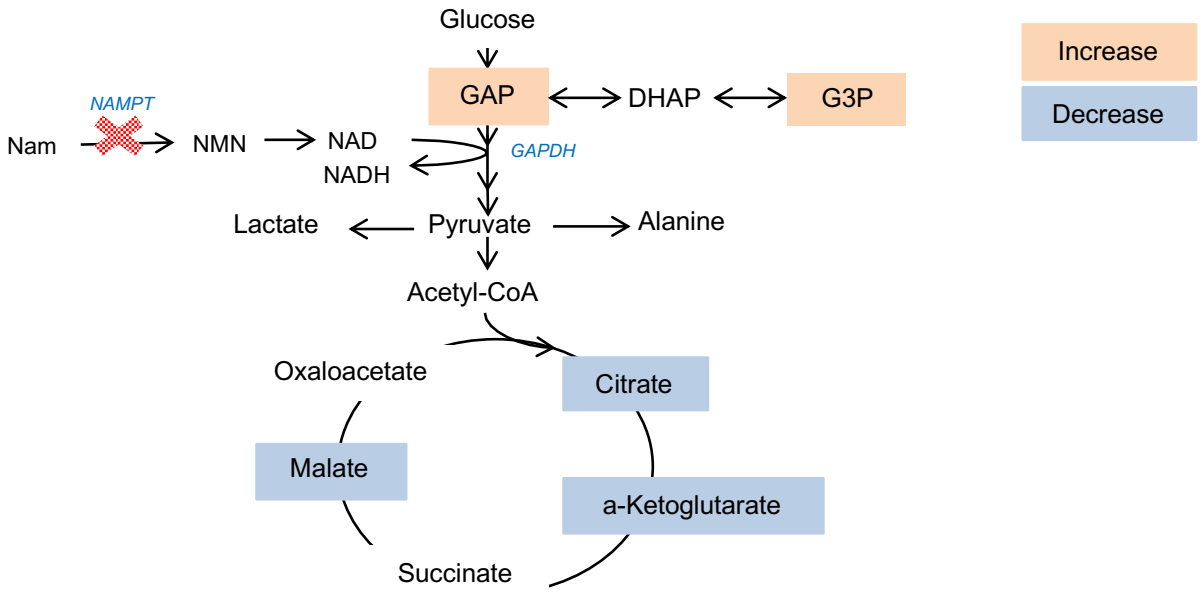


Figure 4.8. Diagrammatic Representation of Block in Glycolysis
A diagrammatic representation of glycolysis and the TCA cycle in C2C12 myotubes treated with FK866 for 48 h. An increase in ion count compared to control shown in peach and a decrease shown in blue.

The changes to glycolytic and TCA metabolite levels are only suggestive of an indirect inhibition of GAPDH, through limitation of NAD^+ bioavailability. To further confirm this observation C2C12s were metabolised with $^{13}C_2$-[1,2]-glucose to incorporate ^{13}C into key metabolites. Fructose-6-phosphate was selected as a metabolite as it is situated above GAPDH on the glycolytic pathway. Investigation of carbon 1 of the 6-carbon molecule through 2D-^{1}H,^{13}C-NMR spectroscopy indicated label incorporation, as shown through peaks on the spectra, in the 48-hour FK866 samples but not the control or 24-hour samples, figure 4.9A. Carbon 1 labelling in these samples is evidence of 1,2-glucose being metabolised to 1,2-fructose-6-phosphate and not proceeding through the pathway any further. In addition to this, carbon 5 of fructose-6-phsophate also shows label incorporation present in the 48-hour FK866 treated samples, figure 4.9B. Further to this, fructose-1,6-bisphosphate was investigated through LC-MS to confirm whether the changes are apparent in an

alternative metabolite using an alternative method. The C2C12 myotubes were treated with $^{13}C_6$-glucose for 24-hours and LC-MS was used to identify the levels of m+6 fructose-6-phosphate. A significant increase in the m+6 portion of fructose-6-phosphate was observed with FK866 treatment, which was normalised to control levels with addition of NR figure 4.9C.

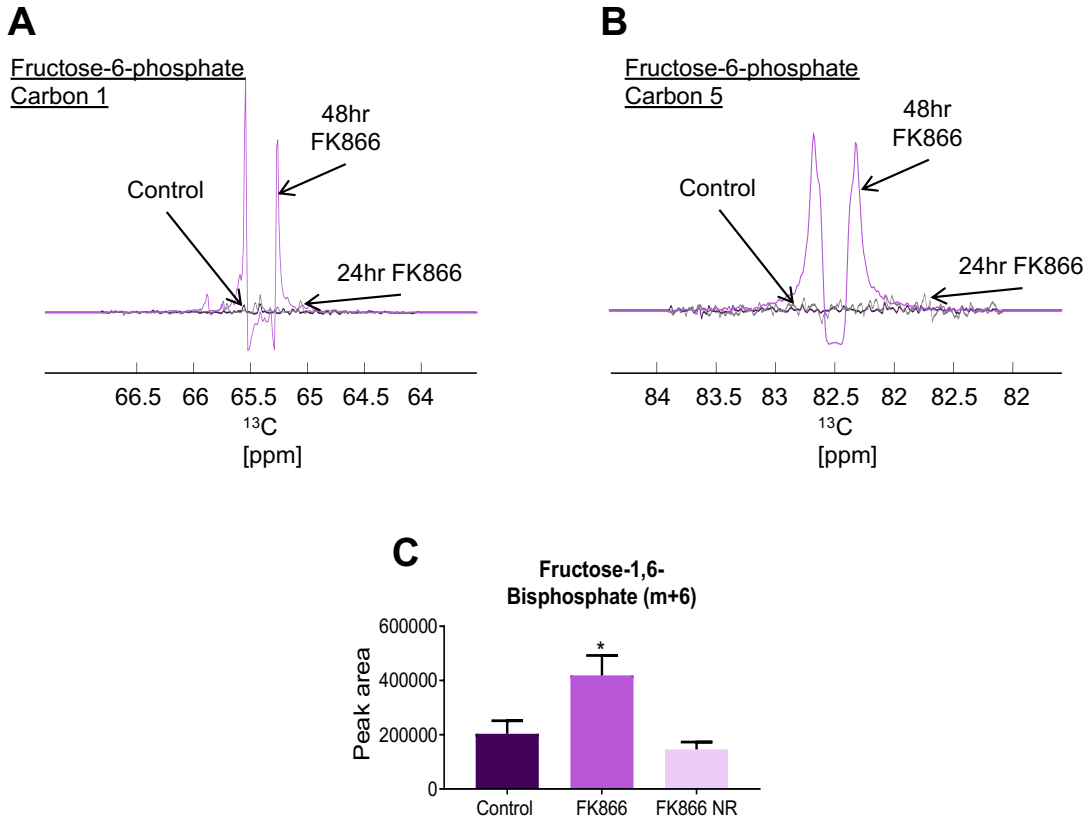


Figure 4.9. Fructose-6-phosphate Labelling Following NAD+ Depletion
Fructose-6-phosphate was used to investigate reversal of glycolytic reactions as it appears before the block at GAPDH. Representative 2D-^{1}H,^{13}C-HSQC spectra were used to show ^{13}C label incorporation in both control and FK866. (**A**) Carbon 1 peaks; **(B)** carbon 5 peaks. **(C)** m+6 portion of fructose-1,6-bisphosphate as shown through LCMS analysis.
* p<0.05, One-way ANOVA performed on LCMS data; Dunnett's multiple comparison test, treatment compared to control. All data are normalised to protein and are the mean ±SEM, *n=3*.

The presence of label incorporation into carbon 5 of fructose-6-phophate and the evidence of elevated fructose-6-phosphate labelling overall can only be achieved through reverse glycolytic flux, figure 4.10A. The low NAD+ effectively inhibits

GAPDH and causes a build-up of G3P, which affects the equilibrium of the enzyme reaction and switches the glycolysis pathway to glycogenesis. A glycogen assay was utilised to identify whether there was elevated glycogen storage within the myotube as a result of the FK866 treatment. There was no change to glycogen levels as a result of FK866 treatment, figure 4.10B.

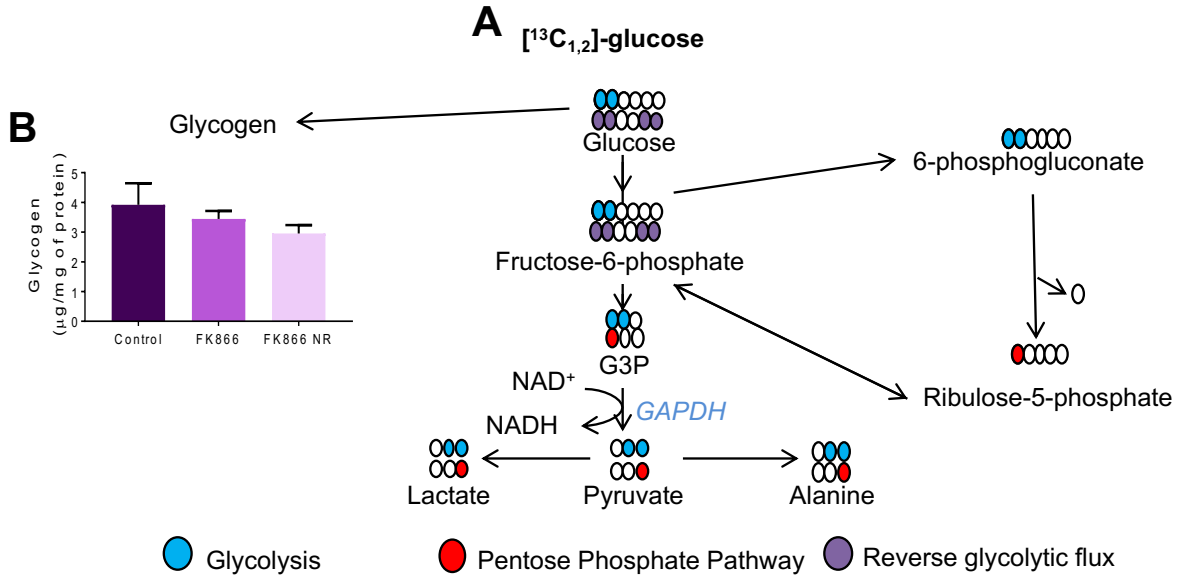


Figure 4.10. Glycolysis Pathway Analysis Following NAD+ Depletion
(A) Labelling pattern analysis shows how $^{13}C_{1,2}$-glucose is metabolised through glycolysis in blue, the PPP in red and via reverse glycolytic flux in purple. **(B)** Glycogen levels of C2C12s shown in response to FK866 (50 nM) for 48 hours with and without NR (0.5 mM) for 4 hours.
One-way ANOVA performed on glycogen data; Dunnett's multiple comparison test, treatment compared to control. All data are normalised to protein and are the mean ±SEM, *n=3*.

4.3.5. NAD+ Depletion Leads to Elevated Mitochondrial Derived Aspartate

Whilst conducting the multiplet analysis for aspartate in the FK866 treated samples there appeared to be reduced signal to noise compared to samples co-treated with NR, figure 4.11. This was suggestive of increased label incorporation with FK866 into aspartate. Through further investigation we found a significantly elevated aspartate concentration in both C2C12 and primary myotubes, figure 4.12A-B. Following the

reduced ion count of key TCA metabolites, as a result of the GAPDH block in FK866 samples, this was an unexpected finding.

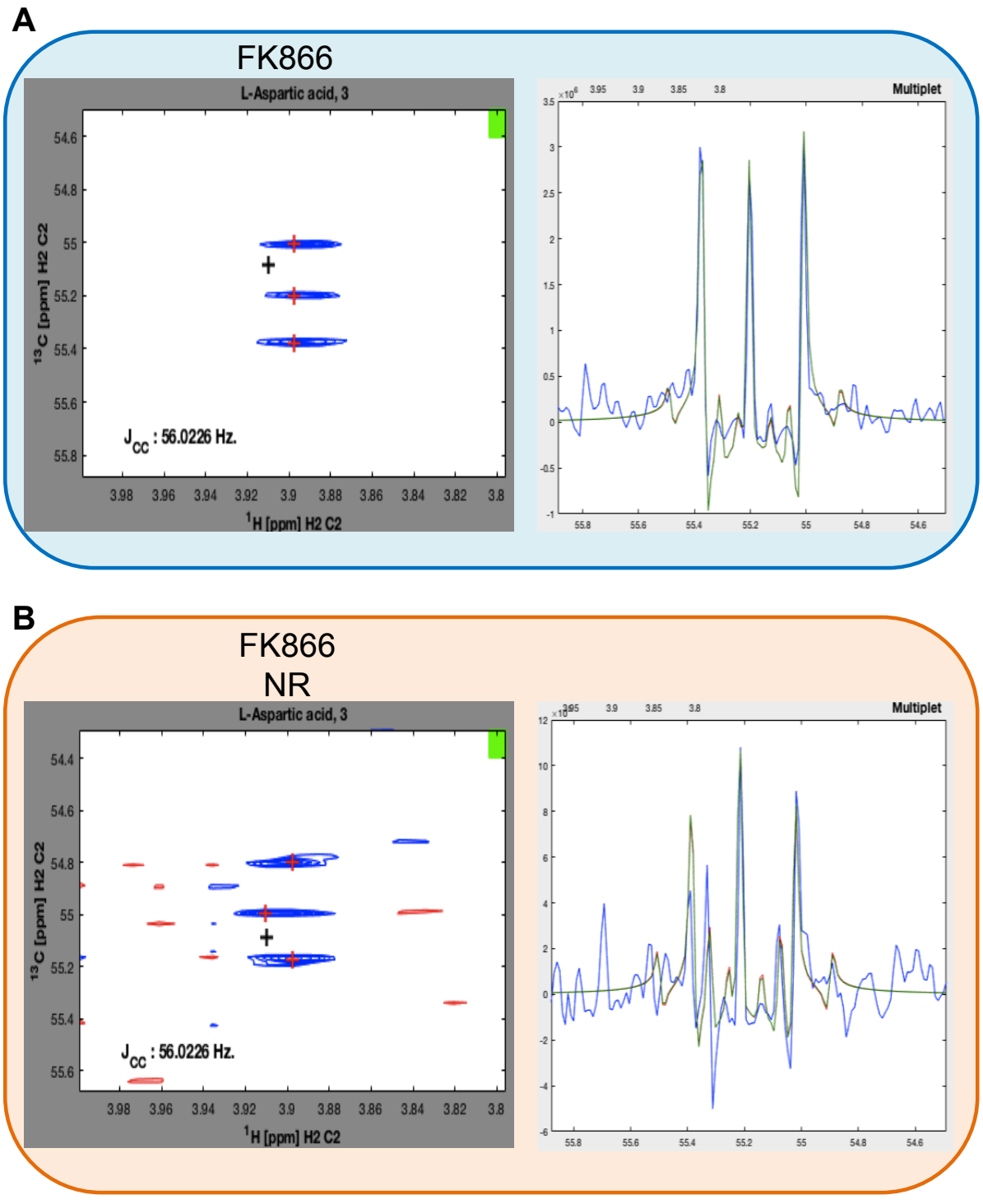


Figure 4.11. Aspartate Multiplet Analysis

The label incorporation into aspartate appears to be elevated in FK866 samples (**A**). There is increased label incorporation and less noise shown through defined blue lines in and neat peaks in with high signal to noise (**A**). This is highlighted when compared with (**B**) FK866 and NR samples. The red dashes in (**B**) show noise, which is followed through to the multiplet analysis where the peaks are less well defined.

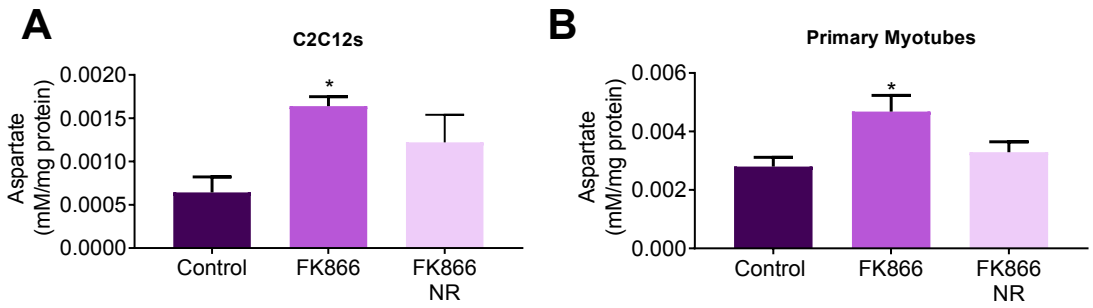


Figure 4.12. Aspartate Production Significantly Altered with NAD+ Depletion
Aspartate concentration in both **(A)** C2C12s and **(B)** primary myotubes from 1D-^{1}H-NMR spectroscopy.
* p<0.05; One-way ANOVA performed; Dunnett's multiple comparisons test, treatment compared to control. All data are normalised to protein and are the mean ±SEM, *n=4.*

Further investigation using combined analysis of the 2D-^{1}H-^{13}C-HSQC spectra and GC-MS data showed significant alterations to pathway utilisation for aspartate. In the C2C12 cell model there was a significant reduction of unlabelled aspartate as a result of FK866 treatment with a concurrent significant increase in 1,2/3,4 labelling, figure 4.13A. Further to this, the primary myotubes expressed a more well defined phenotype with an additional significant increase in 2/4 and 1/5 labelling following NAD+ depletion, figure 4.13B. All of these effects were normalised to control levels with an acute dose of NR, figure 4.13A-B.

Using the aspartate concentration and MIDs the absolute amount of aspartate produced from each pathway can be represented. An outline of which labelling patterns contribute to which pathway is referred to in *section 2.6.5.2*. Both cell models show a significant increase in aspartate produced through glycolysis, the TCA cycle and the PPP, figure 4.13C-D. The primary myotubes once again appear to express an exaggerated phenotype with a significant reduction in PC activity as a

result of FK866 treatment. The addition of NR abolishes any FK866 induced effects on aspartate labelling, figure 4.13C-D.

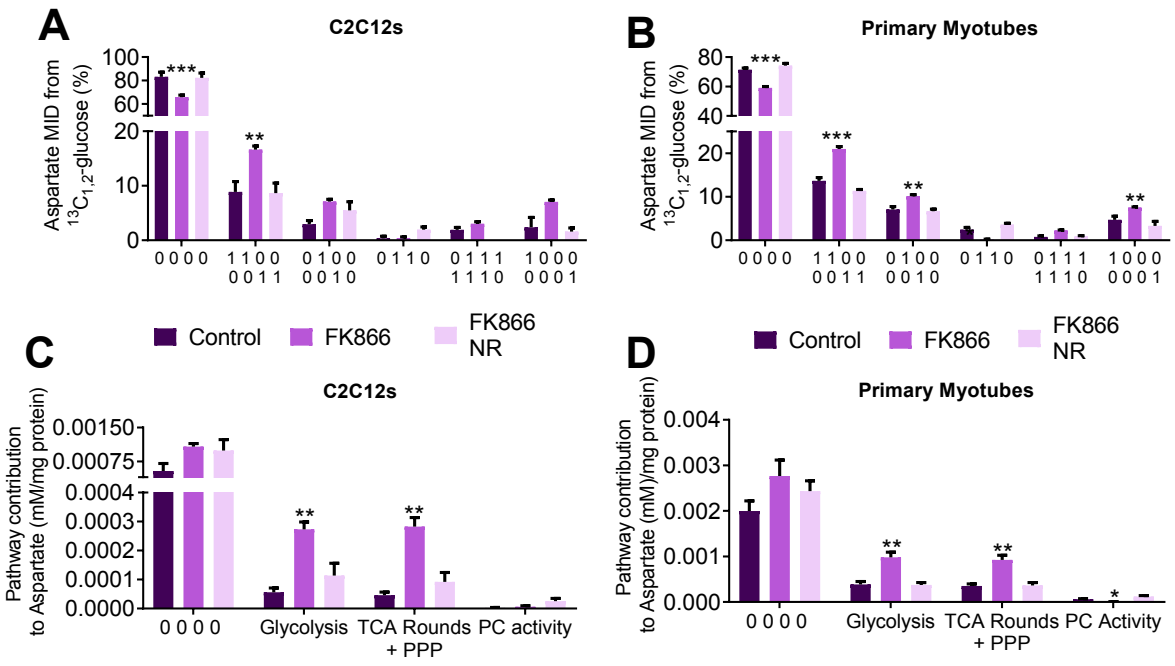


Figure 4.13. Pathway Utilisation for Aspartate Production Significantly Altered with NAD+ Depletion
Cells were treated with 50 nM FK866 for 48 hours with or without 0.5 mM NR for 4 hours. **(A-B)** Combined analysis of 2D-^{1}H,^{13}C-NMR ($^{13}C_{1,2}$-glucose) and GC-MS data provides labelling patterns for aspartate; **(C-D)** analysis of the labelling patterns allows understanding of pathway utilisation for aspartate production.
Glycolysis 1100+0011; *TCA rounds + PPP* 0100+0010, 1111, 0111+1110, 1000+0001; *PC Activity* 0110
* p<0.05, ** p<0.01, *** p<0.005; One-way ANOVA performed on raw data, with individual pathways assessed independently; Dunnett's multiple comparison test, treatment compared to control. All data are normalised to protein and are the mean ±SEM, *n=4.*

4.3.5.1. Glutamine Use for Aspartate Production Following NAD+ Depletion

Albeit not significant it was noted that there appeared an increase in the unlabelled proportion of aspartate with FK866 treatment. Generation of unlabelled aspartate is evidence of a non-glucose carbon source being used. In the absence of NAD+ we postulated that the cell might favour glutamine use over NAD+ dependant glycolysis. To investigate this, we used [U-^{13}C] glutamine as a nutrient. Labelling patterns for aspartate production from glutamine are shown in figure 4.14A and are discussed in

Section 2.6.5.2. From these labelling patterns we are able to infer the number of TCA cycle rounds completed using glutamine. Label incorporation into aspartate was significantly elevated in FK866 samples but only in the 2-only labelled and 3-only labelled portion, figure 4.14B. This data shows that the C2C12s do not use glutamine as a regular source of carbon for aspartate production under normal conditions and only begin to do this in response to FK866 treatment.

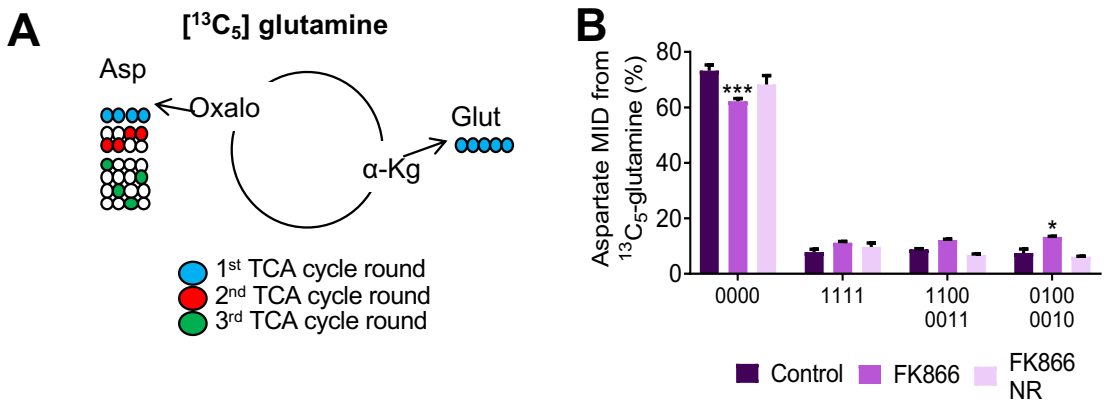


Figure 4.14. Glutamine Contribution to Aspartate Production

(A) Labelling patterns observed through $^{13}C_5$-glutamine tracing in C2C12 myotubes. **(B)** Aspartate MIDs from combined 2D-^{1}H,^{13}C-NMR ($^{13}C_5$-glutamine) and GCMS following treatment with FK866 (50 nM) for 48 hours and NR (0.5 mM) for 4 hours.

* p<0.05, *** p<0.005; One-way ANOVA performed on raw data, with individual pathways assessed independently; Dunnett's multiple comparison test, treatment compared to control. All data are the mean ±SEM, *n=3.*

4.3.5.2. Functional Use of Elevated Aspartate

We hypothesised that the elevated aspartate production may be an intended cellular response to low NAD$^+$ levels. A key role for aspartate within cells is for the synthesis of pyrimidine nucleotides [317], figure 4.15A. We employed LCMS to observe labelling patterns in uridine triphosphate (UTP) to understand if the carbon was passing through aspartate and ultimately being used for the production of nucleotides. There

was no change to UTP labelling detected, with data being constant across the groups, figure 4.15B.

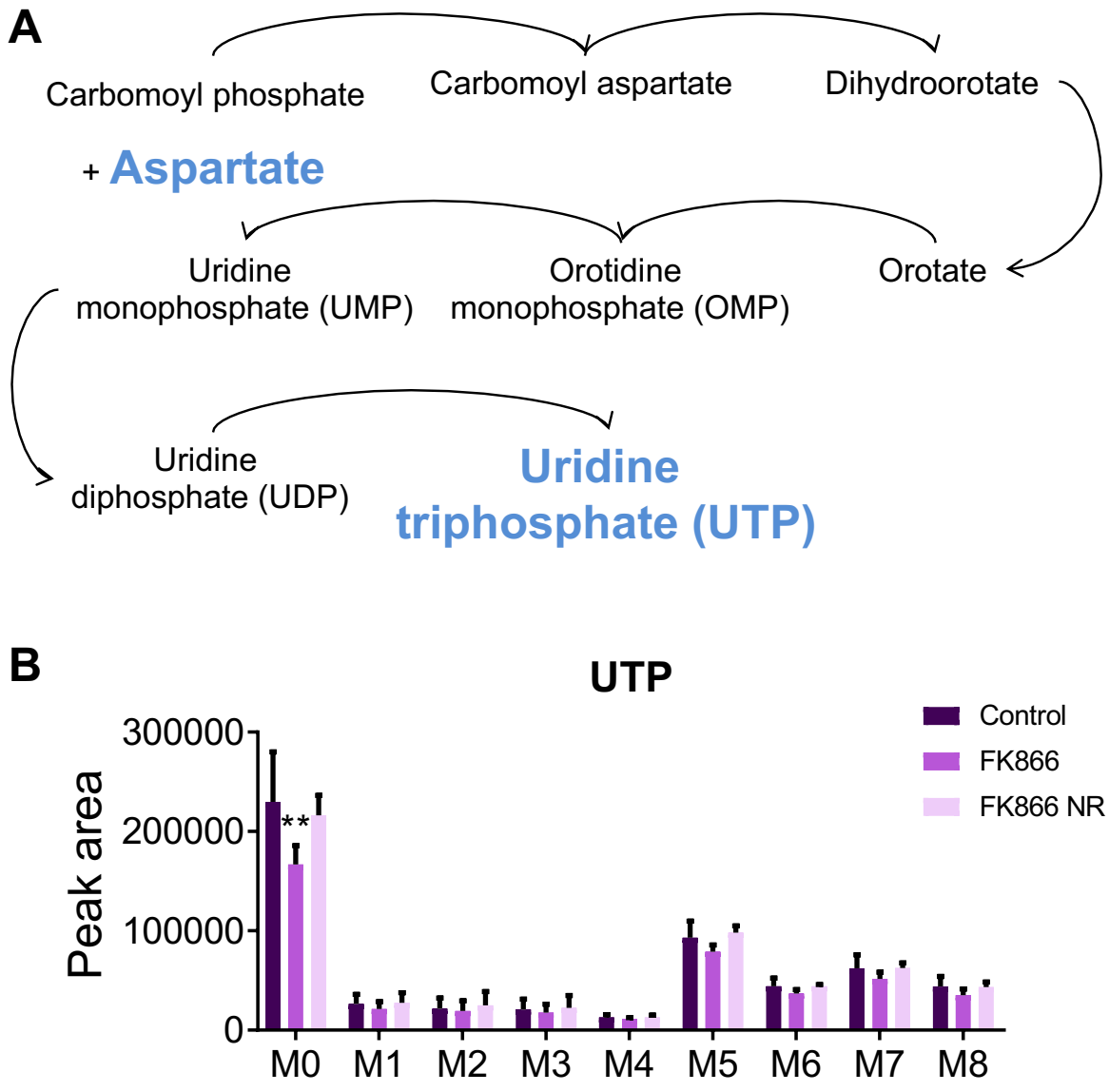


Figure 4.15. Aspartate Use for Nucleotide Synthesis

(A) The pathway for nucleotide synthesis using aspartate. **(B)** The label incorporation from $^{13}C_6$-glucose into UTP as shown through LCMS peak area analysis in response to 50 nM FK866 for 48 hours with and without 0.5 mM NR for 4 hours.

** p<0.01; Two-way ANOVA performed on raw data; Sidak's multiple comparisons test, significant changes between the treatments compared. All data are normalised to protein and are the mean ±SEM, *n=3*.

4.3.5.3. Elevated Aspartate a Cellular Adaptation to NAD+ Depletion

The increased lactate/pyruvate ratio seen with FK866 treatment in C2C12s, figure 4.3, is evidence of a perturbed cytosolic redox potential. The mitochondrial shuttle systems, such as the malate-aspartate shuttle (MAS), are critical in maintaining the redox potential of the cell and transferring electrons across the mitochondrial membrane. We therefore postulated that the functioning of the MAS may be impaired and as a result there was elevated aspartate and increased lactate/pyruvate ratio.

We tested this hypothesis using a MAS inhibitor, AOAA, in combination with [1,2-^{13}C] D-glucose. The lactate/pyruvate ratio was significantly increased in the presence of the inhibitor, figure 4.16A. However this effect appeared to be an NAD$^+$ independent response, as addition of NR did not return levels to control, figure 4.16A. The inhibitor reduced the levels of pyruvate entering the mitochondria and therefore the levels of some key TCA metabolites were decreased, figure 4.16B-C. Evidence of impaired pyruvate uptake into the mitochondria was shown through a significant reduction in the ^{13}C label incorporation into glutamate in the presence of the MAS inhibitor, figure 4.16D. Once again, this response was not affected by the presence of NR, suggesting it is NAD$^+$ independent.

As we postulated that our aspartate effects were a result of impaired MAS functioning we reasoned that the results might be replicated with the inhibitor. Aspartate levels remained constant in the presence of the MAS inhibitor with and without NR, figure 4.17A. Further investigation into the label incorporation into aspartate showed a significant reduction with the MAS inhibitor, figure 4.17B. This is in direct contrast to the results observed with FK866 where there was a significant increase in glucose derived aspartate labelling.

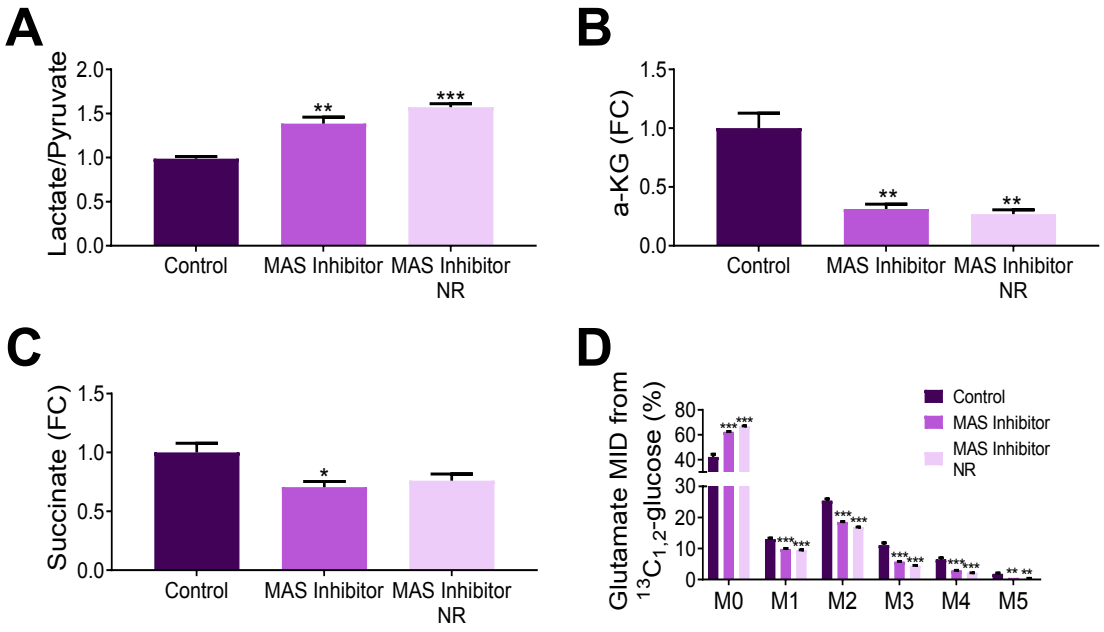


Figure 4.16. C2C12 Response to MAS Inhibitor Treatment

Differentiated C2C12s were treated with 0.5 mM AOAA (MAS Inhibitor) for 24 hours with or without 0.5 mM NR for 4 hours. **(A)** Lactate/Pyruvate ratio from GC-MS analysis using the m=2 portion of the MID. GCMS ion count fold changes compared to control for **(B)** a-KG, **(C)** succinate. **(D)** GCMS MID analysis of glutamate following metabolic tracing with $^{13}C_{1,2}$-glucose in response to MAS inhibitor with and without NR.

* p<0.05, ** p<0.01, ***p<0.005; One-way ANOVA performed on all data, with individual MIDs assessed independently; Dunnett's multiple comparison test, treatment compared to control. All data are normalised to protein and are the mean ±SEM, *n=3*.

As the NR treatment had no effect on the MAS inhibitor results we confirmed whether it had elevated intracellular tNAD. The MAS inhibitor did not affect tNAD levels but addition of NR was successful in raising tNAD significantly above control, figure 4.17C.

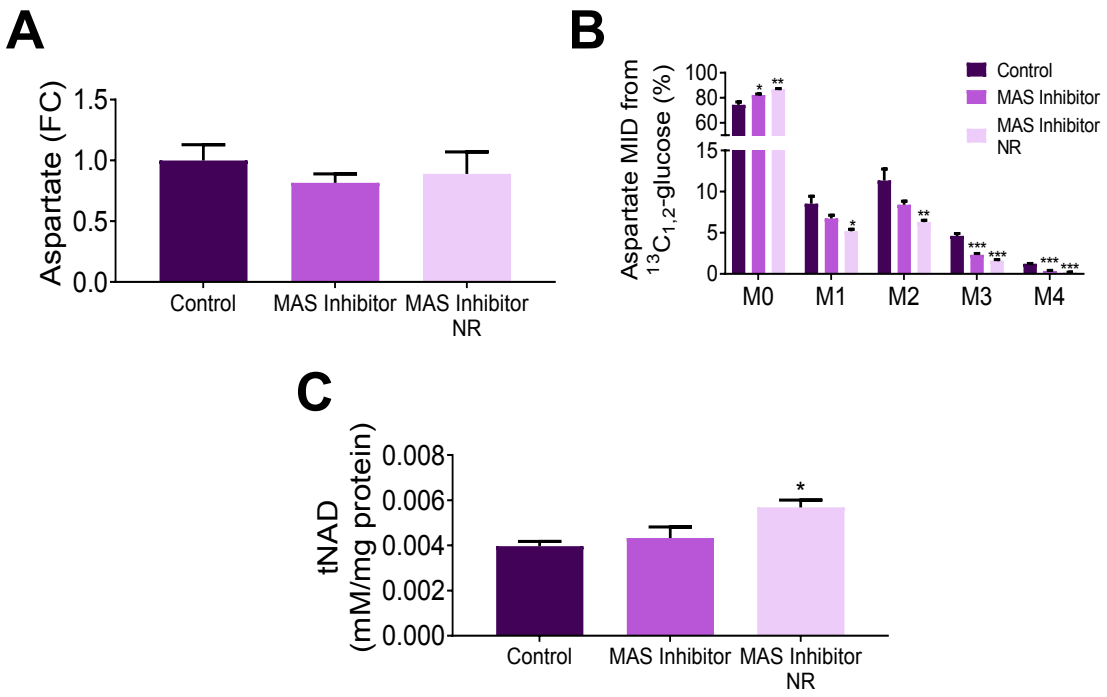


Figure 4.17. Aspartate Changes in Response to MAS Inhibitor Treatment

GCMS analysis of ion count fold change of **(A)** aspartate. **(B)** GCMS MID analysis of aspartate following metabolic tracing with $^{13}C_{1,2}$-glucose in response to MAS inhibitor with and without NR. 1D-^{1}H-NMR spectroscopy shows **(C) t**NAD concentration (mM/mg of protein). MAS – Malate aspartate shuttle.

* p<0.05, ** p<0.01, ***p<0.005; One-way ANOVA performed on all data, with individual MIDs assessed independently; Dunnett's multiple comparison test, treatment compared to control. All data are normalised to protein and are the mean ±SEM, *n=3.*

4.3.6. Primary Myotubes Express an Exaggerated Phenotype

As referred to previously the primary myotubes appeared to express an exaggerated phenotype compared to the C2C12s. For clarity of the message GC-MS analysis was used and condensed into two groups, unlabelled or labelled portion of the metabolite. The label incorporation into citrate showed no significant changes with the treatments in either C2C12 or primary myotubes, figure 4.18A-B.

However, analysis of α-KG showed a significant increase in label incorporation in response to FK866 treatment but this was only evident in the primary myotubes and not the C2C12s, figure 4.18C-D. This result was also observed in fumarate, figure 4.18E-F, and malate, figure 4.18G-H. The increased labelling was matched with a

concurrent decrease in the unlabelled portion of the metabolite. The effects of FK866 were once again reversed with the addition of NR for 4 hours.

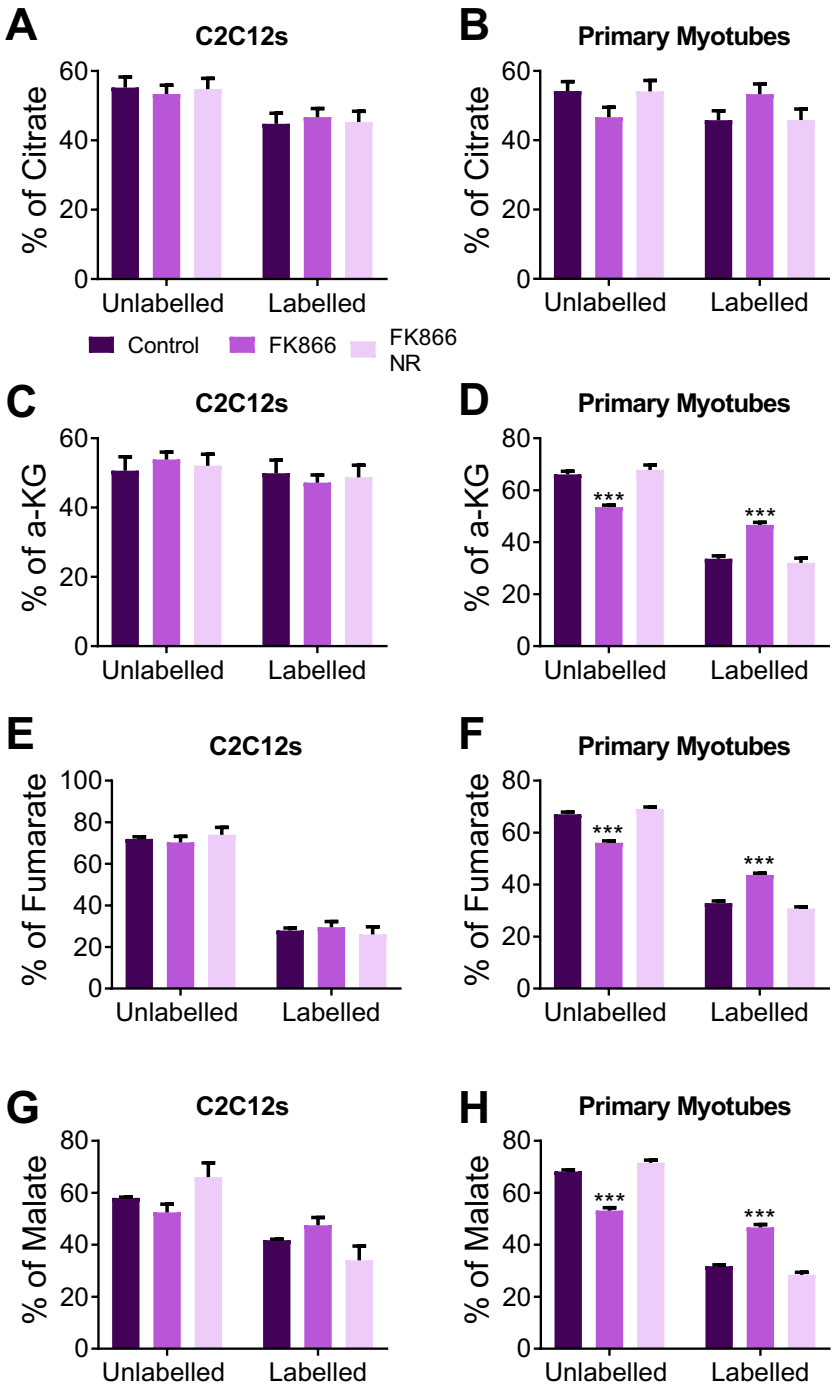


Figure 4.18. Primary Myotubes Show Elevated Label Incorporation into TCA Cycle Metabolites with NAD+ Depletion

Cells were treated with $^{13}C_{1,2}$-glucose and GCMS data analysis was condensed into two pools of unlabelled and labelled metabolite. Percentages of label incorporation into **(A-B)** citrate, **(C-D)** α-ketoglutarate, **(E-F)** fumarate, **(G-H)** malate in C2C12s and primary myotubes.

***p<0.005; Two-way ANOVA performed on data; Sidak's multiple comparisons test, significant changes between unlabelled and labelled compared. All data are the mean ±SEM, *n=4.*

Further work conducted showed no change to glutamate levels in any treatment group in either C2C12 or primary cell models, figure 4.19A. The C2C12s also showed no change to pathway usage in response to differing NAD^+ levels, figure 4.19B. However, the primary myotubes showed a significant increase in the use of glycolysis and also increased rounds of the TCA cycle in response to FK866 treatment, figure 4.19C. The addition of NR to the primary myotubes significantly reduced glutamate production through glycolytic activity and resulted in a significant increase in unlabelled glutamate, figure 4.19C. Glutamine levels were constant in the C2C12s but elevated in FK866 treated primary myotubes. All changes were normalised with addition of NR, figure 4.19D-E.

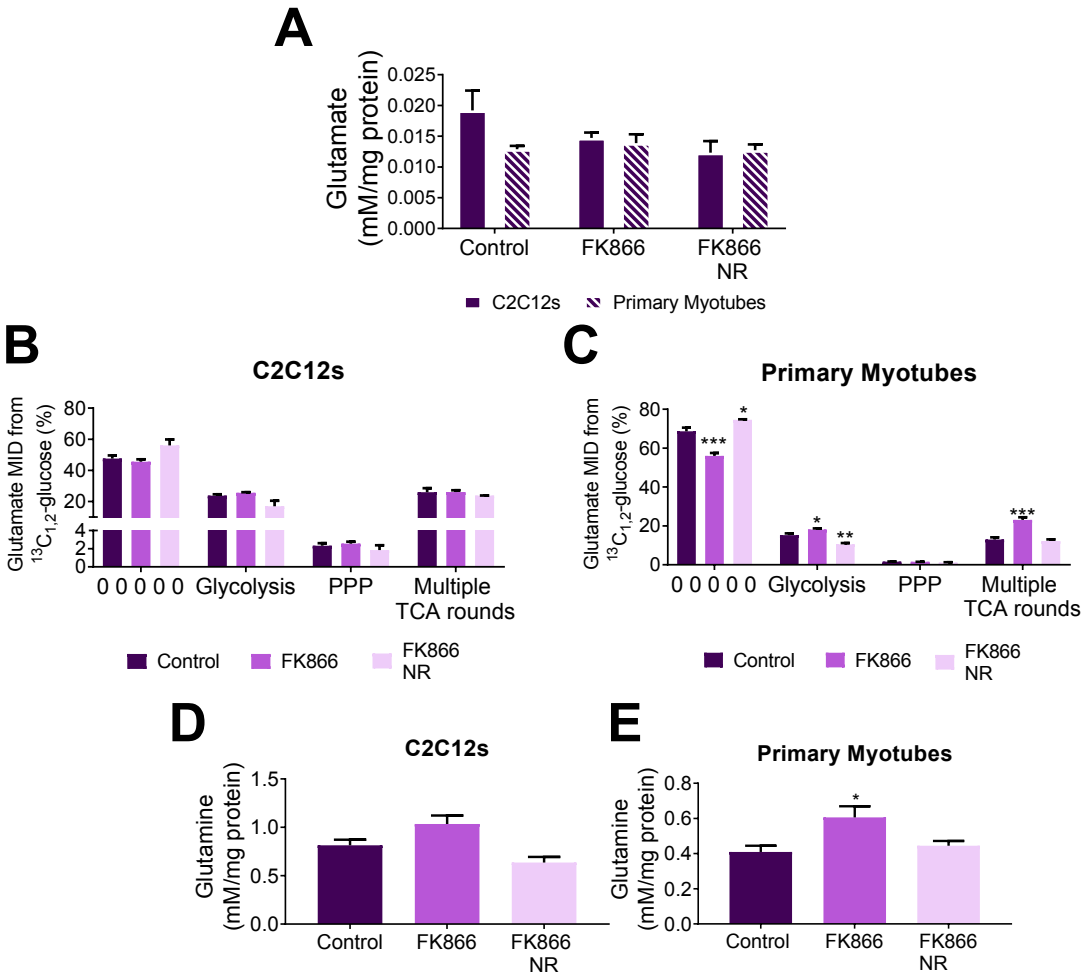


Figure 4.19. Primary Myotubes show Increased Glutamate Labelling

(A) Glutamate concentrations shown through 1D-^{1}H-NMR spectroscopy. Pathway utilisation for glutamate production following $^{13}C_{1,2}$-glucose tracing and combined 2D-^{1}H,^{13}C-NMR spectroscopy in both **(B)** C2C12s and **(C)** primary myotubes. **(D-E)** Glutamine concentrations from 1D-^{1}H-NMR spectroscopy.

Glycolysis 00011; *PPP 00010*; *Multiple TCA rounds* 11000, 01000, 00100, 11011, 11100, 11110, 00111, 11111.

* p<0.05, ** p<0.01, ***p<0.005; One-way ANOVA performed on raw data, with individual pathways assessed independently; Dunnett's multiple comparison test, treatment compared to control. All data are normalised to protein and are the mean ±SEM, *n=4.*

The key differences between how C2C12s and primary myotubes respond to NAD^{+} depletion through FK866 treatment is outlined in figure 4.20. The green boxes represent elevated ^{13}C incorporation into the metabolite above control levels. C2C12s only exhibit the response in aspartate labelling, however primary myotubes have numerous other metabolites showing elevated labelling.

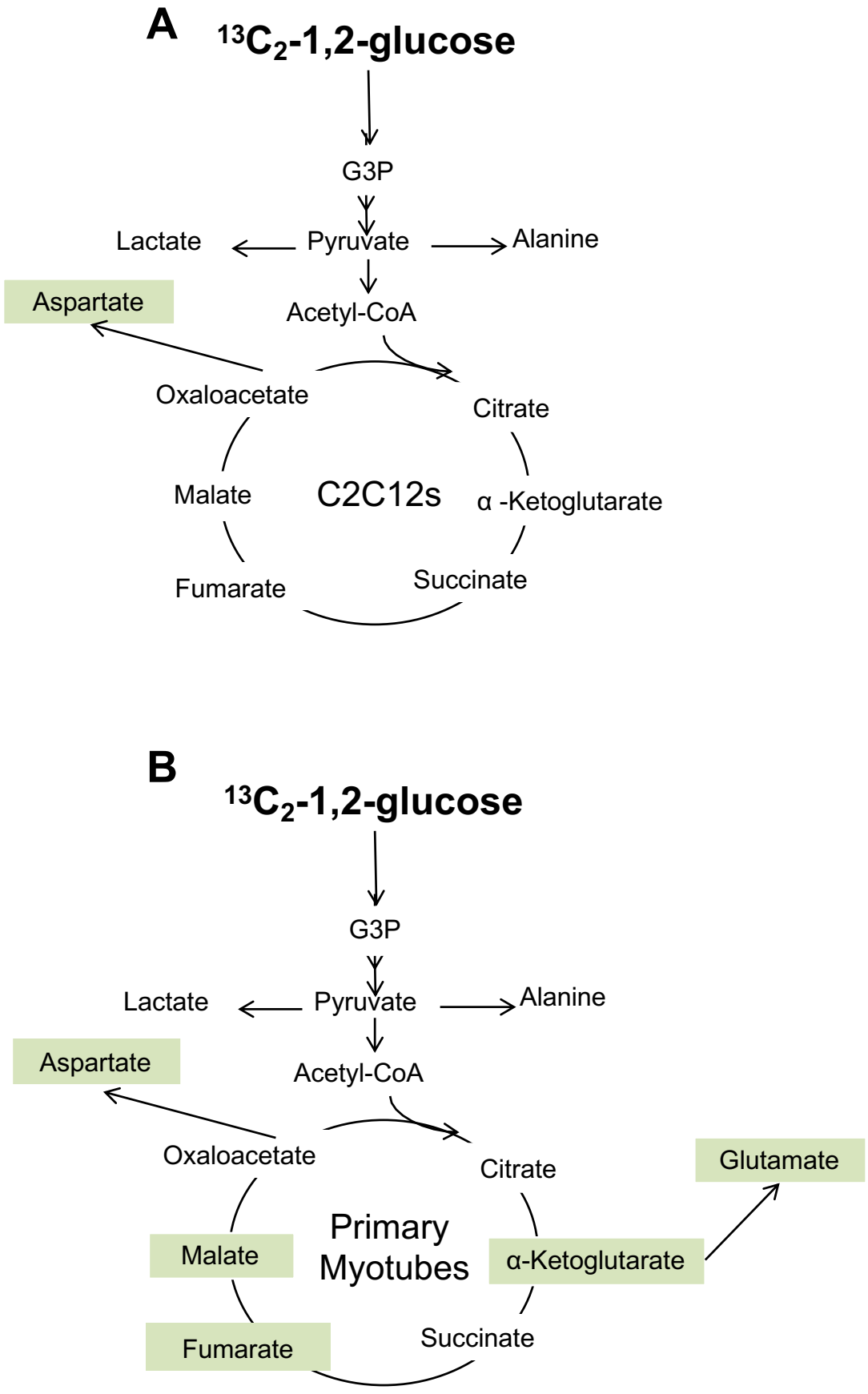


Figure 4.20. Primary Myotubes have an Exaggerated Phenotype

Graphical representation of significant differences in label incorporation following $^{13}C_{1,2}$-glucose tracing. An increase in labelling shown by green boxes in **(A)** C2C12s and **(B)** primary myotubes.

4.3.7. Muscle Specific NAMPT KO Mouse Model

To investigate whether the phenotype observed in our cell culture systems existed *in vivo* a muscle specific NAMPT KO model was used. Intravenous infusion of $^{13}C_6$-glucose was administered to mice and their quadriceps muscle used for analysis. The hypothesis for the experiment was that the NAMPT KO would induce the same results with the metabolic tracing as we observed with FK866.

Initially metabolite levels were investigated using 1D-^{1}H-NMR spectroscopy. As expected, tNAD levels were significantly reduced, as were NAM levels in the knockout mice compared to wild-type controls, figure 4.21A-B. A number of other metabolites were detected and showed no difference between the two groups, figure 4.21C-J.

GC-MS analysis was also employed to once again look at relative changes to metabolite levels between the two groups. Whilst most metabolites showed no change with the NAMPT KO there was a trend upwards observed with G3P, figure 4.22A. This reflected the cell culture results and suggested that the NAMPT KO was causing a block at GAPDH. However, downstream metabolite levels did not support this. A significant increase in fumarate, figure 4.22F, and malate, figure 4.22H, was observed with the KO model, which is in direct contrast with the reported changes with FK866 in the cell culture models. Further to this, the aspartate levels showed no change with the NAMPT knockout, figure 4.21J and figure 4.22I. This suggests that the phenotype was not expressed in this mouse model.

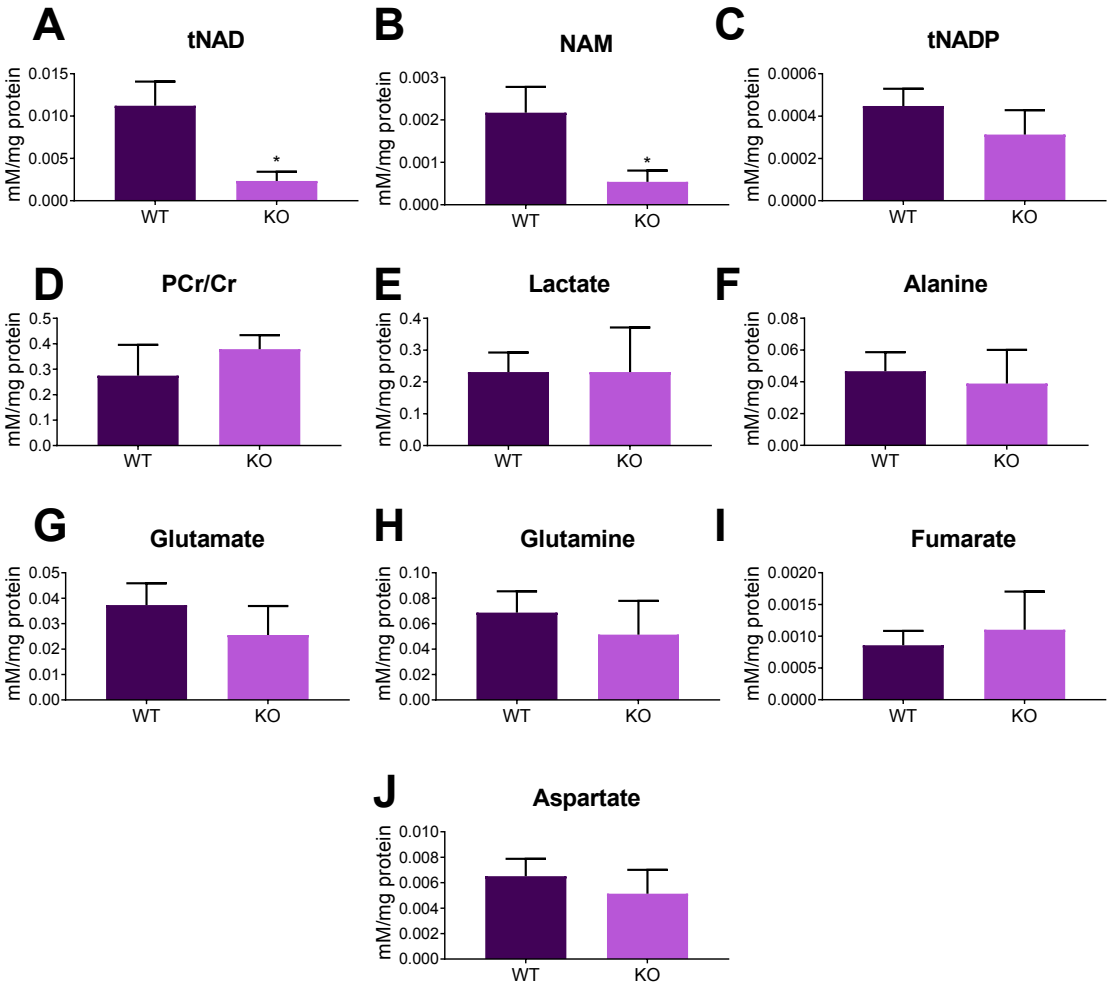


Figure 4.21. 1D-^{1}H-NMR Spectroscopy Analysis of Quadriceps Muscle from NAMPT KO Model

1D-^{1}H-NMR spectroscopy was conducted on quadriceps muscle from a muscle-specific NAMPT KO mouse model and wild-type controls. **(A)** **t**NAD, **(B)** NAM, **(C)** **t**NADP, **(D)** PCr/Cr, **(E)** Lactate, **(F)** Alanine, **(G)** Glutamate, **(H)** Glutamine, **(I)** Fumarate and **(J)** Aspartate.

* $p<0.05$, Unpaired, two-tailed t-tests performed on all data. All data are the mean ±SEM, *n*=7.

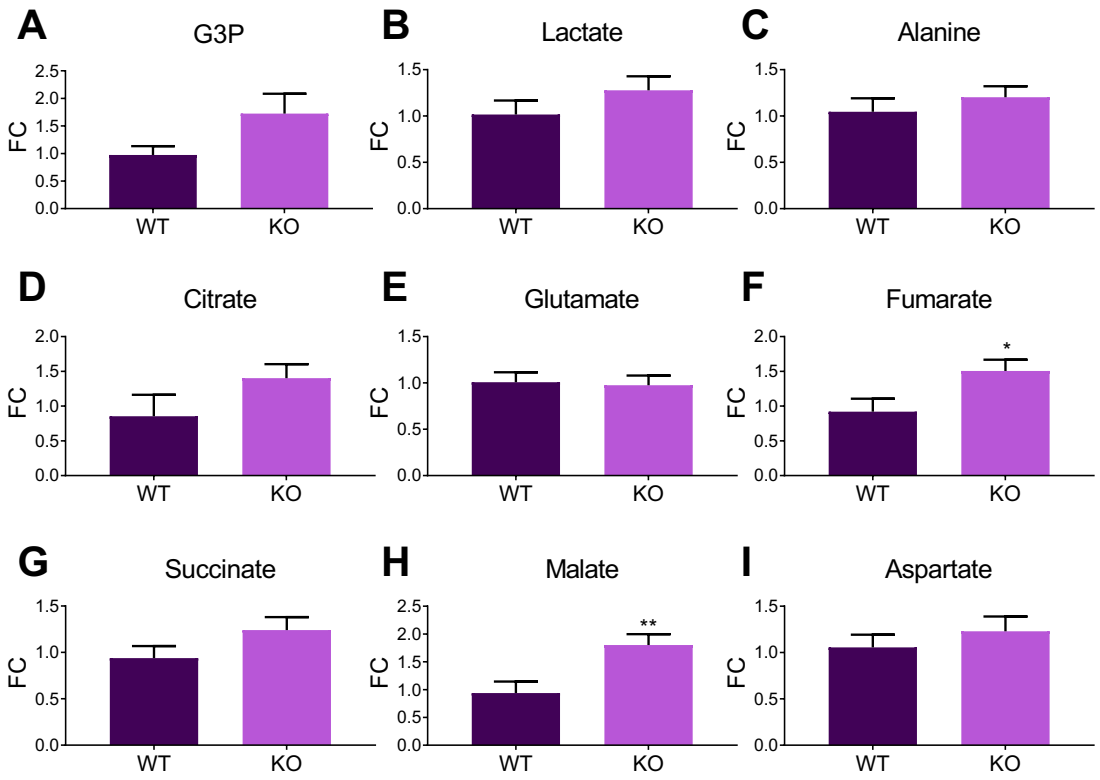


Figure 4.22. GCMS Ion Count Analysis of Quadriceps Muscle from NAMPT KO Model
GCMS ion count analysis was conducted on quadriceps muscle from a muscle-specific NAMPT KO mouse model, with data shown as fold-change compared to wild-type controls. **(A)** G3P, **(B)** Lactate, **(C)** Alanine, **(D)** Citrate, **(E)** Glutamate, **(F)** Fumarate, **(G)** Succinate, **(H)** Malate and **(I)** Aspartate. * $p<0.05$, ** $p<0.01$; Unpaired, two-tailed t-tests performed on raw data. All data are the mean fold-changes ±SEM, *n*=7.

2D-^{1}H,^{13}C-NMR spectroscopy was also utilised however no label incorporation was detected in any of the samples. This indicates an issue with the experimental set up and suggests further optimisation is required to introduce the required level of tracer for incorporation into skeletal muscle metabolism.

4.4. Discussion

The NAMPT salvage pathway is confirmed as the primary route to NAD^+ production in both C2C12 and primary myotubes as FK866 treatment significantly depleted intracellular tNAD, showing a reduction in NAD^+ and NADH [199,263]. A short incubation of NR was able to replete the tNAD levels. This confirms previous work highlighting the NRK pathway as an alternative route for NAD^+ augmentation in skeletal muscle when supplemented with NR [199].

NAM levels are carefully balanced through production as a result of NAD^+ breakdown and consumption through NAD^+ synthesis. FK866 induced NAD^+ depletion had no effect on NAM levels suggesting that the ratio between NAD^+ production and consumption was maintained despite treatment. However, the addition of NR and elevation of NAD^+ above control levels induced a significant increase in NAM. This was not reflected in the NAM clearance pathway with MeNAM levels consistent across the treatment groups. The initial repletion of NAD^+ to basal levels may provide an explanation as to why the build-up of NAM was not cleared in the time shown.

The basal levels of MeNAM were nearly 10x higher in the primary myotubes compared to C2C12s. This was surprising given the relative consistency with the other metabolite levels. The elevated basal MeNAM levels may be the result of increased NNMT activity. C2C12 myotubes showed a 1:5 NAM to MeNAM ratio with primary myotubes showing a 1:1, suggestive of increased NAM turnover. NNMT has shown to be increased in response to oxidative stress in liver tissue [318], which may suggest that primary myotubes are more oxidative compared to C2C12s. Whilst the two cell culture systems responded in the same way to the FK866 and NR treatments

this highlighted that there are differences within the models. This lack of consistency between cell lines and primary cell models has been discussed in the literature [291].

The decreased PCr/Cr ratio suggests inefficient functioning of the ETC. This is to be expected, as NAD^+ is a key cofactor for dehydrogenase enzymes within the TCA cycle, with NADH produced as a result. NADH is then used as a proton donor for the ETC; therefore depletion of NAD^+ will impact oxidative phosphorylation, as previously shown [215,319]. The low PCr/Cr ratio is evidence of the cells employing a buffering system to try and maintain ATP levels in response to low NAD^+ [42–44].

This is further confirmed by the increase in the lactate/pyruvate ratio seen with FK866 in C2C12 myotubes. As pyruvate produces only one peak, which is situated in a 'busy' area of a 1D-^{1}H-NMR spectrum, quantification is not accurate. Therefore, the lactate/pyruvate ratio is generated from the m+2 portion of the MIDs derived from GCMS analysis. This method did not therefore take into account abundance differences as a result of the different treatments but focused on changes to pyruvate metabolism. An increased lactate/pyruvate ratio, as seen in the FK866 samples, suggests dominance of the reduced form of the oxido-reduction coenzymes [320]. The reduction of pyruvate is NAD^+ generating showing the cell's attempt to restore levels despite FK866 treatment [52].

FK866 treatment did not lower maximal respiration in our C2C12s. This was surprising as Frederick *et al*. had reported low oxygen consumption with NAD^+ depletion [215]. However, this study had isolated mitochondria from C2C12s and was therefore not comparable with our work on intact myotubes. The presence of a protected mitochondrial NAD^+ pool is debated. One study using a stably transfected

HEK cell line with a PARP construct designed to detect mitochondrial NAD^+ showed high sensitivity of the organelle to FK866 treatment [170]. Further work has disputed this with a study using mitochondria isolated from cells following FK866 treatment to show a conserved NAD^+ pool with ATP production capability [264]. Another study has shown mitochondrial NAD^+ to be depleted at a slower rate compared to the cytosol and nucleus, again suggestive of a protected mitochondrial pool [213]. The conflicting reports are evidence of the difficulty in accurately quantifying subcellular NAD^+ levels. Our data appears to support the latter, with the 5 % tNAD remaining in the cells possibly residing in the mitochondria to support oxidative phosphorylation.

As fatty acids are the primary source of fuel for skeletal muscles at rest we sought to investigate the impact of FK866 on this NAD^+-dependant pathway [41]. Whilst we hypothesised that there would be a reduction as a result of NAD^+ depletion we were unable to show this experimentally. The initial method employed to observe fatty acid oxidation was through the use of an isotopic sodium palmitate tracer. This yielded no label incorporation into any of the metabolites observed. For this to have occurred the cells were either not using fatty acid oxidation for their energy metabolism or were using an alternative fatty acid source. Alternatively the tracer may not have entered the cell, however the conjugation of the tracer with BSA should have aided diffusion through the phospholipid bilayer [321]. To minimise the chance of other fatty acids being utilised free fatty acid free BSA was used with all serum removed for the final 24 hours of the protocol. Following the negative data we postulated that the presence of glucose within the culture medium negated the need for the cells to undergo fatty acid oxidation. A study has shown that C2C12 fatty acid oxidation only occurs in fasting states when conservation of glucose is essential [322]. We therefore

followed an alternative β-oxidation protocol and added conversion to a low-glucose medium for the final 24 hours, to try and stimulate fatty acid use. This method measured the levels of radiolabelled CO_2 given off from cells and was able to detect fatty acid use. However, there was no change across the different treatment groups. The lack of an effect with FK866 treatment on fatty acid oxidation suggests that the cells are preferentially using glucose or an alternative fuel source for their energy metabolism. Fatty acid oxidation has shown to be decreased in aging mouse models [323]. Expression of fatty acid genes were decreased in aged skeletal muscle tissue with blood metabolomics showing a marked reduction in fatty acid oxidation intermediates [323]. Primary myotubes showed increased ^{13}C labelling into TCA cycle metabolites in response to FK866 treatment, suggesting a more oxidative phenotype. Given that these cells are more oxidative and fatty acid oxidation is implicated in mitochondrial metabolism FK866 treatment may have had a greater impact on fatty acid oxidation in the primary myotubes compared to the C2C12s.

We next sought to study glucose metabolism, as it has been shown that C2C12 metabolism is affected by glucose concentrations [324]. We postulated based on previous work that the FK866 treatment and resultant tNAD depletion would inhibit the functioning of GAPDH [180,263]. We therefore expected a significant impact on the read outs of glycolysis, lactate and alanine. Our results showed no change across the treatment groups in either concentration of metabolite or pathway utilisation through PPP or glycolysis. Whilst the basal levels of alanine were different between C2C12 and primary myotubes neither cell model showed any impact of FK866 treatment. Previous work in cancer cells has shown a decrease in lactate levels in response to FK866 [263], however work conducted in C2C12 myotubes showed no

significant difference [215]. The PPP has two branches, oxidative which is $NADP^+$ dependant and non-oxidative. It is the non-oxidative branch that has been shown to increase with FK866 treatment, however as there is no loss of carbon in this pathway the labelling pattern is the same as for glycolysis [215,263]. Therefore, we are unable to tell using this method whether an increase in the non-oxidative PPP is compensating for a decrease in glycolysis. This could potentially present as no overall change in label incorporation into lactate and alanine despite alternative pathways being used.

GC-MS is able to detect metabolites with much lower abundance than NMR spectroscopy therefore we used relative quantification to observe fold changes of key metabolites. Here we confirmed that FK866 was inducing an NAD^+ dependant attenuation of GAPDH, through elevation of metabolites preceding the enzyme. Further to this we saw significant reductions in TCA cycle metabolites in a time-dependant manner with FK866 treatment in C2C12s. Previous studies have shown the build-up of upper glycolytic metabolites resulting in an overflow of carbon into PPP to confirm reverse glycolytic flux as a result of low NAD^+ [263]. As our method was unable to detect this we instead observed the labelling patterns of fructose-6-phosphate and fructose-1,6-bisphosphate, which were above the suggested block at GAPDH. There was a clear increase in label incorporation of both metabolites, which showed both a slowing down of the pathway and reverse aldolase activity, confirming the suspected reverse glycolytic flux. As a reversal of glycolysis is also known as glycogenesis we postulated that FK866 might increase intracellular glycogen levels, however this wasn't shown experimentally.

An observation during analysis led to further investigation of aspartate in FK866 treated cells. Aspartate was selected as a read out of TCA cycle activity as

oxaloacetate was typically too low to measure. However, it led to an unexpected finding of increased glucose-derived aspartate production in response to tNAD depletion. The elevated use of glucose for aspartate production with FK866 treatment appeared contradictory to the other data showing lower abundance of TCA cycle metabolites. However, a recent study has shown elevated use of glucose and increased glycolysis with a NAMPT knock-down in C2C12 myotubes [326].This highlights the delicate interaction between NAD^+ levels and energy metabolism within skeletal muscle cells.

One of the main uses of aspartate within cells is for nucleotide synthesis, where it is responsible for donating 3 of the 4 carbon atoms to pyrimidine bases [317]. We investigated this through observation of UTP labelling but found no differences in response to NAD^+ depletion. On reflection this may have been expected given that the cells were in a state of stress with limited NAD^+. They were non-proliferative and therefore it was unlikely that they would synthesise nucleotides, which is energetically expensive [327]. Alternatively, aspartate is a key component in the purine nucleotide cycle, which has been reported in skeletal muscle myocytes in response to low ATP [328]. This cycle is responsible for the control of intracellular adenine nucleotide levels through ammonia and fumarate production. This could provide an alternative functional use for the aspartate build up observed in our NAD^+ deplete cells.

Previous work conducted using a malate-aspartate shuttle inhibitor in vascular smooth muscle yielded similar results to our FK866 treatment. Reduced malate and α-KG, increased aspartate, elevated lactate/pyruvate ratio and reduced PCr [329]. This prompted us to utilise the inhibitor in C2C12 myotubes. Whilst we were able to

replicate many of the findings, the inhibitor did not have the same effect on raising aspartate levels in the myotubes and acted to prevent glucose use for aspartate production. A key limitation of the experiment may be the mechanism of action of the inhibitor; it indirectly inhibits the shuttle functioning by acting on cytosolic aspartate aminotransferase [330]. This therefore does not confirm whether a different aspect of the shuttle may be impaired in our model, but does show that the results are not caused by compromised aspartate aminotransferase activity. We also postulated that α-KG levels, which were shown to be decreased with FK866, may limit the shuttle. However, as mitochondrial α-KG is required for aspartate production there must be sufficient levels to fuel the shuttle [331].

Elevated aspartate levels have also been reported in cells treated with FCCP, a strong mitochondrial uncoupler responsible for increasing the permeability of the mitochondrial membrane to protons [332]. This supports the notion that the FK866 effects are a result of perturbed cytosolic redox. The raised GAP and G3P levels observed with NAMPT inhibition may not only show inhibition of GAPDH but could indicate perturbed glycerol-3-phosphate/dihydroxyacetone phosphate shuttle functioning [333]. This shuttle is responsible for regeneration of NAD^+ from NADH. The NADH is generated from glycolysis at the GAPDH step and therefore if this is impacted by NAMPT inhibition it may affect the shuttle. This is also true of the malate/aspartate shuttle, if no cytosolic NADH is generated it could halt the shuttle and lead to elevated metabolite levels [334]. This would occur at the malate dehydrogenase step of the shuttle, which could not be explored through the MAS inhibitor work.

Aspartate has also been shown to initiate an NAD^+ biosynthetic pathway in bacteria [335], and plants [336,337]. Aspartate is converted to quinolinic acid (QA) using the enzymes L-aspartate oxidase (AO) and quinolinate synthase (QS), where it then follows the same pathway as in animals to produce NAD^+ from QA [168]. Whilst under normal conditions animals utilise tryptophan to produce QA the cell may react to the severe NAD^+ depletion through this alternative pathway. To further support this, G3P is used during the production of quinolinic acid from aspartate, which we have shown is significantly elevated in our NAD^+ deplete cells [335]. Animals do not express the genes required to produce QA from aspartate and so this could represent a dead-end pathway [202].

Independent of the mechanism driving aspartate elevation it is evident that there is cellular adaptation to low NAD^+ levels. Aspartate has recently been identified as a limiting metabolite for cancer cell proliferation [338]. As FK866 and other NAMPT inhibitors are showing promise as cancer therapeutics it may be important to understand their impact on aspartate levels and understand whether this could affect the efficacy or safety of FK866 as a treatment [339,340].

Our work highlighted some key differences between our models in their response to FK866. We postulate that these findings are a result of altered metabolic capacity between an immortalised cell line, such as C2C12s, and primary myotubes [324]. Our data suggests that C2C12s are more glycolytic shown by the raised lactate levels compared to primary myotubes. In support of this primary myotubes show an increased oxidative capacity through the elevated label incorporation into TCA metabolites shown with NAD^+ depletion. Despite the fundamental differences

between the two models they both expressed the same phenotype. This suggests that aspartate production is a key skeletal muscle adaptation to low NAD^+.

We attempted to explore this phenotype *in vivo* through ^{13}C-glucose infusion in a muscle-specific NAMPT knockout mouse model. Whilst we were able to confirm a significant reduction in both NAD^+ and NAM in the quadriceps muscle we were not able to detect an increase in aspartate. This may have been the result of aspartate clearance into the blood or directed to other tissues. However, the presence of a build-up within our culture system shows that the muscle cells did not expel the aspartate into the media. This suggests that perhaps the NAD^+ depletion *in vivo* did not lead to elevated aspartate, as there was only an 80 % reduction as opposed to 95 % in our model.

Unfortunately the ^{13}C was not incorporated into any metabolites, meaning pathway analysis could not be conducted. The initial concern was that the levels of tracer infused may have been too low. However, calculation of the end physiological blood concentration of tracer in the mice, using a body weight of 25 g as an example, showed levels in the normal range. The bolus injection caused a blood glucose concentration of 4 μM of glucose, compared to published reference values in mice this was low [341]. The steady state infusion concentration was 2 μM, which was again low and could be the reason the experiment was unsuccessful in triggering glucose uptake into the muscle. The lack of label incorporation may have been due to the membranes being relatively impermeable to the circulating glucose, with a 'pool' of GLUT4 only translocating following exercise [342]. Alternatively, a study has previously calculated that more than half of infused glucose was stored as glycogen in muscle

and liver tissue [343,344]. This suggests that the ^{13}C-glucose may have entered the cell but been converted straight into glycogen.

In summary, we discovered a novel adaptation to low NAD^+ in skeletal muscle that was almost entirely reversed with an acute dose of NR. The methodology and analysis used was complex and allowed us to explore pathway specific adaptations. Ultimately unveiling increased glucose-derived aspartate, produced by elevated glycolysis and TCA cycle activity.

In the wider context, this work acts as an extreme model of NAD^+ decline, with no current disease conditions representing the NAD^+ loss shown in this work. The model allows us to observe how skeletal muscle cells respond to reduced NAD^+ levels, which are observed in some chronic disease states [312,313]. The protection of mitochondrial metabolism and impact on redox shuttles are interesting and may prompt further research to understand the importance of these in disease. Further to this, these aspects may be areas of exploitation in cancer biology to trigger cell death and reduce tumour growth alongside immunological diseases. Importantly, this work shows how NR supplementation can reverse many of the changes shown through NAD^+ depletion. This is promising in the field as it suggests that if a disease pathophysiology is being driven by low NAD^+, supplementation could be a viable treatment strategy.

5. Consequence of Elevated NRK Pathway Activity for Primary Muscle Cell Function

5.1. Introduction

NAD^+ biosynthesis occurs via *de novo* synthesis, the Preiss-Handler pathway, NAM recycling and NR metabolism [119]. The main route to NAD^+ production in the body is through NAM recycling evidenced by global NAMPT knockout being lethal in mice [171,174]. NRK2 is an enzyme in the NAD^+ biosynthetic pathway and is responsible for metabolising NR to NAD^+.

Protein expression showed NRK2 is specifically expressed in skeletal muscle, and therefore suggests that NR metabolism is a route to skeletal muscle NAD^+ generation [199]. Knock-out studies have shown the redundancy of NRK1 and NRK2 for basal skeletal muscle NAD^+ generation [199]. With NAM recycling proving to be the main route to NAD^+ production within the skeletal muscle evidenced by an 85 % reduction in muscle NAD^+ availability in response to depletion of NAMPT [215].

Whilst the enzyme appears to be redundant for basal NAD^+ generation it is highly regulated by injury. A mouse model of lower limb muscle injury showed a significant increase in the Nmrk2 gene after 24 hours [345]. Further to this, a severe muscle myopathy model showed highly dysregulated Nmrk2 expression [346]. This elevation of Nmrk2 has been detected in other muscle injury models of cardiomyopathy [347,348]. These findings have led to the postulation that NRK2 expression is induced in response to injury to aid in NAD^+ biosynthesis. This hypothesis is supported by NR supplementation having a cardio protective effect in mouse models, through maintenance of NAD^+ levels in the heart [348].

Reduced skeletal muscle NAD^+ and lowered oxidative capacity have been observed in aging studies [3–5]. A decline in NAD^+ has also been reported in the skeletal muscle

of HFD fed mice [6]. Given the expression of NRK enzymes within skeletal muscle NR as a therapeutic has gained traction in the field.

NR has been shown to be pharmacologically effective, with a recent study showing NR can safely elevate NAD(H) metabolism in human blood [254]. Treatment with NR in a mouse model of Alzheimer's shows cognitive improvements with a marked increase in NAD^+ levels which promotes PGC-1α, resulting in increased β-secretase degradation [255]. Another study has also shown the beneficial effects of NR feeding with increased endurance performance in mice. Histological studies showed a higher level of succinate dehydrogenase staining in NR treated gastrocnemius muscle vs. non treated equivalents, suggesting a higher oxidative capacity as a result of supplementation [256]. In addition to this there was evidence of NR having a protective effect against HFD induced obesity and insulin resistance, as shown by a significant reduction in fat mass in response to NR as well as a significantly lowered blood insulin level [201]. NAD^+ repletion through NR supplementation shows great improvements in muscle stem cell function, with NR preventing muscle stem cell senescence and enhancing muscle function [257].

An NRK2 knock-out mouse model showed no overt phenotype, with normal development and only modest gene expression differences [199]. However, given the strong regulation of this gene in response to injury models it was of interest to investigate the effect of NRK2 overexpression through development.

An NRK2 overexpressing mouse model (NRK2 Tg) was developed as part of another PhD project within the Molecular Metabolism Research Group at the University of Birmingham. This chapter aims to characterise the consequence of elevated NRK

activity and increased capacity of NR metabolism to NAD^+. The model will be used to assess the wider NAD^+ roles with investigation of structure, development and metabolism.

5.2. Materials and Methods

All products ordered from Sigma-Aldrich, UK, unless otherwise stated.

5.2.1. Cell Culture Treatments

5.2.1.1. Cell Culture Models

The primary cell culture protocol is described in detail in *Section 2.1.2.*

5.2.1.2. Cell Plating

Primary myoblasts were divided equally between 6-well cell culture plates and left in plating media for 72 hours, followed by primary proliferation media for 24 hours and finally primary differentiation media for 6 days, with media changes every other day.

Differences between wild type, NRK2 over expresser (NRK2 Tg) and NRK2 knockout (NRK2 KO) myotubes were compared. The mouse model was developed by Dave Cartwright with collections and primary culture conducted by myself. Some experiments used 50 nM FK866 for 48 hours, 0.5 mM NR (Chromadex) for 24 hours or co-treatment of FK866 and NR.

5.2.2. RNA Analysis

Gene expression data was analysed using qPCR, a detailed outline can be found in *Section 2.3.4*. Briefly, 1 µl of cDNA from each sample was used with 5 µl of master mix, 3.75 µl of NFW and 0.25 µl of the gene probe of interest. Gene probes used were Nmrk1, Nmrk2, NAMPT, PGC1α, SIRT1, Myf5, MyoD, Acrv2, IGF2, Cox7a1

and Col1a1, details of which can be found in Appendix A. All genes were referenced to 18s as the housekeeping gene.

5.2.3. NAD$^+$ Cycling Assay

Once cells were fully differentiated they were treated with 0.5 mM NR for 24 hours. The NAD$^+$ cycling assay was then carried out according to the instructions, which are outlined in detail in *Section 2.10.* Briefly, the cells were washed with PBS and extraction buffer was added. Following two rounds of freeze-thawing the cells were centrifuged at 13000 rpm at 4 °C for 5 minutes and the supernatant collected for total NAD measurements. 200 ul of this was heated for NADH measurements. An enzyme was added to a cycling buffer, which resulted in all NAD$^+$ within the samples being reduced to NADH. A colorimetric probe was used to visualise and quantify the NADH within the samples.

5.2.4. Extraction of Polar Metabolites for GCMS Analysis

All extractions were carried out according to *Section 2.6.6.1.* Briefly, media was aspirated and cells were washed with ice-cold 0.9 % saline solution. Plates were placed on dry ice to quench metabolism and 500 µl pre-chilled HPLC-grade methanol was added with 0.5 µg of D6-glutaric acid. The cells were scraped and transferred to a falcon tube where 500 µl of pre-chilled HPLC-grade chloroform was added. The tube was rocked at 4 °C for 10 minutes before 500 µl of pre-chilled HPLC-grade H_2O was added and left to rest on ice for 10 minutes. Centrifugation of the samples at 4 °C, 14,200 rpm for 15 minutes allowed separation of the polar and non-polar fractions. 500 µl of the polar fraction was removed for GC-MS. The sample was evaporated to dryness using a SpeedVac at 30 °C for 4–5 hours and stored at -80 °C

until further analysis. Protein pellet weights were used for normalisation during analysis.

5.2.5. GCMS Data Acquisition

Detailed explanations of GCMS data acquisition can be found in *Section 2.7*.

5.2.6. Protein Analysis

Western blot analysis was conducted on wild type and NRK2 Tg primary myotube protein lysates made in RIPA buffer with protease inhibitor. Proteins were loaded into a 10 % acrylamide gel run at 100 V. The proteins were transferred to a membrane and blocked with 5 % BSA for 1 hour; NRK2 and α tubulin antibody was added as the primary and left at 4 °C overnight. Anti-rabbit secondary was used before visualisation using ECL. Detailed methods can be found in *Section 2.4.*

The western blots were further analysed using densitometry using ImageJ software's gel analyser feature, with measurements normalised to loading control intensities.

5.2.7. Staining and Confocal Microscopy

Primary cells were seeded in 8-well slides (Ibidi, Germany) and differentiated according to *Section 5.2.1.2.* Each well was washed once with 250 µl PBS before 250 µl of wheat germ agglutinin solution (1:200) was added. Following 10 minute incubation with the antibody in the dark the cells were washed with PBS three times.

The cells were then fixed using 250 µl of Fixation buffer (Invitrogen, UK) for 15 minutes. A perm-buffer solution was made (1:10 in water) using Intracellular Staining Perm Wash Buffer (Biolegend, USA). The cells were washed twice in the solution buffer being incubated in 250 µl for 10 minutes.

Actin was stained using ActinGreen 488 ReadyProbes (Invitrogen, UK). 2 drops of antibody per ml of Perm Buffer was made and cells were incubated for 30 minutes. The final stain is for the nuclei. DAPI is diluted 1:3000 in Perm Buffer before 250 µl is added to the slides and incubated for 1 minute.

The final step involves three washes in Perm Buffer followed by two PBS washes. 250 µl of PBS was left in each well before processing on the confocal microscope.

The imaging on the confocal microscope showed actin in green with blue nuclear staining. Allowing for detection of the myotubes in both the wild type and transgenic models.

5.2.8. Cell IQ

Live cell imaging was conducted using a Cell-IQ. Images were taken every 45 minutes of the cells during development. 3 areas of each well were selected for imaging. For analysis each area of each well was used for every day of differentiation. The data was expressed as the mean and comparison between WT and NRK2 Tg models were made. Further detail outlined in *Section 2.15.*

5.2.9. Data Analysis

5.2.9.1. GC-MS Analysis

The GCMS analysis involved ion quantification. The relative quantification of metabolites was achieved through ion quantification. For each metabolite the associated ions that occurred as a result of the GCMS run could be reconfigured and used to inform on the levels of the metabolite within the sample. Without a standard curve present this information could not be absolutely quantified, but instead samples undergoing differing treatments within the same GCMS run were compared.

5.2.9.2. Statistical Analysis

All statistics have been carried out using the GraphPad Prism 6 software. Student t-tests were used to compare between the wild type and NRK2 over expresser primary cell model. Two-way ANOVAs with Sidak's multiple comparisons test used to assess significant changes between genotypes during development. When multiple treatments were conducted and statistical significance compared to control within genotypes was assessed, two-way ANOVAs with Dunnett's multiple comparisons test was used.

Statistical significance was shown by * $p<0.05$, ** $p<0.01$, *** $p<0.001$.

5.3. Results

5.3.1. NAD^+ Biosynthesis Enzymes

Generation of a primary cell model of the NRK2 Tg mouse was conducted to enable manipulation of the system *in vitro*. The initial study was to establish whether the model showed NRK2 overexpression in a primary cell system. RNA expression analysis of the key skeletal muscle NAD^+ biosynthesis enzymes was conducted after 6 days of differentiation. There was no change between genotypes in the expression of Nmrk1 or NAMPT, figure 5.1A-B. There was a significant increase in Nmrk2 expression in the NRK2 Tg primary cells, figure 5.1C, with a corresponding increase in NRK2 protein expression, shown through western blot analysis. The western blots were further investigated, using densitometry, to show a significant elevation of NRK2 protein in the NRK2 Tg model figure 5.1D-E.

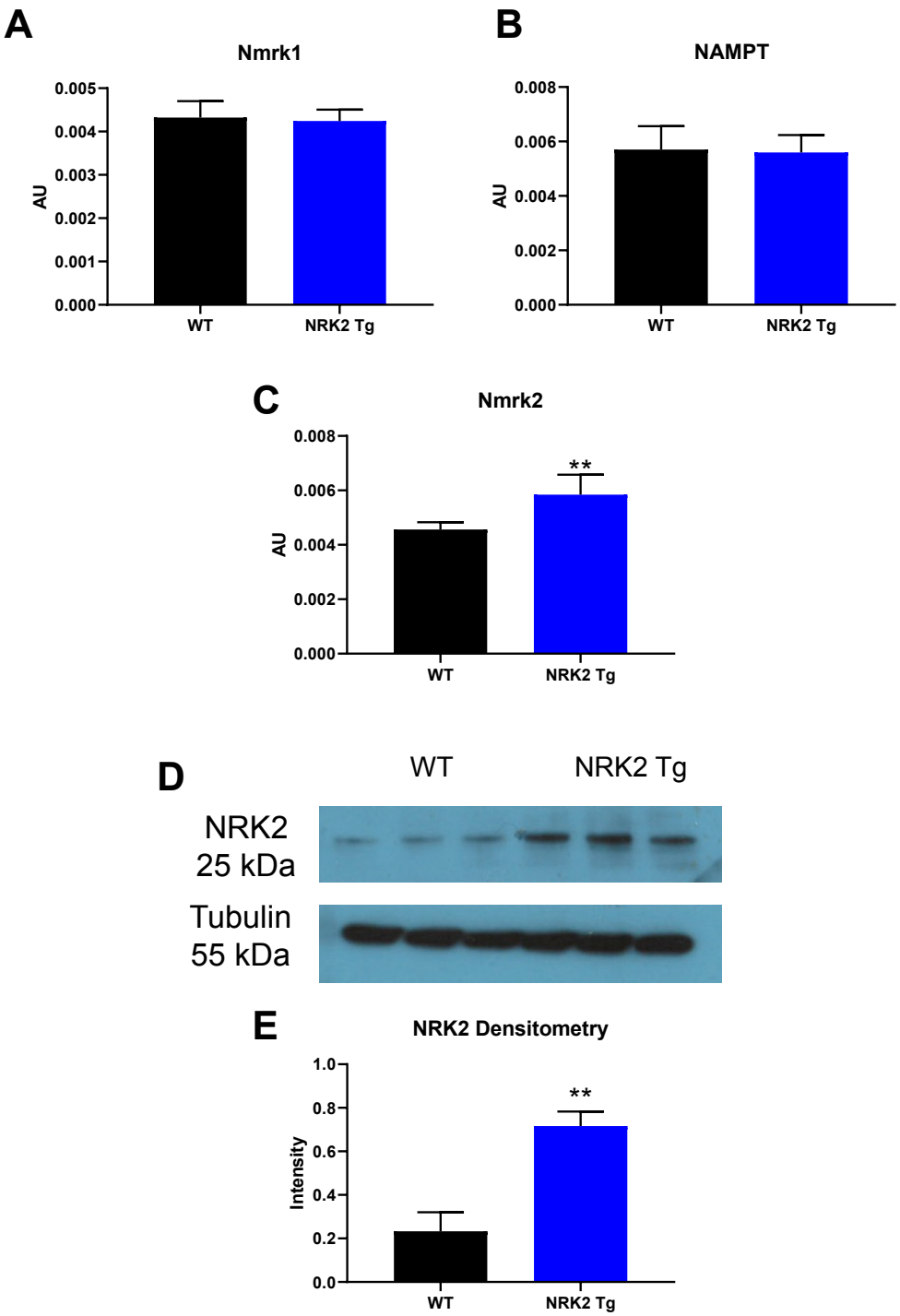


Figure 5.1. NAD^+ Biosynthetic Enzymes

RNA analysis was conducted to assess differences in gene expression between wild type (WT) control mice and NRK2 over expresser mice (NRK2 Tg). **(A)** Nmrk1, **(B)** NAMPT, **(C)** Nmrk2. **(D)** Protein expression of NRK2 was assessed through western blots, with tubulin used as a loading control. **(E)** Densitometry was used to quantify western blot analysis, NRK2 intensity divided by associated tubulin level.

** $p<0.01$; Unpaired, two-tailed t-tests performed on raw data. All data are the mean ±SEM, RNA *n=5*. Protein *n=3*.

5.3.2. NR Supplementation

Given the role of NRK2 in metabolism of NR to NAD^+ we sought to confirm its functional effect in the primary system. There were no basal differences in NAD^+ levels between the WT and NRK2 Tg model, figure 5.2A. Supplementation with NR for 24 hours caused a significant increase in NAD^+ from control in both the WT and NRK2 Tg primary myotubes, figure 5.2A. Further to this, the NRK2 Tg response to NR supplementation was significantly higher than the WT equivalent.

A similar finding was shown in relation to NADH. However, basal NADH was significantly elevated in the NRK2 Tg model compared to WT controls, figure 5.2B. Once again, supplementation with NR caused elevation of NADH levels, more so in the NRK2 Tg model than WT. Given that the NAD^+ and NADH measurements showed a similar increase the ratios remained constant across the treatments and genotypes, figure 5.2C.

Further investigation showed 24 hour NR supplementation caused no change in the expression of NAD^+ biosynthetic, metabolic or developmental genes, figure 5.2D.

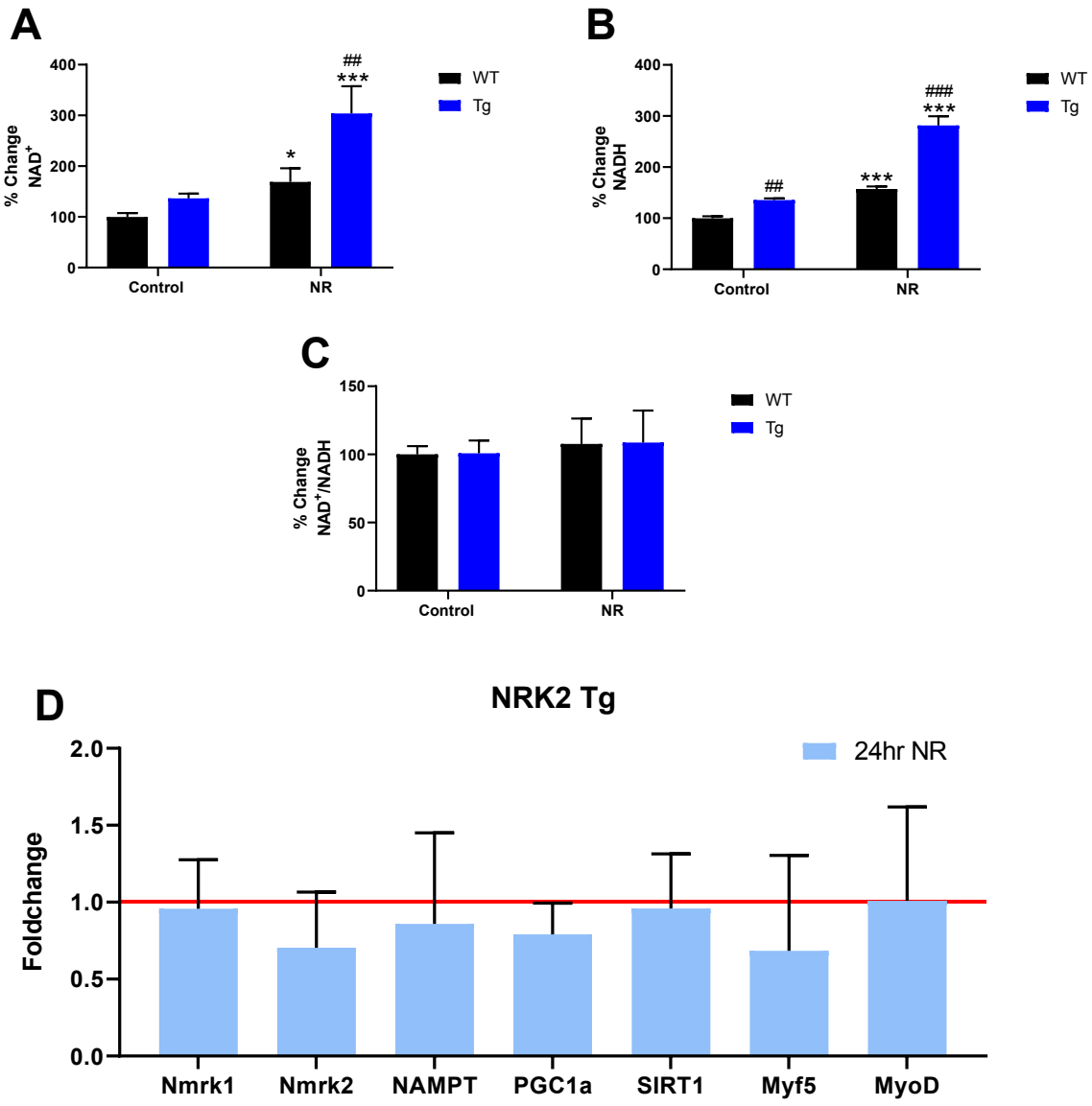


Figure 5.2. NR Supplementation

The percentage change of **(A)** NAD^+, **(B)** NADH and **(C)** NAD^+/NADH ratio compared to WT control following 0.5 mM NR treatment for 24 hours. **(D)** Fold change of gene expression analysis of NRK2 Tg primary myotubes following 24 hour NR treatment compared to control. Red line represents control levels.

Two way ANOVA performed on raw data; Tukey's multiple comparisons test used to compare between treatments and genotypes. * $p<0.05$, *** $p<0.05$ shows statistical significance between treatments; ## $p<0.01$, ### $p<0.05$ shows statistical significance between genotypes; All data are the mean ±SEM, n=3.

5.3.3. Primary Model Imaging

In order to observe any overt structural differences between wild type and NRK2 Tg myotubes staining of the cells was conducted on the 6th day of differentiation, figure 5.3. Actin, which forms an integral part of the muscle contractile unit, was stained in green with the nuclear areas of the myotubes stained in blue. Despite some differences in the staining intensity between the WT and NRK2 Tg models there were no clear structural changes between the two.

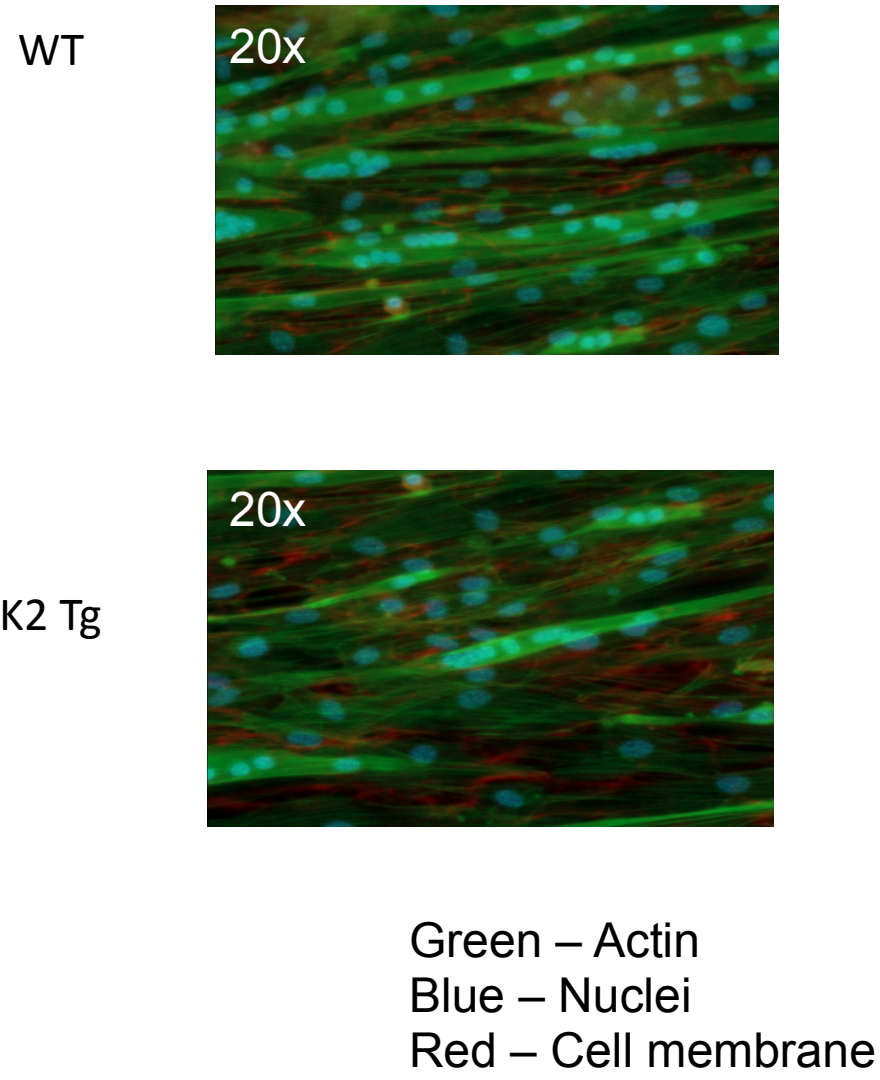


Figure 5.3. Primary Myotube Imaging
Confocal microscope images of WT and NRK2 Tg primary myotubes, 20x.
Green stain for actin filaments, blue nuclear stain and red stain for the cell membranes.

5.3.4. Primary Development

In order to assess the development of the primary myotubes RNA extractions were conducted throughout differentiation. Investigation of Nmrk1 showed a significant elevation of the gene at day 3 of differentiation in the NRK2 Tg model compared to WT, figure 5.4A. This appeared to show an early 'switching on' of the gene as the levels remained elevated in the NRK2 Tg but were matched by the WT Nmrk1 expression by day 6 and were still comparable on day 9 of differentiation.

The Nmrk2 gene expression showed to be activated by day 3 of differentiation in both genotypes, figure 5.4B. This was then switched off in the WT model but remained significantly elevated in the NRK2 Tg myotubes. This was expected given the nature of the overexpressing model.

Interestingly, NAMPT expression showed a significant elevation in the NRK2 Tg model compared to WT at day 9 of differentiation, figure 5.4C. Given that the typical protocol differentiation length was 6 days this meant that this increase had not been noticed in the previous study.

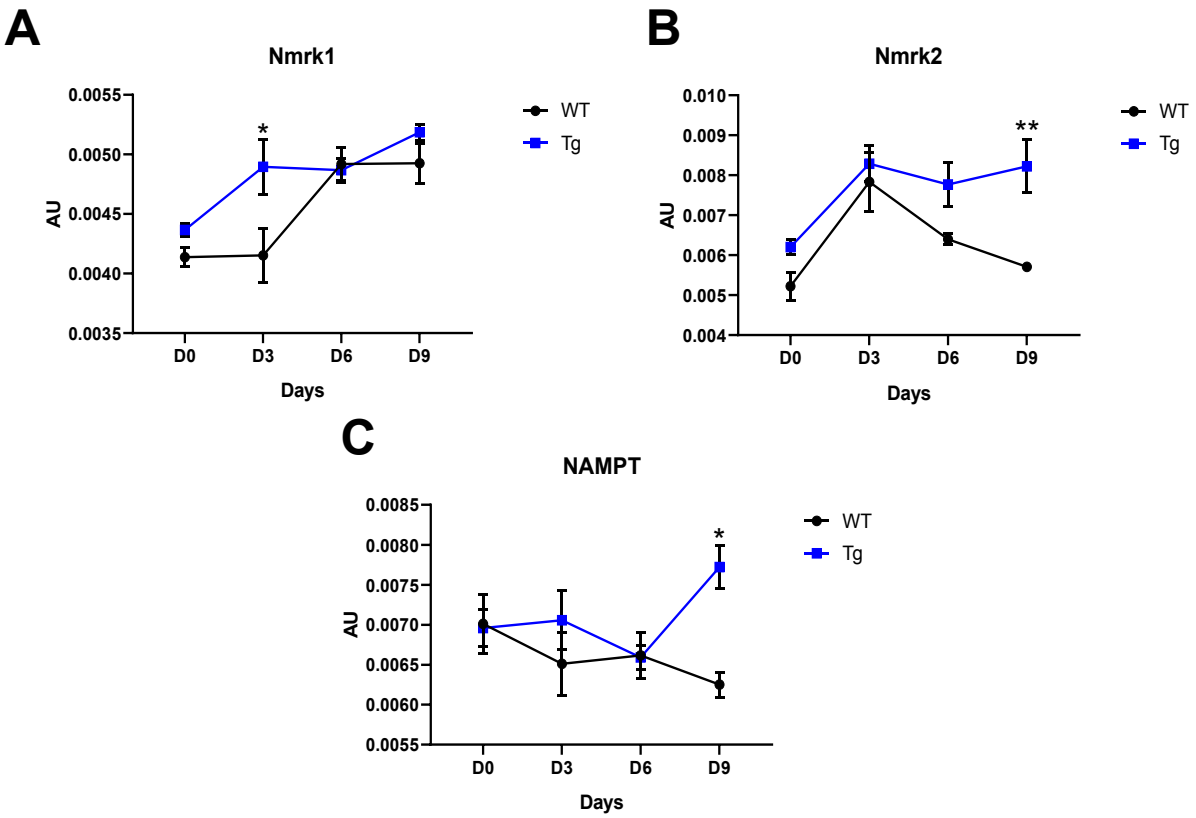


Figure 5.4. Gene Expression Analysis of NAD Biosynthetic Genes During Development
Gene expression analysis of primary myotubes on Days 0, 3, 6 and 9 of differentiation. Black symbols and lines representing wild type (WT) and blue lines representing NRK2 over expresser (NRK2 Tg) expression of **(A)** Nmrk1, **(B)** Nmrk2, **(C)** NAMPT.
* $p<0.05$, ** $p<0.01$; Two way ANOVAs performed; Sidak's multiple comparisons test used to show significance between genotypes. All data are mean ±SEM, *n=3.*

The key skeletal muscle development genes MyoD, MyoG and Pax7 were investigated, figure 5.5A-C. MyoD and Pax7 were highly expressed at day 0 of differentiation, with a steady reduction in levels throughout the study. MyoG appeared to maintain a steady expression throughout differentiation. Importantly, there were no significant differences in expression between the genotypes.

SIRT1 expression was not affected by the NRK2 over expresser model, figure 5.5D. A high expression was observed at day 0 of differentiation with a steady decline shown throughout development in both genotypes.

A genotype difference was observed in the expression of Col1a1 at day 9 of differentiation, figure 5.5E. Once again at day 6 the expression levels were comparable meaning that this would ordinarily have not been observed. We postulated that this may indicate a structural difference in the NRK2 Tg model at a late stage of development.

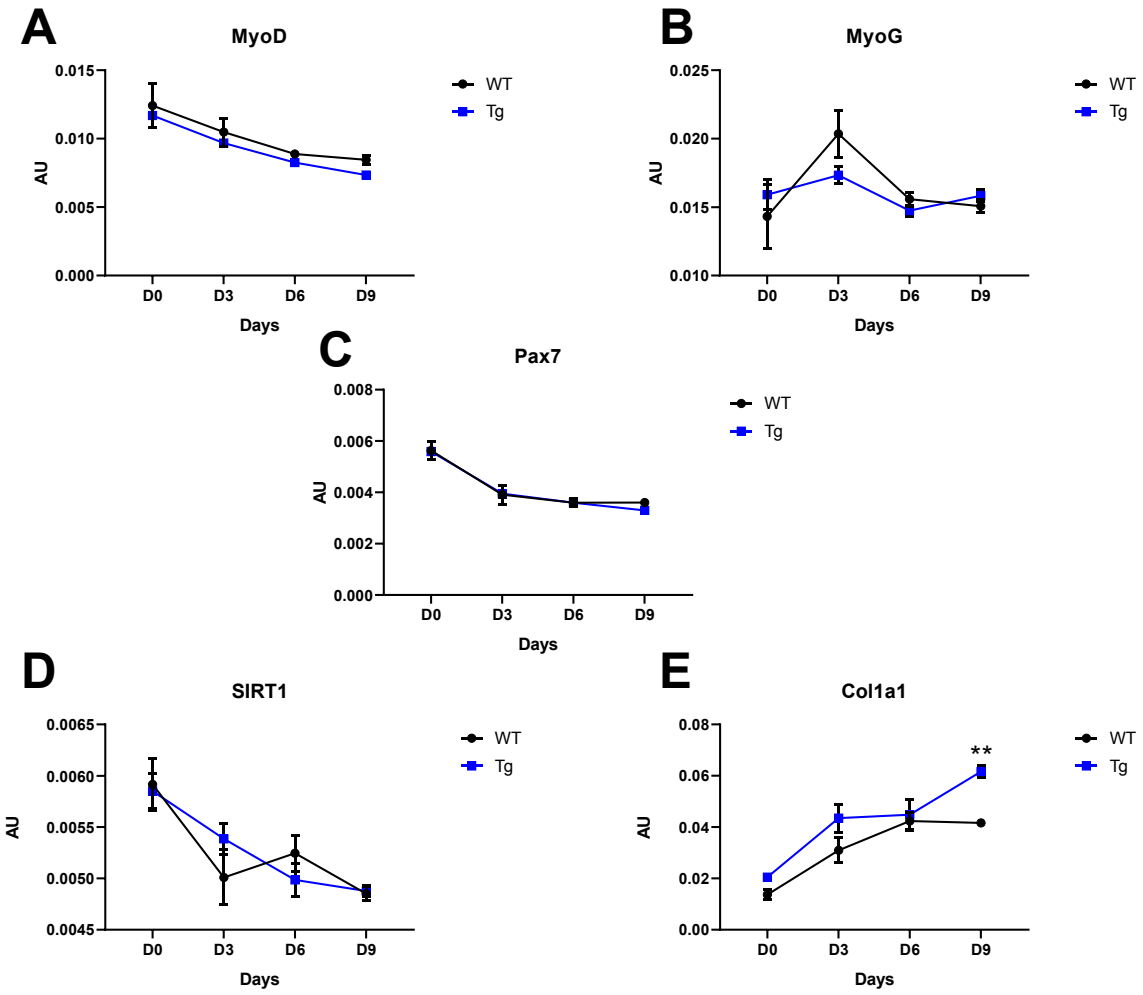
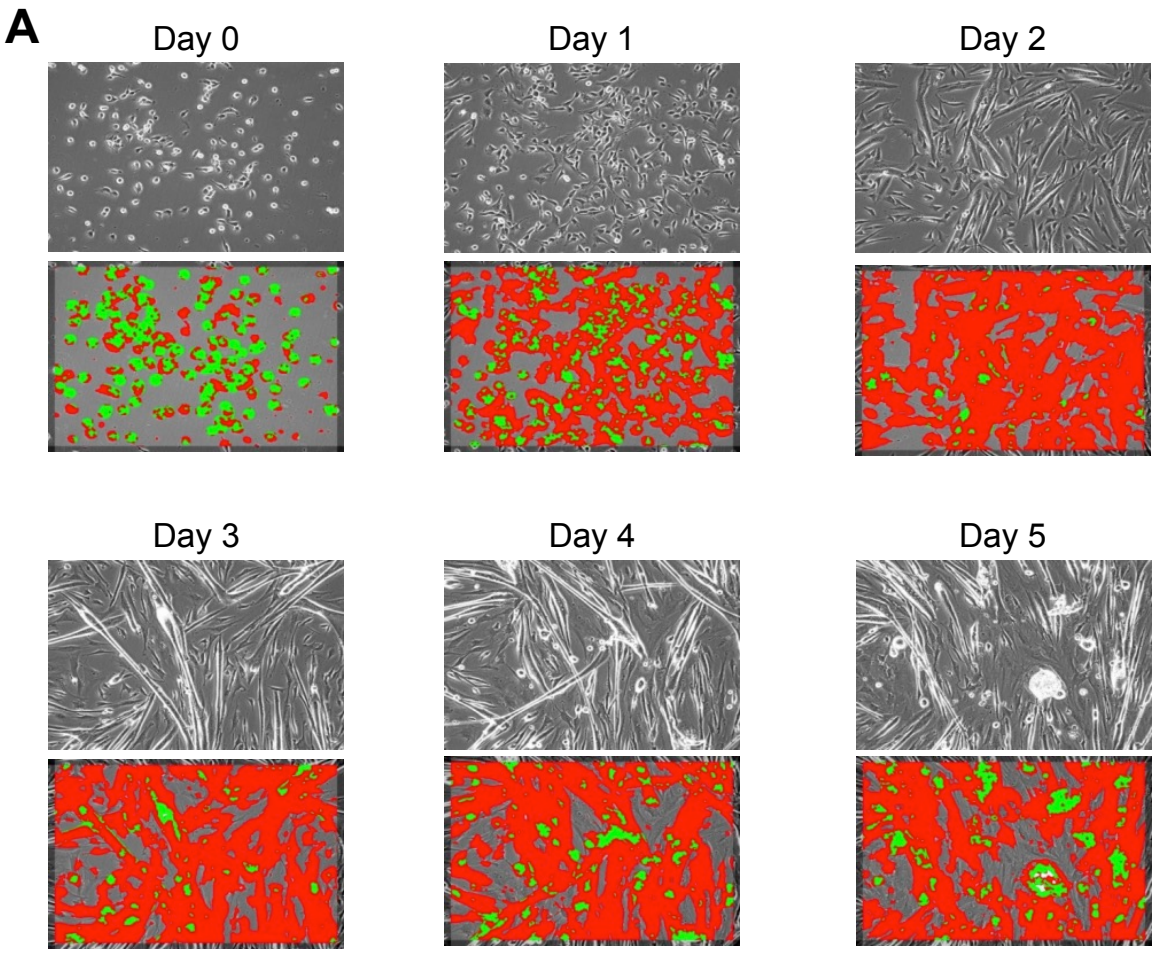


Figure 5.5. Gene Expression Analysis of Developmental Markers and Metabolic Genes
Gene expression analysis of primary myotubes on Days 0, 3, 6 and 9 of differentiation. Black symbols and lines representing wild type (WT) and blue lines representing NRK2 over expresser (NRK2 Tg) expression of **(A)** MyoD, **(B)** MyoG, **(C)** Pax7, **(D)** SIRT1 and **(E)** Col1a1.
** p<0.01; Two way ANOVAs performed; Sidak's multiple comparisons test used to show significance between genotypes. All data are mean ±SEM, *n=3.*

In order to try and observe this we conducted a live cell imaging study using a Cell IQ. This method enabled quantification of undifferentiated cells and differentiated myotubes. Figure 5.6A shows green marks when undifferentiated cells were detected and red markings representing differentiated myotubes. The area of the image containing either cell type was plotted in figure 5.6B. The data show a steady increase in differentiated myotubes from day 0 of differentiation to day 3. The area data plateaus at day 3 throughout the rest of differentiation. However, as can be seen from the images in figure 5.6A the myotubes extend during this period. The WT and NRK2 Tg myotubes appear to differentiate at the same rate. There are also no differences in the levels of myoblasts between the genotypes. A steady level is maintained throughout the study.



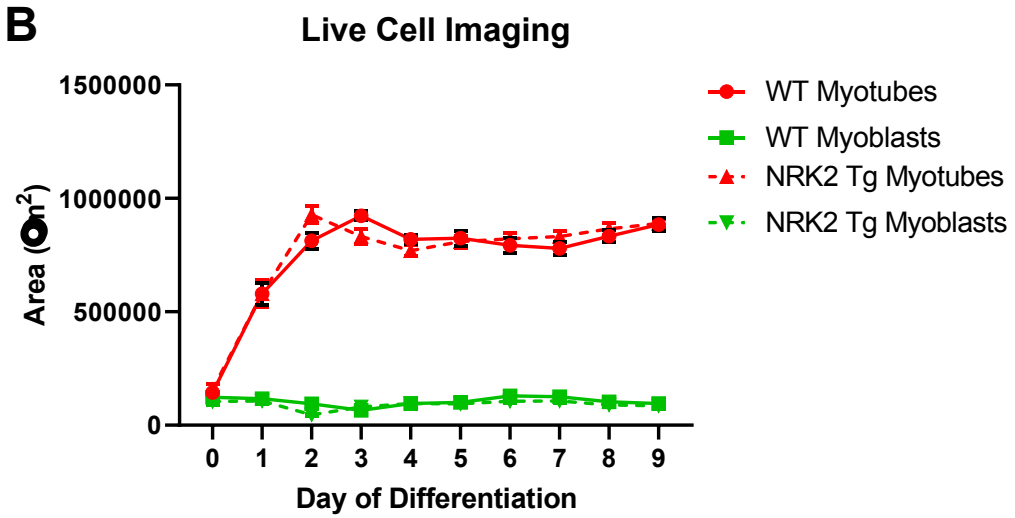


Figure 5.6. Live Cell Imaging Analysis
WT and NRK2 Tg primary cells grown in a Cell IQ machine responsible for conducting live cell imagining during development. **(A)** Representative images showing analysis conducted across day 0-5. The top panel shows the image, the lower panel shows undifferentiated cells (green) and differentiated myotubes (red). **(B)** Data are the area covered by undifferentiated cells (green) and differentiated myotubes (red) in WT (solid lines) and NRK2 Tg (dotted lines) myotubes during development.
All data are the mean ±SEM, n=3.

5.3.5. Metabolomics

The primary WT and NRK2 Tg myotubes were treated with NR and FK866 to create differing states of NAD^+ bioavailability. There were no clear differences observed between treatment groups or genotype in G3P and citrate metabolite levels, figure 5.7A-B.

α-KG showed differential responses to NAD^+ depletion. WT myotubes had comparatively lower levels compared to control, with NRK2 Tg myotubes showing elevated α-KG with FK866 treatment. Figure 5.7C. The addition of NR for 24 hours did not normalise the α-KG levels in the NRK2 Tg myotubes, showing significantly different levels to the WT equivalent group, figure 5.7C.

Glutamate and malate levels were constant, figure 5.7D and F. However, fumarate showed significantly elevated levels in NRK2 Tg control and FK866 treated groups, figure 5.7E. There were no significant changes shown in response to the differential treatments in either genotype.

WT aspartate showed a similar response to previous work with an elevation from control in the FK866 treated samples. This was not replicated in the NRK2 Tg myotubes, which were significantly lower than the WT levels, figure 5.7G.

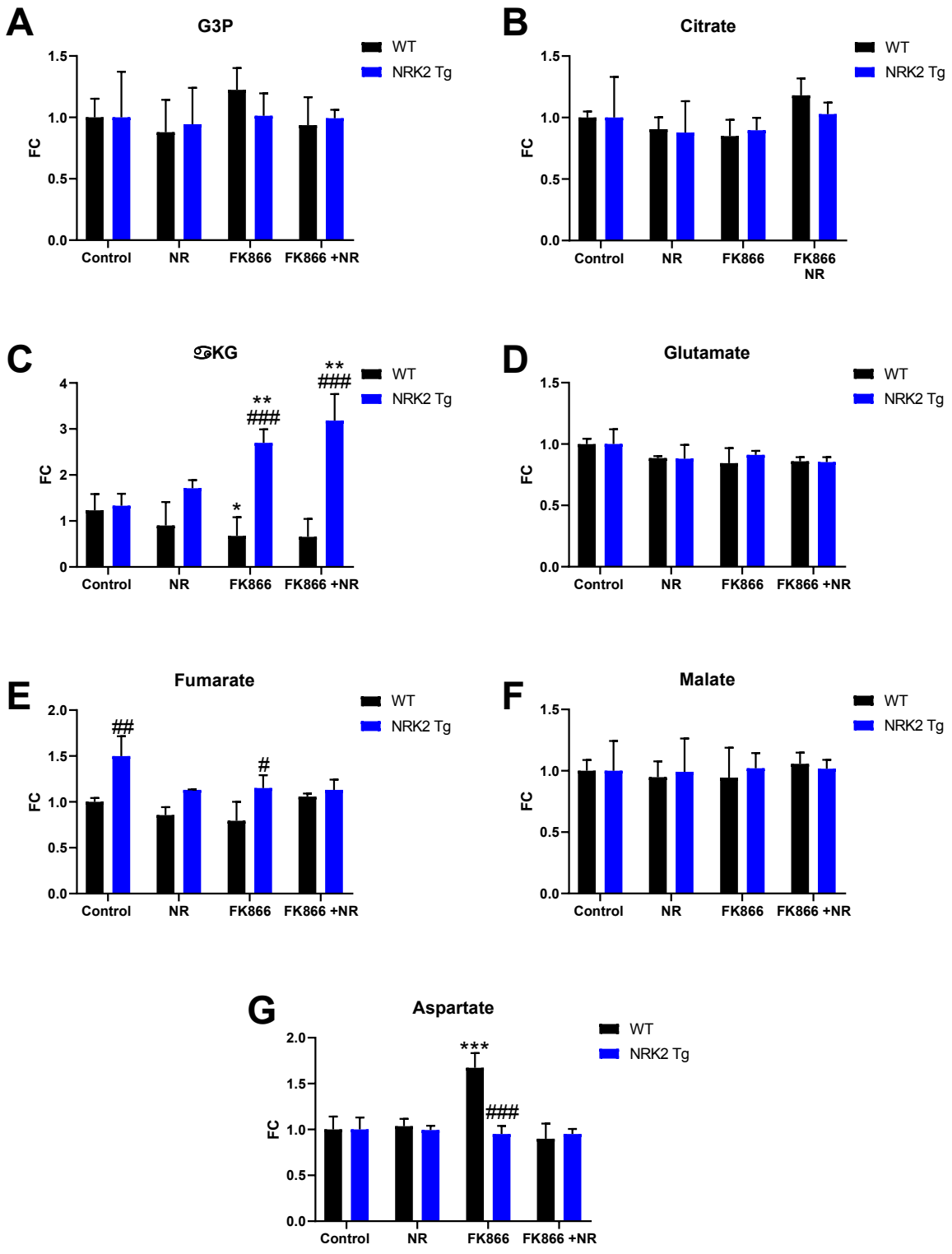


Figure 5.7. NAD+ Manipulation in NRK2 Tg Primary Model
Primary cell myotubes treated with 0.5 mM NR for 24 hours with and without 50 nM FK866 for 48 hours. GCMS metabolomics analysis showed fold change compared to control of **(A)** G3P, **(B)** Citrate, **(C)** aKG, **(D)** Glutamate, **(E)** Fumarate, **(F)** Malate and **(G)** Aspartate.
Two way ANOVA performed; Tukey's multiple comparisons test used to compare between treatments and genotypes. * $p<0.05$, *** $p<0.05$ shows statistical significance from control within genotypes; # $p<0.05$, ## $p<0.01$, ### $p<0.05$ shows statistical significance between genotypes; All data are the mean ±SEM, n=3.

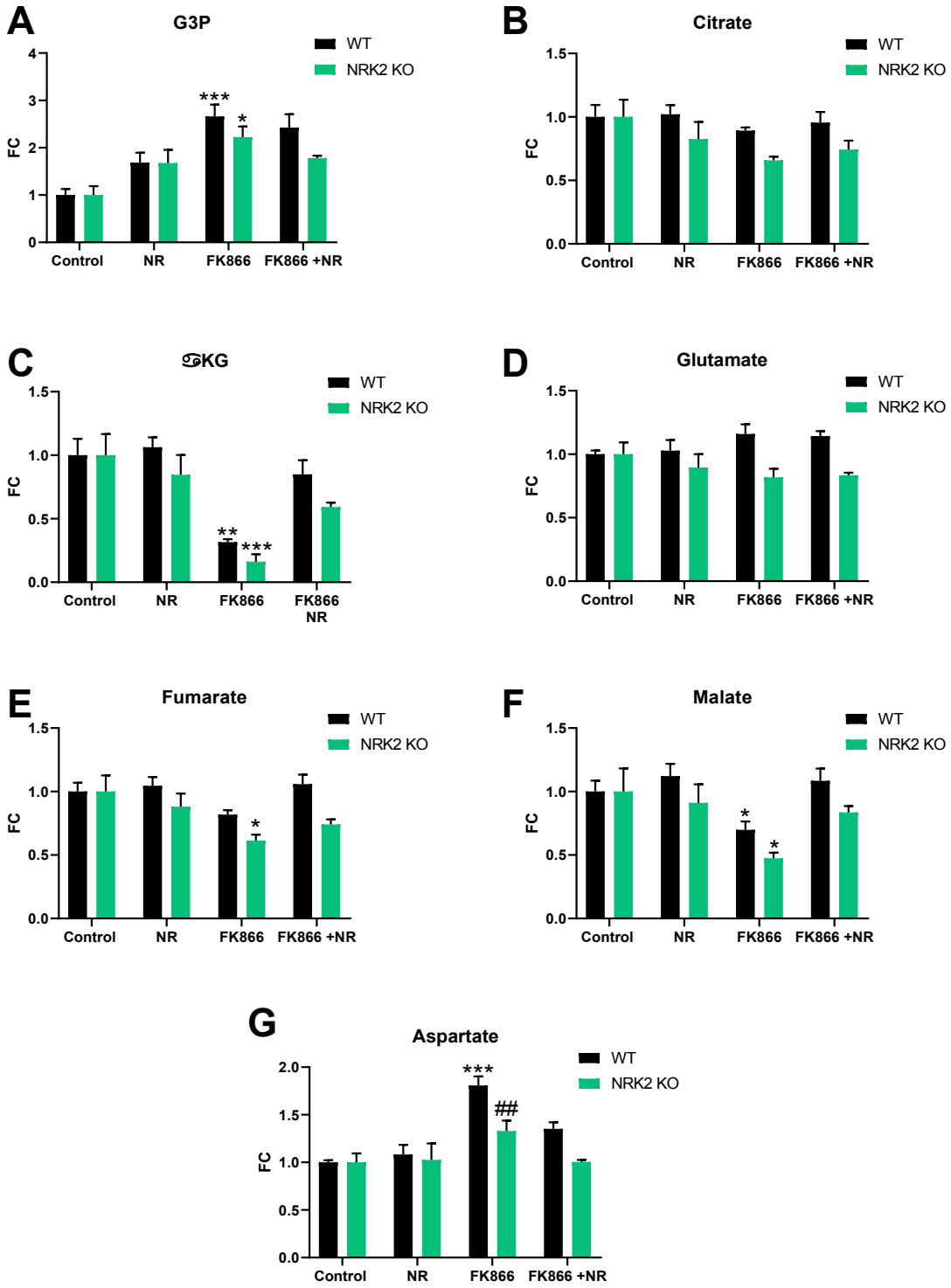


Figure 5.8. NAD^+ Manipulation in NRK2 KO Primary Model

WT and NRK2 KO primary cell myotubes treated with 0.5 mM NR for 24 hours with and without 50 nM FK866 for 48 hours. GCMS metabolomics analysis showed fold change compared to control of **(A)** G3P, **(B)** Citrate, **(C)** aKG, **(D)** Glutamate, **(E)** Fumarate, **(F)** Malate and **(G)** Aspartate.

Two way ANOVA performed; Tukey's multiple comparisons test used to compare between treatments and genotypes. * $p<0.05$, *** $p<0.05$ shows statistical significance from control within genotypes; # $p<0.05$, ## $p<0.01$, ### $p<0.05$ shows statistical significance between genotypes; All data are the mean ±SEM, n=4.

For comparison purposes a primary cell culture of NRK2 KO mice was used and NAD^+ bioavailability manipulation studies conducted. FK866 caused a significant increase in G3P in both WT and NRK2 KO myotubes, which was normalised with the addition of NR, figure 5.8A. No change across treatment group or genotype was observed in citrate (figure 5.8B) and glutamate (figure 5.8D). A significant reduction in α-KG (figure 5.8C) and malate (figure 5.8F) was shown in WT and NRK2 KO myotubes in response to NAD^+ depletion. Aspartate was significantly increased upon FK866 supplementation in both WT and NRK2 KO myotubes, which was once again normalised in response to NR.

To summarise the genotype effects α-KG was reduced in response to FK866 in WT myotubes and NRK2 KO myotubes but was increased in the NRK2 Tg model (figure 5.7C and 5.8C). Fumarate remained unchanged in the WT myotubes but was decreased in NRK2 Tg and increased in NRK2 KO myotubes with NAD^+ depletion (figure 5.7E and 5.8E). Aspartate showed significant elevation in WT myotubes but this was not observed in either genotype (figure 5.7G and 5.8G).

Together this data highlights there are key differences between the primary cell models stemming from the expression of NRK2.

5.4. Discussion

The primary model was used to investigate the effect of altered NAD metabolism. NRK2 gene expression has shown to peak at day 3 of differentiation and 'switch off' for the rest of myotube development [199]. This was replicated in our WT cells but as expected our over expresser showed continued expression of the gene and

ultimately the protein. This elevation in the enzyme enabled increased NAD^+ production in response to NR compared to WT. The NRK2 metabolised NR and increased the cellular content of both NAD^+ and NADH, maintaining the NAD^+/NADH ratio. This ultimately resulted in no effect on transcriptional regulation of genes involved in NAD^+ biosynthesis, metabolism and myotube development.

Previous work conducted in mouse embryonic fibroblasts analysed the gene expression of NAMPT and showed it to be critical for the circadian regulation of NAD^+ [178]. Given that NAMPT is the main route to NAD^+ synthesis in skeletal muscle it follows that oscillations in NAMPT expression ultimately impact NAD^+ levels. The NRK2 Tg mouse model may potentially impact the circadian regulation of NAD^+ with continuous elevation of a key NAD^+ biosynthetic enzyme. However, NAMPT's substrate availability is provided by NAD^+ consumption in the form of NAM. Without an exogenous source of NR the NRK2 enzyme would not be able to produce NAD^+.

Given the limited potential of NAD^+ production in the NRK2 Tg model without exogenous NR we sought to investigate the impact of the elevated NRK2 during development. One key significant difference observed between WT and NRK2 Tg myotubes was the expression of Col1a1. Collagen is a key component of the ECM and has varied functions attributed to it such as structure, mechanical support and signalling [349]. Human exercise studies have shown elevated tendon collagen synthesis in response to exercise [350]. This was also observed in rats where exercise caused a resultant increase in collagen I gene expression believed to represent the regeneration of muscle [351]. The study also showed a morphological observation of centralised nuclei in the myofibres in response to exercise [351]. Investigation of the NRK2 Tg *in vivo* model showed increased centralised nuclei compared to WT. We

therefore postulated that the elevated expression of NRK2 caused increased myotube generation, with a similar phenotype to regenerating muscle. In opposition to this hypothesis, was the stable expression of Pax7 a satellite cell marker [24]. Increased myotube formation is suggestive of elevated active satellite cells and therefore increased Pax7, however this wasn't observed in the model [24].

The metabolomics work uncovered some key differences in the primary cells response to NAD^+ depletion between the two genotypes. The α-KG levels increased with FK866 treatment in the NRK2 Tg model, which was surprising. However the NRK2 Tg myotubes showed to have elevated basal NADH in the NAD^+/NADH cycling assay. This increased NADH may have been sufficient to support oxidative phosphorylation and the TCA cycle in a state of NAD^+ depletion. The α-KG levels did increase above control but this may have been confounded by a reduction in α-KG consumption. As flux data is not shown it is impossible to determine whether the α-KG is a result of increased production or merely an accumulation. α-KG is involved in various metabolic reactions throughout the cell. It is not simply a TCA cycle intermediate but is also a precursor for glutamate and glutamine synthesis [352]. Therefore the elevated α-KG may be a hallmark of reduced glutamate synthesis. This could also provide explanation for the elevated fumarate in FK866 samples, either a result of increased production or reduced consumption.

The NRK2 KO primary myotubes did not show any difference from WT in their basal NAD metabolism [199]. This could therefore explain why the FK866 response in these myotubes reflects the WT. The addition of NR did not normalise the α-KG levels in the NRK2 Tg myotubes. Given the hypothesis that the elevated NADH supported the TCA cycle during NAD^+ depletion, it follows that the addition of NR may merely

enhance this further. The increased α-KG during NAD^+ depletion is evidence of the cell utilising the available NADH to its advantage, therefore NAD^+ repletion would not necessarily reverse the effects.

One key observation was that the elevated aspartate in response to NAD^+ depletion had its main effect in WT myotubes, with a slight increase in FK866 treated NRK KO myotubes. This effect was not observed in the NRK2 Tg myotubes. Together this data suggests that the aspartate increase may be the result of impaired shuttle functioning as a result of NAD^+ depletion. The NRK2 Tg model may exert a protective effect through its elevated basal NADH that prevents the impaired functioning of the shuttle and ultimately limits aspartate accumulation.

The immunofluorescence staining showed no overall structural differences between the genotypes. However, there were some differences in the intensity of the stain. Immunofluorescence stains can show high variability dependent on the tissue used; as both were primary myotubes and each slide was treated identically this was unexpected. A possible suggestion may be the density of the myotubes, the NRK2 Tg slide may have been denser and therefore the resultant stain less intense than the WT.

In order to try and quantify the potential differences in growth and development between the genotypes live cell imaging was conducted. This showed no observable difference between the WT and NRK2 Tg myotubes. The area covered by differentiated myotubes was consistent between the groups along with the rate of differentiation. The area of myoblasts was also consistent and the levels remained steady throughout the study. However, this data does not inform on the viability of

these cells and cannot account for whether the myoblasts are newly formed, existing or dead. The data interpretation using this method is limited, however it informs on the rate of differentiation and shows no clear differences in the growth and development of NRK2 Tg myotubes compared to their WT counterparts.

Overall, this work shows that the primary cell model is capable of expressing the elevated NRK2 protein shown *in vivo*. There are no clear morphological, transcriptional or developmental differences between the WT and NRK2 Tg myotubes in the areas observed. However, there is suggestion of a potential role of NRK2 in protecting cellular metabolism in states of NAD^+ decline.

This work can inform future *in vivo* experiments to try and pull out the protective role of NRK2. Introducing metabolic stress to the *in vivo* model and following up with metabolic phenotyping and skeletal muscle tissue analysis should help to confirm this protective NRK2 role. Metabolic stress inducers could be aging, with the question whether the NRK2 Tg muscles are protected from age-related loss of mass. The animals could also be fed a high fat diet to observe whether the NRK2 Tg animals are protected from the metabolic side effects associated with this such as loss of metabolic flexibility. The elevated NADH evidenced by this work suggested maintenance of mitochondrial metabolism in states of cellular NAD^+ decline. This could have wide-ranging effects on skeletal muscle metabolism *in vivo*, which ultimately feeds into whole body metabolism. This would help further our understanding of the biology of NRK2 specifically and the wider role of NAD^+ metabolism in human health.

6. Final Discussion

NAD^+ is vital for correct cellular metabolism [118]. As a redox molecule it is critical for accepting electrons and facilitating oxidoreductase reactions throughout metabolic pathways within our cells [110]. Glycolysis is fuelled by NAD^+ in the cytoplasm and the mitochondrion relies heavily on the bioavailability of the molecule. This role of NAD^+ is important but recently the consumption of NAD^+ by enzymes has become a prominent research area [102,115,118]. Activation of these enzymes results in reduction of NAD^+ and therefore NAD^+ synthesis is critically important to maintain levels and enable correct cell functioning.

The work within this thesis confirmed NAMPT as the main route to NAD^+ synthesis in skeletal muscle. NR and NMN were also able to significantly elevate NAD^+ within 4 hours in both cell line and primary cell culture of myotubes. The excess NAD^+ study showed NMN to cause significantly less NAM elevation than NR in C2C12 myotubes. NAM has shown to be a sirtuin inhibitor and has showed correlation with reduced NAMPT expression [245]. Therefore, whilst the delayed NMN response compared to NR has previously been considred a disadvantage of the precursor it may in fact be a benefit as it ultimately reduces the excess production of NAM.

Carbon metabolism was mainly affected by low NAD^+ with limited effects as a result of excess NAD^+ levels. In states of NAD^+ excess the cell rapidly increases clearance to maintain redox ratios and therefore limits the effect to core metabolic pathways. As discussed, the elevated NAM may contribute to inflammation which has been linked to eNAMPT [183]. However, it is the eNAMPT monomer that has been shown to be pro-inflammatory and that has no NAD^+-biosynthetic activity [183]. Work conducted in a human clinical trial showed NR supplementation was effective in reducing circulating inflammatory cytokines [273]. Together this suggests excess circulating NAM does not

act as an eNAMPT substrate causing increased inflammation in the human trials conducted thus far.

An observation throughout this work was that although the models act and respond similarly to treatments they are not identical. Most of the work is conducted in both C2C12 cell lines and primary myotubes. Differences in their metabolism have been previously reported and further confirmed by this work [324]. This identifies a flaw in translatability within research. As the majority of work is initially conducted in cell lines prior to being escalated up to *in vivo* animal and human studies it is important that results are reproducible. Typically this is not always the case and within this work it was demonstrated that a reproducible result in cell line and primary cells could not be repeated *in vivo* [353]. This calls in to question the impact of cell work and how useful it is in understanding metabolism in humans.

NR supplements, such as Niagen, are readily available for public consumption. Importantly, NR has shown to be well tolerated and safe in human trials of the nutraceutical and critically was effective at increasing NAD^+ metabolism [273]. However, there has been no publication of data that suggests that these supplements are beneficial to human health. There has been no reported NR induced improvement in insulin sensitivity or mitochondrial bioenergetics [273,354,355].

An initial observation in yeast, which has since been disputed, showed that increased NAD^+ extended lifespan [128–132]. NAD^+ was shown to be reduced in aged mice apparently the result of increased CD38 activity [308]. However, a recent observation has suggested that in healthy aging NAD^+ levels are not reduced [273]. This has been given as the reason for a lack of an NR response in the clinical trials conducted thus

far. This is supported by the work within this thesis. We have shown that NR is effective at normalising changes to metabolism that occur as a result of NAD^+ depletion. However, we have also shown that excess NAD^+ in 'healthy' cells is rapidly cleared to maintain the redox potential. Therefore it follows that without a reduction in NAD^+ there would be no NR impact. This potentially explains why there was no observable change to energy metabolism in our *in vivo* NR supplementation acute exercise study. This does not mean that NR supplementation is not effective merely that it may only have beneficial effects in states of NAD^+ decline.

The metabolomics work in the NRK2 Tg primary cell model shows continued metabolism in FK866 treated cells. This led to the hypothesis that NRK2 expression was effective at protecting cellular metabolism during states of NAD^+ decline. Previous work further supports this hypothesis through highly regulated NRK2 expression in response to muscle injury [346–348]. This increased expression was postulated to be in order to elevate NAD^+ levels in states of stress and the work with the NRK2 Tg potentially supports this notion. A recent study has identified a decreased survival rate in mice following ischemia-induced heart failure in an NRK2 KO model [356]. The study suggests a protective role of NRK2 in cardiomyocytes during ischemic insult. Further investigation using the NRK2 Tg mouse model may demonstrate the level of protection by NRK2 in states of injury. Generation of NAD^+ decline in the NRK2 Tg mouse will help to observe whether the elevated NRK2 protects the mice from NAD^+ dependant metabolic decline.

6.1. Limitations

A limitation of this thesis is that the work was conducted in closed cell systems. Whilst this is important in understanding specific cell-type responses it limits our

understanding of the wider impact of the treatments. As this work is ultimately aimed at improving understanding of human health the lack of evidence of different tissue effects could prevent translatability.

The inability to accurately quantify mitochondrial NAD^+ concentration limited the ability to confirm our hypothesis of differential NAD^+ pools responsible for maintaining mitochondrial respiration.

6.2. Future Work

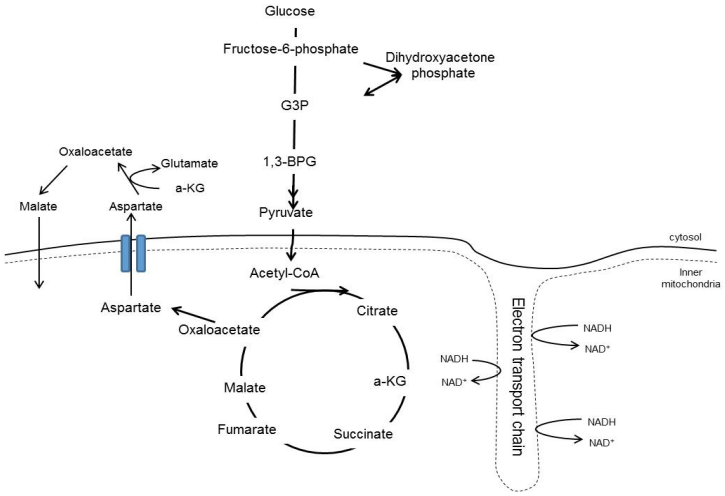
Future work would be required *in vivo* to fully appreciate the effect of NAD^+ clearance on surrounding tissues. *In vivo* tracing studies could potentially be used to understand these metabolic pathways but in a whole body setting. Given the *in vivo* mouse tracing study was unsuccessful in this thesis it would be imperative that any tracing work was first optimised to ensure cells use the exogenous labelled glucose. This may be achieved through subjecting animals to exercise to prompt glucose uptake and glycogenolysis, however this will generate its own problems by affecting metabolic processes. The task of *in vivo* tracing in skeletal muscle is complex, however the information gained would further our understanding of human health. Once optimised the method could be used to observe skeletal muscle metabolism in a range of different diseases known to have low NAD^+ levels. People living with type II diabetes mellitus, muscular dystrophy and those people living a sedentary lifestyle would be interesting cases to explore in this context.

A key question may be whether skeletal muscle specific NAD^+ depletion can be over come by systemic NAD^+ metabolism. NAM in the blood released by other tissues following NAD^+ consumption could be sufficient to maintain skeletal muscle NAD^+ in

states of decline. Equally without the direct effect of the NAD^+ precursors on the cell it is debatable whether they could be as effective at reversing NAD^+-dependant changes. We have shown skeletal muscle cells ability to adapt to very low NAD^+ levels to maintain mitochondrial metabolism. Therefore, it calls in to question whether humans would ever experience the NAD^+ loss required to induce these findings of altered redox and elevated aspartate. Potential situations to induce this loss may be acute or severe metabolic stress where NAD^+ repletion could work as a therapy.

Skeletal muscle is a hugely versatile tissue and is able to adapt to match functional demand [357]. It therefore is expected that myotubes are also able to adapt their metabolism to cope with altered NAD^+ bioavailability. High NAD^+ is cleared to maintain the careful balance within the cell to protect glycolytic and oxidative phosphorylation. Low NAD^+ does cause key changes but the cells still protect their mitochondrial metabolism to ensure energy production despite diminishing NAD^+ levels. This work has utilised different methods and models to understand the impact of altered NAD^+ bioavailability on skeletal muscle metabolism and is summarised in figure 6.1. It has potentially identified a protective role of NRK2 in states of NAD^+ stress and has highlighted the importance and careful cellular regulation of NAD^+/NADH redox within skeletal muscle myotubes.

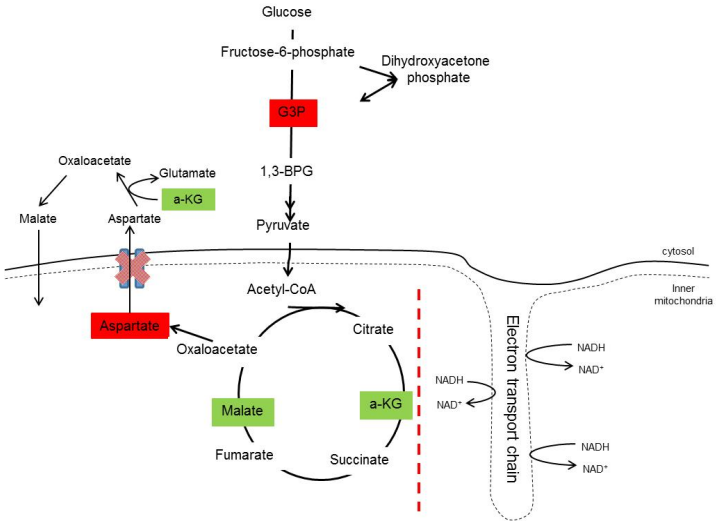
NR and NMN have no effect on energy metabolism in. otherwise untreated C2C12 and primary myotubes.



FK866 blocks glycolysis at GAPDH causing reduction in TCA metabolites.

Increased aspartate observed during NAD^+ depletion.

Observed in C2C12 and primary myotubes.



NRK2 Tg primary myotubes have elevated basal NADH, which potentially protects energy metabolism during FK866 treatment.

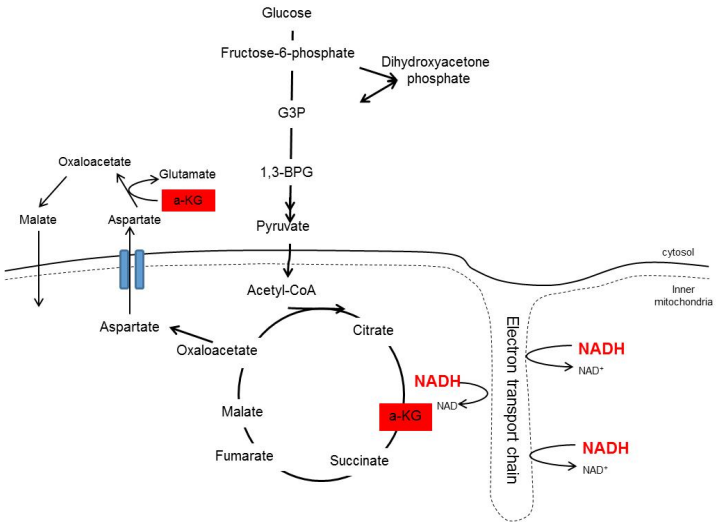


Figure 6.1. Adaptations to Skeletal Muscle Metabolism in Response to Altered NAD Bioavailability
The models used identified that NR and NMN treatment had limited effects on cellular metabolism and simply increased clearance through NAM and MeNAM to maintain cellular redox. FK866 treatment resulted in severe NAD^+ depletion, blocked glycolysis, decreased TCA cycle metabolites and elevated aspartate in C2C12 and primary myotubes. This was postulated to be the result of impaired mitochondrial shuttle functioning and therefore was protected in the NRK2 Tg primary mouse model possibly due to the elevated basal NADH observed.

7. Appendix A - Assay on demand TaqMan probes

Gene	Product number
Nmrk1	Mm00521051_m1
Nampt	Mm00451938_m1
Sirt1	Mm01168521_m1
Pgc1α	Mm01208835_m1
Col1a1	Mm00801666_g1
MyoG	Mm00446194_m1
MyoD1	Mm00440387_m1
Pax7	Mm01354484_m1
Trim63	Mm01185221_m1
Igf2	Mm00439564_m1

8. Appendix B – SYBR Green Primer Sequence

Gene	Primer Sequence
MmNMRK2 For 1.1	5' - AAACTCATCATAGGCATTGGAGG
MmNMRK2 Rev 1.1	5' - GTCCTGGGGCTTGAAGAAG

9. Appendix C - Associated Manuscript

Metabolic tracing reveals novel adaptations to skeletal muscle cell energy production pathways in response to NAD^+ depletion

Check for updates

RESEARCH ARTICLE

REVISED Metabolic tracing reveals novel adaptations to skeletal muscle cell energy production pathways in response to NAD^+ depletion [version 2; peer review: 2 approved]

Lucy A. Oakey [1], Rachel S. Fletcher[1], Yasir S. Elhassan [1], David M. Cartwright[1], Craig L. Doig[1], Antje Garten [1], Alpesh Thakker [1], Oliver D. K. Maddocks [2], Tong Zhang[2], Daniel A. Tennant [1], Christian Ludwig [1], Gareth G. Lavery[1]

[1]Institute of Metabolism and Systems Research, University of Birmingham, UK, Birmingham, B15 2TT, UK
[2]Institute of Cancer Sciences, University of Glasgow, Glasgow, G61 1QH, UK

v2 **First published:** 15 Nov 2018, **3**:147 (https://doi.org/10.12688/wellcomeopenres.14898.1)
Latest published: 17 Sep 2019, **3**:147 (https://doi.org/10.12688/wellcomeopenres.14898.2)

Abstract

Background: Skeletal muscle is central to whole body metabolic homeostasis, with age and disease impairing its ability to function appropriately to maintain health. Inadequate NAD^+ availability is proposed to contribute to pathophysiology by impairing metabolic energy pathway use. Despite the importance of NAD^+ as a vital redox cofactor in energy production pathways being well-established, the wider impact of disrupted NAD^+ homeostasis on these pathways is unknown.

Methods: We utilised skeletal muscle myotube models to induce NAD^+ depletion, repletion and excess and conducted metabolic tracing to provide comprehensive and detailed analysis of the consequences of altered NAD^+ metabolism on central carbon metabolic pathways. We used stable isotope tracers, [1,2-13C] D-glucose and [U-^{13}C] glutamine, and conducted combined 2D-1H,13C-heteronuclear single quantum coherence (HSQC) NMR spectroscopy and GC-MS analysis.

Results: NAD^+ excess driven by nicotinamide riboside (NR) supplementation within skeletal muscle cells resulted in enhanced nicotinamide clearance, but had no effect on energy homeostasis or central carbon metabolism. Nicotinamide phosphoribosyltransferase (NAMPT) inhibition induced NAD^+ depletion and resulted in equilibration of metabolites upstream of glyceraldehyde phosphate dehydrogenase (GAPDH). Aspartate production through glycolysis and TCA cycle activity was increased in response to low NAD^+, which was rapidly reversed with repletion of the NAD^+ pool using NR. NAD^+ depletion reversibly inhibits cytosolic GAPDH activity, but retains mitochondrial oxidative metabolism, suggesting differential effects of this treatment on sub-cellular pyridine pools. When supplemented, NR efficiently reversed these metabolic consequences. However, the functional relevance of increased aspartate levels after NAD^+ depletion remains unclear, and requires further investigation.

Open Peer Review

Reviewer Status ✓ ✓

	Invited Reviewers	
	1	**2**
version 2 (revision) 17 Sep 2019		
version 1 15 Nov 2018	✓ report	✓ report

1 **Paul Caton**, King's College London, London, UK

2 **Joseph A. Baur**, University of Pennsylvania, Philadelphia, USA

Any reports and responses or comments on the article can be found at the end of the article.

Conclusions: These data highlight the need to consider carbon metabolism and clearance pathways when investigating NAD^+ precursor usage in models of skeletal muscle physiology.

Keywords
NAD+, NAMPT, NR, metabolism, skeletal muscle, isotopic tracing, aspartate

Corresponding author: Gareth G. Lavery (g.g.lavery@bham.ac.uk)

Author roles: Oakey LA: Data Curation, Formal Analysis, Investigation, Writing – Original Draft Preparation, Writing – Review & Editing; **Fletcher RS**: Data Curation, Writing – Review & Editing; **Elhassan YS**: Writing – Review & Editing; **Cartwright DM**: Writing – Review & Editing; **Doig CL**: Supervision, Writing – Review & Editing; **Garten A**: Writing – Review & Editing; **Thakker A**: Formal Analysis, Methodology; **Maddocks ODK**: Data Curation, Investigation; **Zhang T**: Data Curation, Formal Analysis; **Tennant DA**: Conceptualization, Writing – Review & Editing; **Ludwig C**: Conceptualization, Data Curation, Formal Analysis, Methodology, Resources; **Lavery GG**: Conceptualization, Funding Acquisition, Investigation, Project Administration, Supervision, Writing – Review & Editing

Competing interests: No competing interests were disclosed.

Grant information: This work was supported by a PhD studentship funded by the University of Birmingham and a Wellcome Trust Senior Fellowship (GGL-104612/Z/14/Z). Metabolic tracing was performed through the University of Birmingham Metabolic Tracing Analysis Core (MTAC). We thank ChromaDex (Irvine, California) for nicotinamide riboside and helpful discussions. TZ and ODKM are funded by Cancer Research UK Career Development Fellowship (C53309/A19702).

Copyright: © 2019 Oakey LA *et al*. This is an open access article distributed under the terms of the Creative Commons Attribution License, which permits unrestricted use, distribution, and reproduction in any medium, provided the original work is properly cited.

How to cite this article: Oakey LA, Fletcher RS, Elhassan YS *et al.* **Metabolic tracing reveals novel adaptations to skeletal muscle cell energy production pathways in response to NAD $^+$ depletion [version 2; peer review: 2 approved]** Wellcome Open Research 2019, **3**:147 (https://doi.org/10.12688/wellcomeopenres.14898.2)

First published: 15 Nov 2018, **3**:147 (https://doi.org/10.12688/wellcomeopenres.14898.1)

REVISED **Amendments from Version 1**

The reviewers comments were noted. The manuscript was edited to justify doses used, clarify the methods sections and include additional references. Figure 4 was also adjusted following reviewer feedback.

Any further responses from the reviewers can be found at the end of the article

Introduction

Nicotinamide adenine dinucleotide (NAD^+) is an essential cofactor responsible for facilitating oxidoreductase reactions throughout glycolysis, the tricarboxylic acid (TCA) cycle, and the electron transport chain (ETC)[1,2]. Maintaining NAD^+/reduced NAD^+ (NADH) redox homeostasis is important for effective ATP production, which is essential for metabolically active tissues to meet functional demand[3]. NAD^+ has since also been recognised as a signalling molecule and is intracellularly consumed by enzymes such as sirtuins, poly-ADP-ribose polymerases (PARPs) and cADP-ribose synthases (CD38s). In order to maintain normal cellular function, it is critical for NAD^+ to be replenished through either biosynthetic or salvage pathways[4–6].

Pathological changes to skeletal muscle have consequences on whole body energy metabolism as seen in disease states such as obesity, diabetes and sarcopenia[7–9]. A reduction in NAD^+ levels of between 30 and 85% have been reported in the muscle tissue of aged mice with an associated impairment in mitochondrial function[5,10–14]. Reduced NAD^+ availability may also be a molecular mechanism involved in the aetiology of muscle dysfunction in more common metabolic diseases, including obesity and type II diabetes[10–12]. Augmentation of muscle NAD^+ levels through precursor supplementation (i.e. nicotinamide riboside (NR), nicotinamide mononucleotide (NMN)) may be a means to improve metabolic capacity and function in a range of age-related disease states[15]. NR and NMN are often supplemented in large doses and can lead to increased cellular NAD^+ content. Chronically increasing NAD^+ beyond normal physiological levels could have a wider impact on metabolic homeostasis, which is yet to be fully understood.

The role of NAD^+ in accepting electrons from glycolytic and TCA cycle metabolites enables oxidative phosphorylation and highlights the NAD^+/NADH redox couple as being vital to central carbon metabolism. Based on the decline in NAD^+ observed in chronic disease we studied the impact this may have on energy homeostasis. In light of the recent work showing NR can safely elevate NAD^+ concentration in human blood[16], alongside the increasing focus on NAD^+ precursors as a treatment strategy for metabolic diseases, we sought to explore the metabolic impact of altered NAD^+ levels in the context of skeletal muscle[16–18].

Here we established scenarios of NAD^+ excess and depletion, previously modelled in other studies[12,19,20], and aimed to more intensively define the consequences of disrupted NAD^+ on essential metabolic pathways in skeletal muscle, providing advances to the current work in the field. We initially employed 1D-^{1}H-NMR, which has higher resolution and reproducibility than other quantification methods, such as GCMS[21]. Further to this, we utilised metabolic tracing to understand the impact of altered NAD^+ levels on carbon metabolism. The stable isotope tracer [1,2-^{13}C] D-glucose was used to generate metabolite labelling patterns and visualised through advanced 2D-^{1}H,^{13}C-heteronuclear single quantum coherence (HSQC) nuclear magnetic resonance (NMR) spectroscopy and gas chromatography–mass spectrometry (GC-MS) analysis[22]. This methodology allowed for in-depth analysis of glucose-derived carbon molecules, with the ability to determine information regarding specific metabolic pathways within different compartments[23]. Detailed analysis of lactate and alanine enable greater understanding of the changes to glycolysis and the pentose phosphate pathway (PPP) within the cytosol. Investigation of glutamate and aspartate, using this method, can determine whether synthesis has occurred from pyruvate entering the mitochondria via pyruvate dehydrogenase or pyruvate carboxylase[22,23]. Further to this, information regarding the number of rounds of the TCA cycle can be determined, which once again can be used to understand changes to the activity of the TCA cycle in response to differing NAD^+ states.

Here we present detailed evidence of adaptations to pathway utilisation within central carbon metabolism in response to low NAD^+ levels in skeletal muscle, which are reversible with short-term NR supplementation.

Methods

Unless otherwise stated all materials and reagents were acquired from Sigma-Aldrich, UK

Culture of the murine C2C12 muscle cell line

C2C12 myoblasts were grown in Dulbecco's Modified Eagle's Medium (DMEM) 25 mM glucose supplemented with 10% foetal bovine serum (FBS) and 1% Penicillin/Streptomycin (P/S). Once cells reached 70% confluence, differentiation medium was added (DMEM 25 mM glucose supplemented with 5% horse serum (HS) and 1% P/S) and the cells were cultured for 5 days with fresh medium added every other day, sufficient to differentiate myoblasts into mature contractile myotubes.

Primary myotube culture

Experiments were conducted consistent with current UK Home Office regulations in accordance with the UK Animals (Scientific Procedures) Act 1986, and approved by the local Animal Welfare and Ethical Review Body. Gastrocnemius muscle was collected from 16-week-old male C57BL/6NJ mice and placed in 0.2% collagenase, to allow for myofibre detachment and digestion and then washed in DMEM. Myofibres were placed in wells coated with Matrigel (BD biosciences), with DMEM containing 30% FBS, 10% HS, 1% chick embryo extract (CEE), 1% P/S and 0.1% fibroblast growth factor (FGF). Following satellite cell migration the media was replaced with proliferation media; DMEM supplemented with 10% HS, 0.5% CEE and 1% P/S. Once cells had attained 70–80% confluence the media was replaced with differentiation media (DMEM supplemented with 2% HS, 0.5% CEE and 1% P/S) and left to differentiate for 6 days, as previously described[24].

Cell treatments

Cells were either left as control or treated with 50 nM FK866 for 24 or 48 hours and then co-treated with 0.5 mM NR (Chromadex, California) for 4 hours. NMN treatments were the same as NR; 0.5 mM NMN for 4 hours. These concentrations were selected to provide a maximal effect on cellular NAD levels following previously published work in myotubes[25].

^{13}C-glucose and ^{13}C-glutamine labelling

Cells ($2x10^6$) were seeded into 15 cm dishes and differentiated for 5 days. For glucose labelling, freshly made flux media (DMEM powder (without glucose, L-glutamine, phenol red, sodium pyruvate or sodium bicarbonate), diluted in 1 litre of distilled water, supplemented with 2 mM glutamine and 45 mM sodium bicarbonate) was added to the cells 24 hours prior to extraction; 10 mM $^{13}C_2$-[1,2]-D-Glucose was then added and the cells were left to metabolise. For glutamine labelling the media was alternatively supplemented with 10 mM glucose, 45 mM sodium bicarbonate and 2 mM $^{13}C_5$-glutamine.

Extraction of metabolites from cells

Media was aspirated and plates were washed with ice-cold 0.9% saline solution before being placed on dry ice to quench metabolism prior to extraction of metabolites. 1.2 ml HPLC-grade methanol (-80°C) was added to the plate. The cells were scraped using a cell scraper and transferred to a falcon tube where 1.2 ml of HPLC-grade chloroform (-20°C) was added. The tube was rocked at 4°C for 10 minutes before 1.2 ml pre-chilled HPLC-grade H_2O was added and left to rest on ice for 10 minutes. Separation of the polar and non-polar fractions was achieved through centrifugation at 4°C, 14,200 rpm for 15 minutes. Next, 2 ml of the polar fraction was stored for NMR analysis, with 200 µl removed for GC-MS. Both fractions were evaporated to dryness using a SpeedVac at 30°C for 4–5 hours and stored at -80°C until further analysis. Protein pellet weights were used for normalisation during analysis; extractions were conducted on at least three different experiments.

NMR spectroscopy

Dried NMR samples were re-suspended in 100 mM sodium phosphate buffer containing 500 µM 4,4-dimethyl-4-silapentant-1-sulfonic acid (DSS) and 10% deuterium (D_2O), pH 7.0. Samples were sonicated and transferred to glass vials before being moved to 1.7 mm NMR tubes using a Gilson robotic system.

A Bruker Avance III 600 MHz NMR spectrometer equipped with a 1.7 mm z-PFG TCI Cryoprobe was used to acquire 2D 1H,13C-HSQC NMR spectra. The HSQC spectra were acquired with echo/anti-echo gradient coherence selection with an additional pre-saturation for suppressing the water resonance. The spectral widths were 13.018 ppm and 160.0544 ppm in the direct and indirect dimension, 512 complex data points were acquired for the 1H dimension and 29.9927% (2457) out of 8192 complex data points were acquired for the 13C indirect dimension using a non-uniform sampling scheme. The interscan relaxation delay was set to 1.5 s. 2D 1H,13C-HSQC spectra were reconstructed via the compressed sensing algorithm using the MDDNMR (version 2.5) and NMRPipe (version 9.2) software[26–28]. All spectra were processed without baseline correction as this can present challenges for the multiplet analysis procedure.

A total of 128 transients were acquired for each 1D-^{1}H NMR spectrum with a relaxation delay of 4 s. Each sample underwent automatic tuning and matching before they were shimmed (1D-TopShimm) to a DSS line width of <1 Hz prior to acquisition of the first spectrum. Total experiment time was 4 h 45 min per sample; ~15 min for 1D-^{1}H-NMR and 4.5 h for 2D-^{1}H,^{13}C-HSQC NMR spectra. All 1D-1H NMR spectra were processed using MetaboLab software (version 1). Data analysis was performed using MetaboLab with the methyl group of lactate used to calibrate the chemical shift[29]. Prior to Fourier Transformation all 1D-^{1}H-NMR spectra were zero-filled to 131,072 data points, the chemical shift was then calibrated by referencing the DSS signal to 0 ppm and the spectra were manually phase-corrected. Once complete, the baseline correction was conducted using a spline function (ref: 61) and the spectra were exported into Bruker format to allow for metabolite identification and quantification using the Chenomx software package (ChenomxINC, version 7.0). All metabolite concentrations were normalised to pellet weight.

GC-MS

Polar metabolites were solubilised in 2% methoxyamine hydrochloric acid (HCL) in pyridine. The samples were vortexed before being incubated at 60°C for 60 minutes. Following this incubation the derivatisation reagent was added; 60 µl N-tertbutyldimethylsilyl-N-methyltrifluoroacetamide (MTBSTFA) with 1% (w/v) tertbutyldimethyl-chlorosilane (TBDMSCI) (Sigma-Aldrich). The suspension was incubated for 1 h at 60°C in a closed tube to prevent evaporation. The samples were centrifuged at 13,000 rpm for 5 min and the clear supernatant was transferred to a chromatography vial with a glass insert (Thermo Fisher). Derivatised samples were analysed using an Agilent 7890B Series GC/MSD gas chromatograph with a medium polar range polydimethylsiloxane GC column (DB35-MS), in association with a mass spectrometer (GC-MS) (Agilent Technologies). Metabolite ion counts were normalised to pellet weight.

Glycogen assay

Glycogen was extracted from differentiated C2C12s and quantified using a Glycogen Assay Kit (Sigma-Aldrich) according to the manufacturer's instructions.

Respirometry

C2C12s were differentiated for 5 days and treated with 50 nM FK866 for 48 or 72 h. Mitochondrial function was then determined using a two-chamber Oxygraph (OROBOROS Instruments) derived from polarographic oxygen flux measurements. Prior to loading into the chambers cells were removed from the plates by Trypsin and spun down to form a pellet before being suspended in 2 ml DMEM. Once within the chambers the cells were left to incubate for 10 min to measure their endogenous respiration. Following this 10 µg/2 ml of digitonin was added to permeabilise the cells. Assessment of oxidation capacity was carried out by sequentially subjecting the cells to differing concentrations of substrate as follows; 2 mM malate

and 10 mM glutamate as a substrate for complex I and determination of complex I respiratory capacity, 5 mM increments of ADP until maximal oxidative phosphorylation and induction of state III respiration, 10 µM cytochrome c as a control for mitochondrial membrane damage, 20 mM succinate as a substrate for complex II and assessment of complex I + II respiratory capacity, 0.5 mM carbonyl cyanide-*4*-(trifluoromethoxy) phenylhydrazone (FCCP) titrations until maximal respiration increase to determine maximal uncoupled respiratory capacity, 0.5 µM rotenone for inhibition of complex I and assessment of complex II maximal respiratory capacity, and 2.5 µM antimycin A for inhibition of complex III to determine residual oxygen consumption. Following experiment chamber contents were collected, spun down, washed in PBS and a Bradford assay was conducted to calculate protein levels within each sample. These were then used to determine oxygen flux/mg of protein. Respiratory substrate stocks were diluted in ddH_2O, while uncouplers and inhibitors were diluted in absolute ethanol.

LCMS

Prepared samples were analysed on a LCMS platform consisting of an Accela 600 LC system and an Exactive mass spectrometer (Thermo Scientific). A Sequant ZIC-pHILIC column (4.6 mm × 150 mm, 5 µm) (Merck) was used to separate the metabolites with the mobile phase mixed by A= 20 mM ammonium carbonate in water and B= acetonitrile. A gradient program starting at 20% of A and linearly increasing to 80% at 30 min was used followed by washing (92% of A for 5 min) and re-equilibration (20% of A for 10 min) steps. The total run time of the method was 45 min. The LC stream was desolvated and ionised in the HESI probe. The Exactive mass spectrometer was operated in full scan mode over a mass range of 70–1,200 m/z at a resolution of 50,000 with polarity switching. The LCMS raw data was converted into mzML files by using ProteoWizard (v3.0.4472, 64-bit) and imported to MZMine (2.10) for peak extraction and sample alignment. A house-made database including all possible ^{13}C isotopic m/z values of the relevant metabolites was used for the assignment of LCMS signals. Finally the peak areas were used for comparative quantification.

Statistical analysis

All statistical analyses were carried out using the GraphPad Prism 6 software. One-way ANOVA analysis has been conducted on the concentrations of metabolites and percentages of label incorporation, with Dunnett's multiple comparisons post hoc test. This was to test differences between the treatment groups with statistical significance shown by * $p<0.05$, ** $p<0.01$, *** $p<0.001$, compared to control.

Results

NAD^+ excess does not impact pathway use in central carbon metabolism

NR and NMN supplementation as a strategy to increase or recover NAD^+ availability has been extensively used in models of pathophysiology associated with NAD^+ deficiency and impaired metabolism[11]. The wider metabolic consequences of increasing cellular NAD^+ above physiological levels have yet to be established. Therefore, we first examined the consequences of NAD^+ excess on metabolic pathway use and energetic status in muscle cells. Using 1D-^{1}H-NMR spectroscopy we quantified changes to key metabolites involved in NAD^+ metabolism following 0.5 mM NR or NMN supplementation in control cells. As expected, 4-hour NR and NMN were effective at significantly elevating intracellular NAD^+ levels in C2C12 cells, with a similar significant increase seen in primary myotubes following NR supplementation (Figure 1B, C). There was no effect of NR or NMN supplementation on $NADP^+$ in either C2C12s or primary myotubes (Figure 1D, E). NAM, the breakdown product and precursor of NAD^+, was significantly elevated in cells treated with NR and NMN. NR had a greater effect on NAM with a 9-fold increase above control compared to NMN (1.8-fold) (Figure 1F, G). NAM clearance was also elevated, with methylated NAM (MeNAM) levels significantly increased with NR but not NMN supplementation in C2C12s (Figure 1H). Interestingly, there was no change in MeNAM after NR supplementation in primary myotubes despite a large increase in NAM (Figure 1I). We used the phosphocreatine/creatine (PCr/Cr) ratio, to show there was no change in ATP demand as a result of NAD^+ excess following supplementation with either precursor in C2C12s or primary myotubes (Figure 1J, K).

To further characterise the effect of NAD^+ excess on carbon metabolism we used [1,2-^{13}C] D-glucose and conducted combined analysis of GC-MS and 2D-^{1}H,^{13}C-HSQC spectra to elucidate changes to metabolic pathway utilisation (Figure 1L). The use of [1,2-^{13}C] D-glucose as an isotopic tracer delivers distinct labelling patterns based on whether the PPP has been utilised, which we may expect to change with varying NAD^+ levels. Lactate was used as a measure of glycolytic and PPP activity, with no change observed in concentration or pathway utilisation with NR or NMN (Figure 1L–N). In order to identify TCA cycle changes aspartate was used as a surrogate; once again, no change in concentration or pathway use was observed (Figure 1O–R). To investigate whether a longer supplementation of NR would induce changes to carbon metabolism we conducted a 24-hour NR study. Similar to the 4-hour supplementation period, both NAM and MeNAM levels were elevated suggesting increased clearance of NAD^+ metabolites (Supplementary Figure 1C, D) but carbon metabolism was unchanged (Supplementary Figure 1G–H).

These data show that both acute and chronic NAD^+ excess within a skeletal muscle cell results in increased NAM clearance but has no immediate effect on energy homeostasis or central carbon metabolism based on the endpoints measured. We proceeded to use the 4-hour NR supplementation for our NAD^+ rescue experiments to show the acute effects of NAD^+ repletion using NR.

NR supplementation can rescue NAD^+ depletion and reverse FK866 induced energy stress

We next created a model of NAD^+ depletion in muscle cells to assess the consequences for central carbon metabolism. The NAMPT inhibitor FK866 was used to deplete NAD^+, and NR as a means to rescue (Figure 2A). We used 1D-^{1}H-NMR spectroscopy to confirm that the cell models were effective at altering NAD^+ levels and quantify key NAD^+-related metabolites. Treatment of both fully differentiated C2C12 and primary myotubes with 50 nM FK866 for 48-hours resulted in a 95% reduction in

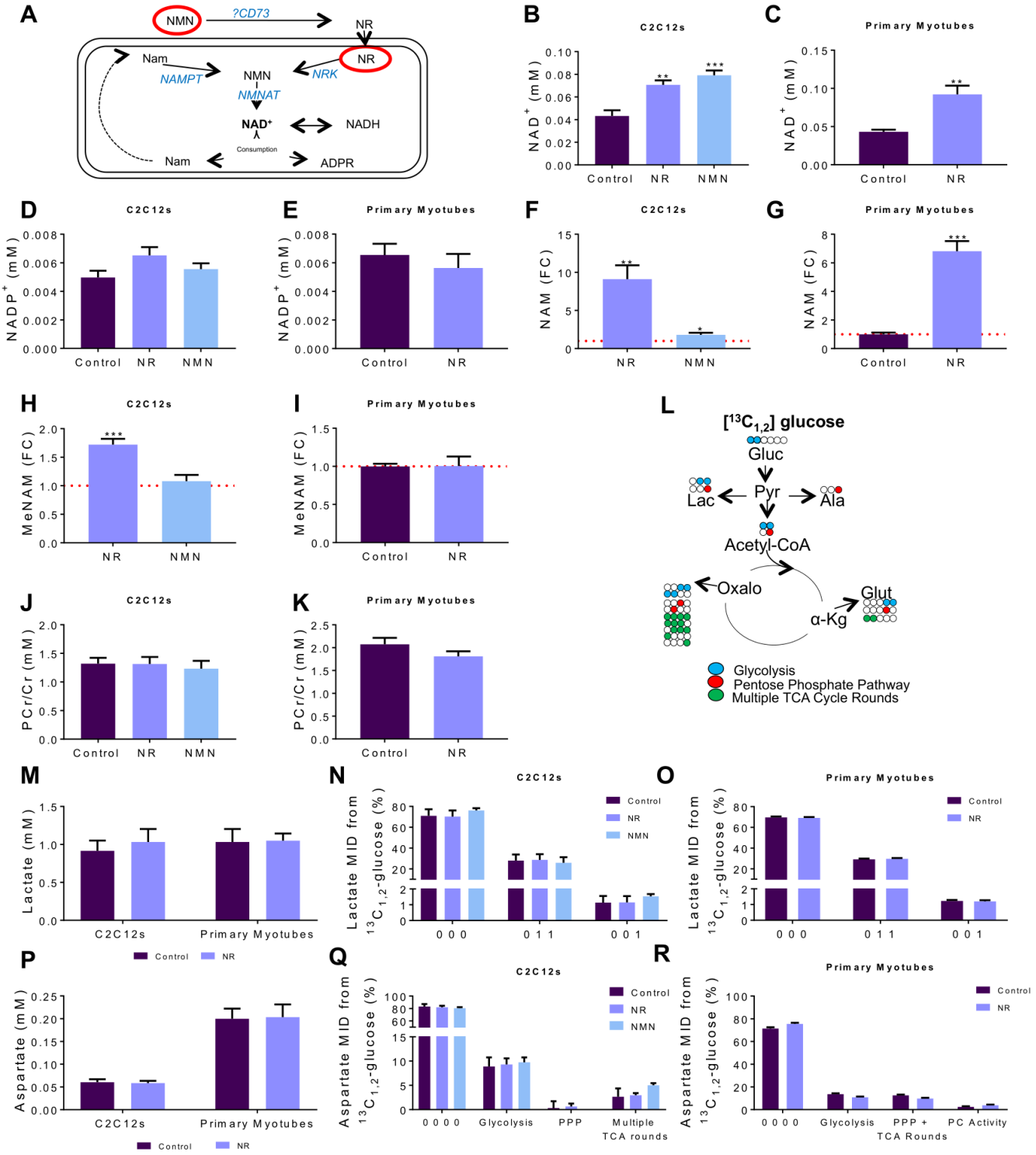


Figure 1. NAD⁺ excess has no consequence on pathway use within central carbon metabolism. Differentiated C2C12 and primary myotubes were treated with NR or NMN (0.5 mM) for 4 hours, pathway shown in (**A**). Key metabolites were identified and quantified using 1D-1H-NMR spectroscopy and used to inform on the energetic status of the cell; (**B**, **C**) NAD^+, (**D**, **E**) $NADP^+$. Fold-change compared to control were shown for (**F**, **G**) nicotinamide (NAM) and (**H**–**I**) methylated-nicotinamide (MeNAM); red line is representative of control levels. (**J**, **K**) The phosphocreatine (PCr)/creatine (Cr) ratio. (**L**) Resulting labelling patterns of glucose flux through metabolic pathways. Concentration and labelling patterns detected through combined analysis of 2D-^{1}H,^{13}C-NMR ($^{13}C_{1,2}$-glucose) and GC-MS data of (**M**–**O**) lactate and (**P**–**R**) aspartate. ^{13}C represented by 1 with ^{12}C represented by 0; % MID of total metabolite. All concentrations in mM. * p<0.05, ** p<0.01, ***p<0.005; One-way ANOVA performed on raw data; Dunnett's multiple comparison test, treatment compared to control. All data are the mean ±SEM, C2C12s n=6. Primary myotubes n=4. FC, fold change compared to control; MID, mass isotopomer distribution.

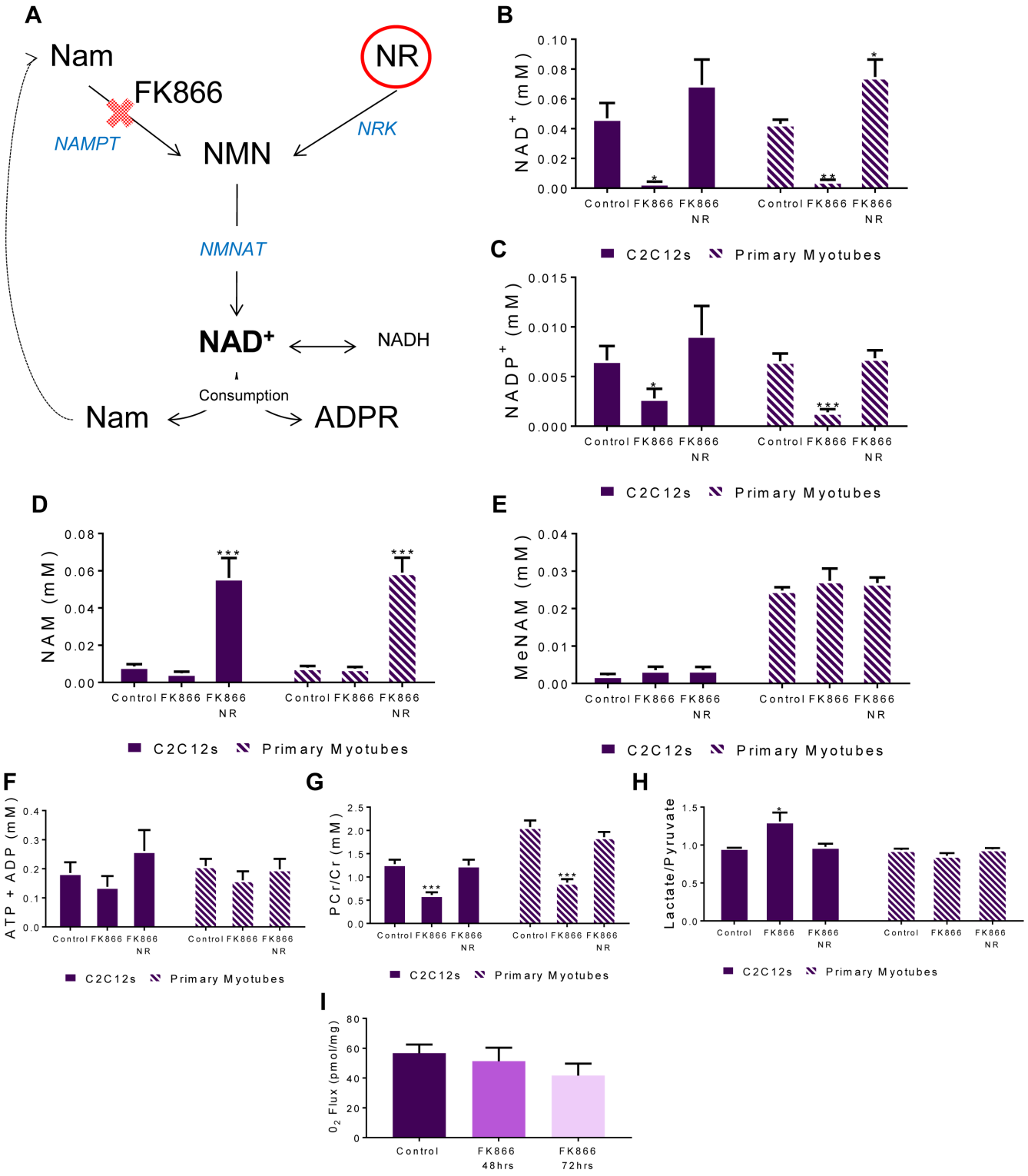


Figure 2. NAMPT inhibition induces energetic stress in skeletal muscle. Differentiated C2C12 and primary myotubes were treated with FK866 (50 nM) for 48 hours with and without NR (0.5 mM) for 4 hours, pathway shown in (**A**). Key metabolites were identified and quantified using 1D-^{1}H-NMR spectroscopy and used to inform on the energetic status of the cell; (**B**) NAD^{+}, (**C**) $NADP^{+}$, (**D**) nicotinamide (NAM), (**E**) methylated-nicotinamide (MeNAM), (**F**) combined ATP and ADP and (**G**) the phosphocreatine (PCr)/ creatine (Cr) ratio. (**H**) Lactate/ Pyruavte ratio from GC-MS analysis using the m=2 portion of the MID. (**I**) High resolution respirometry was carried out on differentiated C2C12s treated with 50 nM FK866 for 24, 48 or 72 hours. * $p<0.05$, ** $p<0.01$, ***$p<0.005$; One-way ANOVA performed on raw data; Dunnett's multiple comparison test, treatment compared to control. All data are the mean ±SEM, C2C12s n=6. Primary myotubes n=4.

NAD^+, which was rescued to above normal levels with 4-hour 0.5 mM NR supplementation (Figure 2B). $NADP^+$ levels were also significantly supressed by FK866 and restored with NR (Figure 2C), consistent with previous data[20]. NAM levels were unchanged with FK866 treatment but increased with the addition of NR (Figure 2D). Despite basal MeNAM concentrations being higher in primary myotubes compared to C2C12s the levels remained unchanged throughout the different treatment groups (Figure 2E). Additional metabolites of interest were measured by 1D-^{1}H-NMR (Table 1). There was no significant change detected in either lactate or alanine production through glycolysis following NAD^+ depletion (Supplementary Figure 2).

Although there was no change in overall ATP and ADP levels across the groups in either C2C12 or primary myotubes, the decrease in the PCr/Cr ratio shown in the FK866 samples is evidence the cells are buffering ATP availability in the face of metabolic stress induced by NAD^+ depletion (Figure 2F, G). Also suggestive of altered cytosolic redox is an increase in the lactate/pyruvate ratio, though this was only present in C2C12s (Figure 2H). To further understand whether the change to the PCr/Cr ratio and redox potential with NAD^+ depletion impacted energy metabolism, high-resolution mitochondrial respirometery was conducted and showed lowered maximal respiration following 72-hour FK866 treatment (Figure 2F).

Together these data show that NAD^+ depletion by inhibition of NAMPT alters the energy status of the cell through changes to the PCr/Cr ratio, which can be rescued through short-term NR supplementation, via the NRK enzymes[30]. The unchanged lactate and alanine data is equally interesting as it highlights how adaptable skeletal muscle cells are at coping with severely depleted NAD^+ levels.

NAD^+ depletion causes reversal of glycolytic reactions at NAD^+ dependent GAPDH

To understand how changes to energy metabolism pathways within the muscle cell affect metabolite levels, GC-MS ion count analysis was conducted on both C2C12s and primary myotubes. A significant increase in metabolites glyceraldehyde-3-phosphate (G3P) (Figure 3A) and glycerol-3-phosphate (Figure 3B), upstream of GAPDH were detected in 48-hour FK866 treated C2C12 and primary myotubes compared to untreated control myotubes. This effect was not observed in the 24-hour FK866-treated cells. Corroborating previous studies, this data is suggestive of an NAD^+-dependent reduction in activity of GAPDH, occurring between 24- and 48-hour NAD^+ depletion[19,20]. NR rescue in FK866-treated C2C12s was able to release the block evidenced by a reduction of GAP to control levels. This was not shown in the primary myotubes, with G3P levels remaining above control following NR supplementation. Presence of a block after 48-hour FK866 treatment was further supported by significantly reduced levels of downstream TCA cycle metabolites citrate, a-ketoglutarate (a-KG), and malate in C2C12s and primary myotubes (Figure 3C–H). NR rescue was effective at returning all metabolites to control levels in both models. The data is summarised as a schematic in Figure 3I. A number of other metabolites were identified through GC-MS ion count analysis (Table 2).

Table 1. Cellular metabolite concentrations from 1D-NMR spectra. Metabolite concentrations taken from 1D-NMR spectra analysed through Chenomx software.

Metabolite	Cellular Metabolite Concentrations (mM/mg of protein)					
	Control		FK866		FK866 NR	
	Mean	SEM	Mean	SEM	Mean	SEM
1,3-Dimethylurate	0.00	0.03	0.00	0.01	0.00	0.01
1,7-Dimethylxanthine	0.00	0.00	0.00	0.00	0.00	0.05
2-Aminoadipate	0.01	0.01	0.01	0.01	0.01	0.01
2-Aminobutyrate	0.06	0.08	0.06	0.08	0.07	0.07
2-Hydroxyisobutyrate	0.00	0.00	0.00	0.00	0.00	0.01
2-Hydroxyisocaproate	0.02	0.08	0.04	0.06	0.03	0.05
2-Oxoisocaproate	0.00	0.02	0.00	0.01	0.00	0.01
3-Hydroxyisovalerate	0.00	0.00	0.00	0.00	0.00	0.00
3-Methyl-2-oxovalerate	0.01	0.01	0.01	0.01	0.01	0.01
Acetoacetate	0.01	0.01	0.01	0.02	0.01	0.01
Alanine	0.07	0.12	0.08	0.10	0.09	0.15
Arabinose	0.03	0.05	0.04	0.22	0.04	0.04
Asparagine	0.00	0.01	0.00	0.01	0.01	0.01
Choline	0.01	0.02	0.01	0.01	0.01	0.02
Citrate	0.01	0.02	0.01	0.02	0.02	0.02
Dimethylamine	0.00	0.00	0.00	0.01	0.00	0.00
Fumarate	0.00	0.00	0.00	0.00	0.00	0.00
Galactarate	0.01	0.03	0.02	0.03	0.01	0.03
Glucose	0.00	0.01	0.14	0.01	0.01	0.09
Glutathione	0.05	0.06	0.05	0.06	0.06	0.06
Glycine	0.08	0.18	0.11*	0.21	0.15	0.20
Hydroxyacetone	0.01	0.02	0.01	0.02	0.02	0.02
Imidazole	0.00	0.02	0.01	0.00	0.00	0.01
Nicotinamide N-oxide	0.00	0.00	0.00	0.00	0.00	0.00
O-Acetylcarnitine	0.00	0.01	0.00	0.01	0.00	0.01
O-Acetylcholine	0.01	0.02	0.01	0.02	0.01	0.01
Phenylalanine	0.04	0.12	0.05	0.10	0.03	0.09
Pyruvate	0.01	0.01	0.01	0.02	0.01	0.02
Succinate	0.00	0.01	0.01	0.01	0.01	0.01
Taurine	0.26	0.45	0.29*	0.47	0.22	0.51
Threonine	0.07	0.09	0.09*	0.24	0.07	0.09
Tryptophan	0.01	0.02	0.01	0.01	0.01	0.02
Tyrosine	0.05	0.16	0.08	0.14	0.04	0.12
Valine	0.06	0.20	0.10	0.18	0.06	0.16

*$p<0.05$; Two-way ANOVA performed on all data; Dunnett's multiple comparison test. n=6.

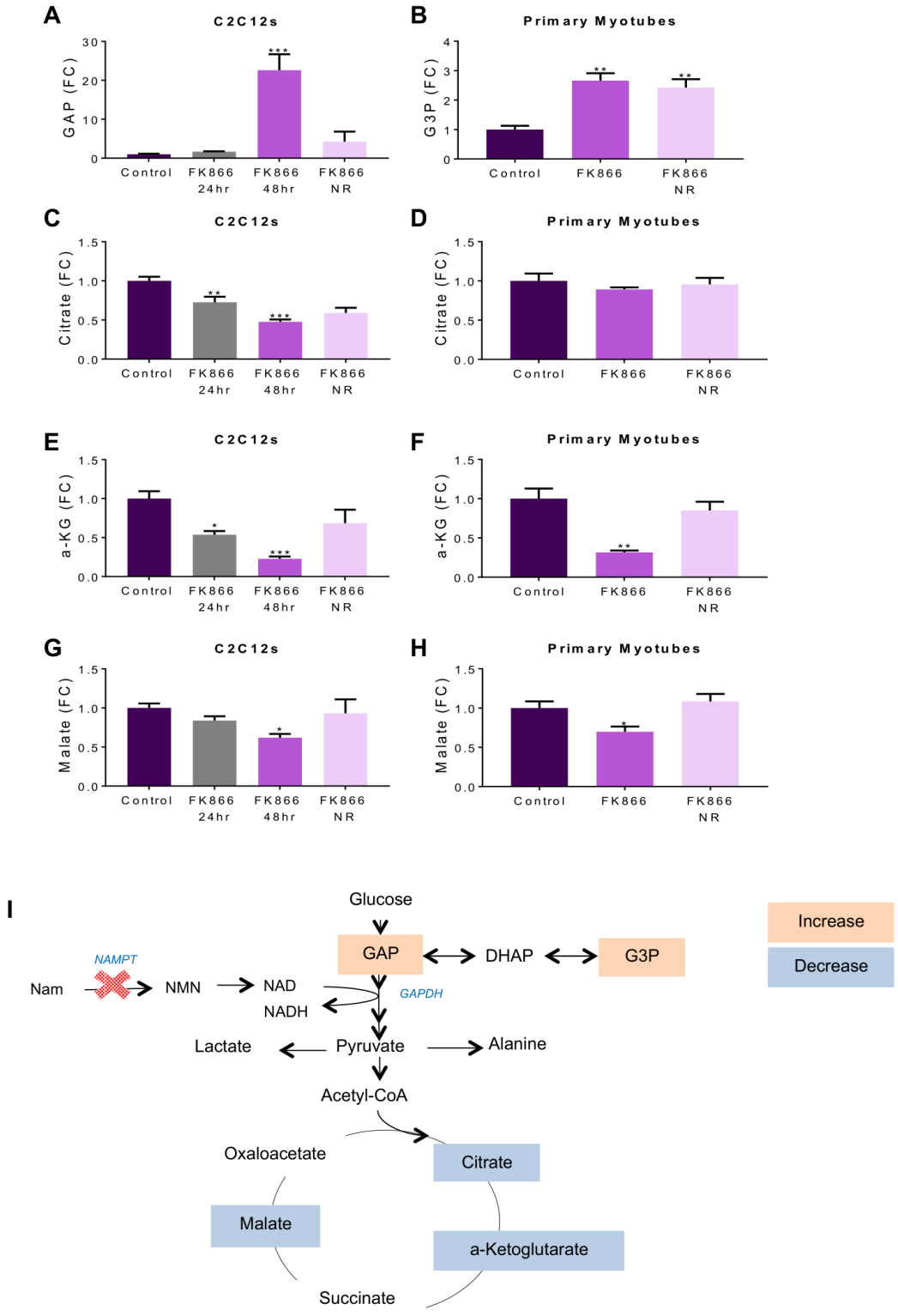


Figure 3. Block in glycolysis at GAPDH following NAD⁺ depletion. Data shown are fold changes of ion counts from GCMS compared to control in both NAD⁺ deplete (FK866; 48 h) and replete (FK866; 48 h + NR; 4 h) cells, showing (**A**) glyceraldehyde-3-phosphate, (**B**) glycerol-3-phosphate, (**C**, **D**) citrate, (**E**, **F**) a-ketoglutarate, (**G**, **H**) malate. (**I**) A diagrammatic representation of glycolysis and the TCA cycle in C2C12 and primary myotubes treated with FK866 for 48 h. An increase in ion count compared to control shown in peach and a decrease shown in blue. * p<0.05, ** p<0.01, ***p<0.005; One-way ANOVA performed on raw data; Dunnett's multiple comparison test, treatment compared to control. All data are the mean ±SEM, n=4.

Table 2. Cellular metabolite ion counts from GCMS. Ion counts taken from GCMS. No significant changes seen between conditions.

Metabolite	Cellular metabolite ion counts							
	Control		FK866 24h		FK866 48 h		FK866 48 h, NR 4h	
	Mean	SEM	Mean	SEM	Mean	SEM	Mean	SEM
Tryptophan	49720	57190	64405	55845	53202	52914	55327	47893
Serine	415367	164737	237489	187173	845253	783737	686931	1055501
Pyruvate	255065	168133	146860	97016	124497	13889	358317	191197
Proline	163717	121858	231244	177360	174065	207804	15691	11678
Malate	147186	112783	114083	89299	73951	64911	142479	159432
Lactate	8345878	7825695	8367333	5174489	7446052	5382583	8998869	3275040
Histidine	646757	551284	741234	488925	706205	654021	605624	362069
Glycine	9116697	7104045	8635419	6465350	7972076	7955743	8503790	6814356
G3P	1174906	826308	1530734	1046045	2273705	2037600	1700887	1223394
Glutamine	942572	1003918	1448528	791723	1545368	1797213	898866	858392
Fumarate	81303	67667	90462	60750	91008	76830	95761	69124
Cysteine	203170	263833	356747	119714	369724	210067	311876	86770
Alanine	1541322	730418	967774	739846	1398345	1367006	1349550	1382444
3-PG	11227	11048	15149	6286	22499	33977	16770	11633

*** p<0.005; Two-way ANOVA performed on all data; Dunnett's multiple comparison test. n=4.

We hypothesised that the accumulation of G3P would result in a shift in equilibrium and therefore reversal of glycolytic reactions. In order to study this, we measured fructose-6-phosphate using 2D-^{1}H-^{13}C-HSQC NMR spectroscopy. The resultant labelling patterns from the different metabolic routes are outlined in Figure 4A. We noted elevated ^{13}C-label incorporation in carbon 1 of 48-hour FK866 samples compared to both control and 24-hour FK866 samples. This was interesting but could be anticipated as a result of glycolysis using [1,2-^{13}C] D-glucose (Figure 4B). Investigation of the label incorporation into carbon 5 of fructose-6-phopshate also highlighted 48-hour FK866 samples as showing a differential labelling pattern compared to 24-hour FK866 and control samples (Figure 4C). We concluded that these labelling patterns could only be produced through reverse glycolytic flux which we suggest to be the result of an NAD^{+}-dependent block at GAPDH. To test this hypothesis using an alternative method we employed LCMS analysis of FK866 samples traced with [U-^{13}C] D-glucose. A significant increase in the m+6 portion of fructose-1,6-bisphosphate is shown with 48-hour FK866 treatment which is normalised with the addition of NR (Figure 4D). Again, this suggests NAD^{+} depletion can cause a build-up of metabolites above GAPDH and a reversal of glycolytic reactions. We postulated that this may constitute glycogenesis and therefore result in elevated glycogen levels within the FK866 samples, however glycogen storage appeared to be unaffected (Figure 4E).

NAD^{+} depletion leads to elevated mitochondrial derived aspartate

Following the reduced ion count shown of key TCA metabolites, as a result of the GAPDH block in FK866 samples, we were surprised to find a significantly elevated aspartate concentration in both C2C12 and primary myotubes (Figure 5A, B). Combined analysis of the 2D-^{1}H-^{13}C-HSQC spectra and GC-MS data showed significant alterations to pathway utilisation for aspartate, evidenced by differential labelling patterns occurring after FK866 treatment, which were reversed with an acute dose of NR (Figure 5C, D). The absolute amount of aspartate produced from each pathway is presented in Figure 5E, F, which not only shows increased aspartate production through glycolysis and the TCA cycle, but also an elevated unlabelled proportion of the metabolite. Generation of unlabelled aspartate is evidence of a non-glucose carbon source being used; in the absence of NAD^{+} we postulated that the cell may favour glutamine use over NAD^{+} dependent glycolysis. To investigate this, we used [U-^{13}C] glutamine as a nutrient. Label incorporation into aspartate from glutamine was significantly elevated in FK866 samples, but only in the 2-only labelled and 3-only labelled portion (Figure 5H). The metabolic route to these labelling patterns is shown in Figure 5G, and depicts increased glutamine use is only evident following multiple TCA cycle rounds. This shows that the cells do not use glutamine as a regular source of carbon for aspartate production under normal conditions, and only begin to do this in response to FK866 treatment.

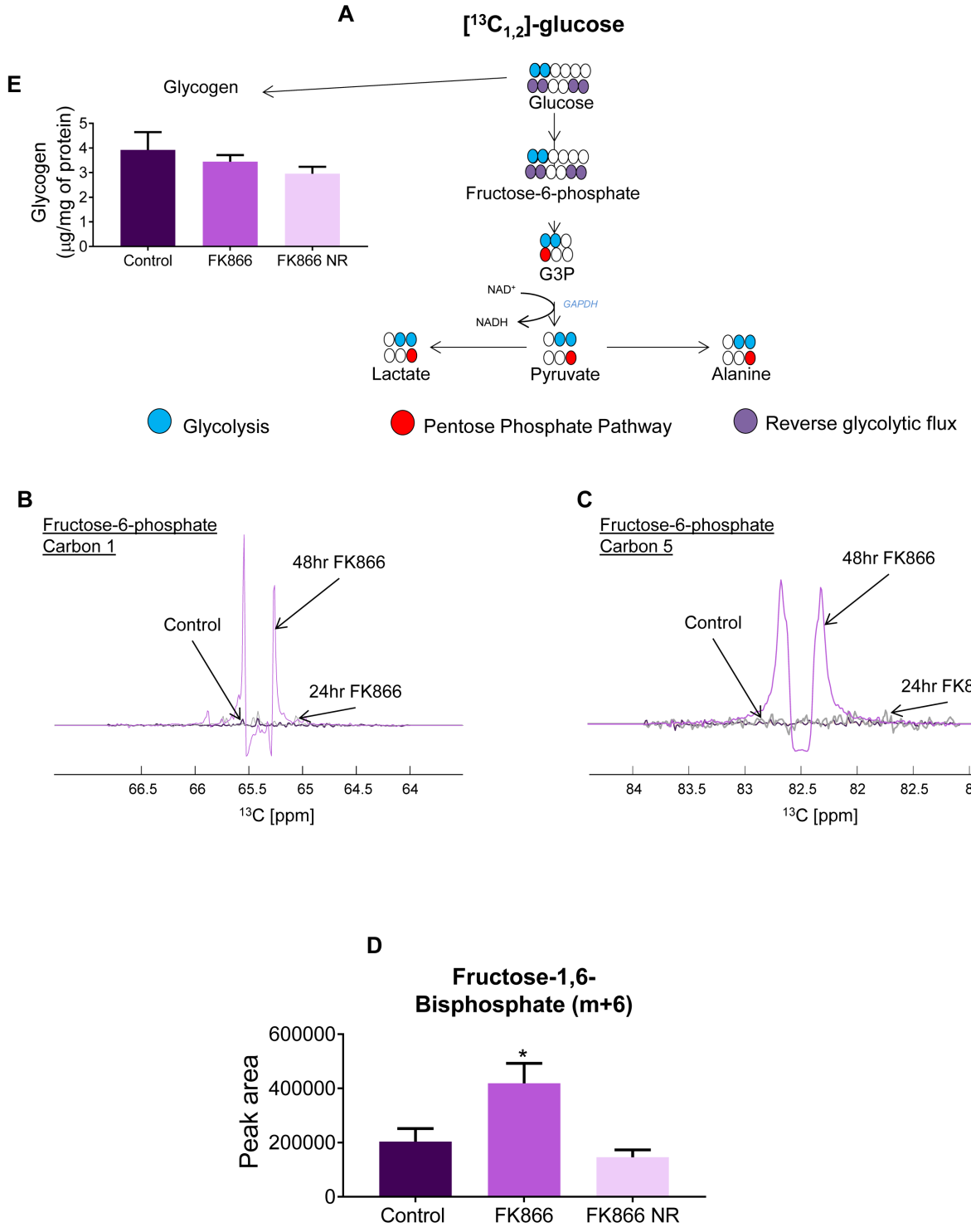


Figure 4. Investigation of reversed glycolytic reactions. Fructose-6-phosphate was used to investigate reversal of glycolytic reactions as it appears before the block at GAPDH. Representative 2D-^{1}H,^{13}C-HSQC spectra were used to show ^{13}C label incorporation in both control and FK866. (**A**) Carbon 1 shows peaks, therefore ^{13}C label, in both 48-hour FK866 samples; (**B**) carbon 5 shows peaks in the FK866 samples, with no presence of ^{13}C label in control or 24-hour FK866 samples. (**C**) Labelling pattern analysis shows how $^{13}C_{1,2}$-glucose is metabolised to 1,2-labelled fructose-6-phosphate during glycolysis, explaining the label incorporation in carbon 1 in both control and FK866 samples. The route to ^{13}C label in carbon 5 of fructose-6-phosphate is via 1,2-labelled glyceraldehyde-3-phosphate taking the backward reaction to fructose-1,6-bisphosphate. The presence of label incorporation in carbon 5 of FK866 samples is evidence of reversal of these reactions as a result of an NAD^{+}-dependent build-up of G3P. (**D**) Glycogen levels of C2C12s. (**E**) m+6 portion of fructose-1,6-bisphosphate as shown through LCMS analysis. * $p<0.05$, One-way ANOVA performed on raw data; Dunnett's multiple comparison test, treatment compared to control. All data are the mean ±SEM, n=3.

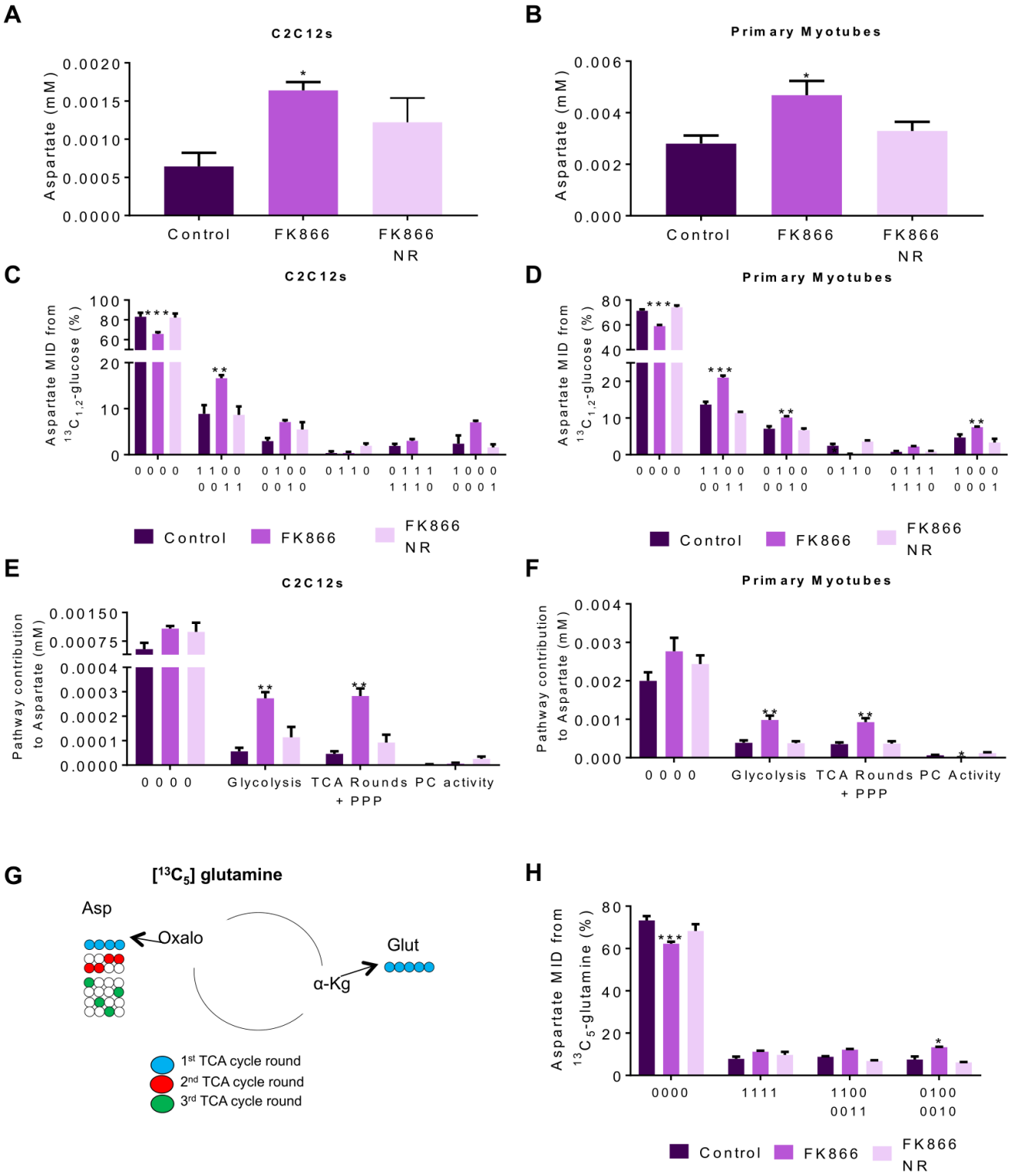


Figure 5. Pathway utilisation for aspartate production is significantly altered with NAD⁺ depletion. Differentiated C2C12 and primary myotubes were treated with FK866 (50 nM) for 48 hours with and without NR (0.5 mM) for 4 hours. Aspartate concentration in both (**A**) C2C12s and (**B**) primary myotubes from 1D-NMR spectra. (**C**, **D**) Combined analysis of 2D-1H,13C-NMR (13C1,2-glucose) and GC-MS data provides labelling patterns for aspartate; (**E**, **F**) labelling patterns allow analysis of pathway utilisation for aspartate production. (**G**) Labelling patterns observed through $^{13}C_6$-glutamine tracing. (**H**) Aspartate MIDs from combined 2D-1H,13C-NMR (13C5-glutamine) and GC-MS. Glycolysis 1100+0011; TCA rounds + PPP 0100+0010, 1111, 0111+1110, 1000+0001; PC Activity 0110. * p<0.05, ** p<0.01, ***p<0.005; One-way ANOVA performed on raw data; Dunnett's multiple comparison test, treatment compared to control. All data are the mean ±SEM, n=4.

We postulated that the build-up of aspartate may be a result of impaired malate-aspartate shuttle (MAS) functioning as a result of perturbed cytosolic redox potential, as evidenced by the elevated lactate/pyruvate ratio. We tested this hypothesis using a MAS inhibitor in combination with [1,2-^{13}C] D-glucose. We were successful in increasing the lactate/pyruvate ratio (Supplementary Figure 3A) and as a result increased NADH oxidation for this reaction in the cytosol. We decreased pyruvate entering the mitochondria, resulting in depleted TCA metabolite levels (Supplementary Figure 3B, C) and significantly less glucose label incorporation into glutamate (Supplementary Figure 3F). However, the effect on aspartate did not follow what we had previously seen with NAD$^+$ depletion, with no increased levels and less label incorporation as opposed to more (Supplementary Figure 3D, E). NR was able to elevate NAD$^+$ levels but had no other effect on the MAS inhibitor treated cells (Supplementary Figure 3G). Aspartate production following NAD$^+$ depletion may serve as a muscle adaptive response, reversible with NR.

Discussion

Observation of elevated cellular NAD$^+$ content in response to exercise[31,32] and calorie restriction[33] as a metabolic switch signalling augmented energy harvesting in muscle has prompted a focus on ways to increase NAD$^+$ availability for treatment of metabolic disease in humans. Despite measurements linking a decline in NAD$^+$ levels to altered metabolism, there is limited data showing the impact that NAD$^+$ depletion, and also excess, could have on core cellular metabolism in muscle[10–12].

Supplementation of NAD$^+$ precursors in untreated cells results in an 'NAD$^+$-boost' above control levels. The methodology employed in this study is key to understanding changes to metabolic pathway usage. It was therefore surprising to discover that there was no alteration to the PPP activity or glycolysis in response to elevated NAD$^+$. It became apparent that skeletal muscle cells rapidly adapt to an 'NAD$^+$-boost' by increasing NAD$^+$ clearance through NAM and MeNAM to protect the careful redox balance, seemingly to ensure central carbon metabolism is unaffected[34].

A better understanding of the potential consequences of increased NAM and MeNAM clearance following NAD$^+$ excess is important. Increased clearance will lead to increased levels circulating in the blood and ultimately elevated excretion in the urine, with previous studies suggesting high levels may exhibit adverse effects[35–37]. With elevated NAM in the blood there is increased substrate availibility for eNAMPT, extracellular NAMPT. The role of eNAMPT, although controversial, has been linked to modulating the immune response and regulating glucose stimulated insulin secretion from β-cells of the pancreas[38]. This could suggest that excess NAM may affect glucose homeostasis within the body. In addition, these metabolites could also be taken up by various tissues and have shown to cross the blood-brain barrier where there is strong evidence that they exhibit neuroprotection[39–41]. However, at high concentrations NAM and MeNAM can have a toxic effect on neurons, as shown in Parkinson's and Huntington's disease models[42–44]. Similarly, NAM has been shown to be effective for management of hyperphosphatemia in patients with renal disease[45]; however, it is also suggested to be a uremic toxin contributing to thrombocytopenia[46,47]. Whilst there have been studies showing NR safely elevates NAD$^+$ in human blood[16,17,48] it is important to consider that creating a state of NAD$^+$ excess and increasing clearance of NAM and MeNAM could potentially have unintended effects in the CNS and for kidney function, alongside other possible off-target effects.

Supplementation with NR and NMN in pre-clinical animal studies has shown similar therapeutic effects in disease conditions to preserve metabolic health and ameliorate age-related decline[15]. This prompted us to utilise both of these supplements to create an NAD$^+$ excess and understand the impact they have on a skeletal muscle cell. These data show a difference between the NAD$^+$ precursors, with a greater elevation of the clearance products, NAM and MeNAM, in NR compared to NMN treated cells. In order for mammalian cells to take up NMN and utilise it for NAD$^+$ synthesis, it must first be converted to NR, which could account for the apparent decreased clearance rate compared to NR[24,49]. This is consistent with recent work conducted in mice showing that skeletal muscle metabolises NR faster than NMN[50]. An alternative explanation for the elevated NAM detected with NR may be due to its relative instability compared to NMN in culture medium, meaning it is possible that we are measuring NAM taken up by cells from the media due to NR degradation as opposed to intracellular NAD$^+$ consumption[49].

NAMPT inhibition significantly depletes NAD$^+$, confirming this as the main pathway for basal NAD$^+$ synthesis within skeletal muscle[12]. NAM levels are carefully balanced between consumption, through NAD$^+$ synthesis, and production, through NAD$^+$ breakdown. NR rescue of FK866 treated cells causes an increase in NAM, suggestive of increased NAD$^+$ breakdown, with NAMPT inhibition preventing NAM being used for NAD$^+$ synthesis, therefore causing an accumulation. However, this build-up did not result in increased clearance through MeNAM possibly due to a delay in establishing NAD$^+$ and NAM excess as FK866 treated cells must recover basal NAD$^+$ levels first.

Evidence of disrupted energy homeostasis was seen with the reduction of the PCr/Cr ratio in NAD$^+$-depleted cells. The hydrolysis of phosphocreatine and the resultant release of a phosphate group provides an alternative route to ATP production, avoiding carbohydrate metabolism and oxidative phosphorylation, which are both NAD$^+$ dependent[51,52]. However, the levels of PCr are finite and therefore the cell cannot rely on this method of ATP synthesis indefinitely[35]. Importantly, supplementation with NR was sufficient to normalise NAD$^+$ levels and prevented requirement for alternative ATP synthesis.

A significant effect of NAD$^+$ depletion is inhibition of GAPDH, the first NAD$^+$-dependent step of glycolysis. The build-up of metabolites before the enzyme, coupled with the decrease in metabolites observed downstream in response to NAMPT inhibition corroborates previous studies in cancer cells and C2C12s[12,19]. The advanced analysis conducted through the

combined NMR and GCMS methodology allowed us to confirm the reversal of the glycolytic reactions above the block, not just through steady-state metabolite levels, but also through label incorporation into fructose-6-phosphate. This highlighted that although changes to metabolite concentrations were observed after 24-hour FK866 treatment, the inhibition of cytosolic GAPDH, and reversal of glycolytic reactions, is not detected until the 48-hour time-point.

Aspartate is a partner in a number of cellular metabolic energy cycles. Previous work using a malate-aspartate shuttle inhibitor in vascular smooth muscle yielded similar results to our FK866 treatment of an increase in glucose-derived aspartate[36]. A key limitation of our experiment may be the mechanism of action of the inhibitor, given it indirectly inhibits the shuttle functioning by acting on cytosolic aspartate aminotransferase[37]. This therefore does not confirm whether a different aspect of the shuttle may be impaired in our model, but does show that the results are unlikely to be a result of compromised cytosolic aspartate aminotransferase activity. Aspartate is also a key component in the purine nucleotide cycle, which is active in skeletal muscle in response to energy depletion, removing AMP to promote ATP synthesis and could provide an alternative use for the aspartate build-up[53]. Elevated aspartate has also been reported in cells treated with the mitochondrial uncoupler FCCP[54], supporting the notion that the effects are a result of perturbed cytosolic redox. Elevated GAP and G3P observed with NAMPT inhibition may represent an attempt to maintain the redox potential within the cytosol, by utilising the glycerol-3-phosphate/dihydroxyacetone phosphate shuttle to regenerate NAD^+ and provide protons to the electron transport chain[55].

Aspartate could be a marker of a preserved mitochondrial NAD^+ pool allowing for continued TCA cycle activity despite cytosolic NAD^+ depletion. This is supported by our data indicating mitochondrial respiration still occurs despite severe NAD^+ depletion. NAD^+/NADH ratios differ greatly between subcellular compartments, with mitochondrial redox more tightly regulated compared to the cytosol[56,57]. The notion of a protected mitochondrial NAD^+ pool is suggested in other studies, which have indicated that FK866 treatment affects cytosolic NAD^+ but does not disrupt the mitochondrial NAD^+ pool[12,20,58]. Together this suggests that skeletal muscle is able to resist disruptions to mitochondrial metabolism and maintain oxidative function despite severe NAD^+ depletion.

The methods employed in this study provide a high-resolution insight into metabolism and changes to metabolic pathways. Detailed analysis of energy metabolism pathways, as conducted here, could be key to understanding disease pathophysiology and may uncover novel cellular adaptations, which are not seen using other methods.

In conclusion, these data show NR is acutely effective at reversing changes to central carbon metabolism observed following severe NAD^+ depletion. NR and NMN in skeletal muscle cells does not impact carbon metabolism but does increase clearance products of NAD^+, which may impact other tissues in whole body metabolism. We observed a change in aspartate production with regard to both concentration and route to production. Understanding whether this is a cellular adaptation to low NAD^+ or if there is a functional use of the aspartate requires further investigation and could provide insight into how our skeletal muscle copes with energy stress.

Data availability

Datasets for the study "Metabolic tracing reveals novel adaptations to skeletal muscle cell energy production pathways in response to NAD+ depletion" are available on figshare; DOI: https://doi.org/10.6084/m9.figshare.7271573[59]. Included are raw NMR data, GC-MS data, and raw and processed concentrations of metabolites.

Data are available under the terms of the Creative Commons Zero "No rights reserved" data waiver (CC0 1.0 Public domain dedication).

Extended data

The supplementary figures are available to view on figshare,

Supplementary Figure 1. Chronic NR supplementation.
1D-1H-NMR spectroscopy shows (A) NAD+ and (B) NADP+ concentrations in C2C12s in response to 24-hour NR supplementation. Fold-change compared to control shown for (C) NAM and (D) MeNAM. Energetic status of the cell was investigated through (E) ATP and (F) PCr/Cr ratio. Combined analysis of 2D-1H,13C-NMR (13C1,2-glucose) and GC-MS data of (G) lactate and (H) aspartate. One-way ANOVA performed on raw data; Dunnett's multiple comparison test, treatment compared to control. All data are the mean ±SEM, C2C12s n=4. DOI: 10.6084/m9.figshare.9785156

Supplementary Figure 2. Glycolytic outputs, lactate and alanine, unaffected by NAD+ depletion.
Differentiated C2C12 and primary myotubes were treated with FK866 (50 nM) for 48 hours with and without NR (0.5 mM) for 4 hours. 1D-1H-NMR spectroscopy shows (A) Lactate concentration in C2C12 and primary myotubes (mM/mg of protein). Combined 2D-1H-13C-NMR and GC-MS analysis shows pathway contribution to lactate in (B) C2C12 and (C) primary myotubes. Alanine concentration (mM/mg of protein) in (D) C2C12s and (E) primary myotubes with alanine pathway analysis in (F) C2C12 and (G) primary myotubes. One-way ANOVA performed on all data, with individual pathways assessed independently; Dunnett's multiple comparison test, treatment compared to control. All data are the mean ±SEM, n=4. DOI: 10.6084/m9.figshare.9785165

Supplementary Figure 3. MAS Inhibitor does not have same effect as FK866 treatment.
Differentiated C2C12s were treated with 0.5 mM AOAA (MAS Inhibitor) for 24 hours with or without 0.5 mM NR for 4 hours. (A) Lactate/Pyruvate ratio from GC-MS analysis using the m=2 portion of the MID. GCMS ion count fold changes

compared to control for (B) a-KG, (C) succinate and (D) aspartate. MIDs from GCMS analysis for (E) aspartate and (F) glutamate. 1D-1H-NMR spectroscopy shows (G) NAD+ concentration (mM/mg of protein). MAS – Malate aspartate shuttle. * p<0.05, ** p<0.01, ***p<0.005; One-way ANOVA performed on all data, with individual MIDs assessed independently; Dunnett's multiple comparison test, treatment compared to control. All data are the mean ±SEM, n=3. DOI: 10.6084/m9.figshare.9785168

Acknowledgements

We thank ChromaDex (Irvine, California) for providing nicotinamide riboside and for helpful discussions.

Supplementary material

Supplementary Figure 1. Chronic NR supplementation.
1D-1H-NMR spectroscopy shows (A) NAD+ and (B) NADP+ concentrations in C2C12s in response to 24-hour NR supplementation. Fold-change compared to control shown for (C) NAM and (D) MeNAM. Energetic status of the cell was investigated through (E) ATP and (F) PCr/Cr ratio. Combined analysis of 2D-1H,13C-NMR (13C1,2-glucose) and GC-MS data of (G) lactate and (H) aspartate. One-way ANOVA performed on raw data; Dunnett's multiple comparison test, treatment compared to control. All data are the mean ±SEM, C2C12s n=4.
Click here to access the data

Supplementary Figure 2. Glycolytic outputs, lactate and alanine, unaffected by NAD+ depletion.
Differentiated C2C12 and primary myotubes were treated with FK866 (50 nM) for 48 hours with and without NR (0.5 mM) for 4 hours. 1D-1H-NMR spectroscopy shows (A) Lactate concentration in C2C12 and primary myotubes (mM/mg of protein). Combined 2D-1H-13C-NMR and GC-MS analysis shows pathway contribution to lactate in (B) C2C12 and (C) primary myotubes. Alanine concentration (mM/mg of protein) in (D) C2C12s and (E) primary myotubes with alanine pathway analysis in (F) C2C12 and (G) primary myotubes. One-way ANOVA performed on all data, with individual pathways assessed independently; Dunnett's multiple comparison test, treatment compared to control. All data are the mean ±SEM, n=4.
Click here to access the data

Supplementary Figure 3. MAS Inhibitor does not have same effect as FK866 treatment.
Differentiated C2C12s were treated with 0.5 mM AOAA (MAS Inhibitor) for 24 hours with or without 0.5 mM NR for 4 hours. (A) Lactate/Pyruvate ratio from GC-MS analysis using the m=2 portion of the MID. GCMS ion count fold changes compared to control for (B) a-KG, (C) succinate and (D) aspartate. MIDs from GCMS analysis for (E) aspartate and (F) glutamate. 1D-1H-NMR spectroscopy shows (G) NAD+ concentration (mM/mg of protein). MAS – Malate aspartate shuttle. * p<0.05, ** p<0.01, ***p<0.005; One-way ANOVA performed on all data, with individual MIDs assessed independently; Dunnett's multiple comparison test, treatment compared to control. All data are the mean ±SEM, n=3.
Click here to access the data

References

1. Hung YP, Albeck JG, Tantama M, *et al.*: **Imaging cytosolic NADH-NAD$^+$ redox state with a genetically encoded fluorescent biosensor.** *Cell Metab.* 2011; **14**(4): 545–54.
PubMed Abstract | Publisher Full Text | Free Full Text
2. Rongvaux A, Andris F, Van Gool F, *et al.*: **Reconstructing eukaryotic NAD metabolism.** *Bioessays.* 2003; **25**(7): 683–690.
PubMed Abstract | Publisher Full Text
3. Kushmerick MJ, Moerland TS, Wiseman RW: **Mammalian skeletal muscle fibers distinguished by contents of phosphocreatine, ATP, and Pi.** *Proc Natl Acad Sci U S A.* 1992; **89**(16): 7521–5.
PubMed Abstract | Publisher Full Text | Free Full Text
4. Belenky P, Racette FG, Bogan KL, *et al.*: **Nicotinamide riboside promotes Sir2 silencing and extends lifespan via Nrk and Urh1/Pnp1/Meu1 pathways to NAD$^+$.** *Cell.* 2007; **129**(3): 473–484.
PubMed Abstract | Publisher Full Text
5. Camacho-Pereira J, Tarragó MG, Chini CCS, *et al.*: **CD38 Dictates Age-Related NAD Decline and Mitochondrial Dysfunction through an SIRT3-Dependent Mechanism.** *Cell Metab.* 2016; **23**(6): 1127–1139.
PubMed Abstract | Publisher Full Text | Free Full Text
6. Bai P, Cantó C, Oudart H, *et al.*: **PARP-1 inhibition increases mitochondrial metabolism through SIRT1 activation.** *Cell Metab.* 2011; **13**(4): 461–468.
PubMed Abstract | Publisher Full Text | Free Full Text
7. Argilés JM, Campos N, Lopez-Pedrosa JM, *et al.*: **Skeletal Muscle Regulates Metabolism via Interorgan Crosstalk: Roles in Health and Disease.** *J Am Med Dir Assoc.* 2016; **17**(9): 789–796.
PubMed Abstract | Publisher Full Text
8. Fu X, Zhu M, Zhang S, *et al.*: **Obesity Impairs Skeletal Muscle Regeneration Through Inhibition of AMPK.** *Diabetes.* 2016; **65**(1): 188–200.
PubMed Abstract | Publisher Full Text | Free Full Text
9. Phielix E, Mensink M: **Type 2 diabetes mellitus and skeletal muscle metabolic function.** *Physiol Behav.* 2008; **94**(2): 252–258.
PubMed Abstract | Publisher Full Text
10. Gomes AP, Price NL, Ling AJ, *et al.*: **Declining NAD$^+$ induces a pseudohypoxic state disrupting nuclear-mitochondrial communication during aging.** *Cell.*

2013; **155**(7): 1624–1638.
PubMed Abstract | Publisher Full Text | Free Full Text

11. Yoshino J, Mills KF, Yoon MJ, *et al.*: **Nicotinamide mononucleotide, a key NAD⁺ intermediate, treats the pathophysiology of diet- and age-induced diabetes in mice.** *Cell Metab.* 2011; **14**(4): 528–536.
PubMed Abstract | Publisher Full Text | Free Full Text

12. Frederick DW, Loro E, Liu L, *et al.*: **Loss of NAD Homeostasis Leads to Progressive and Reversible Degeneration of Skeletal Muscle.** *Cell Metab.* 2016; **24**(2): 269–282.
PubMed Abstract | Publisher Full Text | Free Full Text

13. Mouchiroud L, Houtkooper RH, Moullan N, *et al.*: **The NAD(+)/Sirtuin Pathway Modulates Longevity through Activation of Mitochondrial UPR and FOXO Signaling.** *Cell.* 2013; **154**(2): 430–41.
PubMed Abstract | Publisher Full Text | Free Full Text

14. Frederick DW, Davis JG, Dávila A Jr, *et al.*: **Increasing NAD synthesis in muscle via nicotinamide phosphoribosyltransferase is not sufficient to promote oxidative metabolism.** *J Biol Chem.* 2015; **290**(3): 1546–1558.
PubMed Abstract | Publisher Full Text | Free Full Text

15. Yoshino J, Baur JA, Imai SI: **NAD⁺ Intermediates: The Biology and Therapeutic Potential of NMN and NR.** *Cell Metab.* 2018; **27**(3): 513–528.
PubMed Abstract | Publisher Full Text | Free Full Text

16. Martens CR, Denman BA, Mazzo MR, *et al.*: **Chronic nicotinamide riboside supplementation is well-tolerated and elevates NAD⁺ in healthy middle-aged and older adults.** *Nat Commun.* 2018; **9**(1): 1286.
PubMed Abstract | Publisher Full Text | Free Full Text

17. Trammell SA, Schmidt MS, Weidemann BJ, *et al.*: **Nicotinamide riboside is uniquely and orally bioavailable in mice and humans.** *Nat Commun.* 2016; **7**: 12948.
PubMed Abstract | Publisher Full Text | Free Full Text

18. Elhassan YS, Philp AA, Lavery GG: **Targeting NAD+ in Metabolic Disease: New Insights Into an Old Molecule.** *J Endocr Soc.* 2017; **1**(7): 816–835.
PubMed Abstract | Publisher Full Text | Free Full Text

19. Tan B, Dong S, Shepard RL, *et al.*: **Inhibition of Nicotinamide Phosphoribosyltransferase (NAMPT), an Enzyme Essential for NAD⁺ Biosynthesis, Leads to Altered Carbohydrate Metabolism in Cancer Cells.** *J Biol Chem.* 2015; **290**(25): 15812–15824.
PubMed Abstract | Publisher Full Text | Free Full Text

20. Tan B, Young DA, Lu ZH, *et al.*: **Pharmacological inhibition of nicotinamide phosphoribosyltransferase (NAMPT), an enzyme essential for NAD⁺ biosynthesis, in human cancer cells: metabolic basis and potential clinical implications.** *J Biol Chem.* 2013; **288**(5): 3500–3511.
PubMed Abstract | Publisher Full Text | Free Full Text

21. Barding GA Jr, Béni S, Fukao T, *et al.*: **Comparison of GC-MS and NMR for metabolite profiling of rice subjected to submergence stress.** *J Proteome Res.* 2013; **12**(2): 898–909.
PubMed Abstract | Publisher Full Text

22. Chong M, Jayaraman A, Marin S, *et al.*: **Combined Analysis of NMR and MS Spectra (CANMS).** *Angew Chem Int Ed Engl.* 2017; **56**(15): 4140–4144.
PubMed Abstract | Publisher Full Text

23. Smith TB, Patel K, Munford H, *et al.*: **High-Speed Tracer Analysis of Metabolism (HS-TrAM) [version 2; referees: 4 approved].** *Wellcome open Res.* 2018; **3**: 5.
PubMed Abstract | Publisher Full Text | Free Full Text

24. Fletcher RS, Ratajczak J, Doig CL, *et al.*: **Nicotinamide riboside kinases display redundancy in mediating nicotinamide mononucleotide and nicotinamide riboside metabolism in skeletal muscle cells.** *Mol Metab.* 2017; **6**(8): 819–832.
PubMed Abstract | Publisher Full Text | Free Full Text

25. Cantó C, Houtkooper RH, Pirinen E, *et al.*: **The NAD⁺ precursor nicotinamide riboside enhances oxidative metabolism and protects against high-fat diet-induced obesity.** *Cell Metab.* 2012; **15**(6): 838–47.
PubMed Abstract | Publisher Full Text | Free Full Text

26. Kazimierczuk K, Orekhov VY: **Accelerated NMR spectroscopy by using compressed sensing.** *Angew Chem Int Ed Engl.* 2011; **50**(24): 5556–5559.
PubMed Abstract | Publisher Full Text

27. Delaglio F, Grzesiek S, Vuister GW, *et al.*: **NMRPipe: a multidimensional spectral processing system based on UNIX pipes.** *J Biomol NMR.* 1995; **6**(3): 277–293.
PubMed Abstract | Publisher Full Text

28. Orekhov VY, Jaravine VA: **Analysis of non-uniformly sampled spectra with multi-dimensional decomposition.** *Prog Nucl Magn Reson Spectrosc.* 2011; **59**(3): 271–292.
PubMed Abstract | Publisher Full Text

29. Wishart DS, Tzur D, Knox C, *et al.*: **HMDB: the Human Metabolome Database.** *Nucleic Acids Res.* 2007; **35**(Database issue): D521–6.
PubMed Abstract | Publisher Full Text | Free Full Text

30. Bieganowski P, Brenner C: **Discoveries of nicotinamide riboside as a nutrient and conserved NRK genes establish a Preiss-Handler independent route to NAD⁺ in fungi and humans.** *Cell.* 2004; **117**(4): 495–502.
PubMed Abstract | Publisher Full Text

31. Cantó C, Gerhart-Hines Z, Feige JN, *et al.*: **AMPK regulates energy expenditure by modulating NAD⁺ metabolism and SIRT1 activity.** *Nature.* 2009; **458**(7241): 1056–1060.
PubMed Abstract | Publisher Full Text | Free Full Text

32. Costford SR, Bajpeyi S, Pasarica M, *et al.*: **Skeletal muscle NAMPT is induced by exercise in humans.** *Am J Physiol Endocrinol Metab.* 2010; **298**(1): E117–E126.
PubMed Abstract | Publisher Full Text | Free Full Text

33. Chen D, Bruno J, Easlon E, *et al.*: **Tissue-specific regulation of SIRT1 by calorie restriction.** *Genes Dev.* 2008; **22**(13): 1753–1757.
PubMed Abstract | Publisher Full Text | Free Full Text

34. Wu J, Jin Z, Zheng H, *et al.*: **Sources and implications of NADH/NAD⁺ redox imbalance in diabetes and its complications.** *Diabetes Metab Syndr Obes.* 2016; **9**: 145–53.
PubMed Abstract | Publisher Full Text | Free Full Text

35. Bogdanis GC, Nevill ME, Boobis LH, *et al.*: **Contribution of phosphocreatine and aerobic metabolism to energy supply during repeated sprint exercise.** *J Appl Physiol (1985).* 1996; **80**(3): 876–884.
PubMed Abstract | Publisher Full Text

36. Barron JT, Gu L, Parrillo JE: **Malate-aspartate shuttle, cytoplasmic NADH redox potential, and energetics in vascular smooth muscle.** *J Mol Cell Cardiol.* 1998; **30**(8): 1571–1579.
PubMed Abstract | Publisher Full Text

37. Kauppinen RA, Sihra TS, Nicholls DG: **Aminooxyacetic acid inhibits the malate-aspartate shuttle in isolated nerve terminals and prevents the mitochondria from utilizing glycolytic substrates.** *Biochim Biophys Acta.* 1987; **930**(2): 173–178.
PubMed Abstract | Publisher Full Text

38. Di Stefano M, Conforti L: **Diversification of NAD biological role: the importance of location.** *FEBS J.* 2013; **280**(19): 4711–28.
PubMed Abstract | Publisher Full Text

39. Spector R: **Niacinamide transport through the blood-brain barrier.** *Neurochem Res.* 1987; **12**(1): 27–31.
PubMed Abstract | Publisher Full Text

40. Holland MA, Tan AA, Smith DC, *et al.*: **Nicotinamide treatment provides acute neuroprotection and GFAP regulation following fluid percussion injury.** *J Neurotrauma.* 2008; **25**(2): 140–152.
PubMed Abstract | Publisher Full Text

41. Maiese K, Chong ZZ: **Nicotinamide: necessary nutrient emerges as a novel cytoprotectant for the brain.** *Trends Pharmacol Sci.* 2003; **24**(5): 228–232.
PubMed Abstract | Publisher Full Text

42. Parsons RB, Smith SW, Waring RH, *et al.*: **High expression of nicotinamide *N*-methyltransferase in patients with idiopathic Parkinson's disease.** *Neurosci Lett.* 2003; **342**(1–2): 13–16.
PubMed Abstract | Publisher Full Text

43. Naia L, Rosenstock TR, Oliveira AM, *et al.*: **Comparative Mitochondrial-Based Protective Effects of Resveratrol and Nicotinamide in Huntington's Disease Models.** *Mol Neurobiol.* 2017; **54**(7): 5385–5399.
PubMed Abstract | Publisher Full Text

44. Mori Y, Sugawara A, Tsuji M, *et al.*: **Toxic effects of nicotinamide methylation on mouse brain striatum neuronal cells and its relation to manganese.** *Environ Health Prev Med.* 2012; **17**(5): 371–376.
PubMed Abstract | Publisher Full Text | Free Full Text

45. El Borolossy R, El Wakeel LM, El Hakim I, *et al.*: **Efficacy and safety of nicotinamide in the management of hyperphosphatemia in pediatric patients on regular hemodialysis.** *Pediatr Nephrol.* 2016; **31**(2): 289–296.
PubMed Abstract | Publisher Full Text

46. Rutkowski B, Slominska E, Szolkiewicz M, *et al.*: **N-methyl-2-pyridone-5-carboxamide: a novel uremic toxin?** *Kidney Int Suppl.* 2003; **63**(Supplement 84): S19–S21.
PubMed Abstract | Publisher Full Text

47. Lenglet A, Liabeuf S, Bodeau S, *et al.*: **N-methyl-2-pyridone-5-carboxamide (2PY)-Major Metabolite of Nicotinamide: An Update on an Old Uremic Toxin.** *Toxins (Basel).* 2016; **8**(11): pii: E339.
PubMed Abstract | Publisher Full Text | Free Full Text

48. Airhart SE, Shireman LM, Risler LJ, *et al.*: **An open-label, non-randomized study of the pharmacokinetics of the nutritional supplement nicotinamide riboside (NR) and its effects on blood NAD+ levels in healthy volunteers.** *PLoS One.* 2017; **12**(12): e0186459.
PubMed Abstract | Publisher Full Text | Free Full Text

49. Ratajczak J, Joffraud M, Trammell SA, *et al.*: **NRK1 controls nicotinamide mononucleotide and nicotinamide riboside metabolism in mammalian cells.** *Nat Commun.* 2016; **7**: 13103.
PubMed Abstract | Publisher Full Text | Free Full Text

50. Liu L, Su X, Quinn WJ 3rd, *et al.*: **Quantitative Analysis of NAD Synthesis-Breakdown Fluxes.** *Cell Metab.* 2018; **27**(5): 1067–1080.e5.
PubMed Abstract | Publisher Full Text | Free Full Text

51. Hultman E, Bergström J, Anderson NM: **Breakdown and resynthesis of phosphorylcreatine and adenosine triphosphate in connection with muscular work in man.** *Scand J Clin Lab Invest.* 1967; **19**(1): 56–66.
PubMed Abstract | Publisher Full Text

52. Wallimann T, Wyss M, Brdiczka D, *et al.*: **Intracellular compartmentation, structure and function of creatine kinase isoenzymes in tissues with high and fluctuating energy demands: the 'phosphocreatine circuit' for cellular energy homeostasis.** *Biochem J.* 1992; **281**(Pt 1): 21–40.
PubMed Abstract | Publisher Full Text | Free Full Text

53. Lowenstein JM, Goodman MN: **The purine nucleotide cycle in skeletal muscle.** *Fed Proc.* 1978; **37**(9): 2308–12.
PubMed Abstract

54. Balcke GU, Kolle SN, Kamp H, *et al.*: **Linking energy metabolism to dysfunctions in mitochondrial respiration--a metabolomics *in vitro* approach.** *Toxicol Lett.* 2011; **203**(3): 200–209.
PubMed Abstract | Publisher Full Text

55. Mráček T, Drahota Z, Houštěk J: **The function and the role of the mitochondrial glycerol-3-phosphate dehydrogenase in mammalian tissues.** *Biochim Biophys Acta.* 2013; **1827**(3): 401–410.
PubMed Abstract | Publisher Full Text

56. Stein LR, Imai S: **The dynamic regulation of NAD metabolism in mitochondria.** *Trends Endocrinol Metab.* 2012; **23**(9): 420–428.
PubMed Abstract | Publisher Full Text | Free Full Text

57. Krebs HA: **The redox state of nicotinamide adenine dinucleotide in the cytoplasm and mitochondria of rat liver.** *Adv Enzyme Regul.* 1967; **5**: 409–434.
PubMed Abstract | Publisher Full Text

58. Cerna D, Li H, Flaherty S, *et al.*: **Inhibition of nicotinamide phosphoribosyltransferase (NAMPT) activity by small molecule GMX1778 regulates reactive oxygen species (ROS)-mediated cytotoxicity in a p53- and nicotinic acid phosphoribosyltransferase1 (NAPRT1)-dependent manner.** *J Biol Chem.* 2012; **287**(26): 22408–22417.
PubMed Abstract | Publisher Full Text | Free Full Text

59. Oakey L: **Metabolic tracing reveals novel adaptations to skeletal muscle cell energy production pathways in response to NAD+ depletion.** *figshare.* Fileset. 2018.
http://www.doi.org/10.6084/m9.figshare.7271573.v1

10. References

1. Frontera, W. R. & Ochala, J. Skeletal Muscle: A Brief Review of Structure and Function. *Calcif. Tissue Int.* **96,** 183–195 (2015).

2. Salway, J. G. *Metabolism at a Glance*. (Blackwell Publishing, 2004).

3. Massudi, H. *et al.* Age-associated changes in oxidative stress and NAD+ metabolism in human tissue. *PLoS One* **7,** (2012).

4. Yoshino, J., Mills, K. F., Yoon, M. J. & Imai, S. I. Nicotinamide mononucleotide, a key NAD+intermediate, treats the pathophysiology of diet- and age-induced diabetes in mice. *Cell Metab.* **14,** 528–536 (2011).

5. Gomes, A. P. *et al.* Declining NAD+induces a pseudohypoxic state disrupting nuclear-mitochondrial communication during aging. *Cell* **155,** 1624–1638 (2013).

6. Frederick, D. W. *et al.* Increasing NAD synthesis in muscle via nicotinamide phosphoribosyltransferase is not sufficient to promote oxidative metabolism. *J. Biol. Chem.* **290,** 1546–1558 (2015).

7. Janssen, I., Heymsfield, S. B., Wang, Z. & Ross, R. Skeletal muscle mass and distribution in 468 men and women aged 18–88 yr. *J. Appl. Physiol.* **89,** 81–88 (2000).

8. Pedersen, B. K. & Febbraio, M. A. Muscles, exercise and obesity: skeletal muscle as a secretory organ. *Nat. Rev. Endocrinol.* **8,** 457–465 (2012).

9. NCERT. *Biology - Class 11*. (2014).

10. Wehrwein, E. A., Orer, H. S. & Barman, S. M. Overview of the Anatomy, Physiology, and Pharmacology of the Autonomic Nervous System. in *Comprehensive Physiology* 1239–1278 (2016). doi:10.1002/cphy.c150037

11. Institute, N. C. Structure of Skeletal Muscle. *SEER Training Modules* Available at: https://training.seer.cancer.gov/anatomy/muscular/structure.html. (Accessed: 1st September 2018)

12. Light, N. & Champion, A. E. Characterization of muscle epimysium, perimysium and endomysium coliagens. *Biochem. J* **219,** 1017–1026 (1984).

13. Pocock, G. & Richards, C. *Human Physiology: The Basis of Medicine*. (Oxford University Press, 2006).

14. Farah, C. S. & Reinach, F. C. The troponin complex and regulation of muscle contraction. *FASEB J.* **9,** 755–767 (1995).

15. Squire, J. M. Architecture and function in the muscle sarcomere. *Current Opinion in Structural Biology* **7,** 247–257 (1997).

16. Wingertzahn, M. A. & Ochs, R. S. Control of calcium in skeletal muscle excitation-contraction coupling: implications for malignant hyperthermia. *Mol Genet Metab* **65,** 113–120 (1998).

17. Huxley, H. & Hanson, J. Changes in the Cross-Striations of Musle during Contraction and Stretch and their Structural interpretation. *Nature* **173,** 973–976 (1954).

18. Huxley, A. F. & Niedergerke, R. Structural changes in muscle during contraction; interference microscopy of living muscle fibres. *Nature* **173,** 971–973 (1954).

19. Cooper, W. G. & Konigsberg, I. R. Dynamics of myogenesis in vitro. *Anat. Rec.* **140,** 195–205 (1961).

20. Mauro, A. Satellite cell of skeletal muscle fibers. *J. Biophys. Biochem. Cytol.* **9,** 493–495 (1961).

21. Schmalbruch, H. & Lewis, D. M. Dynamics of nuclei of muscle fibers and connective tissue cells in normal and denervated rat muscles. *Muscle and Nerve* **23,** 617–626 (2000).

22. Collins, C. A. *et al.* Stem cell function, self-renewal, and behavioral heterogeneity of cells from the adult muscle satellite cell niche. *Cell* **122,** 289–301 (2005).

23. Kuang, S., Kuroda, K., Le Grand, F. & Rudnicki, M. A. Asymmetric Self-Renewal and Commitment of Satellite Stem Cells in Muscle. *Cell* **129,** 999–1010 (2007).

24. Olguin, H. C. & Olwin, B. B. Pax-7 up-regulation inhibits myogenesis and cell cycle progression in satellite cells: A potential mechanism for self-renewal. *Dev. Biol.* **275,** 375–388 (2004).

25. Florian Bentzinger, C., Wang, Y. X. & Rudnicki, M. A. Building muscle: Molecular regulation of myogenesis. *Cold Spring Harb. Perspect. Biol.* **4,** (2012).

26. Tierney, M. T. & Sacco, A. Satellite Cell Heterogeneity in Skeletal Muscle Homeostasis. *Trends in Cell Biology* (2016). doi:10.1016/j.tcb.2016.02.004

27. Wells, L., Edwards, K. A. & Bernstein, S. I. Myosin heavy chain isoforms regulate muscle function but not myofibril assembly. *EMBO J.* **15,** 4454–9 (1996).

28. Barany, M. ATPase Activity of Myosin Correlated with Speed of Muscle Shortening. *J. Gen. Physiol.* **50,** 197–218 (1967).

29. Johnson, M. A., Polgar, J., Weightman, D. & Appleton, D. Data on the distribution of fibre types in thirty-six human muscles. An autopsy study. *J. Neurol. Sci.* **18,** 111–129 (1973).

30. Liu, G., Mac Gabhann, F. & Popel, A. S. Effects of Fiber Type and Size on the Heterogeneity of Oxygen Distribution in Exercising Skeletal Muscle. *PLoS One* **7,** (2012).

31. Schiaffino, S. & Reggiani, C. Fiber types in mammalian skeletal muscles. *Physiol. Rev.* **91,** 1447–531 (2011).

32. Hilber, K. & Galler, S. Mechanical properties and myosin heavy chain isoform composition of skinned skeletal muscle fibres from a human biopsy sample. *Pflugers Arch. Eur. J. Physiol.* **434,** 551–558 (1997).

33. Pette, D. & Staron, R. S. Mammalian skeletal muscle fiber type transitions. *Int. Rev. Cytol.* **170,** 143–223 (1997).

34. Lin, J. *et al.* Transcriptional co-activator PGC-1α drives the formation of slow-twitch muscle fibres. *Nature* **418,** 797–801 (2002).

35. Seene, T. & Kaasik, P. Biological Characteristics of Structural and Functional Remodelling in Skeletal Muscle : Effect of Exercise. *Adv. Stud. Biol.* **5,** 251–278 (2013).

36. De Meis, L., Wolosker, H. & Engelender, S. Regulation of the channel function of Ca2+-ATPase. in *Biochimica et Biophysica Acta - Bioenergetics* **1275,** 105–110 (1996).

37. Homsher, E. REVIEW - Muscle enthalpy production and its relationship to actomyosin ATPase. *Annu. Rev. Physiol.* **49,** 673–90 (1987).

38. Kushmerick, M. J., Moerland, T. S. & Wiseman, R. W. Mammalian skeletal muscle fibers distinguished by contents of phosphocreatine, ATP, and Pi. *Proc. Natl. Acad. Sci. U. S. A.* **89,** 7521–7525 (1992).

39. Galgani, J. & Ravussin, E. Energy metabolism, fuel selection and body weight regulation. *Int. J. Obes. (Lond).* **32 Suppl 7,** S109-19 (2008).

40. Abbott, W. G. *et al.* Short-term energy balance: relationship with protein, carbohydrate, and fat balances. *Am. J. Physiol.* **255,** E332–E337 (1988).

41. Jensen, M. D. Fate of fatty acids at rest and during exercise: Regulatory mechanisms. in *Acta Physiologica Scandinavica* **178,** 385–390 (2003).

42. Matthews, P. M., Bland, J. L., Gadian, D. G. & Radda, G. K. A 31P-NMR saturation transfer study of the regulation of creatine kinase in the rat heart. *Biochim. Biophys. Acta - Mol. Cell Res.* **721,** 312–320 (1982).

43. Hultman, E., Bergström, J. & Anderson, N. M. Breakdown and resynthesis of phosphorylcreatine and adenosine triphosphate in connection with muscular work in man. *Scand. J. Clin. Lab. Invest.* **19,** 56–66 (1967).

44. Wallimann, T., Wyss, M., Brdiczka, D., Nicolay, K. & Eppenberger, H. M. Intracellular compartmentation, structure and function of creatine kinase isoenzymes in tissues with high and fluctuating energy demands: the

'phosphocreatine circuit' for cellular energy homeostasis. *Biochem. J.* **281,** 21–40 (1992).

45. Wallimann, T., Turner, D. C. & Eppenberger, H. M. Localization of creatine kinase isoenzymes in myofibrils: I. chicken skeletal muscle. *J. Cell Biol.* **75,** 297–317 (1977).

46. Marsh, G. D., Paterson, D. H., Potwarka, J. J. & Thompson, R. T. Transient changes in muscle high-energy phosphates during moderate exercise. *J. Appl. Physiol.* **75,** 648–56 (1993).

47. Bogdanis, G. C., Nevill, M. E., Boobis, L. H. & Lakomy, H. K. Contribution of phosphocreatine and aerobic metabolism to energy supply during repeated sprint exercise. *J. Appl. Physiol.* **80,** 876–884 (1996).

48. Vollestad, N. K. & Blom, P. C. S. Effect of varying exercise intensity on glycogen depletion in human muscle fibres. *Acta Physiol. Scand.* **125,** 395–405 (1985).

49. Watt, M. J., Howlett, K. F., Febbraio, M. A., Spriet, L. L. & Hargreaves, M. Adrenaline increases skeletal muscle glycogenolysis, pyruvate dehydrogenase activation and carbohydrate oxidation during moderate exercise in humans. *J. Physiol.* **534,** 269–278 (2001).

50. Howlett, R. a *et al.* Regulation of skeletal muscle glycogen phosphorylase and PDH at varying exercise power outputs. *Am. J. Physiol.* **275,** R418–R425 (1998).

51. Chasiotis, D., Sahlin, K. & Hultman, E. Regulation of glycogenolysis in human muscle at rest and during exercise. *J. Appl. Physiol.* **53,** 708–715 (1982).

52. HUCKABEE, W. E. Relationships of pyruvate and lactate during anaerobic metabolism. II. Exercise and formation of O-debt. *J. Clin. Invest.* **37,** 255–263 (1958).

53. Felig, P., Pozefsky, T., Marliss, E. & Cahill, G. F. Alanine: key role in gluconeogenesis. *Science* **167,** 1003–4 (1970).

54. Felig, P. & Wahren, J. Amino acid metabolism in exercising man. *J. Clin. Invest.* **50,** 2703–2714 (1971).

55. McCommis, K. S. & Finck, B. N. Mitochondrial pyruvate transport: a historical perspective and future research directions. *Biochem. J.* **466,** 443–454 (2015).

56. UTTER, M. F. & KEECH, D. B. Formation of oxaloacetate from pyruvate and carbon dioxide. *J. Biol. Chem.* **235,** (1960).

57. Mitchell, P. & Moyle, J. Chemiosmotic hypothesis of oxidative phosphorylation. *Nature* **213,** 137–139 (1967).

58. Hargreaves, M. Skeletal muscle metabolism during exercise in humans. *Clin. Exp. Pharmacol. Physiol.* **27,** 225–8 (2000).

59. Nickerson, J. G. *et al.* Greater transport efficiencies of the membrane fatty acid transporters FAT/CD36 and FATP4 compared with FABPpm and FATP1 and differential effects on fatty acid esterification and oxidation in rat skeletal muscle. *J. Biol. Chem.* **284,** 16522–16530 (2009).

60. Ramsay, R. R., Gandour, R. D. & Van Der Leij, F. R. Molecular enzymology of carnitine transfer and transport. *Biochimica et Biophysica Acta - Protein Structure and Molecular Enzymology* **1546,** 21–43 (2001).

61. Van der Leij, F. R., Huijkman, N. C. A., Boomsma, C., Kuipers, J. R. G. & Bartelds, B. Genomics of the human carnitine acyltransferase genes. *Molecular Genetics and Metabolism* **71,** 139–153 (2000).

62. Beermann, C. *et al.* Short term effects of dietary medium-chain fatty acids and n-3 long-chain polyunsaturated fatty acids on the fat metabolism of healthy volunteers. *Lipids Health Dis.* **2,** 1–10 (2003).

63. Laffel, L. Ketone bodies: A review of physiology, pathophysiology and application of monitoring to diabetes. *Diabetes/Metabolism Research and Reviews* **15,** 412–426 (1999).

64. Ren, W., Li, Y., Yin, Y. & Blachier, F. Structure, metabolism and functions of amino acids: An overview. in *Nutritional and Physiological Functions of Amino Acids in Pigs* **9783709113,** 91–108 (2013).

65. Shambaugh 3rd. G.E., G. E. Urea biosynthesis I. The urea cycle and relationships to the citric acid cycle. *American Journal of Clinical Nutrition* **30,** 2083–2087 (1977).

66. Pisters, P. W. & Brennan, M. F. Amino acid metabolism in human cancer cachexia. *Annu Rev Nutr* **10,** 107–132 (1990).

67. Argilés, J. M., Campos, N., Lopez-Pedrosa, J. M., Rueda, R. & Rodriguez-Mañas, L. Skeletal Muscle Regulates Metabolism via Interorgan Crosstalk: Roles in Health and Disease. *Journal of the American Medical Directors Association* **17,** 789–796 (2016).

68. Engelking, L. R. & Engelking, L. R. Chapter 36 – Oxidative Phosphorylation. in *Textbook of Veterinary Physiological Chemistry* 219–224 (2015). doi:10.1016/B978-0-12-391909-0.50036-0

69. Jensen, P. K. Antimycin-insensitive oxidation of succinate and reduced nicotinamide-adenine dinucleotide in electron-transport particles. I. pH dependency and hydrogen peroxide formation. *Biochim. Biophys. Acta* **122,** 157–66 (1966).

70. José, C. *et al.* GSH transport in mitochondria: Defense against TNF-induced oxidative stress and alcohol-induced defect. *Am. J. Physiol.* **273,** (1997).

71. Madamanchi, N. R. & Runge, M. S. Mitochondrial dysfunction in atherosclerosis. *Circulation Research* **100,** 460–473 (2007).

72. Liou, G.-Y. & Storz, P. Reactive oxygen species in cancer. *Free Radic. Res.* **44,** 479–96 (2010).

73. Harman, D. Aging: A Theory Based on Free Radical and Radiation Chemistry. *J. Gerontol.* **11,** 298–300 (1956).

74. Gray, M. W., Burger, G. & Lang, B. F. Mitochondrial evolution. *Science* **283,** 1476–1481 (1999).

75. Emelyanov, V. V. Rickettsiaceae, rickettsia-like endosymbionts, and the origin of mitochondria. *Bioscience Reports* **21,** 1–17 (2001).

76. Taanman, J. W. The mitochondrial genome: Structure, transcription, translation and replication. *Biochimica et Biophysica Acta - Bioenergetics* (1999). doi:10.1016/S0005-2728(98)00161-3

77. Anderson, S. *et al.* Sequence and organization of the human mitochondrial genome. *Nature* **290,** 457–465 (1981).

78. Yakes, F. M. & Van Houten, B. Mitochondrial DNA damage is more extensive and persists longer than nuclear DNA damage in human cells following oxidative stress. *Proc. Natl. Acad. Sci. U. S. A.* **94,** 514–9 (1997).

79. Wallace, D. C. Mitochondrial diseases in man and mouse. *Science* **283,** 1482–1488 (1999).

80. Holloszy, J. O. Biochemical adaptations in muscle. Effects of exercise on mitochondrial oxygen uptake and respiratory enzyme activity in skeletal muscle. *J. Biol. Chem.* **242,** 2278–2282 (1967).

81. Bruce, C. R., Kriketos, A. D., Cooney, G. J. & Hawley, J. A. Disassociation of muscle triglyceride content and insulin sensitivity after exercise training in patients with Type 2 diabetes. *Diabetologia* **47,** 23–30 (2004).

82. L pez-Lluch, G. *et al.* Calorie restriction induces mitochondrial biogenesis and bioenergetic efficiency. *Proc. Natl. Acad. Sci.* **103,** 1768–1773 (2006).

83. Fernandez-Marcos, P. & Auwerx, J. Regulation of PGC-1a , a nodal regulator of mitochondrial biogenesis. *Am. J. Clin. …* **93,** 884–890 (2011).

84. Wright, D. C., Geiger, P. C., Han, D.-H., Jones, T. E. & Holloszy, J. O. Calcium induces increases in peroxisome proliferator-activated receptor gamma coactivator-1alpha and mitochondrial biogenesis by a pathway leading to p38 mitogen-activated protein kinase activation. *J. Biol. Chem.* **282,** 18793–9 (2007).

85. Jäger, S. S., Handschin, C. C., St-Pierre, J. J. & Spiegelman, B. M. B. M. AMP-activated protein kinase (AMPK) action in skeletal muscle via direct phosphorylation of PGC-1alpha. *Pnas* **104,** 12017–12022 (2007).

86. Safdar, A. *et al.* Exercise increases mitochondrial PGC-1α content and promotes nuclear-mitochondrial cross-talk to coordinate mitochondrial

biogenesis. *J. Biol. Chem.* **286,** 10605–10617 (2011).

87. Rodgers, J. T. *et al.* Nutrient control of glucose homeostasis through a complex of PGC-1a and SIRT1. *Nature* **434,** 113–118 (2005).

88. Gerhart-Hines, Z. *et al.* Metabolic control of muscle mitochondrial function and fatty acid oxidation through SIRT1/PGC-1alpha. *EMBO J.* **26,** 1913–23 (2007).

89. Cant??, C. & Auwerx, J. PGC-1??, SIRT1 and AMPK, an energy sensing network that controls energy expenditure. *Current Opinion in Lipidology* **20,** 98–105 (2009).

90. Russell, A. P., Foletta, V. C., Snow, R. J. & Wadley, G. D. Skeletal muscle mitochondria: a major player in exercise, health and disease. *Biochim. Biophys. Acta* **1840,** 1276–84 (2014).

91. Duchen, M. R. Roles of mitochondria in health and disease. *Diabetes* **53 Suppl 1,** S96-102 (2004).

92. Marín-García, J., Akhmedov, A., Rybin, V. & Moe, G. W. *Mitochondria and their role in cardiovascular disease*. *Mitochondria and Their Role in Cardiovascular Disease* **9781461445,** (2013).

93. Sun, N., Youle, R. J. & Finkel, T. The Mitochondrial Basis of Aging. *Molecular Cell* **61,** 654–666 (2016).

94. Sivitz, W. I. & Yorek, M. A. Mitochondrial Dysfunction in Diabetes: From Molecular Mechanisms to Functional Significance and Therapeutic Opportunities. *Antioxid. Redox Signal.* **12,** 537–577 (2010).

95. Ballinger, S. W. Mitochondrial dysfunction in cardiovascular disease. *Free Radic. Biol. Med.* **38,** 1278–95 (2005).

96. Martins, I. J. Autoimmune disease and mitochondrial dysfunction in chronic diseases. *Res Chron Dis* **1,** 10–12 (2017).

97. Nicolson, G. L. Mitochondrial Dysfunction and Chronic Disease: Treatment With Natural Supplements. *Integr. Med. (Encinitas).* **13,** 35–43 (2014).

98. Stocco, D. M. & Hutson, J. C. Quantitation of mitochondrial DNA and protein in the liver of Fischer 344 rats during aging. *Journals Gerontol.* **33,** 802–809 (1978).

99. Herbener, G. H. A morphometric study of age-dependent changes in mitochondrial population of mouse liver and heart. *J. Gerontol.* **31,** 8–12 (1976).

100. Yen, T. C., Chen, Y. S., King, K. L., Yeh, S. H. & Wei, Y. H. Liver mitochondrial respiratory functions decline with age. *Biochem. Biophys. Res. Commun.* **165,** 994–1003 (1989).

101. Holloszy, J. O. Biochemical adaptations in muscle. Effects of exercise on

mitochondrial oxygen uptake and respiratory enzyme activity in skeletal muscle. *J. Biol. Chem.* (1967).

102. Sauve, A. A., Wolberger, C., Schramm, V. L. & Boeke, J. D. The Biochemistry of Sirtuins. *Annu Rev Biochem* **75,** 435–465 (2006).

103. Rongvaux, A., Andris, F., Van Gool, F. & Leo, O. Reconstructing eukaryotic NAD metabolism. *Bioessays* **25,** 683–690 (2003).

104. Harden, A. & Young, W. J. The Alcoholic Ferment of Yeast-Juice. *Proc. R. Soc. B Biol. Sci.* **77,** 405–420 (1906).

105. Berger, F., Ramírez-Hernández, M. H. & Ziegler, M. The new life of a centenarian: Signalling functions of NAD(P). *Trends in Biochemical Sciences* **29,** 111–118 (2004).

106. Bollet, A. J. Politics and pellagra: The epidemic of pellagra in the U.S. in the early twentieth century. *Yale J. Biol. Med.* **65,** 211–221 (1992).

107. Hegyi, J., Schwartz, R. A. & Hegyi, V. Pellagra: Dermatitis, dementia, and diarrhea. in *International Journal of Dermatology* **43,** 1–5 (2004).

108. Rajakumar, K. Pellagra in the United States: a historical perspective. *South. Med. J.* **93,** 272–7 (2000).

109. Elvehjem, C. A. Concentration of Antipelhgra Factor.

110. Warburg, O. Hydorgen-transferring co-enzyme, its composition and mode of functioning. *Biochem. J.* **280,** 157–205 (1935).

111. Vanlinden, M. R., Skoge, R. H. & Ziegler, M. Discovery , metabolism and functions of NAD and NADP. *Biochem. (Lond).* **37,** 9–13 (2015).

112. Agledal, L., Niere, M. & Ziegler, M. The phosphate makes a difference: cellular functions of NADP. *Redox Rep.* **15,** 2–10 (2010).

113. Winkler, B. S., DeSantis, N. & Solomon, F. Multiple NADPH-producing pathways control glutathione (GSH) content in retina. *Exp. Eye Res.* **43,** 829–847 (1986).

114. Geiszt, M. NADPH oxidases: New kids on the block. *Cardiovascular Research* **71,** 289–299 (2006).

115. Okamoto, H. Cyclic ADP-ribose-mediated insulin secretion and Reg, regenerating gene. in *Journal of Molecular Medicine* **77,** 74–78 (1999).

116. Mészáros, L. G., Bak, J. & Chu, A. Cyclic ADP-ribose as an endogenous regulator of the non-skeletal type ryanodine receptor Ca2+ channel. *Nature* **364,** 76–79 (1993).

117. Guse, A. H. *et al.* Regulation of calcium signalling in T lymphocytes by the second messenger cyclic ADP-ribose. *Nature* **398,** 70–73 (1999).

118. Cantó, C. & Auwerx, J. NAD+as a signaling molecule modulating metabolism. *Cold Spring Harb. Symp. Quant. Biol.* **76,** 291–298 (2011).

119. Houtkooper, R. H., Cantó, C., Wanders, R. J. & Auwerx, J. The secret life of NAD+: An old metabolite controlling new metabolic signaling pathways. *Endocrine Reviews* **31,** 194–223 (2010).

120. Houtkooper, R. H., Pirinen, E. & Auwerx, J. Sirtuins as regulators of metabolism and healthspan. *Nat. Rev. Mol. Cell Biol.* **13,** 225–238 (2012).

121. Imai, S. I., Armstrong, C. M., Kaeberlein, M. & Guarente, L. Transcriptional silencing and longevity protein Sir2 is an NAD-dependent histone deacetylase. *Nature* **403,** 795–800 (2000).

122. Vaziri, H. *et al.* hSIR2SIRT1 functions as an NAD-dependent p53 deacetylase. *Cell* **107,** 149–159 (2001).

123. Luo, J. *et al.* Negative control of p53 by Sir2α promotes cell survival under stress. *Cell* **107,** 137–148 (2001).

124. Michishita, E. Evolutionarily Conserved and Nonconserved Cellular Localizations and Functions of Human SIRT Proteins. *Mol. Biol. Cell* **16,** 4623–4635 (2005).

125. Wang, F., Nguyen, M., Qin, F. X. F. & Tong, Q. SIRT2 deacetylates FOXO3a in response to oxidative stress and caloric restriction. *Aging Cell* **6,** 505–514 (2007).

126. Onyango, P., Celic, I., McCaffery, J. M., Boeke, J. D. & Feinberg, A. P. SIRT3, a human SIR2 homologue, is an NAD- dependent deacetylase localized to mitochondria. *Proc. Natl. Acad. Sci.* **99,** 13653–13658 (2002).

127. Kupis, W., Pałyga, J., Tomal, E. & Niewiadomska, E. The role of sirtuins in cellular homeostasis. *Journal of Physiology and Biochemistry* **72,** 371–380 (2016).

128. Rogina, B. & Helfand, S. L. Sir2 mediates longevity in the fly through a pathway related to calorie restriction. *Proc. Natl. Acad. Sci.* **101,** 15998–16003 (2004).

129. Viswanathan, M., Kim, S. K., Berdichevsky, A. & Guarente, L. A role for SIR-2.1 regulation of ER stress response genes in determining C. *elegans life span. Dev. Cell* **9,** 605–615 (2005).

130. Tissenbaum, H. A. & Guarente, L. Increased dosage of a sir-2 gene extends lifespan in Caenorhabditis elegans. *Nature* **410,** 227–230 (2001).

131. Kaeberlein, M., McVey, M. & Guarente, L. The SIR2/3/4 complex and SIR2 alone promote longevity in Saccharomyces cerevisiae by two different mechanisms. *Genes Dev.* **13,** 2570–2580 (1999).

132. Burnett, C. *et al.* Absence of effects of Sir2 overexpression on lifespan in C. elegans and Drosophila. *Nature* **477,** 482–485 (2011).

133. Zhang, T. & Kraus, W. L. SIRT1-dependent regulation of chromatin and transcription: Linking NAD+ metabolism and signaling to the control of cellular functions. *Biochimica et Biophysica Acta - Proteins and Proteomics* **1804,** 1666–1675 (2010).

134. Nakahata, Y. *et al.* The NAD+-Dependent Deacetylase SIRT1 Modulates CLOCK-Mediated Chromatin Remodeling and Circadian Control. *Cell* **134,** 329–340 (2008).

135. Grubisha, O., Smith, B. C. & Denu, J. M. Small molecule regulation of Sir2 protein deacetylases. *FEBS Journal* **272,** 4607–4616 (2005).

136. Zhang, T. *et al.* Enzymes in the NAD+ salvage pathway regulate SIRT1 activity at target gene promoters. *J. Biol. Chem.* **284,** 20408–20417 (2009).

137. Bishop, N. A. & Guarente, L. Genetic links between diet and lifespan: Shared mechanisms from yeast to humans. *Nature Reviews Genetics* **8,** 835–844 (2007).

138. Mei, Z. *et al.* Sirtuins in metabolism, DNA repair and cancer. *Journal of Experimental and Clinical Cancer Research* **35,** (2016).

139. ANDRES, R., CADER, G. & ZIERLER, K. L. The quantitatively minor role of carbohydrate in oxidative metabolism by skeletal muscle in intact man in the basal state; measurements of oxygen and glucose uptake and carbon dioxide and lactate production in the forearm. *J. Clin. Invest.* **35,** 671–682 (1956).

140. Liu, Y. *et al.* A fasting inducible switch modulates gluconeogenesis via activator/coactivator exchange. *Nature* **456,** 269–273 (2008).

141. Cantó, C. *et al.* Interdependence of AMPK and SIRT1 for metabolic adaptation to fasting and exercise in skeletal muscle. *Cell Metab.* **11,** 213–9 (2010).

142. Feige, J. N. *et al.* Specific SIRT1 Activation Mimics Low Energy Levels and Protects against Diet-Induced Metabolic Disorders by Enhancing Fat Oxidation. *Cell Metab.* **8,** 347–358 (2008).

143. Lagouge, M. *et al.* Resveratrol Improves Mitochondrial Function and Protects against Metabolic Disease by Activating SIRT1 and PGC-1α. *Cell* **127,** 1109–1122 (2006).

144. Pfluger, P. T., Herranz, D., Velasco-Miguel, S., Serrano, M. & Tschop, M. H. Sirt1 protects against high-fat diet-induced metabolic damage. *Proc. Natl. Acad. Sci.* **105,** 9793–9798 (2008).

145. Jukarainen, S. *et al.* Obesity is associated with low nad+/sirt pathway expression in adipose tissue of BMI-discordant monozygotic twins. *J. Clin. Endocrinol. Metab.* **101,** 275–283 (2016).

146. He, W., Newman, J. C., Wang, M. Z., Ho, L. & Verdin, E. Mitochondrial sirtuins: Regulators of protein acylation and metabolism. *Trends in Endocrinology and Metabolism* **23,** 467–476 (2012).

147. Sack, M. N. & Finkel, T. Mitochondrial metabolism, sirtuins, and aging. *Cold Spring Harb. Perspect. Biol.* **4,** (2012).

148. Ding, R. B., Bao, J. L. & Deng, C. X. Emerging roles of SIRT1 in fatty liver diseases. *International Journal of Biological Sciences* **13,** 852–867 (2017).

149. Jungmichel, S. *et al.* Proteome-wide identification of poly(ADP-Ribosyl)ation targets in different genotoxic stress responses. *Mol. Cell* **52,** 272–285 (2013).

150. Jacobson, M. K. & Alvarez-Gonzale, R. Characterization of Polymers of Adenosine Diphosphate Ribose Generated in Vitro and in Vivo. *Biochemistry* **26,** 3218–3224 (1987).

151. Juarez-Salinas, H., Levi, V., Jacobson, E. L. & Jacobson, M. K. Poly(ADP-ribose) has a branched structure in vivo. *J. Biol. Chem.* **257,** 607–609 (1982).

152. Ray Chaudhuri, A. & Nussenzweig, A. The multifaceted roles of PARP1 in DNA repair and chromatin remodelling. *Nature Reviews Molecular Cell Biology* **18,** 610–621 (2017).

153. De Vos, M., Schreiber, V. & Dantzer, F. The diverse roles and clinical relevance of PARPs in DNA damage repair: Current state of the art. *Biochemical Pharmacology* **84,** 137–146 (2012).

154. Krietsch, J. *et al.* Reprogramming cellular events by poly(ADP-ribose)-binding proteins. *Molecular Aspects of Medicine* **34,** 1066–1087 (2013).

155. Koh, D. W. *et al.* Failure to degrade poly(ADP-ribose) causes increased sensitivity to cytotoxicity and early embryonic lethality. *Proc. Natl. Acad. Sci.* **101,** 17699–17704 (2004).

156. Zhang, T. *et al.* Regulation of poly(ADP-ribose) polymerase-1-dependent gene expression through promoter-directed recruitment of a nuclear NAD + synthase. *J. Biol. Chem.* **287,** 12405–12416 (2012).

157. Park, S. D., Kim, C. G. & Kim, M. G. Inhibitors of poly(ADP-ribose) polymerase enhance DNA strand breaks, excision repair, and sister chromatid exchanges induced by alkylating agents. *Environ. Mutagen.* **5,** 515–525 (1983).

158. Rajamohan, S. B. *et al.* SIRT1 Promotes Cell Survival under Stress by Deacetylation-Dependent Deactivation of Poly(ADP-Ribose) Polymerase 1. *Mol. Cell. Biol.* **29,** 4116–4129 (2009).

159. Bai, P. *et al.* PARP-2 regulates SIRT1 expression and whole-body energy expenditure. *Cell Metab.* **13,** 450–460 (2011).

160. Cantó, C., Sauve, A. A. & Bai, P. Crosstalk between poly(ADP-ribose) polymerase and sirtuin enzymes. *Molecular Aspects of Medicine* **34,** 1168–1201 (2013).

161. Bai, P. *et al.* PARP-1 inhibition increases mitochondrial metabolism through SIRT1 activation. *Cell Metab.* **13,** 461–468 (2011).

162. Lee, H. C. Structure and Enzymatic Functions of Human CD38. *Mol. Med.* **12,** 317–323 (2006).

163. Aarhus, R., Graeff, R. M., Dickey, D. M., Walseth, T. F. & Lee, H. C. ADP-ribosyl cyclase and CD38 catalyze the synthesis of a calcium-mobilizing metabolite from NADP. *J. Biol. Chem.* **270,** 30327–30333 (1995).

164. Howard, M. *et al.* Formation and hydrolysis of cyclic ADP-ribose catalyzed by lymphocyte antigen CD38. *Science (80-.).* **262,** 1056–1059 (1993).

165. Aksoy, P., White, T. A., Thompson, M. & Chini, E. N. Regulation of intracellular levels of NAD: A novel role for CD38. *Biochem. Biophys. Res. Commun.* **345,** 1386–1392 (2006).

166. Aksoy, P. *et al.* Regulation of SIRT 1 mediated NAD dependent deacetylation: a novel role for the multifunctional enzyme CD38. *Biochem. Biophys. Res. Commun.* **349,** 353–359 (2006).

167. Quarona, V. *et al.* CD38 and CD157: A long journey from activation markers to multifunctional molecules. *Cytometry Part B - Clinical Cytometry* **84,** 207–217 (2013).

168. Dolle, C., Skoge, R. H., Vanlinden, M. R. & Ziegler, M. NAD biosynthesis in humans--enzymes, metabolites and therapeutic aspects. *Curr Top Med Chem* **13,** 2907–2917 (2013).

169. Terakata, M. *et al.* Establishment of True Niacin Deficiency in Quinolinic Acid Phosphoribosyltransferase Knockout Mice. *J. Nutr.* 2148–2153 (2012). doi:10.3945/jn.112.167569

170. Nikiforov, A., Dölle, C., Niere, M. & Ziegler, M. Pathways and subcellular compartmentation of NAD biosynthesis in human cells: From entry of extracellular precursors to mitochondrial NAD generation. *J. Biol. Chem.* **286,** 21767–21778 (2011).

171. Di Stefano, M. & Conforti, L. Diversification of NAD biological role: The importance of location. *FEBS J.* **280,** 4711–4728 (2013).

172. Bogan, K. L. & Brenner, C. Nicotinic acid, nicotinamide, and nicotinamide riboside: a molecular evaluation of NAD+ precursor vitamins in human nutrition. *Annu. Rev. Nutr.* **28,** 115–130 (2008).

173. Fricker, R. A., Green, E. L., Jenkins, S. I. & Griffin, S. M. The Influence of Nicotinamide on Health and Disease in the Central Nervous System. *International Journal of Tryptophan Research* **11,** (2018).

174. Mills, K. F. *et al.* Nampt/PBEF/Visfatin Regulates Insulin Secretion in ?? Cells as a Systemic NAD Biosynthetic Enzyme. *Cell Metab.* **6,** 363–75 (2007).

175. Revollo, J. R. *et al.* Nampt/PBEF/Visfatin Regulates Insulin Secretion in β Cells as a Systemic NAD Biosynthetic Enzyme. *Cell Metab.* **6,** 363–375 (2007).

176. Galassi, L. *et al.* Characterization of human nicotinate phosphoribosyltransferase: Kinetic studies, structure prediction and functional analysis by site-directed mutagenesis. *Biochimie* **94,** 300–309 (2012).

177. Hara, N. *et al.* Elevation of cellular NAD levels by nicotinic acid and involvement of nicotinic acid phosphoribosyltransferase in human cells. *J Biol Chem* **282,** 24574–24582 (2007).

178. Nakahata, Y., Sahar, S., Astarita, G., Kaluzova, M. & Sassone-Corsi, P. Circadian Control of the NAD+ Salvage Pathway by CLOCK-SIRT1. *Science (80-.).* **324,** 654–657 (2009).

179. Ramsey, K. M. *et al.* Circadian clock feedback cycle through NAMPT-Mediated NAD+ biosynthesis. *Science (80-.).* **324,** 651–654 (2009).

180. Tan, B. *et al.* Pharmacological inhibition of nicotinamide phosphoribosyltransferase (NAMPT), an enzyme essential for NAD+ biosynthesis, in human cancer cells: metabolic basis and potential clinical implications. *J Biol Chem* **288,** 3500–3511 (2013).

181. Kieswich, J., Silvestre, M., Harwood, S., Yaqoob, M. & Caton, P. eNAMPT-monomer plays a critical role in pathophysiology of experimental diabetes and represents a novel target for treatment of type 2 diabetes. *Endocr. Abstr.* (2015). doi:10.1530/endoabs.38.p201

182. Moschen, A. R. *et al.* Visfatin, an Adipocytokine with Proinflammatory and Immunomodulating Properties. *J. Immunol.* **178,** 1748–1758 (2007).

183. Kieswich, J. *et al.* Monomeric eNAMPT in the development of experimental diabetes in mice: a potential target for type 2 diabetes treatment. *Diabetologia* **59,** 2477–2486 (2016).

184. Caton, P. W., Kieswich, J., Yaqoob, M. M., Holness, M. J. & Sugden, M. C. Nicotinamide mononucleotide protects against pro-inflammatory cytokine-mediated impairment of mouse islet function. *Diabetologia* **54,** 3083–3092 (2011).

185. Hara, N., Yamada, K., Shibata, T., Osago, H. & Tsuchiya, M. Nicotinamide phosphoribosyltransferase/visfatin does not catalyze nicotinamide mononucleotide formation in blood plasma. *PLoS One* **6,** (2011).

186. Yoshida, M. *et al.* Extracellular Vesicle-Contained eNAMPT Delays Aging and Extends Lifespan in Mice. *Cell Metab.* (2019). doi:10.1016/j.cmet.2019.05.015

187. Costford, S. R. *et al.* Skeletal muscle NAMPT is induced by exercise in humans. *AJP Endocrinol. Metab.* **298,** E117-26 (2010).

188. Kim, J. S., Yoon, C.-S. & Park, D. R. NAMPT regulates mitochondria biogenesis via NAD metabolism and calcium binding proteins during skeletal muscle contraction. *J. Exerc. Nutr. Biochem.* **18,** 259–66 (2014).

189. de Guia, R. M. *et al.* Aerobic and resistance exercise training reverses age-

dependent decline in NAD+ salvage capacity in human skeletal muscle. *Physiol. Rep.* **7,** (2019).

190. Carbone, F. *et al.* Regulation and function of extracellular nicotinamide phosphoribosyltransferase/visfatin. *Compr. Physiol.* (2017). doi:10.1002/cphy.c160029

191. Montecucco, B. F. *et al.* Nicotinamide Phosphoribosyltransferase (NAMPT) Inhibitors as Therapeutics: Rationales, Controversies, Clinical Experience. *Curr. Drug Targets* (2013). doi:10.2174/1389450111314060003

192. Watson, M. *et al.* The small molecule GMX1778 is a potent inhibitor of NAD+ biosynthesis: strategy for enhanced therapy in nicotinic acid phosphoribosyltransferase 1-deficient tumors. *Mol Cell Biol* **29,** 5872–5888 (2009).

193. Del Nagro, C., Xiao, Y., Rangell, L., Reichelt, M. & O'Brien, T. Depletion of the Central Metabolite NAD Leads to Oncosis-mediated Cell Death. *J. Biol. Chem.* **289,** 35182–92 (2014).

194. Bruzzone, S. *et al.* Catastrophic NAD+ depletion in activated T lymphocytes through Nampt inhibition reduces demyelination and disability in EAE. *PLoS One* **4,** e7897 (2009).

195. Garten, A. *et al.* Physiological and pathophysiological roles of NAMPT and NAD metabolism. *Nature Reviews Endocrinology* **11,** 535–546 (2015).

196. Bieganowski, P. & Brenner, C. Discoveries of nicotinamide riboside as a nutrient and conserved NRK genes establish a preiss-handler independent route to NAD+ in fungi and humans. *Cell* **117,** 495–502 (2004).

197. Grozio, A. *et al.* CD73 protein as a source of extracellular precursors for sustained NAD+ biosynthesis in FK866-treated tumor cells. *J. Biol. Chem.* **288,** 25938–49 (2013).

198. Bogan, K. L. & Brenner, C. 5-Nucleotidases and their new roles in NAD+ and phosphate metabolism. *New J. Chem.* **34,** 845–853 (2010).

199. Fletcher, R. S. *et al.* Nicotinamide riboside kinases display redundancy in mediating nicotinamide mononucleotide and nicotinamide riboside metabolism in skeletal muscle cells. *Mol. Metab.* **6,** 819–832 (2017).

200. Kulikova, V. *et al.* Generation, release, and uptake of the NAD precursor nicotinic acid riboside by human cells. *J. Biol. Chem.* **290,** 27124–27137 (2015).

201. Canto, C. *et al.* The NAD(+) precursor nicotinamide riboside enhances oxidative metabolism and protects against high-fat diet-induced obesity. *Cell Metab* **15,** 838–847 (2012).

202. Mori, V. *et al.* Metabolic profiling of alternative NAD biosynthetic routes in mouse tissues. *PLoS One* **9,** (2014).

203. Tempel, W. *et al.* Nicotinamide riboside kinase structures reveal new pathways to NAD +. *PLoS Biol.* **5,** 2220–2230 (2007).

204. Dölle, C., Niere, M., Lohndal, E. & Ziegler, M. Visualization of subcellular NAD pools and intra-organellar protein localization by poly-ADP-ribose formation. *Cell. Mol. Life Sci.* **67,** 433–43 (2010).

205. Alano, C. C. *et al.* Differences among cell types in NAD+ compartmentalization: A comparison of neurons, astrocytes, and cardiac myocytes. in *Journal of Neuroscience Research* **85,** 3378–3385 (2007).

206. Lu, M. *et al.* Role of the malate-aspartate shuttle on the metabolic response to myocardial ischemia. *J. Theor. Biol.* **254,** 466–475 (2008).

207. Dawson, A. G. Oxidation of cytosolic NADH formed during aerobic metabolism in mammalian cells. *Trends in Biochemical Sciences* **4,** 171–176 (1979).

208. Fried, H. M. Nutrient-sensitive mitochondrial NAD+ levels dictate cell survival. *Chemtracts* **20,** 160–161 (2007).

209. Davila, A. *et al.* Nicotinamide adenine dinucleotide is transported into mammalian mitochondria. *Elife* (2018). doi:10.7554/eLife.33246

210. Yamamoto, M. *et al.* Nmnat3 is dispensable in mitochondrial NAD level maintenance in vivo. *PLoS One* (2016). doi:10.1371/journal.pone.0147037

211. Krebs, H. A. A. The redox state of nicotinamide adenine dinucleotide in the cytoplasm and mitochondria of rat liver. *Adv. Enzyme Regul.* **5,** 409–434 (1967).

212. Veech, R. L., Guynn, R. & Veloso, D. The time-course of the effects of ethanol on the redox and phosphorylation states of rat liver. *Biochem. J.* **127,** 387–397 (1972).

213. Cambronne, X. A. *et al.* Biosensor reveals multiple sources for mitochondrial NAD+. *Science (80-.).* **352,** 1474–1477 (2016).

214. VanLinden, M. R. *et al.* Subcellular distribution of NAD+ between cytosol and mitochondria determines the metabolic profile of human cells. *J. Biol. Chem.* **290,** 27644–27659 (2015).

215. Frederick, D. W. D. W. W. *et al.* Loss of NAD Homeostasis Leads to Progressive and Reversible Degeneration of Skeletal Muscle. *Cell Metab.* **24,** 269–282 (2016).

216. Goody, M. F., Sher, R. B. & Henry, C. A. Hanging on for the ride: Adhesion to the extracellular matrix mediates cellular responses in skeletal muscle morphogenesis and disease. *Developmental Biology* **401,** 75–91 (2015).

217. Zolkiewska, A. & Moss, J. Integrin α7 as substrate for a glycosylphosphatidylinositol-anchored ADP- ribosyltransferase on the surface of skeletal muscle cells. *J. Biol. Chem.* **268,** 25273–25276 (1993).

218. Zolkiewska, A. & Moss, J. Processing of ADP-ribosylated integrin α7 in skeletal muscle myotubes. *J. Biol. Chem.* **270,** 9227–9233 (1995).

219. Hohenester, E. & Yurchenco, P. D. Laminins in basement membrane assembly. *Cell Adhesion and Migration* **7,** 56–63 (2013).

220. Goody, M. F., Kelly, M. W., Lessard, K. N., Khalil, A. & Henry, C. A. Nrk2b-mediated NAD+ production regulates cell adhesion and is required for muscle morphogenesis in vivo. Nrk2b and NAD+ in muscle morphogenesis. *Dev. Biol.* **344,** 809–826 (2010).

221. Fulco, M. *et al.* Sir2 regulates skeletal muscle differentiation as a potential sensor of the redox state. *Mol. Cell* **12,** 51–62 (2003).

222. Oláh, G. *et al.* Differentiation-associated downregulation of poly(ADP-Ribose) polymerase-1 expression in myoblasts serves to increase their resistance to oxidative stress. *PLoS One* **10,** (2015).

223. Ryall, J. G. *et al.* The NAD(+)-dependent SIRT1 deacetylase translates a metabolic switch into regulatory epigenetics in skeletal muscle stem cells. *Cell Stem Cell* **16,** 171–83 (2015).

224. Larsson, L. *et al.* Sarcopenia: Aging-Related Loss of Muscle Mass and Function. *Physiol. Rev.* **99,** 427–511 (2018).

225. Einsiedel, L. J. & Luff, A. R. Effect of partial denervation on motor units in the ageing rat medial gastronemius. *J. Neurol. Sci.* **112,** 178–184 (1992).

226. Baker, B. A. & Cutlip, R. G. Skeletal muscle injury versus adaptation with aging: Novel insights on perplexing paradigms. *Exercise and Sport Sciences Reviews* **38,** 10–16 (2010).

227. HARMAN, D. The Biologic Clock: The Mitochondria? *J. Am. Geriatr. Soc.* **20,** 145–147 (1972).

228. Crane, J. D., Devries, M. C., Safdar, A., Hamadeh, M. J. & Tarnopolsky, M. A. The effect of aging on human skeletal muscle mitochondrial and intramyocellular lipid ultrastructure. *Journals Gerontol. - Ser. A Biol. Sci. Med. Sci.* **65,** 119–128 (2010).

229. Welle, S. *et al.* Reduced amount of mitochondrial DNA in aged human muscle. *J. Appl. Physiol.* **94,** 1479–1484 (2015).

230. Bua, E. *et al.* Mitochondrial DNA–Deletion Mutations Accumulate Intracellularly to Detrimental Levels in Aged Human Skeletal Muscle Fibers. *Am. J. Hum. Genet.* **79,** 469–480 (2006).

231. Short, K. R. *et al.* Decline in skeletal muscle mitochondrial function with aging in humans. *Proc. Natl. Acad. Sci.* **102,** 5618–5623 (2005).

232. Beregi, E. & Regius, O. Comparative morphological study of age related mitochondrial changes of the lymphocytes and skeletal muscle cells. *Acta*

Morphol. Hung. **35,** 219–24 (1987).

233. Koltai, E. *et al.* Exercise alters SIRT1, SIRT6, NAD and NAMPT levels in skeletal muscle of aged rats. *Mech. Ageing Dev.* **131,** 21–28 (2010).

234. Minor, R. K. *et al.* SRT1720 improves survival and healthspan of obese mice. *Sci. Rep.* **1,** 1–10 (2011).

235. Howitz, K. T. *et al.* Small molecule activators of sirtuins extend Saccharomyces cerevisiae lifespan. *Nature* **425,** 191–196 (2003).

236. Goody, M. F. & Henry, C. A. A need for NAD+ in muscle development, homeostasis, and aging. *Skeletal Muscle* **8,** (2018).

237. Stump, C. S., Henriksen, E. J., Wei, Y. & Sowers, J. R. The metabolic syndrome: Role of skeletal muscle metabolism. *Ann. Med.* **38,** 389–402 (2006).

238. Smith, A. G. & Muscat, G. E. O. Skeletal muscle and nuclear hormone receptors: Implications for cardiovascular and metabolic disease. *Int. J. Biochem. Cell Biol.* **37,** 2047–2063 (2005).

239. Petersen, K. F. *et al.* Mitochondrial dysfunction in the elderly: Possible role in insulin resistance. *Science (80-.).* **300,** 1140–1142 (2003).

240. Gastebois, C. *et al.* Transition from physical activity to inactivity increases skeletal muscle miR-148b content and triggers insulin resistance. *Physiol. Rep.* **4,** (2016).

241. Van Der Hoorn, J. W. A. *et al.* Niacin increases HDL by reducing hepatic expression and plasma levels of cholesteryl ester transfer protein in APOE*3Leiden.CETP mice. *Arterioscler. Thromb. Vasc. Biol.* **28,** 2016–2022 (2008).

242. Luria, M. H. & Sapoznikov, D. Raising HDL cholesterol with low-dose nicotinic acid and bezafibrate: Preliminary experience. *Postgrad. Med. J.* **69,** 296–299 (1993).

243. Ye, X. *et al.* Sirtuins in glucose and lipid metabolism. *Oncotarget* **8,** (2017).

244. Canto, C., Menzies, K. J. & Auwerx, J. NAD(+) Metabolism and the Control of Energy Homeostasis: A Balancing Act between Mitochondria and the Nucleus. *Cell Metab* **22,** 31–53 (2015).

245. Mitchell, S. J. *et al.* Nicotinamide Improves Aspects of Healthspan, but Not Lifespan, in Mice. *Cell Metab.* **27,** 667–676.e4 (2018).

246. Bitterman, K. J., Anderson, R. M., Cohen, H. Y., Latorre-Esteves, M. & Sinclair, D. A. Inhibition of silencing and accelerated aging by nicotinamide, a putative negative regulator of yeast Sir2 and human SIRT1. *J. Biol. Chem.* **277,** 45099–45107 (2002).

247. Uddin, G. M., Youngson, N. A., Sinclair, D. A. & Morris, M. J. Head to head

comparison of short-term treatment with the NAD+ precursor nicotinamide mononucleotide (NMN) and 6 weeks of exercise in obese female mice. *Front. Pharmacol.* **7,** (2016).

248. Mills, K. F. *et al.* Long-Term Administration of Nicotinamide Mononucleotide Mitigates Age-Associated Physiological Decline in Mice. *Cell Metab.* **24,** 795–806 (2016).

249. Yao, Z., Yang, W., Gao, Z. & Jia, P. Nicotinamide mononucleotide inhibits JNK activation to reverse Alzheimer disease. *Neurosci. Lett.* **647,** 133–140 (2017).

250. Wang, X., Hu, X., Yang, Y., Takata, T. & Sakurai, T. Nicotinamide mononucleotide protects against β-amyloid oligomer-induced cognitive impairment and neuronal death. *Brain Res.* **1643,** 1–9 (2016).

251. de Picciotto, N. E. *et al.* Nicotinamide mononucleotide supplementation reverses vascular dysfunction and oxidative stress with aging in mice. *Aging Cell* **15,** 522–530 (2016).

252. Grozio, A. *et al.* Slc12a8 is a nicotinamide mononucleotide transporter. *Nat. Metab.* **1,** 47–57 (2019).

253. Ratajczak, J. *et al.* NRK1 controls nicotinamide mononucleotide and nicotinamide riboside metabolism in mammalian cells. *Nat. Commun.* **7,** (2016).

254. Trammell, S. A. J. *et al.* Nicotinamide riboside is uniquely and orally bioavailable in mice and humans. *Nat. Commun.* **7,** (2016).

255. Gong, B. *et al.* Nicotinamide riboside restores cognition through an upregulation of proliferator-activated receptor-γ coactivator 1α regulated β-secretase 1 degradation and mitochondrial gene expression in Alzheimer's mouse models. *Neurobiol. Aging* **34,** 1581–1588 (2013).

256. Cantó, C. *et al.* The NAD+precursor nicotinamide riboside enhances oxidative metabolism and protects against high-fat diet-induced obesity. *Cell Metab.* **15,** 838–847 (2012).

257. Zhang, H. *et al.* NAD+ repletion improves mitochondrial and stem cell function and enhances life span in mice. *Science (80-.).* **352,** aaf2693 (2016).

258. Liu, L. *et al.* Quantitative Analysis of NAD Synthesis-Breakdown Fluxes. *Cell Metab.* **27,** 1067–1080.e5 (2018).

259. Yang, Y., Mohammed, F. S., Zhang, N. & Sauve, A. A. Dihydronicotinamide riboside is a potent NAD + concentration enhancer in vitro and in vivo . *J. Biol. Chem.* jbc.RA118.005772 (2019). doi:10.1074/jbc.ra118.005772

260. Giroud-Gerbetant, J. *et al.* A reduced form of nicotinamide riboside defines a new path for NAD+ biosynthesis and acts as an orally bioavailable NAD+ precursor. *Mol. Metab.* (2019). doi:10.1016/j.molmet.2019.09.013

261. Fang, E. F. *et al.* NAD+ in Aging: Molecular Mechanisms and Translational Implications. *Trends in Molecular Medicine* **23,** 899–916 (2017).

262. Yaffe, D. & Saxel, O. Serial passaging and differentiation of myogenic cells isolated from dystrophic mouse muscle. *Nature* **270,** 725–727 (1977).

263. Tan, B. *et al.* Inhibition of nicotinamide phosphoribosyltransferase (NAMPT), an enzyme essential for NAD^+ biosynthesis, leads to altered carbohydrate metabolism in cancer cells. *J. Biol. Chem.* **290,** 15812–15824 (2015).

264. Kazimierczuk, K. & Orekhov, V. Y. Accelerated NMR spectroscopy by using compressed sensing. *Angew. Chemie - Int. Ed.* **50,** 5556–5559 (2011).

265. Delaglio, F. *et al.* NMRPipe: A multidimensional spectral processing system based on UNIX pipes. *J. Biomol. NMR* **6,** 277–293 (1995).

266. Orekhov, V. Y. & Jaravine, V. A. Analysis of non-uniformly sampled spectra with multi-dimensional decomposition. *Prog. Nucl. Magn. Reson. Spectrosc.* **59,** 271–292 (2011).

267. Wishart, D. S. *et al.* HMDB: The human metabolome database. *Nucleic Acids Res.* **35,** (2007).

268. Chong, M. *et al.* Combined Analysis of NMR and MS Spectra (CANMS). *Angew. Chemie - Int. Ed.* **56,** 4140–4144 (2017).

269. McArdle, A. Skeletal muscle loss: sarcopenia and inactivity. *Bone Abstr.* (2013). doi:10.1530/boneabs.1.s2.1

270. Mouchiroud, L. *et al.* XThe NAD+/sirtuin pathway modulates longevity through activation of mitochondrial UPR and FOXO signaling. *Cell* **154,** (2013).

271. Yoshino, J., Baur, J. A. & Imai, S. NAD + Intermediates: The Biology and Therapeutic Potential of NMN and NR. *Cell Metab.* (2017). doi:10.1016/j.cmet.2017.11.002

272. Trammell, S. A. J. *et al.* Nicotinamide riboside opposes type 2 diabetes and neuropathy in mice. *Sci. Rep.* **6,** (2016).

273. Elhassan, Y. S. *et al.* Nicotinamide Riboside Augments the Aged Human Skeletal Muscle NAD+ Metabolome and Induces Transcriptomic and Anti-inflammatory Signatures. *Cell Rep.* **28,** 1717–1728.e6 (2019).

274. Cantó, C. *et al.* AMPK regulates energy expenditure by modulating NAD + metabolism and SIRT1 activity. *Nature* **458,** 1056–1060 (2009).

275. Chen, D. *et al.* Tissue-specific regulation of SIRT1 by calorie restriction. *Genes Dev.* **22,** 1753–1757 (2008).

276. Samal, B. *et al.* Cloning and characterization of the cDNA encoding a novel human pre-B-cell colony-enhancing factor. *Mol. Cell. Biol.* **14,** 1431–1437 (1994).

277. Otero, M. *et al.* Changes in plasma levels of fat-derived hormones adiponectin, leptin, resistin and visfatin in patients with rheumatoid arthritis. *Ann. Rheum. Dis.* **65,** 1198–1201 (2006).

278. Gross, V., Andus, T., Caesar, I., Roth, M. & Schölmerich, J. Evidence for continuous stimulation of interleukin-6 production in Crohn's disease. *Gastroenterology* **102,** 514–519 (1992).

279. Spector, R. Niacinamide transport through the blood-brain barrier. *Neurochem. Res.* **12,** 27–31 (1987).

280. Holland, M. A., Tan, A. A., Smith, D. C. & Hoane, M. R. Nicotinamide treatment provides acute neuroprotection and GFAP regulation following fluid percussion injury. *J. Neurotrauma* **25,** 140–152 (2008).

281. Maiese, K. & Chong, Z. Z. Nicotinamide: Necessary nutrient emerges as a novel cytoprotectant for the brain. *Trends in Pharmacological Sciences* **24,** 228–232 (2003).

282. Naia, L. *et al.* Comparative Mitochondrial-Based Protective Effects of Resveratrol and Nicotinamide in Huntington's Disease Models. *Mol. Neurobiol.* **54,** 5385–5399 (2017).

283. Mori, Y. *et al.* Toxic effects of nicotinamide methylation on mouse brain striatum neuronal cells and its relation to manganese. *Environ. Health Prev. Med.* **17,** 371–376 (2012).

284. Parsons, R. B., Smith, S. W., Waring, R. H., Williams, A. C. & Ramsden, D. B. High expression of nicotinamide N-methyltransferase in patients with idiopathic Parkinson's disease. *Neurosci. Lett.* **342,** 13–16 (2003).

285. El Borolossy, R., El Wakeel, L. M., El Hakim, I. & Sabri, N. Efficacy and safety of nicotinamide in the management of hyperphosphatemia in pediatric patients on regular hemodialysis. *Pediatr. Nephrol.* **31,** 289–296 (2016).

286. Rutkowski, B. *et al.* N-methyl-2-pyridone-5-carboxamide: A novel uremic toxin? *Kidney Int.* **63,** S19–S21 (2003).

287. Lenglet, A. *et al.* N-methyl-2-pyridone-5-carboxamide (2PY) — Major metabolite of nicotinamide: An update on an old uremic Toxin. *Toxins* **8,** (2016).

288. Martens, C. R. *et al.* Chronic nicotinamide riboside supplementation is well-Tolerated and elevates NAD+in healthy middle-Aged and older adults. *Nat. Commun.* **9,** (2018).

289. Airhart, S. E. *et al.* An open-label, non-randomized study of the pharmacokinetics of the nutritional supplement nicotinamide riboside (NR) and its effects on blood NAD+ levels in healthy volunteers. *PLoS One* **12,** (2017).

290. Yan, L.-J., Wu, J., Jin, Z. & Zheng, H. Sources and implications of NADH/NAD+ redox imbalance in diabetes and its complications. *Diabetes,*

Metab. Syndr. Obes. Targets Ther. 145 (2016). doi:10.2147/DMSO.S106087

291. Kaur, G. & Dufour, J. M. Cell lines: Valuable tools or useless artifacts. *Spermatogenesis* **2,** 1–5 (2012).

292. Ramsden, D. B., Waring, R. H., Barlow, D. J. & Parsons, R. B. Nicotinamide N-methyltransferase in health and cancer. *International Journal of Tryptophan Research* **10,** (2017).

293. Davila, A. *et al.* Nicotinamide adenine dinucleotide is transported into mammalian mitochondria. *Elife* **7,** (2018).

294. Yang, Y., Mohammed, F. S., Zhang, N. & Sauve, A. A. Dihydronicotinamide riboside is a potent NAD concentration enhancer in vitro and in vivo. *J. Biol. Chem.* **294,** 9295–9307 (2019).

295. Trammell, S. A. J. & Brenner, C. Targeted, LCMS-based metabolomics for quantitative measurement of NAD+ metabolites. *Computational and Structural Biotechnology Journal* **4,** e201301012 (2013).

296. Morio, B. *et al.* Muscle fatty acid oxidative capacity is a determinant of whole body fat oxidation in elderly people. *Am. J. Physiol. - Endocrinol. Metab.* **280,** (2001).

297. B.C., B. & G.A., B. Respiratory gas-exchange ratios during graded exercise in fed and fasted trained and untrained men. *Journal of Applied Physiology* **86,** 479–487 (1999).

298. Schefer, V. & Talan, M. I. Oxygen consumption in adult and aged C57BL/6J mice during acute treadmill exercise of different intensity. *Exp. Gerontol.* **31,** 387–392 (1996).

299. Fernández-Verdejo, R., Ravussin, E., Speakman, J. R. & Galgani, J. E. Progress and challenges in analyzing rodent energy expenditure. *Nat. Methods* **16,** 797–799 (2019).

300. Kourtzidis, I. A. *et al.* Nicotinamide riboside supplementation dysregulates redox and energy metabolism in rats: Implications for exercise performance. *Exp. Physiol.* **103,** 1357–1366 (2018).

301. Doig, C. L. *et al.* Induction of the nicotinamide riboside kinase NAD⁺ salvage pathway in skeletal muscle of H6PDH KO mice. *bioRxiv* 567297 (2019). doi:10.1101/567297

302. White, a. T. & Schenk, S. NAD+/NADH and skeletal muscle mitochondrial adaptations to exercise. *AJP Endocrinol. Metab.* **303,** E308–E321 (2012).

303. Shibata, K., Matsumoto, K., Fushiki, T. & Sugimoto, E. Effects of Exercise on the Metabolism of NAD in Rats. *Biosci. Biotechnol. Biochem.* **58,** 1763–1766 (1994).

304. Graham, T., Sjøgaard, G., Löllgen, H. & Saltin, B. NAD in muscle of man at rest

and during exercise. *Pflügers Arch. Eur. J. Physiol.* **376,** 35–39 (1978).

305. Gardell, S. J. *et al.* Boosting NAD+ with a small molecule that activates NAMPT. *Nat. Commun.* (2019). doi:10.1038/s41467-019-11078-z

306. Hung, Y. P., Albeck, J. G., Tantama, M. & Yellen, G. Imaging cytosolic NADH-NAD(+) redox state with a genetically encoded fluorescent biosensor. *Cell Metab.* **14,** 545–54 (2011).

307. Belenky, P. *et al.* Nicotinamide Riboside Promotes Sir2 Silencing and Extends Lifespan via Nrk and Urh1/Pnp1/Meu1 Pathways to NAD+. *Cell* **129,** 473–484 (2007).

308. Camacho-Pereira, J. *et al.* CD38 Dictates Age-Related NAD Decline and Mitochondrial Dysfunction through an SIRT3-Dependent Mechanism. *Cell Metab.* **23,** 1127–1139 (2016).

309. Fu, X. *et al.* Obesity impairs skeletal muscle regeneration through inhibition of AMPK. *Diabetes* **65,** 188–200 (2016).

310. Phielix, E. & Mensink, M. Type 2 Diabetes Mellitus and Skeletal Muscle Metabolic Function. *Physiol. Behav.* **94,** 252–258 (2008).

311. Garten, A., Petzold, S., Körner, A., Imai, S. ichiro & Kiess, W. Nampt: linking NAD biology, metabolism and cancer. *Trends in Endocrinology and Metabolism* **20,** 130–138 (2009).

312. Escande, C. *et al.* Flavonoid apigenin is an inhibitor of the NAD+ase CD38: Implications for cellular NAD+ metabolism, protein acetylation, and treatment of metabolic syndrome. *Diabetes* **62,** 1084–1093 (2013).

313. Borradaile, N. M. & Pickering, G. J. Nicotinamide phosphoribosyltransferase imparts human endothelial cells with extended replicative lifespan and enhanced angiogenic capacity in a high glucose environment. *Aging Cell* **8,** 100–112 (2009).

314. Schafer, Z. T. *et al.* Antioxidant and oncogene rescue of metabolic defects caused by loss of matrix attachment. *Nature* **461,** 109–13 (2009).

315. Yang, J. P. *et al.* Effects of antioxidants in reducing accumulation of fat in hepatocyte. *Int. J. Mol. Sci.* **19,** (2018).

316. Bielefeld, D. R., Vary, T. C. & Neely, J. R. Inhibition of carnitine palmitoyl-CoA transferase activity and fatty acid oxidation by lactate and oxfenicine in cardiac muscle. *J. Mol. Cell. Cardiol.* **17,** 619–625 (1985).

317. Lane, A. N. & Fan, T. W. M. Regulation of mammalian nucleotide metabolism and biosynthesis. *Nucleic Acids Research* **43,** 2466–2485 (2015).

318. Dostalek, M. *et al.* Development of oxidative stress by cytochrome P450 induction in rodents is selective for barbiturates and related to loss of pyridine nucleotide-dependent protective systems. *J. Biol. Chem.* **283,** 17147–17157

(2008).

319. Hikosaka, K. *et al.* Deficiency of nicotinamide mononucleotide adenylyltransferase 3 (Nmnat3) causes hemolytic anemia by altering the glycolytic flow in mature erythrocytes. *J. Biol. Chem.* **289,** 14796–14811 (2014).

320. Debray, F. G. *et al.* Diagnostic accuracy of blood lactate-to-pyruvate molar ratio in the differential diagnosis of congenital lactic acidosis. *Clin. Chem.* **53,** 916–921 (2007).

321. Fleischer, A. B., Shurmantine, W. O., Luxon, B. A. & Forker, E. L. Palmitate uptake by hepatocyte monolayers. Effect of albumin binding. *J. Clin. Invest.* **77,** 964–970 (1986).

322. Bastie, C. C. *et al.* FoxO1 stimulates fatty acid uptake and oxidation in muscle cells through CD36-dependent and -independent mechanisms. *J. Biol. Chem.* **280,** 14222–14229 (2005).

323. Houtkooper, R. H. *et al.* The metabolic footprint of aging in mice. *Sci. Rep.* **1,** (2011).

324. Elkalaf, M., Anděl, M. & Trnka, J. Low Glucose but Not Galactose Enhances Oxidative Mitochondrial Metabolism in C2C12 Myoblasts and Myotubes. *PLoS One* **8,** (2013).

325. Ekberg, K. *et al.* Contributions by kidney and liver to glucose production in the postabsorptive state and after 60 h of fasting. *Diabetes* **48,** 292–298 (1999).

326. Agerholm, M. *et al.* Perturbations of NAD + salvage systems impact mitochondrial function and energy homeostasis in mouse myoblasts and intact skeletal muscle . *Am. J. Physiol. Metab.* **314,** E377–E395 (2017).

327. Ashiharab, B. A. M. and H. Purine and Pyrimidine Nucleotide Metabolism. *Arab. Book. Am. Soc. Plant Biol.* **1,** 1–20 (2002).

328. Lowenstein, J. M. & Goodman, M. N. The purine nucleotide cycle in skeletal muscle. *Fed. Proc.* **37,** 2308–12 (1978).

329. Barron, J. T., Gu, L. & Parrillo, J. E. Malate-aspartate shuttle, cytoplasmic NADH redox potential, and energetics in vascular smooth muscle. *J. Mol. Cell. Cardiol.* **30,** 1571–1579 (1998).

330. Kauppinen, R. A., Sihra, T. S. & Nicholls, D. G. Aminooxyacetic acid inhibits the malate-aspartate shuttle in isolated nerve terminals and prevents the mitochondria from utilizing glycolytic substrates. *BBA - Mol. Cell Res.* **930,** 173–178 (1987).

331. Ahn, C. S. & Metallo, C. M. Mitochondria as biosynthetic factories for cancer proliferation. *Cancer and Metabolism* **3,** (2015).

332. Balcke, G. U. *et al.* Linking energy metabolism to dysfunctions in mitochondrial

respiration - A metabolomics in vitro approach. *Toxicol. Lett.* **203,** 200–209 (2011).

333. Mráček, T., Drahota, Z. & Houštěk, J. The function and the role of the mitochondrial glycerol-3-phosphate dehydrogenase in mammalian tissues. *Biochim. Biophys. Acta (BBA)- …* **1827,** 401–410 (2013).

334. Eto, K. *et al.* Role of NADH shuttle system in glucose-induced activation of mitochondrial metabolism and insulin secretion. *Science (80-.).* **283,** 981–985 (1999).

335. Nasu, S., Wicks, F. D. & Gholson, R. K. L-Aspartate oxidase, a newly discovered enzyme of Escherichia coli, is the B protein of quinolinate synthetase. *J. Biol. Chem.* **257,** 626–632 (1982).

336. Katoh, A. Early Steps in the Biosynthesis of NAD in Arabidopsis Start with Aspartate and Occur in the Plastid. *PLANT Physiol.* **141,** 851–857 (2006).

337. Katoh, A., Hashimoto, T., Kato, A. & Hashimoto, T. MOLECULAR BIOLOGY OF PYRIDINE NUCLEOTIDE AND NICOTINE BIOSYNTHESIS. *Front. Biosci.* **9,** 1577–1586 (2004).

338. Garcia-Bermudez, J. *et al.* Aspartate is a limiting metabolite for cancer cell proliferation under hypoxia and in tumours. *Nat. Cell Biol.* **20,** 775–781 (2018).

339. Zhao, G. *et al.* Discovery of a Highly Selective NAMPT Inhibitor That Demonstrates Robust Efficacy and Improved Retinal Toxicity with Nicotinic Acid Co-administration. *Mol. Cancer Ther.* molcanther.0674.2016 (2017). doi:10.1158/1535-7163.MCT-16-0674

340. Espindola-Netto, J. M. *et al.* Preclinical efficacy of the novel competitive NAMPT inhibitor STF-118804 in pancreatic cancer. *Oncotarget* **8,** (2017).

341. R.N., S., W.J.F., E., T.M., B. & F.C., H. Establishment of blood analyte intervals for laboratory mice and rats by use of a portable clinical analyzer. *J. Am. Assoc. Lab. Anim. Sci.* **46,** 47–52 (2007).

342. Messina, G. *et al.* Exercise causes muscle GLUT4 translocation in an insulin-independent manner. *Biol. Med.* **7,** (2015).

343. Shulman, G. I. *et al.* Quantitation of muscle glycogen synthesis in normal subjects and subjects with non-insulin-dependent diabetes by ^{13}C nuclear magnetic resonance spectroscopy. *N. Engl. J. Med.* **322,** (1990).

344. Nilsson, L. H. & Hultman, E. Liver and muscle glycogen in man after glucose and fructose infusion. *Scand. J. Clin. Lab. Invest.* **33,** 5–10 (1974).

345. Aguilar, C. A. *et al.* In vivo monitoring of transcriptional dynamics after lower-limb muscle injury enables quantitative classification of healing. *Sci. Rep.* **5,** (2015).

346. Lavery, G. G. *et al.* Deletion of hexose-6-phosphate dehydrogenase activates

the unfolded protein response pathway and induces skeletal myopathy. *J. Biol. Chem.* **283,** 8453–8461 (2008).

347. Xu, W. *et al.* Lethal Cardiomyopathy in Mice Lacking Transferrin Receptor in the Heart. *Cell Rep.* **13,** 533–545 (2015).

348. Diguet, N. *et al.* Nicotinamide riboside preserves cardiac function in a mouse model of dilated cardiomyopathy. *Circulation* **137,** 2256–2273 (2018).

349. Grzelkowska-Kowalczyk, K. The Importance of Extracellular Matrix in Skeletal Muscle Development and Function. in *Composition and Function of the Extracellular Matrix in the Human Body* (2016). doi:10.5772/62230

350. Miller, B. F. *et al.* Coordinated collagen and muscle protein synthesis in human patella tendon and quadriceps muscle after exercise. *J. Physiol.* **567,** 1021–1033 (2005).

351. Han, X. Y. *et al.* Increased mRNAs for procollagens and key regulating enzymes in rat skeletal muscle following downhill running. *Pflugers Arch. Eur. J. Physiol.* **437,** 857–864 (1999).

352. He, L. *et al.* The Physiological Basis and Nutritional Function of Alpha-ketoglutarate. *Curr. Protein Pept. Sci.* **16,** 576–581 (2015).

353. Drucker, D. J. Never Waste a Good Crisis: Confronting Reproducibility in Translational Research. *Cell Metabolism* **24,** 348–360 (2016).

354. Dollerup, O. L. *et al.* Effects of nicotinamide riboside on endocrine pancreatic function and incretin hormones in obese, non-diabetic men. *J. Clin. Endocrinol. Metab.* (2019). doi:10.1210/jc.2019-01081

355. Dollerup, O. L. *et al.* A randomized placebo-controlled clinical trial of nicotinamide riboside in obese men: Safety, insulin-sensitivity, and lipid-mobilizing effects. *Am. J. Clin. Nutr.* **108,** 343–353 (2018).

356. Erum, J. Van, Dam, D. Van & Deyn, P. P. De. Jo ur na l P of. *Neurosci. Biobehav. Rev.* 100632 (2019). doi:10.1016/j.neubiorev.2019.07.019

357. Pette, D. The adaptive potential of skeletal muscle fibers. *Can. J. Appl. Physiol.* **27,** 423–448 (2002).